Decentralized Morphological Stiffness Tunable Interface for Continuum Manipulators

Sadati, Seyedmohammadhadi

Awarding institution:
King's College London

King's College London
Department of Informatics

Decentralized Morphological Stiffness Tunable Interface for Continuum Manipulators

S.M.Hadi Sadati

Supervisors:

Dr. Thrishantha Nanayakkara

Dr. Matthew Howard

Submitted in part fulfilment of the requirements for the degree of
Doctor of Philosophy in Robotics of King's College London

Dedication

This thesis is dedicated to may parents, *Mahboubeh & Habib*, whose sacrifices are the reason for my achievements,

and to my beloved wife, *Elnaz*, who is the only one who made every stage of my PhD joyful.

'Everything should be made as simple as possible, but no simpler.'

Albert Einstein

Declaration

I hereby declare that except where specific reference is made to the work of others, the contents of this dissertation are original and have not been submitted in whole or in part for consideration for any other degree or qualification in this, or any other university. This dissertation is my own work and contains nothing which is the outcome of work done in collaboration with others, except as specified in the text and Acknowledgements.

Seyedmohammadhadi Sadati

August 2017

Acknowledgements

I would like to express my highest gratitude to:

- Dr. Thrishantha Nanayakkara, Prof. Kaspar Althoefer, Dr. Matthew Howard and Prof. Ian D. Walker for their contribution, support and encouragement that I enjoyed throughout my PhD;
- Prof. Jonathan Rossiter and Dr. Dana D. Damian for their helpful comments and suggestions;
- My colleagues and friends Ali Shiva, Dr. S. Elnaz Naghibi, Luis Sullivan, Aditya Gupta, Hadha Afrisal, Michael Zheng and Pendar Ghalamchi for their contributions in my research;
- My parents, Mahboubeh & Habib, and my beloved wife, Elnaz, for their unconditional support throughout my research.

This work is supported in part by the Seventh Framework Program of the European Commission in the framework of EU project STIFF-FLOP, grant agreement 287728; the U.K. Engineering and Physical Sciences Research Council (EPSRC) under MOTION Grant: EP/N03211X/2; and European Union H2020 project FourByThree code 637095.

Abstract

This thesis investigates how the problem of stiffness regulation of continuum manipulators can be simplified by inspiration from morphology of biological fish scales and experimental observation of manipulator geometry deformation. Soft continuum trunk and tentacle manipulators have high inherent dexterity and reconfigurability and have become an attractive candidate for safe manipulation and explorations in surgical and space robotic applications recently. The passive shape adaptation and large reachable configuration space features of this class of manipulators, due to their highly deformable nature, make them a perfect choice for minimally invasive insertion of surgical tools in the confined maze-like space in many robotic surgery sites. However, achieving accuracy in precise tasks is a challenge with these highly flexible structures, for which stiffness variable designs based on jamming, smart material, antagonistic actuation and morphing structures are introduced in the recent years. After a careful review and comparative study of current methods on modeling and stiffness modulation of continuum manipulators, an analytical model is presented based on the geometry deformation of continuum manipulators and the Rivlins work on continuum media and adopted the Ritz and Galerkin methods to solve the dynamics of continuum manipulators based on Cosserat beam theory and principle of virtual work. Our new approach reduces model and control space dimension while preserving the accuracy. This enabled us to solve the stiffness regulation actuation and computation problems in the morphological level which highly simplifies the central control design. Two novel integrable helical interfaces inspired by the shape and special arrangement of fish scales morphology is designed using tendon driven and thermoactive low melting point actuation mechanisms. High stiffness range, very low hysteresis and easy integration to different manipulator designs are the advantages of our design compared to the previous research. An analytical model is derived based on which the performance of the design is optimized. A comparison between the presented robotic interface designs and a real fish skin suggests that natural scales may contribute in stiffness modulation of the fish body through jamming, e.g. due to external stream and steady water pressure. Finally, a novel decentralized morphological approach is implemented to regulate the regional stiffness of the continuum manipulator integrated with the designed jamming interfaces to

reject configuration disturbances and modulate the task space stiffness with possible application in soft tissue palpation.

Contents

List of Tables

List of Figures

Nomenclature

$'$	Superscript for deformed states in Geometry Deformation method
$[x]_\times$	Operator to create skew-symmetric matrix from vector x
α	Jagged surface slope angle
Δl	Axial deformation in experiments
δ	Variation
η	Displacement vector
η, ζ, ξ	Euler-angle set for each segment in Lumped System model
$\Gamma_{\mathrm{r}i}$	Transformation matrix for each segment in Lumped System model
γ	Helix lead angle
γ	Thread helix lead angle w.r.t. tube axis
$\hat{b}$	Binormal director in Frenet − Serret frame
$\hat{d}_i$	Direction vector for physical curvilinear frame with subscript 1 initially aligned with Cartesian x-direction
$\hat{n}$	Normal director in Frenet − Serret frame
$\hat{t}$	Tangential director in Frenet − Serret frame
κ	Curvature in Constant Curvature model
Λ	Cauchy-Green stretch tensor first invariant
λ_i	Cauchy-Green principle stretches for the i^{th} direction or state
μ_{r}	Bending damping in static tests

μ_{t} Axial damping in static tests

μ_{u} Bending viscous damping in dynamic tests

μ_{v} Axial viscous damping in dynamic tests

ν_{j0} LuGre model Stirbeck velocity coefficient

ν_{j} Relative velocity of contacting surfaces

ω Angular velocity

ϕ Polar location angle

Ψ Shape function matrix in identification based, Ritz and Ritz-Galerkin methods

ψ Polar location in local frame

ρ Position vector

σ Material density

σ_{j} LuGre model Stirbeck viscosity coefficient

τ Moment

θ Bent angle in Constant Curvature model

Υ Time-dependent coefficients in identification based method

* Superscript for guessed values

$_0$ Subscript for initial and boundary values

$_{(\ )}$ Bracket Subscript for independent variables

$_{,}$ Operator to take derivative w.r.t. the following parameters

$_\kappa$ Subscript for total value of Constant Curvature parameters

$_{\mathrm{b}}$ Subscript for body load

$_{\mathrm{c}}$ Subscript for cross-section

$_{\mathrm{d}}$ Subscript for deformed state

$_{\mathrm{E}}$ Subscript for elastic deformation

G	Subscript for air pressure
heal	Healing strategy for temperature control
heat	Heating strategy for temperature control
h	Subscript for interface helix
js	Thermoactive joint structure parameters
j	Inter-locking scale joint parameters
L	Subscript for external load
pt	Subscript for pneumatic chamber shell
P	Subscript for plastic deformation
p	subscript for pressure chamber
r	Subscript for rotational terms in chapters 2-3 and tendon radial force in chapter 4
sc	Subscript for scale
sp	Low stiffness helical backbone parameters
th	Subscript for braid thread
tip	Subscript for tip position
t	Subscript for transnational terms in chapters 2-3 and tendon tension in chapter 4
y	Subscript for yield point
A	General coefficient
a	Area
A_{MD}	Correction factor for Constant Curvature Modified model
B	General coefficient
b	Mass of a disk in Lumped System model
b	Module body mass
b_{L}	External load mass at tip

C General coefficient

$c_{(t)}$ Time-dependent coefficients in Ritzand Ritz-Galerkin methods

C_Ψ Modification coefficient for shape function in Ritz and Ritz-Galerkin methods

D Matrix of velocity dependent inertial terms

d Vector of velocity dependent inertial terms

E Material Elasticity modulus

f_q Non-conservative forces in Lumped System model

f_{fh} Tendon tension reduction due to friction

f_{G} General kinematic map in continuum manipulator model

f_{g} External gravity force in Lumped System model

f_{r} Tendon radial force

f_{S} Body specific static and dynamic map in continuum manipulator model

f_{t} Tendon tension

G Shear modulus

h_{w} Shaft active length in thermoactive setup

I Electric current value

J Second moment of area

J_{ϕ_κ} Second moment of area around bending axis

J_{m} Inertial matrix

K Stiffness matrix

k Stiffness coefficient

l Continuum cylinder length

l Module initial length

l_{fs} Force sensor length between segments

M Mass matrix

m Moment in local curvilinear frame

n Loads in local curvilinear frame

n_q Number of generalized coordinates

n_{h} Number of interface helix turns

n_{sc} Number of scales in a full turn

n_{th} Number of helix turns

p Input air pressure

q Generalized coordinates

R Rotation matrix

r radius

R^*_{r} Rotation matrix between Frenet − Serret and physical curvilinear frames

r_{c1} Body shell inner radius

r_{c2} Body shell outer radius

r_{o} Placement radius for pneumatic chambers

r_{p1} Pressure chamber inner radius

r_{p2} Pressure chamber outer radius

r_{b} Bent radius in Constant Curvature model

$r_{J\hat{d}_i}$ Effective radius for second moment of inertia along $\hat{d}_i$

R_{ri} Rotation matrix for each segment in Lumped System model

s Position along backbone

T Transformation matrix between generalized and Cartesian coordinates in chapters 2-3 and Temperature in chapter 5

U Unit deformation energy

u	vector of curvatures and torsion
V	Volume
v	strain vector
W	Weight matrix in Ritz and Ritz-Galerkin methods
w	Action in Principle of Virtual Work
CC	Constant Curvature
EB	Euler-Bernoulli model
g	Gravity
MD	Constant Curvature Modified model
NH	Neo-Hookean assumption
pid	PID closed-loop control term
PVW	Principle of Virtual Work
VC	Variable Curvature kinematics

Chapter 1

Introduction

1.1 Background

Performing complicated biological tasks such as manipulation in unpredictable conditions where safe interaction with the environment are important requires dexterity and compliance where low actuation energy, high dexterity, reachability, maneuverability, back drivability and self adjustablbility of continuum mechanisms are shown to be advantageous [1]. In nature, biological creatures benefit from compliant muscle-tendon-bone structures capable of exerting instantaneous high-peak forces and velocities necessary for such tasks [2]. On the other hand, to address the common problems with current actuation methods in robotics research, such as back drivability, stiffness control and energy consumption, different methods such as compliance actuation [3], Antagonistic actuation [4, 5], reconfigurable design [6], and more recently use of stiffness tuneable material [7] and morphing structures [8] are employed. The control of damping to achieve a desired stiffness is shown to be important too, for task accuracy and control stability [9, 10]. However, compliance has disadvantages such as reduced control bandwidth, stability issues and underdamped modes where high stiffness modes are required to achieve precision in tasks involving working against external loads [10].

Soft continuum manipulators, mostly inspired by octopus arms, snake, land animals' tongue and trunk, with high inherent dexterity and reconfigurability, have become an attractive candidate for safe manipulation and explorations in surgical and space robotic applications in recent years. The passive shape adaptation and large reachable configuration space features of this class of manipulators due to their highly deformable nature made them a perfect choice for minimally invasive insertion of surgical tools in the confined maze-like space in a robotic surgery [11, 12]. Among the continuum manipulator designs, braided pneumatic and hydraulic actuators provide a uniform homogeneous deformation, robust geometry and force control, and linear and reversible behavior [13, 14, 15, 16] compared to the non-braided versions [17, 18, 19] which circumferential expansion limits their application in confined space. The control design of such manipulators is mostly limited to simple kinematic and static models for the configuration and force control and observation [20]. Real-time accurate dynamic control of this class of manipulators considering their inhomogeneity and compound structure is still an open question where even the advantages and shortcomings of the current solutions are not addressed clearly in a comparative study of the methods in literature. Besides, accuracy in precise tasks is a challenge with highly flexible structures for which stiffness variable designs based on jamming, smart material, antagonistic actuation and morphing structures are introduced in the recent years [21]. The uncertainty in the material deformation due to highly elastic environment, insufficient flexibility and lack of control feedback are the limitations of continuum manipulators [22]. While most of the research have been focused on the design and modeling of soft manipulators, methods of stiffness control for soft media has recently shown to be important for efficient minimalist actuation, minimal invasive interaction, and control and sensing precision [23]. A review on different continuum manipulator designs is presented in Fig. 1.1.

As a biological solution, animal skin and scale in nature show stiffness regulation in response to irritation or penetrating forces. Many animal species such as fish, turtles, armadillo and snake have hard scale or osteoderms as flexible armor and a means

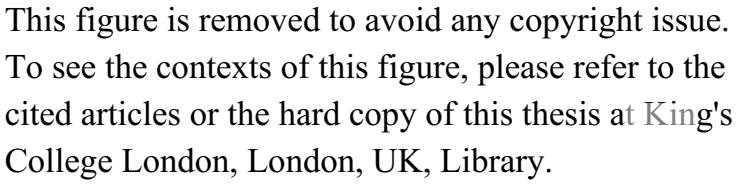

Figure 1.1: Review of different continuum manipulator designs, (a) an inflatable tendon driven design [24], (b) OCTArm with braided extensile pneumatic actuators [14], (c) a design with external braids and hydraulic actuators [25], (d) STIFF-FLOP with silicon actuator and body shell [26], (e) a shrinkable design with antagonistic tendon and pneumatic actuation [4], (f) a long tendon driven tendril design [27], (g) a SMA driven bio-inspired design [28].

of friction regulation in contact with the environment where finite size hard plates provides flexibility, protection, transparency and breathability with light weight [29]. While the scales slide almost freely in general movements, the overlapping scales are jammed as a result of normal penetration force while the overlapping area increases by inward bending of the skin to provide protective functionality [30]; however, the role of the passive or active scales jamming on the body stiffness adaptation has not yet been addressed.

In engineering tasks such as minimal invasive surgery [21], industrial [31] and in-space [32, 27] inspection, where continuum and soft robots are shown to be advantageous, multiple tools with different but fixed compliance and stiffness are usually used in different steps of a task. For examples, the tip bending stiffness of commercially available catheters varies between 16 and 31 [KNmm^2] [21]. Jamming concept

and stiffness tunable material are used in variable compliance continuum robot manipulation and inspection studies to achieve a universal solution for different steps of a task that requires different structural stiffness [21]. Such designs are beneficial for other futuristic variable compliance robotic studies too which are not utilized in real-life engineering applications yet. Jamming concept, for stiffness control through modulating the Coulomb friction and viscous damping between the jammed media, has been utilized in design of stiffness controllable actuators [33], flexible manipulators [34], variable stiffness joints [35], rehabilitation devices [36], stiffness displays [37], biomimetic organs [38], reconfigurable mechanisms [39] and grippers [40] of which a comprehensive review is presented in [21]. The comparative study by Wall et. al. on granular, layer and scale jamming used in a selective stiffness controllable pneumatic actuator, PneuFlex, showed the layer jamming arrangement to be the most capable design with an eight times increase in the stiffens and 2.23 times increase in the resisting force [33]. Tendon driven jamming is introduced recently to overcome portability limitation of pneumatic enabled jamming in underwater and space applications where a continuum rod flexural stiffness is controlled by modulating the shear friction force between the scales [38, 41] and helical rings [42]. The resulting Coulomb damping opposes the inter-layer shear forces caused by the external load bending momentum.

thermoactive stiffness tuneable structures and material have attracted much research in the past few years due to their high range of stiffness change, easy electrical modulation through heating and possible 3D printing fabrication [43]. Low melting point (LMP) alloy such as field's metal [44, 45, 46, 47, 48, 49, 43] and LMP composite material with inherent thermal instability such as wax [50] and ABS which are used as the base material in many standard 3D printing devices has been utilized to design 3D printable thermally stiffness tunable structures [51, 52, 53, 54]. As a result, new compound micro actuators capable of actuation and shape fixation with high reversibility and load bearing capacity are designed such as thermally stiffness tunable actuator fiber in [55] and thermally tunable shape memory electroactive

polymer in [56]. A series of publications by Yang and Chen in the last year on 3D printable thermally stiffness tunable structures shows the promising features of these LMP material including a hyper redundant robotic manipulator using a LMP composite to modulate the damping coefficient of spherical joints fabricated by a purpose built multi-extrude 3D printer [52], where a 4.65-5.76 times increase in the stiffness through glass transition of the LMP composite is observed [51]. A comprehensive review on the applications of LMP material in fabricating shape memory polymers for stiffness control, self healing, and shape reconfigurable applications can be found in the recent review article by Van Meerbeek, et. al. [43]. A review on different stiffening designs for continuum manipulators is presented in 1.2.

The reconfigurability and adoptive morphology of stiffness controllable mechanisms enable adaptive functionalities by minimizing trade-offs during certain tasks [64]; however, requires cumbersome analytical and computation tools to plan and control which cannot be addressed solely with the traditional approaches [65, 66, 67]. Recently, a new field of research, so-called embodied intelligence or morphological computation, has emerged where the physical body morphology is exploited as a means of control or computation [23, 68]. In this context, the traditional central numerical or neural circuits are replaced with the morphological computation power of available local and peripheral physical hardware. This results in a uniform and disperse control system where the tasks is fulfilled locally in separate portions and in different places, known as decentralized control design which is recently introduced in the soft robotic research [69]. It is shown in biological [70] and robotic [71, 72] studies that in a decentralized control system, while the local sensory and computation capabilities may be limited to simple or repetitive tasks, the system benefits from parallel computation and execution capability, lack of communication delay and breaking a complex problem into simple sub-problems. Following this short introduction, the used hardware and experimental procedure in this thesis is explained in the next section.

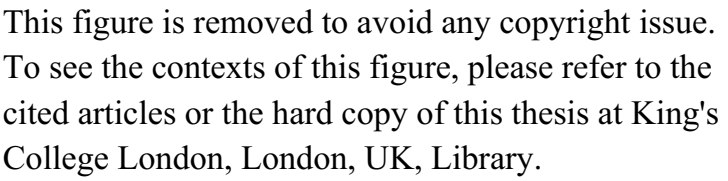

Figure 1.2: Review of different stiffness control designs for continuum manipulators, (a) a tendon driven interlocking design [57], (b) a fiber jamming design [58], (c) an tendon stiffening design for STIFF-FLOP [59], (d) granular jamming stiffening design for STIFF-FLOP [60], (e) tendon driven sccale jamming design for long tendril [38], (f) layer jamming design with overlapping flaps [61], (g) anisotropic stiffness control of a continuum manipulator with granular jamming [62], (h) granular jamming for stiffness control of continuum manipulator [63], (i) thermoactive stiffness controllable designs based on LMP alloy (Field's metal) [48] and (j) LMP composite (a wax coated 3D printed lattice structure) [50].

1.2 Used Hardware and Experimental Procedure

We used STIFF-FLOP (STIFFness controllable Flexible and Learn-able manipulator for surgical OPerations) pneumatic actuator modules [15] as a standard, simple yet accurate and durable design without inhomogeneous deformations, i.e. due to structure swell as in [19, 73]. A similar design is used in recent research [20, 74, 75]. A single STIFF-FLOP soft actuator module is a three degree of freedom (DOF) pneumatic continuum actuator with three braided extensor actuator chambers placed

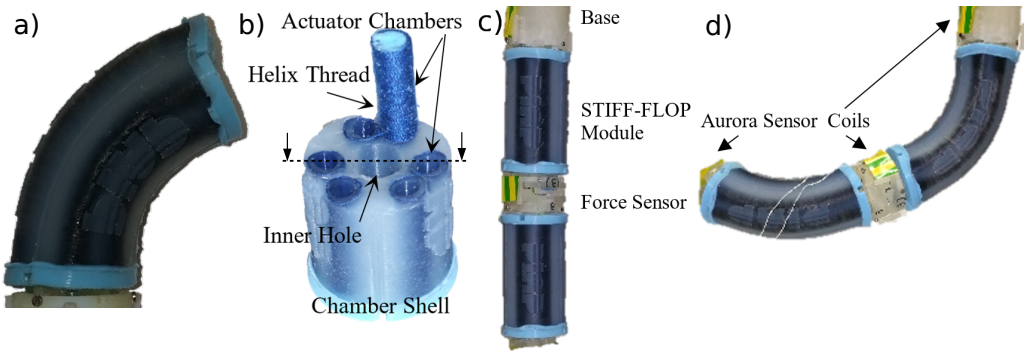

Figure 1.3: (a) A STIFF-FLOP module bending due to pressurization of one of its three pneumatic chambers, (b) module structure in a cross-section view, showing the 120 [deg] placement of three sets of double pneumatic chambers, (c) a continuum manipulator with two STIFF-FLOP pneumatic actuator modules, (d) the continuum manipulator in action.

with an offset from the module central axis and enclosed in a soft body shell shown in Fig. 1.3 [16, 15]. Soft silicon structures are molded using Ecoflex 50 (tensile strength 2.17 [MPa] and 100% modulus ($E_{100\%}$) 82.73 [KPa], from www.smooth-on.com) [16]. Structural parameters are presented in Table 1.1. Synchronized actuation of the pneumatic chambers causes the module to elongate while asynchronized actuation causes it to bend laterally. The module cross-section deforms from a perfect circular shape while bending, shown in Fig. 1.4. STIFF-FLOP pneumatic actuator chambers are Mckibben like highly elastic extensile pneumatic artificial muscles, threaded helically with an ordinary sewing thread (Fig. 1.6). The thread helix converts radial expansion of the pressurized tube to axial deformation. An extensile chamber, with a braid helix lead angle of more than 54.7 [deg], elongates while a contractile chamber, with a braid helix lead angle of less than 54.7 [deg], shrinks as they are pressurized [76, 77]. The thread constraints the radial and axial deformation of the tube while it should be free to slide tangentially. Braids in the well-known "OCT-Arm" series of continuum robots introduced by Pritts and Rahn [78], are to some extent free to slide tangentially [79] while they are implanted in the tube silicon body for the STIFF-FLOP. The threads may fold locally if they are constrained tangentially to the body as in the STIFF-FLOP case (Fig. 1.6.c). A body shell is required to constraint unwanted deformations of the chambers since the inhomogeneity of molding and braiding causes a single chamber to bend ran-

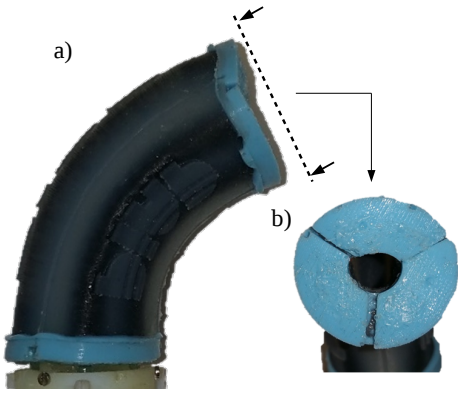

Figure 1.4: (a) A STIFF-FLOP module bending due to pressurization of one pneumatic chamber, (b) module cross-section deforms from a perfect circular shape when bent.

domly instead of pure elongation depicted in Fig. 1.6.b. The body shell is molded using Ecoflex 50 silicon around the braided chambers. A temporary fixture, which is replaced with silicone caps, hold the chambers in place while the silicone cures.

The modules are inherently compliant and soft, making them suitable for safe interaction in minimally invasive medical tasks. The uniform and tick body shell results in linear repeatable and durable performance. The relatively high actuation pressure range of the pneumatic actuators (0-2 [bar]) provides the necessary force and stiffness required for most of the minimal invasive surgeries (MIS)(17.2 [N/rad]) [61] and close to the specifications of the commercially available endoscopes (15-31 [KNmm^2]) [21]. We chose STIFF-FLOP modules because of their high repeatability and negligible performance change due to aging and fatigue during the experimental trials. The experimental results for different lateral external forces acting at the tip of a single STIFF-FLOP with new design module [15] shows small variance ($S^2 = 0.0016 - 0.0064$) and standard deviation ($S = 0.04 - 0.08$) for a straight and bent ($S^2 = 0.01 - 0.03$ and $S = 0.1 - 0.18$) configuration [59]. These values are very small for module deformation (elongation and bending angle) in different actuation scenarios [15]. However, accurate modeling of these modules are challenging due to inhomogeneities as a result of the fabrication process.

The STIFF-FLOP modules are highly flexible and sensitive to changes in the input pressure. Our tests show good repeatability in their actuation and fast linear re-

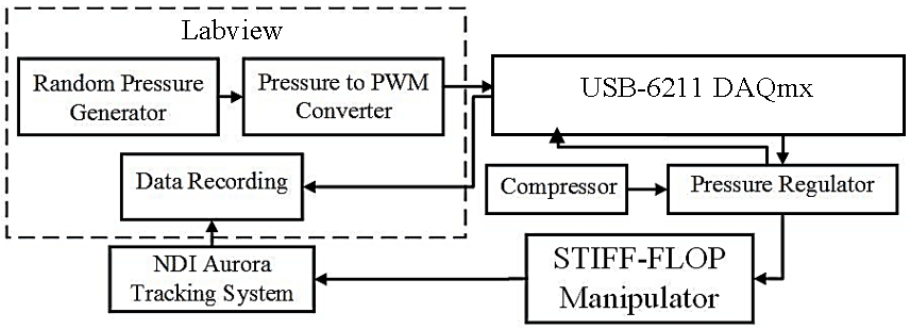

Figure 1.5: Experiment setup and control system diagram.

sponse to the input pressure. The molding process guarantees a robust module that can operate for a long time; however, their long-term repeatability has not been investigated yet. The handmade fabrication of the modules results in structural and performance differences. Different volume ratios of the silicone components, air bubbles trapped in the molding process, imperfections in the radial and angular positioning of the twin chambers and small differences in the active length and active surface area of the chambers due to excessive use of glue to support the caps in some cases result in differences in structural and performance characteristics of the modules. Two STIFF-FLOP modules have been used for the tests in this chapter. They have almost identical dimensions but different active length due to differences in their molding process. The different parameters are marked with a † in Table 1.1.

The modules are driven by a set of ITV0030-3BS-Q compact pressure regulators (SMC Pneumatic Ltd, Noblesville, United States) connected to a BAMBI MD Range, Model 150/500 pneumatic compressor (Bambi Air Compressors Ltd, Birmingham, United Kingdom). A LabView program is designed to feedback control the pressure regulators through USB connection and a USB-6211 DAQmx (National Instrument Ltd, Texas, United States) data acquisition board. We used a NDI Aurora (Northern Digital Inc, Ontario, Canada) tracking system to record the movement of each module tip. A control diagram for the experiment setup is presented in Fig. 1.5.

The results in this thesis are based on experimental setup dimensions (Table 1.1) and compared with the results from the following set of experiments.

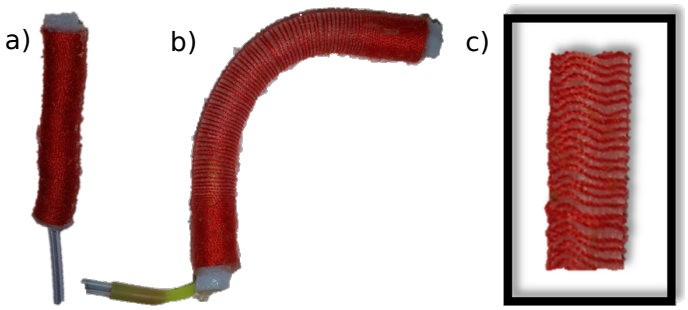

Figure 1.6: (a) A STIFF-FLOP braided extensor actuator, (b) the actuator bends instead of pure elongation due to inhomogeneity in the braiding and tube molding, (c) side view of a pressurized pneumatic chamber showing that the braid folds locally because the thread cannot slide on the tube while the chamber elongates and the tube cross-section (not shown in the figure) decreases (EXP.1).

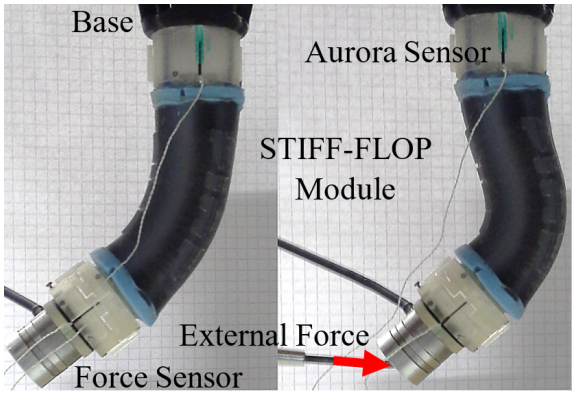

Figure 1.7: Experiments on one STIFF-FLOP module, (left) without and (right) with extensive external load at the tip (EXP.2).

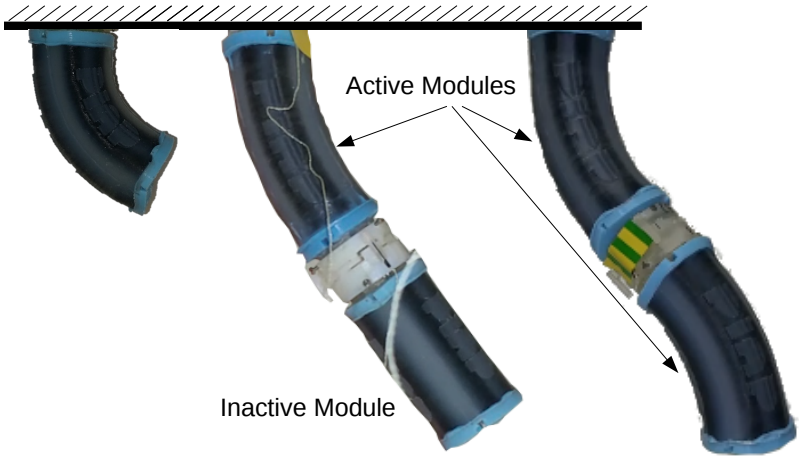

Figure 1.8: Experiments on general 3D deformation of, (left) one STIFF-FLOP module, (middle: EXP.3-I) a continuum manipulator with two STIFF-FLOP modules with one active module and (right: EXP.3-II) two active modules.

1. EXP.1: Actuation of a pneumatic braided extensile chamber (Fig. 1.6) to identify the properties of the most important compound of a continuum manipulator. The axial deformation of a single isolated chamber, which is placed

horizontally on a flat surface, is measured for six different pressure values in static loading condition.

2. EXP.2: Planar deformation of a STIFF-FLOP module with extensive external load at the tip (task space) (Fig. 1.7). The manipulator response to task space extensive load is an important, but merely investigated in literature, factor to evaluate a continuum manipulator analytical model and structure design performance in medical applications involving palpation and working against body tissue. Different combination of planar external force and moment are exerted at the tip of a STIFF-FLOP module bent with two equally pressurized active chambers and one inactive chamber inside the bend. The external load value varies with time and the test is repeated for two different pressure input values. Static data for the equilibrium points, when the setup remains static for more than 5 [s] after a change in the input pressure or external load values, and dynamic data are recorded.

3. EXP.3: Random pressurization of a continuum manipulator with two STIFF-FLOP modules to study the general 3D deformation a multi-segment continuum manipulator under extensive body load (Fig. 1.8). Once, only one module is actuated while the second inactive module acts as an external load (EXP.3-I: Fig. 1.8.middle), then both modules are actuated to evaluate the manipulator performance with multiple segments (EXP.3-II: Fig. 1.8.right). The segments are actuated independently with random pressure values generated by a LabView program. Static data for the equilibrium points, when the setup remains static for more than 5 [s] after a change in the input pressure, and dynamic data are recorded.

All the setups are fixed upside down, with the tip toward the gravity direction, as the initial orientation of a continuum manipulator in most medical applications. This is also an inherent stable orientation for an inactive continuum manipulator. Absolute and reference values are used for error analysis where necessary. Absolute

Symbol [unit]	Description	Value$^{(a)}$	value$^{(b)}$
r_{p1} [mm]	Pressure chamber inner radius	2.5	2.5
r_{p2} [mm]	Pressure chamber outer radius	3.0	3.0
γ[deg]	Thread helix lead angle w.r.t. tube axis	89.38	89
r_{o} [mm]	Placement radius for pneumatic chambers	9.0	8.5
r_{c2} [mm]	Body shell outer radius	12.5 (12)†	12.5
r_{c1} [mm]	Body shell inner radius	4.5	4.5
l [mm]	Module initial length	44.0	44.0
l_{fs} [mm]	Force sensor length between segments	16.6 (17)	10.0
$E^{\ddagger}$ [KPa]	Material Elasticity modulus	100 (205)	100 (205)
g [m/s2]	Gravity	9.81	9.81
b [grams]	Module body mass	24.0	24.5
b_{L} [grams]	External load mass at tip	1.0	11.0
$\mu_{\mathrm{t}}^{\ddagger}$ [Ns/m]	Axial damping in static tests	0.1	0.1
$\mu_{\mathrm{r}}^{\ddagger}$ [Nms/rad]	Bending damping in static tests	$5e-4$	$5e-4$
$\mu_{\mathrm{v}}^{\ddagger}$ [Ns/m]	Axial viscous damping in dynamic tests	$1e-3$	$1e-3$
$\mu_{\mathrm{u}}^{\ddagger}$ [Nms/rad]	Bending viscous damping in dynamic tests	$4e-5$	$4e-5$
σ [Kg/m^3]	Material density	1300	1300

†Values which are different for the experiments carried out in section 3.3.
‡Identified parameters.

Table 1.1: STIFF-FLOP Parameters for the experiments with the body loads (a) and extensive external loads (b). The module parameters are slightly different due to fabrication inaccuracy.

error is the deviation of the predicted values from the actual ones and is used to compare different methods that are implemented in this research. Reference error is used to compare results from different studies with different manipulator designs in the literature [74, 75] and is defined as the absolute error divided by a reference value which is the manipulator initial length.

1.3 Motivation and Objectives

Following the short introduction on the background related to this thesis topic and the overview of the used experimental setup and procedure, the motivation and objectives of this thesis are explained below. Soft continuum manipulators with high inherent dexterity and reconfigurability have become an attractive candidate for safe manipulation and exploration in surgical and space robotic applications

in recent years. The passive shape adaptation and large reachable configuration space features of this class of manipulators due to their highly deformable nature made them a perfect choice for minimally invasive insertion of surgical tools in the confined maze-like space in a robotic surgery. However, *accuracy in precise tasks* is a challenge with highly flexible structures, for which stiffness variable designs based on jamming, smart material, antagonistic actuation and morphing structures are introduced in the recent years. The control design of such manipulators is mostly limited to simple kinematic and static models for the configuration and force control and observation. *Real-time accurate dynamic control* of this class of manipulators considering their inhomogeneity and compound structure is still an open question where the advantages and shortcomings of the current solutions are not addressed clearly in a comparative study of the methods in literature. On the other hand, the efforts for stiffness regulation of this class of manipulators is limited to preliminary designs as proof of concept, usually with uniform homogeneous modulation along the axis or cross-section of the manipulator and for static cases based on simple model-free feedback control designs. Most designs in this context do not go further than the available technologies and despite the manipulator design itself, *bio-inspiration* from design and control of similar structures in nature is less addressed in the literature. Such inspiration can improve the current design and improve our knowledge of the natural mechanisms. There is limited research on *regional and directional stiffness, force and configuration control* of continuum manipulators. **Limitations in the modeling of continuum manipulators, stiffness regulation designs being in their early steps of proof of concept and challenges in the real-time force and configuration control of such highly dexterous designs are current challenges that prevent them from real-world applications.**

Such challenges cannot be addressed solely with the traditional centralized deterministic approaches. The concept of *morphological computation* is a new approach toward design, understanding and control of intelligent systems where the body is considered as an intelligent element in the system and contributes to the compu-

tation, cognition and effective engagement with the task space. **While the community is still at the stage of providing a universal definition for this approach and identifying and unraveling the examples of such behavior in their design, a mathematical approach to identifying, implement and test the concept of morphological computation in the design and control of stiffness tunable continuum manipulators is yet to be not addressed.** Unraveling how an intelligent morphology design contributes to the effective performance of a system, through mathematical models and experimental observation and prototype test, helps with reducing the complexity of design and control problems for the complex behavior of stiffness tunable continuum mechanisms with large state and control space.

This thesis investigates how the problem of stiffness regulation of continuum manipulators can be simplified by inspiration from morphology of biological fish scales and experimental observation of manipulator geometry deformation. It is important to note that, in contrast with a common engineering thesis, in which a modeling or technology should be introduced in the context of some specific requirements or specifications that need to be achieved; in this thesis, we try to understand the underlying principles related to the aforementioned objectives and to identify the opportunities that these basic principles can offer in different real-world continuum manipulator applications, with a more specific focus on minimally invasive surgery and medical applications. To this end, the advantages of the proposed methods and designs in this thesis are discussed in response to the challenges, that are identified in our survey, and compared to the available approaches and technologies in the literature. We believe that the presented discussions on the relative performance improvement by our methods and designs show new opportunities for reducing the distance of current technologies to their feasibility in real scenarios.

1.4 Contributions

The contributions of this thesis are:

- For the first time, a comparative study of five main methods in the literature for kinematic, static and dynamic modeling of continuum manipulators is presented in a unified mathematical framework and in comparison with experiments.

- A new analytical framework, based on Rivlin's work on 'The Problem of Flexure' and Ritz and Ritz-Galerkin solutions, is established to describe the cross-section and backbone geometry deformation and mechanics of a continuum manipulator based on experimental observations. The presented approximate solution for modeling of continuum manipulator backbone is shown to be the most accurate model with the smallest possible number of modeling states, in comparison with the available methods in literature, and suitable for real-time modeling, observation and control applications. For the first time, the model in this thesis provides an approximate analytical solution for the manipulator cross-section deformation and introduces the bending effect in the model of a braided extensile pneumatic actuator with both stiff and bendable threads. The importance of considering mechanical effects of planar and axial highly elastic deformation on the manipulator modeling accuracy is established. The presented framework can be used for modeling state space reduction, exact modeling and design optimization of compound continuum manipulators by using approximate empirical shape functions, incorporating structural parameters and providing an analytical tool for sensitivity analysis.

- The possibility of biological scale jamming in a real fish skin is observed through modulation of the normal force between the scales, especially when they are on the inner side of the bend. We observed a reversible and smooth load cycle with small hysteresis due to the biological scales special morphology

and special inclined stacking formation in jamming which shows the possible role of a jamming mechanism in stiffness modulation of the fish body.

- Two novel integrable helical interface inspired by the shape and special arrangement of teleost fish scales is designed and mathematically modeled in which the stiffness is adjustable through tendon driven actuation, as a way for active modulation of the normal force on the jammed scales, and use of a thermoactive stiffness tunable polymer, as a means for regulating the inter-scale interaction. The presented tendon driven design is the first and only jamming enable design that presents a very small hysteresis in the full return cycle. The thermoactive design provides the most comprehensive control over local and directional stiffness available for continuum manipulators. Notable increase in the stiffness range, shape locking ability, large bending and elongation deformation, and easy integration on different manipulator designs are the advantages of the presented jamming interface compared to the previous research.

- For the first time, a two step model is presented for the integration of a stiffness control mechanism on a continuum manipulator and a piecewise model is derived for the equivalent stiffness of a jamming media, valid for the full return actuation cycle.

- The novel concept of morphological observer is introduced where the estimating computer model in a traditional observer architecture is substituted with the morphological computational power of a fully monitored physical replica of the actual system. For the first time in continuum robotic research and by relating the mathematical terms in the presented analytical model with the real morphology of a continuum manipulator, a decentralized morphological approach is presented to regulate the regional stiffness of a continuum manipulator for task space stiffness control and configuration disturbances compensation and isolation.

1.5 Publications

Journal Publications:

- [80] **S.M.Hadi Sadati**, Luis Sullivan, Ian. D. Walker, Kaspar Althoefer, Thrishantha Nanayakkar., 3D-Printable Thermoactive Helical Interface with Decentralized Morphological Stiffness Control for Continuum Manipulators., IEEE Robotics and Automation Letters (RA-L), IEEE International Conference on Robotics and Automation (ICRA), 2018.

- [81] **S.M.Hadi Sadati**, S. Elnaz Naghibi, Ian. D. Walker, Kaspar Althoefer, Thrishantha Nanayakkara., Control Space Reduction and Real-Time Accurate Modeling of Continuum Manipulators Using Ritz and Ritz-Galerkin Methods., IEEE Robotics and Automation Letters (RA-L) Journal, 2018.

- [82] **S.M.Hadi Sadati**, S. Elnaz Naghibi, Ali Shiva, Yohan Noh, Aditya Gupta, Ian. D. Walker, Kaspar Althoefer, Thrishantha Nanayakkar., A Geometry Deformation Model for Braided Continuum Manipulators., Frontiers in Robotics and AI Journal, 2017.

- A. Shiva, **S.M.H. Sadati**, Y. Noh, J. Fras, A. Ataka, H. Wurdemann, H. Hauser, I. Walker, T. Nanayakkara, K. Althoefer., Elasticity vs. Hyperelasticity Considerations in Quasi-Static Modelling of a Soft Finger-like Robotic Appendage for Real-time Position & Force Estimation., Soft Robotics, 2018 (Accepted- under print).

Book Chapter:

- [83] Daniel Guevara Mosquera, **S.M.Hadi Sadati**, Kaspar Althoefer, Thrishantha Nanayakkar., Smart Hydrogel for Stiffness Controllable Continuum Manipulators: A Conceptual Design., *in* Soft and Stiffness-controllable Robotics Solutions for Minimally Invasive Surgery: The STIFF-FLOP Approach, River

Publishers Series in Automation, Control and Robotics, Denmark, ISBN: 9788793519725, April 2018.

Peer-Reviewed Conference Proceedings:

- [80] **S.M.Hadi Sadati**, Luis Sullivan, Ian. D. Walker, Kaspar Althoefer, Thrishantha Nanayakkar., 3D-Printable Thermoactive Helical Interface with Decentralized Morphological Stiffness Control for Continuum Manipulators., IEEE Robotics and Automation Letters (RA-L), IEEE International Conference on Robotics and Automation (ICRA), 2018.

- **S.M.Hadi Sadati**, S. Elnaz Naghibi, Kaspar Althoefer, Thrishantha Nanayakkar., Toward a Low Hysteresis Helical Scale Jamming Interface Inspired by Teleost Fish Scale Morphology and Arrangement., IEEE RAS International Conference on Soft Robotics (RoboSoft), 2018.

- [84] **S.M.Hadi Sadati**, S. Elnaz Naghibi, Ali Shiva, Ian D. Walker, Althoefer Kaspar, Thrishantha Nanayakkara., Mechanics of Continuum Manipulators, A Comparative Study of Five Methods with Experiments., 18th Towards Autonomous Robotic Systems (TAROS) Conference, 2017.

- [85] **S.M.Hadi Sadati**, Ali Shiva, Ahmad Ataka, S. Elnaz Naghibi, Ian D. Walker, Kaspar Althoefer, Thrishantha Nanayakkara., A Geometry Deformation Model for Compound Continuum Manipulators with External Loading., IEEE International Conference on Robotics and Automation (ICRA), 2016.

- [86] Hadha Afrisal and **S.M.Hadi Sadati**, Thrishantha Nanayakkara., A Bio-Inspired Electro-Active Velcro Mechanism Using Shape Memory Alloy for Wearable and Stiffness Controllable Layers., Information and Automation for Sustainability (ICIAfS), 2016 8th International Conference on. IEEE, 2016.

- [41] **S.M.Hadi Sadati**, Yohan Noh, S. Elnaz Naghibi, Althoefer Kaspar, Thrishantha Nanayakkara., Stiffness Control of Soft Robotic Manipulator for

Minimally Invasive Surgery (MIS) Using Scale Jamming., In Intelligent Robotics and Applications, pp. 141-151. Springer International Publishing, 2015.

- [87] **S.M.Hadi Sadati**, S. Elnaz Naghibi, and Mahyar Naraghi., An Automatic Algorithm to Derive Linear Vector Form of Lagrangian Equation of Motion with Collision and Constraint., Procedia Computer Science 76 (2015): 217-222.

- [88] Michael Zheng, **S.M.Hadi Sadati**, Pendar Ghalamchi, Thrishantha Nanayakkara., Passive dynamics of high frequency bat wing flapping with an anisotropic membrane., Information and Automation for Sustainability (ICIAfS), 2014 7th International Conference on. IEEE, 2014 (Winner of the Best Student Paper Award).

Conference Workshop Presentations:

- **S.M.Hadi Sadati**, S. Elnaz Naghibi, Kaspar Althoefer, Thrishantha Nanayakkara., Geometrical Jamming for a Low Hysteresis Stiffness Controllable Helical Interface Inspired by Teleost Fish Scale Arrangement., IROS 2018 Workshop on Shape Changing Robotic Structures and Interfaces, Madrid, Spain, 2018.

- **S.M.Hadi Sadati**, S. E. Naghibi, A. Shiva, S. Zschaler, H. Hauser, I. Walker, K. Althoefer and T. Nanayakkara., AutoTMTDyn: A Matlab Software Package to Drive TMT Lagrange Dynamics of Series Rigid- and Continuum-link Mechanisms., IROS 2018 Soft Robotic Modeling and Control: Bringing Together Articulated Soft Robots and Soft-Bodied Robots, Madrid, Spain, 2018.

1.6 Thesis Structure

The structure of this thesis and how it is done toward our main objectives are summarized in Fig. 1.9 and below.

- Chapter 1 presents the overall scope of this thesis, state of the art and current technologies and findings related to the framework of this thesis. The motivations, objectives, and contributions are summarized.

- Chapter 2 presents a comparative study of five main methods in the literature for kinematic, static and dynamic modeling of continuum manipulators in comparison with experiments, in order to clarify their methodological differences.

- Chapter 3 presents a comprehensive insight into exact modeling of compound continuum manipulators with braided actuators. It introduces the bending effect in the model of a braided extensile pneumatic actuator. Then, the effect of the manipulator cross-section deformation modeling accuracy is investigated using simple analytical results from a novel geometry deformation method which is useful for the sensitivity analysis based design optimization. A novel series solution is presented for variable-curvature Cosserat rod static and Lagrangian dynamics of a continuum manipulator, based of which a unified easy to implement vector formalism is proposed for real-time impedance and configuration control of a continuum manipulator with the smallest possible number of modeling states.

- Chapter 4 investigates the possibility of biological scale jamming based on experiments on a real fish skin. Inspired by the shape and helical arrangement of teleost fish scales to control the stiffness of continuum manipulators, the idea of scale jamming is presented and the effectiveness of three different designs are investigated through modeling and experiments.

- Chapter 5 presents the design for a 3D-printable thermoactive scale jamming interface with functionally graded joints, as a new way to control a continuum manipulator dexterity. The interface performance is investigated through mathematical modeling, comprehensive study of the wax melting profile and empirical forward control relations. A decentralized modeling and

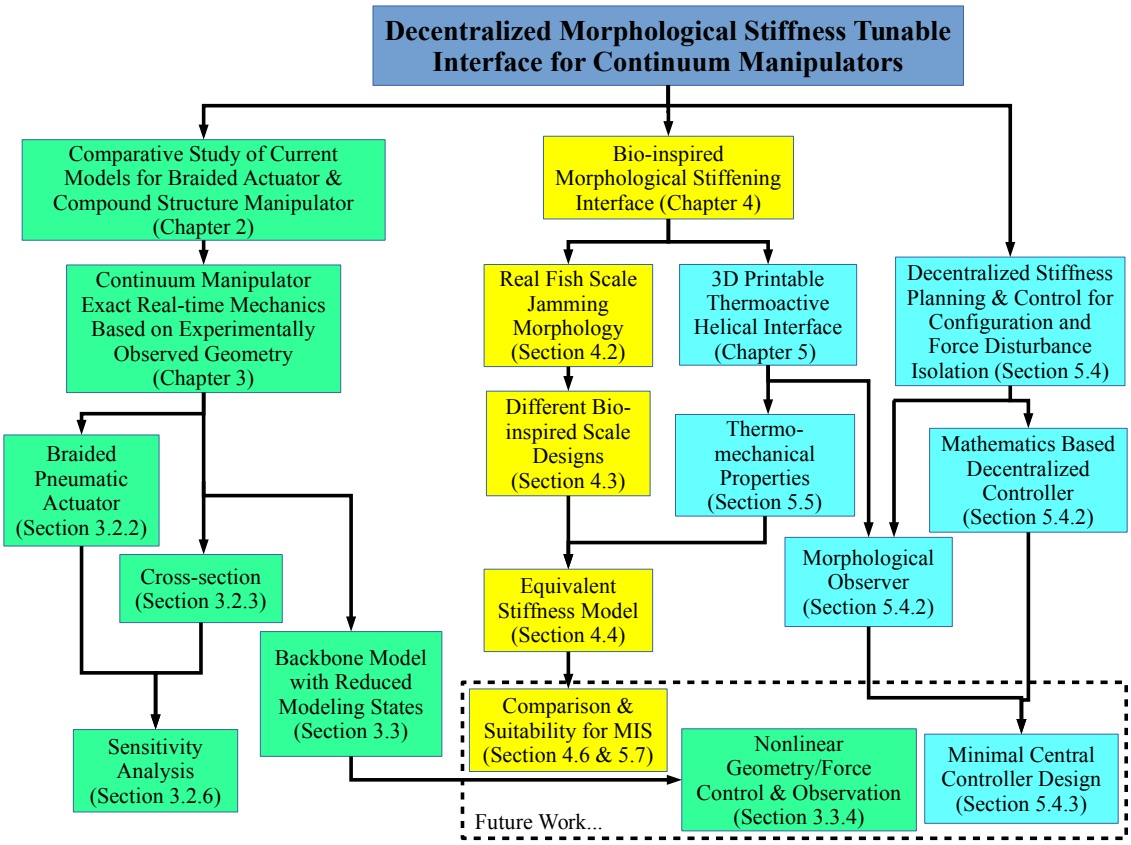

Figure 1.9: The thesis structure.

control approach is employed based of which a minimalistic central controller is designed and successfully tested for passive shape adaptation, task space anisotropic stiffness control and geometrical disturbance compensation and isolation by integrating the interface on a braided pneumatic continuum manipulator. The novel concept of morphological observer is presented and tested in experiments.

- Chapter 6 summarizes all the findings and contributions of this thesis and discuss potential applications and future works based on this thesis framework.

Chapter 2

Mechanics of Continuum Manipulators: A Comparative Study

Abstract

Investigations on control and optimization of continuum manipulators have resulted in a number of kinematic and dynamic modeling approaches each having their own advantages and limitations in various applications. As the main objective of this chapter, a comparative study of five main methods in the literature for kinematic, static and dynamic modeling of continuum manipulators is presented in a unified mathematical framework. The five widely used methods of Lumped system dynamic model, Constant curvature, two-step modified constant curvature, variable curvature Cosserat rod and beam theory approach, and series solution identification are re-viewed here with derivation details in order to clarify their methodological differences. To analyze a stiffness controllable interface integrated on a continuum manipulator, as the ultimate goal of this research, a general exact solution that incorporates the structural properties of the manipulator is preferable. Such model makes it easy to integrate the interface stiffness model with the manipulator model

and is valid for general loading conditions. To evaluate our objective in this chapter, a comparison between computer simulations and experimental results using a continuum manipulator with one STIFF-FLOP module is presented to study the advantages of each modeling method.

2.1 Introduction on Continuum Manipulator Modeling

taking inspiration from biological examples such as the octopus arms, chameleon tongues and elephant trunks, researchers are looking into the possibility of replicating similar maneuverability and grasping characteristics by harnessing the corresponding hyper-redundancy demonstrated in nature [89]. The class of continuum robots promises considerable performance improvements in different areas which currently witness the presence of traditional robots, such as surgical applications, underwater manipulation and inspection, etc. [90, 4, 42]. Real-time accurate modeling, observation and controller design, suitable for this class of manipulators, are shown to be complex and challenging tasks due to their high dexterity and deformability [20].

A Continuum manipulator model is described using a general kinematic map for the deformation-configuration relation and a robot-specific mechanical map for the loads-deformation relation. The Constant curvature (CC) model, which is the most common assumptions in continuum robotic research, simplifies the kinematics of a continuum manipulator by expressing the backbone deformation as a planar CC profile [20]. Although being commonly used as a simplifying assumption, the CC assumption suffers from local singularities around the straight configuration and low accuracy in the presence of significant body and external loads. Variable curvature (VC) [74, 91] and identification based series-solutions [92] provide more accurate singularity free kinematic maps. The dynamic models introduced in the literature to provide a better modeling accuracy can be categorized into six groups, a comparative study of which in comparison with experiments is presented in this chapter [84]. 1) Lumped system Lagrange dynamics with discrete VC kinematics, similar to a series rigid link mechanism, where a series of finite or infinite number of rigid disks are interconnected using compliant joints [93]. 2) Euler-Bernoulli (EB) beam

mechanics with CC [94] or discrete VC kinematics [95]. 3) Continuum form of Lagrange dynamics [92, 96] or the Principle of Virtual Work (PVW) [85, 82] using CC, continuous VC or series-solutions as kinematic maps, where the kinematic map parameters are the dynamic model states. 4) Cosserat rod model [74, 11] and beam theory method, as a simplified version of that [82], which result in a boundary value problem (BVP) to be solved using numerical optimization methods [74, 75]. 5) approximate identification based series-solutions where coefficients of a simple [97] or complex [25] series solution are identified using experimental results to construct a hardware-specific model. 6) Numerical finite element methods for the manipulator mechanics and VC kinematics using EB [98] or Galerkin weak-form series-solution [99].

Simple but less accurate predictions can be made by models based on constant curvature assumptions and be used as a reference for model-based learning, control and observation of continuum manipulators. A simple model enhances the accuracy, generality and identification time, especially in medical applications where observations are limited and less reliable due to limited sensory equipment in the confined space of many surgeries, lack of accessibility and general uncertainties related to sensing of a soft tissue [100]. The identification based models are more accurate and computationally efficient; however, their validity is limited to their experiment conditions, external loads, input values and training data set [25, 92]. Besides, they do not account for the structural characteristics necessary for dealing with unknown conditions and design optimization. On the other hand, the lumped system and Cosserat rod models provide a general solution, but not suitable for control design due to high computational cost and large number of modeling states. Use of series-solution based models for identification of kinematic map by Godage [92] have shown to be real-time but with a complex hard to interpret shape function and limitations related to identification based methods. Series-solution based Galerkin method for static modeling of complex deformation in a discretized finite element domain by Tunay [99] is accurate and comprehensive, but with a complex shape function and

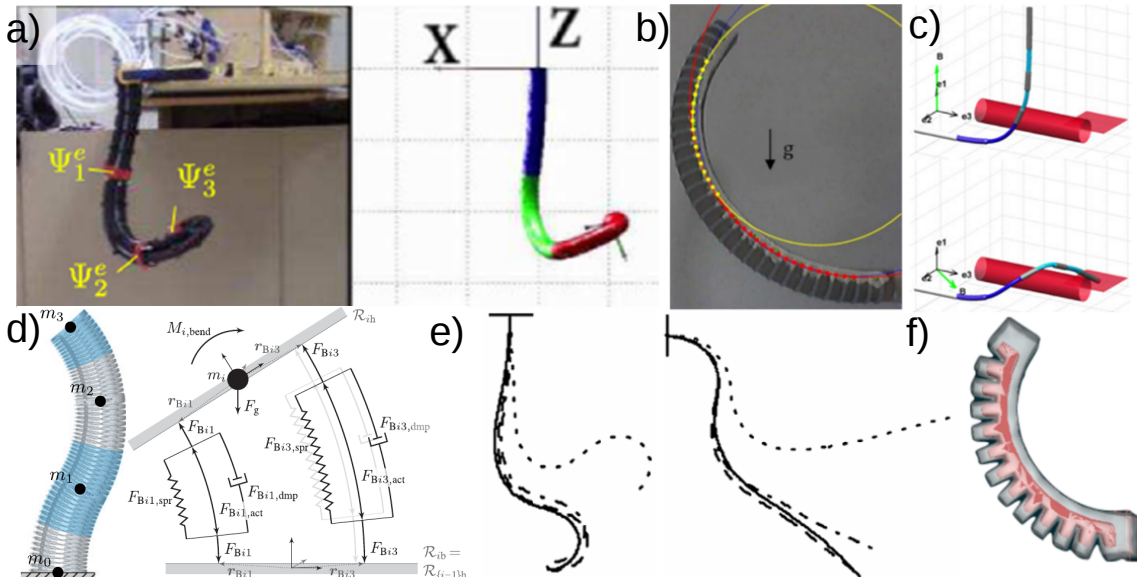

Figure 2.1: A review on modeling methods for continuum manipulators, (a) identification based series solution with appropriate choice of shape functions [75], (b) using constant curvature and Euler-Bernoulli beam method [94], (c) finite element model based on Galerkin method [99], (d) lumped system method [101], (e) Cosserat rod method [74], (f) real-time finite element solution [102].

limitations related to finite element and Cosserat rod method.

Accuracy of these methods is compared based on their forward control performance and a feedback term, such as PID, should be considered in the controller design to deal with real working disturbances and setup uncertainties. The large modeling state space results in difficulties with impedance observation and control which are essential for safe surgical, inspection and human-robot interaction applications. A review on different modeling methods for continuum manipulators is presented in 2.1.

In this chapter, a comparative study between five modeling approaches for kinematic, static and dynamic modeling of a continuum manipulator is presented and their accuracy, advantages and limitations are discussed in comparison to experimental results using a STIFF-FLOP continuum actuator module [26, 15] (EXP.1-3). In the process; simple mathematic derivation of the manipulator deformation energy for the body and braided actuator chambers and mechanical maps based on Neo-Hookean (NH) assumptions are discussed; a comparison between different models for

a braided extensile pneumatic actuator is presented and a novel tow-step modified solution is presented based on CC kinematics and Castigliano's method for beam deflections to enable using of CC assumption in the presence of high body and external loading.

The experiment procedure and hardware design are discussed in section 1.2. In section 2.2 a review of derivation and implementation of the five modelling methods for continuum manipulators (Lumped system dynamic model, CC, two-step modified CC, VC Cosserat rod and beam theory approach, and series solution identification) are presented. The models' applications are discussed based on our simulation result performance and accuracy in section 2.3 followed by conclusions and discussions.

2.2 Manipulator Modeling Framework

The continuum manipulator modeling problem is reduced to modeling general deformation (elongation, bending and torsion) of a hyper-elastic holow cylinder (tube). The spatial configuration of a continuum manipulator (ρ) as the system control outputs can be derived based on CC or VC kinematics. This general map can be used as the system control model by relating the actuator pneumatic chambers length (l_{p}) and manipulator tip position and orientation (ρ_{tip}); however, a more precise model should consider the mechanical properties of the manipulator too [74]. Slenderness and softness of most continuum manipulators make external and body forces important in the modeling of their behavior. Body specific static and dynamic map (f_{S}) are used to relate these loads with the parameters of a continuum manipulator general kinematic map (f_{G}), which are discussed in this section.

The absolute error is defined as the difference in the length of the tip position vector in simulation and experiments and the error is the ratio of the error to the experimental value of the tip position vector length. A reference error is defined as the ratio of the absolute error to the manipulator initial length (l) to make

our results comparable with other similar research. Experimental conditions and inputs are used in the simulations where Matlab functions such as "fsolve", "ode113" and "fmincon" are used for direct single shooting optimization, time integration and parameter identification. Trapezoidal numerical method is used for numerical integration as needed.

2.2.1 Mechanical Effect of Cross-Section Highly Elasticity

The module active cross-section area ($a_{\rm c}$) and second moments of area ($J_{\hat{d}_1}, J_{\hat{d}_2}, J_{\hat{d}_3}$) are

$$\begin{aligned} a_{\rm c} &= \pi(r_{\rm c_2}^2 - r_{\rm c_1}^2 - 6r_{\rm p_1}^4), \\ J_o &= \pi/4(r_{\rm c_2}^4 - r_{\rm c_1}^4 - 6r_{\rm p_1}^2),\ J_{\hat{d}_1} = 2J_o - 6a_{\rm p}r_o^2, \\ J_{\hat{d}_2|\hat{d}_3} &= J_o - 2a_{\rm p}r^{\rm T}_{J\hat{d}_2|\hat{d}_3}.r_{J\hat{d}_2|\hat{d}_3}, \end{aligned} \tag{2.1}$$

where $(\hat{d}_2, \hat{d}_1\hat{d}_3)$ is the local frame directors with $\hat{d}_1$ along the module axis and $\hat{d}_2$ places the first pneumatic chamber (Fig. 2.9),$a_{\rm p} = \pi r_{\rm p1}^2$ is the pressure chamber cross-section area, $r_{J\hat{d}_2|\hat{d}_3} = r_o[{\rm S|C}_{(0)}, {\rm S|C}_{(2\pi/3)}, {\rm S|C}_{(-2\pi/3)}]^{\rm T}$, $r_{\rm c1|2}$ is the module cross-section inner—outer radius, $r_{\rm p1|2}$ is the pneumatic chamber inner—outer radius, $r_{\rm o}$ is the pressure chamber placing radius and ${\rm S|C}_{(x)} = \sin|\cos(x)$.

For an incompressible media we have $\prod_{i=1}^{3}\lambda_i = 1$, where λ_i is the Cauchy-Green principle stretches (the stretch in the i principle direction) [74]. To satisfy incompressibility criteria, a homogeneous incompressible material in uniaxial elongation with axial stretch λ_l, experiences planar deformations with lateral strains, in Cartesian coordinates, and radial and circumferential strains, in cylindrical coordinates, equal to $1/\sqrt{\lambda}$. To incorporate the mechanical effect of the manipulator highly elastic deformation, we assume a symmetric uni-axial deformation for the incompressible material to update deformed cross-section radius (r), area (a) and moment

of inertia or second moment of area (J) as

$$r_{\mathrm{d}} = r/\sqrt{\lambda_l},\ a_{\mathrm{d}} = a/\lambda_l,\ J_{\mathrm{d}} = J/\lambda_l^2, \tag{2.2}$$

where $\lambda_l = l_{\mathrm{d}}/l$ is the axial stretch, l is the module initial length and the deformed state is shown by subscript ($_{\mathrm{d}}$) [103].

2.2.2 Equivalent Lumped System Model

Discrete Variable Curvature Kinematics

A continuum manipulator can be assumed as a highly articulated rigid link system with an infinite number of disks connected through spring-damper supported spherical joints [6], [17] (Fig. 2.2). We used an axial transformation (ρ_{r}) followed by a 3-2-1 Euler angle set (η, ζ, ξ) to relate the consecutive joints,

$$R_{\mathrm{r}i} = R_z(\eta_i).R_y(\zeta_i).R_x(\xi_i) \rightarrow \Gamma_{\mathrm{r}i} = \begin{bmatrix} R_{\mathrm{r}i} & \rho_{\mathrm{r}i} \\ 0 & 1 \end{bmatrix},\ R_i = \prod_{j=1}^{i} R_{\mathrm{r}j},\ \Gamma_i = \prod_{j=1}^{i} \Gamma_{\mathrm{r}j}, \tag{2.3}$$

where R_a is the rotation matrix around a axis in the local frame, Γ is the transformation matrix, subscript ($_{\mathrm{r}}$) denotes the relative rotation matrix between each two disks, i denotes the disk number and j is a general numerator. Center of masses (COM) position vector ($\rho_i = \Gamma_i \rho_{\mathrm{r}i}/2$) assuing the COM to be at the middle of each segment length ($\rho_{\mathrm{r}i}$), linear velocity ($\rho_{i,t}$) and angular velocity ($[\omega_i]_\times = R_{i,t}.R_i^{\mathrm{T}}$) in Cartesian coordinates and w.r.t the spatial frame can be found afterward. $[\omega]_\times$ is the skew-symmetric matrix of the vector ω and subscript comma ($_{,}$) means derivative w.r.t. the following parameters. The axial linear transformation and Euler angle rotations of all joints can be assumed to be equal to model a uniformly deforming link [104] while assuming separate free DOFs results in a discrete VC kinematic model.

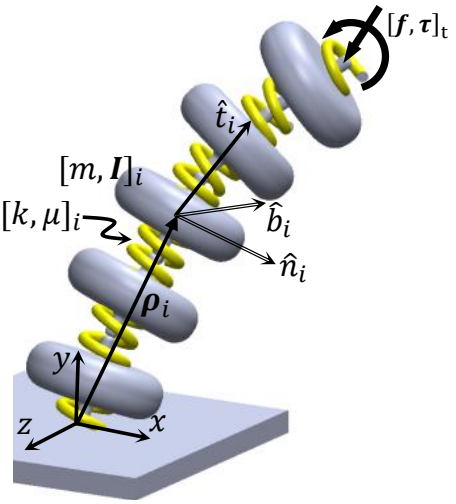

Figure 2.2: Lumped system model diagram.

Joints rotational and linear stiffness ($k_{t|r}$) and damping ($\mu_{t|r}$) values can be identified from experimental results or can be derived using deformation energy of elastic material [93]. We left these two values to be constant as in Table 1.1. Cross-sectional deformation can be considered as a change in the inertia and diameter of the rigid links.

Discrete Lagrange Dynamic Model

Having the stiffness values and the gravitational potential energy function based on the initial shape of the manipulator, principle of virtual work (PVW) in static case and Lagrange method in the dynamic case can be used to model the system mechanics [93]. A high DOF Boundary Value Problem (BVP) is formed in the static case and can be solved by a numerical optimization method. The dynamic equations are more efficient to be solved using a forward Runge-Kutta numerical integration method. A matrix form of equation of motion (EOM) using TMT method is presented to derive the dynamic model [87]. TMT method is a simple and clear approach which eliminates the highest order derivatives in each step and results in a simplified matrix form for unconstrained Lagrange EOM, ideal for numerical simulation of large complex dynamic systems. The general form ofthe TMT method is

[87].

$$
\begin{aligned}
T_{(q)} &= \left[\begin{array}{ccc} \rho_i & \dots \end{array}\right]^{\mathrm{T}}_{[3n_{\mathrm{m}}\times 1]}, \quad \omega_i = \bar{\omega}_i q_{,t}, \\
M &= \mathrm{diag}\left[b_i b_i b_i J_{\mathrm{m}i[3\times 3]} \ \cdots\right], \quad \bar{T} = \left[\begin{array}{c} \left[\begin{array}{c} T_{(q),q} \\ \bar{\omega} \end{array}\right]_i \\ \vdots \end{array}\right] \\
d &= \left(\bar{T} q_{,t}\right)_{,q} q_{,t}, \quad \bar{M} = \bar{T}^{\mathrm{T}} M \bar{T}, \quad d_{\mathrm{EOM}} = \bar{T}^{\mathrm{T}}\left[\sum f_{\mathrm{g}} - M d\right] + f_q, \quad \bar{M} q_{,tt} = d_{\mathrm{EOM}}
\end{aligned}
\tag{2.4}
$$

where $q = [\rho_{\mathrm{r}i}, \eta_i, \zeta_i, \xi_i]$ is the generalized state vector with initial value $q_0 = [l/n_i, 0, 0, 0]$ at a straight undeformed configuration, T is the transformation matrix for links COM position and orientation vector of a multibody system in terms of generalized coordinates, M is the systems mass and inertia matrix, b_i and $J_{\mathrm{m}i}$ are the i^{th} link mass and inertia matrices, d is the vector of velocity dependent inertial terms, f_{g} and f_q are the external conservative and non-conservative forces in Cartesian (i.e. gravitational forced) and joint space (i.e. joint inputs) respectively, n_{m} is the number of bodies, n_q is the number of states, n_i is the number of segments and $\mu_{\mathrm{t|r}}$ is the joint transnational and rotational viscous damping coefficients. $\bar{\omega}_i$ is a $3 \times n_q$ coefficient matrix derived by collecting $q_{,t}$ elements in ω_i. The actuator forces are considered as concentrated force and torque acting uniformly on all DOFs. The translational and rotational stiffness are found from EB relation for each segment and by considering a symmetric deformation for the cross-section assuming an incompressible beam, $k_{\mathrm{t}} = n_i E a_{\mathrm{c}} / (\lambda_l^2 l)$ and $k_{\mathrm{r}} = n_i E J_{\hat{d}_1} / (\lambda_l^3 l)$, where E is the modules of elasticity, $\lambda_l = \Sigma_{i=1}^{n_i} \lambda_{li}$ is the manipulator total axial elongation and $\lambda_{li} = n_i \rho_{\mathrm{r}i}/l$ is the axial elongation of each segment.

We used AutoTMTDyn, a software package in Matlab programming language that drives the TMT vector form of the Lagrange EOM using simple inputs about the kinematics of the system [87], to simulate a three-segment lumped model of a STIFF-FLOP manipulator module (Fig. 2.2). A sample input code for planar motion is presented in Fig. 2.3. The model can capture transient behavior of the manipulator

```
body(i).type = 'rigid'; Body type for the i^th disk
body(i).m = m_b/n; i^th disk mass, n: number of disks
body(i).I = I_b/n; i^th disk length
body(i).l_com = [ 0 0 l/(2n) ]; i^th disk COM position
joint(i).first = i-1; First body of the i^th joint
joint(i).second = i; Second body of the i^th joint
joint(i).tr(1).trans = [ 0 0 I_b/n ]; First translation of the i^th joint
joint(i).tr(1).rot = [ 0 0 ]; First rotation of the i^th joint
joint(i).tr(2).trans = [ 0 0 inf ]; Second translation of the i^th joint,
                                    inf: set for free DOFs
joint(i).tr(2).rot = [ 2 inf ]; Second translation of the i^th joint
joint(i).dof(1).init = 0; Initial condition for the first DOF
joint(i).dof(2).init = 1e-5; Initial condition of the second DOF
joint(i).dof(1).spring = [ k_t, 0 ]; Spring coeff. & initial length for the first DOF
joint(i).dof(1).damp = [μ_t, 0 ]; Viscous & Coulomb damping for the first DOF
joint(i).dof(1).spring = [ k_r, 0 ]; Spring coeff. & initial length for the second DOF
joint(i).dof(1).damp = [μ_r, 0 ]; Viscous & Coulomb damping for the second DOF
exload(1).body = n; Reference body where the external load is exerted
exload(1).tr(1).trans = [ 0 0 l/n ]; External load relative position
exload(1).tr(1).rot = [ 0 0 ]; External load relative orientation
```

Figure 2.3: Sample AutoTMTDyn input code for one disk in the lumped model for a continuum manipulator with planar motion.

with high accuracy and good performance [93]. Despite the static models, the role of proper identification or modeling of the damping coefficient is important to capture an accurate dynamic model for the system. The model may become unstable and hard to simulate for higher number of links without the uniform deformation assumption; however, shows to be accurate even for a small number of DOFs. The forward dynamics of the system is easier to solve. Thus, this method is suitable for dynamic control design purpose using traditional control theories for rigid body systems. Although some structural characteristics of the system is considered in the modeling procedure, this method cannot provide a detailed insight in the effect of the manipulator material property for structural design and optimization purposes. Simulation results are presented in Fig. 2.4, showing 22% mean error compared to the dynamic experimental results of EXP.3-I.

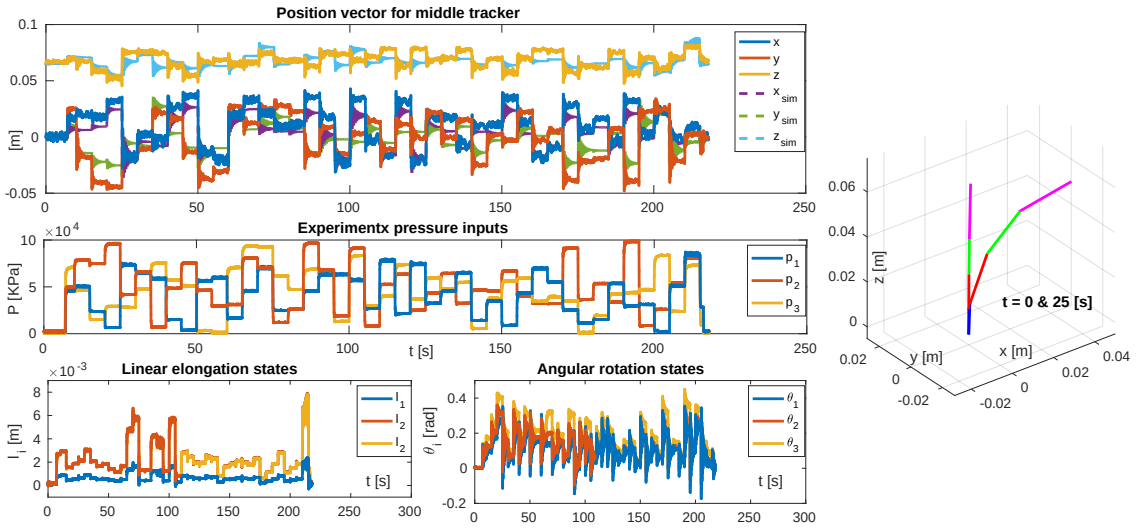

Figure 2.4: Lumped system dynamic model results for a model with three rigid links and independent joints compared to the experimental results of EXP.3-I.

2.2.3 Constant Curvature Kinematics and Mechanics

Constant Curvature Kinematics As The System Model

The kinematics of a continuum manipulator used herein is a geometric map for n modules (f_{G}) between the CC state parameters and the manipulator spatial orientation, usually in Cartesian coordinates. As the most common used model for the kinematic representation, the manipulator is considered as a continuous CC curve as in Fig. 2.5 [20]. We start with the constant curvature assumption shown in Figure 2.5 where the manipulator backbone geometry in Cartesian coordinates is given based on the curvature parameters ($[\kappa, \phi, l_{\mathrm{d}}]$,) as the system states, where $\kappa = 1/r_{\kappa}$, l_{d} is the central axis length, κ is the curvature and ϕ is polar orientation angle. This map is expressed in terms of a set of transformations given by $R_{y(\phi)} - \rho_{\mathrm{r}} - R_{z(\kappa l_{\mathrm{d}})} - R_{y(-\phi)}$ [20],

$$R_{y_{(\phi)}} = \begin{bmatrix} \mathrm{C}_{(\phi)} & 0 & \mathrm{S}_{(\phi)} \\ 0 & 1 & 0 \\ -\mathrm{S}_{(\phi)} & 0 & \mathrm{C}_{(\phi)} \end{bmatrix}, \quad R_{z(\kappa l_{\mathrm{d}})} = \begin{bmatrix} \mathrm{C}_{(\kappa l_{\mathrm{d}})} & -\mathrm{S}_{(\kappa l_{\mathrm{d}})} & 0 \\ \mathrm{S}_{(\kappa l_{\mathrm{d}})} & \mathrm{C}_{(\kappa l_{\mathrm{d}})} & 0 \\ 0 & 0 & 1 \end{bmatrix}, \tag{2.5}$$

$$\rho_{\mathrm{r}} = \begin{bmatrix} \left(1 - \mathrm{C}_{(\kappa l_{\mathrm{d}})}\right)/\kappa & \mathrm{S}_{(\kappa l_{\mathrm{d}})}/\kappa & 0 \end{bmatrix}^{\mathrm{T}}. \tag{2.6}$$

The transformation matrix for one module is

$$T_{(\kappa,\phi,l_{\mathrm{d}})} = \begin{bmatrix} R_{\mathrm{y}(\phi)} & 0 \\ 0 & 1 \end{bmatrix} . \begin{bmatrix} R_{\mathrm{z}(\kappa l_{\mathrm{d}})} & \rho_{\mathrm{r}} \\ 0 & 1 \end{bmatrix} . \begin{bmatrix} R_{\mathrm{y}(-\phi)} & 0 \\ 0 & 1 \end{bmatrix}, \tag{2.7}$$

where $R_{y(-\phi)}$ is added to correct the final cross-section orientation, because the module does not actually twist but bends in the direction specified by ϕ (Fig. 2.5). The transformation vector of a point on the backbone with axial location s of the i^{th} module in a manipulator consisting of several modules is $T_{(s)} = \left(\prod_{j=1}^{i-1} T_{j\left(\kappa_j,\phi_j,l_{j_{\mathrm{d}}}\right)}\right) T_{i\left(\kappa_i,\phi_i,\lambda_{l_j} s\right)}$, from which the position vector $(\rho_{(s)})$ and orientation matrix $(R_{(s)})$ can be found. For the backbone curve length of the pneumatic chambers $(l_{\mathrm{p_d}})$, in a module with three actuators, we have,

$$\begin{cases} l_{\mathrm{p1_d}} = l_{\mathrm{d}}\left(1 - \kappa r_{\mathrm{o_d}} \mathrm{C}_{(-\phi)}\right) \\ l_{\mathrm{p2_d}} = l_{\mathrm{d}}\left(1 - \kappa r_{\mathrm{o_d}} \mathrm{C}_{(-\phi+2\pi/3)}\right) \\ l_{\mathrm{p3_d}} = l_{\mathrm{d}}\left(1 - \kappa r_{\mathrm{o_d}} \mathrm{C}_{(-\phi-2\pi/3)}\right) \end{cases} \tag{2.8}$$

This map suffers from inherent singularity for $\kappa = 0$. An effective method to overcome this singularity is using $l_{\mathrm{p_d}}$ as the system states in the differential inversion method to find the system model [20, 92]. f_{S} maps the input parameters space (actuator lengths $(l_{\mathrm{p_d}})$ for hydraulic and tendon driven models) to curvature parameters space. For a module with three actuators we have [3],

$$f_{\mathrm{S}} = \begin{cases} \phi = \tan^{-1}\left(\sqrt{3}\left(l_{\mathrm{p2_d}} - l_{\mathrm{p3_d}}\right)/\left(l_{\mathrm{p2_d}} + l_{\mathrm{p3_d}} - 2l_{\mathrm{p1_d}}\right)\right) \\ \kappa = \sqrt{\left(l_{\mathrm{p1_d}}^2 + l_{\mathrm{p2_d}}^2 + l_{\mathrm{p3_d}}^2 - l_{\mathrm{p1_d}} l_{\mathrm{p2_d}} - l_{\mathrm{p1_d}} l_{\mathrm{p3_d}} - l_{\mathrm{p2_d}} l_{\mathrm{p3_d}}\right)}/\left(r_{\mathrm{o_d}}\left(l_{\mathrm{p1_d}} + l_{\mathrm{p2_d}} + l_{\mathrm{p3_d}}\right)\right) \\ l_{\mathrm{d}} = \left(l_{\mathrm{p1_d}} + l_{\mathrm{p2_d}} + l_{\mathrm{p3_d}}\right)/3 \end{cases} \tag{2.9}$$

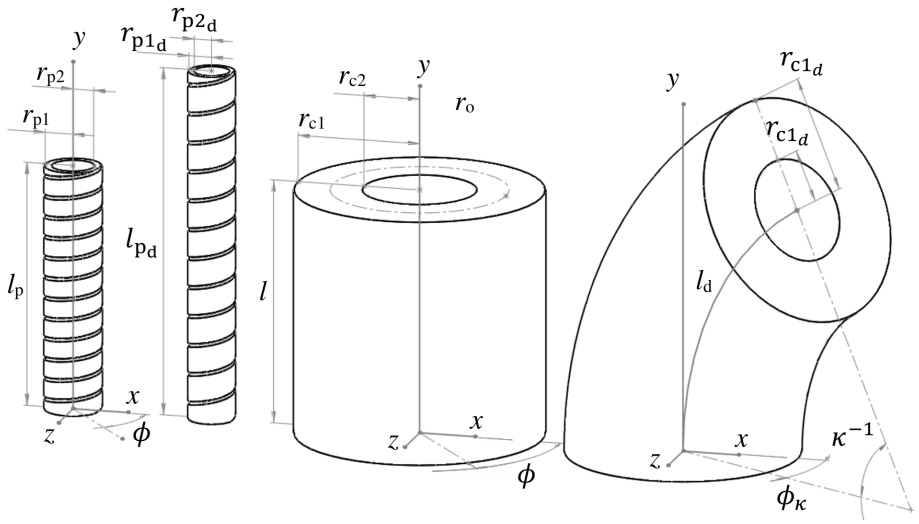

Figure 2.5: Parameters for uniaxial elongation of a pneumatic actuator and constant curvature elongation-bending of a module body shell. Prameters are defined in Table 1.1.

Euler-Bernoulli Beam Model

For pneumatic actuators, a second step is needed to find f_{S} and map the pressure inputs to actuator curvature parameters. A simple model can be derived by assuming the manipulator deformation, as superposition of the elongation and bending of an EB beam in the ϕ direction, due to the static balance between the axial force (f_{EB}) and bending moment (τ_{EB}) of the actuators at the tip, external and the body loads. The axial elongation is $\lambda_l = 1 + f_{\mathrm{EB}}/(Ea_{\mathrm{c}})$ or more precisely by considering the cross-section symmetric deformation of an incompressible material and solving for λ_l in $\lambda_l = 1 + f_{\mathrm{EB}}\lambda_l^2/(Ea_{\mathrm{c}})$, as explained later. The curvature is $\kappa = \tau_{\mathrm{EB}}/EJ_{\phi_\kappa}$ or more precisely $\kappa = \tau_{\mathrm{EB}}\lambda_l^2/EJ_{\phi_\kappa}$, by considering the cross-section deformation after elongation. $J_{\phi_\kappa} = \mathrm{S}^2_{(\psi)}J_{\hat{d_2}} + \mathrm{C}^2_{(\psi)}J_{\hat{d_3}}$ is the second moment of area around the bending axis. The simulation results assuming a fixed cross-section for the pneumatic chambers in comparison to experiments with body loads (EXP.3-I) is presented in Fig. 2.8.

Principle of Virtual Work for Compound Structures

Among all possible changes in the states of a system, the system follows the one set that minimizes the system action (w). This is known as the principle of virtual work or the principle of least action, which can be used to derive the system's equations of motion (EOM). The summation of all the virtual works in the system maintains an equilibrium described as $\sum_i w_{i,q} = 0$. In the case of STIFF-FLOP manipulator we have

$$w_{\mathrm{L},q} + w_{\mathrm{b},q} + w_{\mathrm{c},q} + w_{\mathrm{pt},q} + w_{\mathrm{p},q} = 0, \tag{2.10}$$

where $w_{,q} = f\rho_{\mathrm{d},q}$ is for the point loads (i.e. external loads ($w_{\mathrm{L},q}$), body and inertial loads ($w_{\mathrm{b},q}$)) and $w_{,q} = \int_V U_{,q}\mathrm{d}V$ is for 3D distributed energy fields (i.e. body ($w_{\mathrm{c},q}$) and pneumatic chamber ($w_{\mathrm{pt},q}$) shell deformation energy, air pressure work ($w_{\mathrm{p},q}$)), where U is the unit deformation action and V is the material initial volume [105].

Body loads are distributed forces and moments on the body unit volume, such as the body weight. The body load action can be found by integrating the gravitational unit action over the initial volume as $w_{\mathrm{b},q} = \int\limits_V \sigma \mathrm{g}\rho_{(s),q}\mathrm{d}V$. It can also be calculated based on the virtual displacement of the load's center of distribution (center of mass (COM) in the case of the weight). Neglecting the deformation of the manipulator cross-section and considering the constant curvature assumption, the COM position vector of the i^{th} module is found from the post-multiplication of the traversing modules transformation matrices ($T(\kappa, \phi, l_{\mathrm{d}})$), a rotation mapping to the bending plane ($R_{y_{(\phi_i)}}$), and local position vector of the curve COM in the bending plane as

$$\rho_i = \left(\prod_{j=1}^{i-1} T_j\left(\kappa_j, \phi_j, l_{j_{\mathrm{d}}}\right)\right) \begin{bmatrix} R_{\mathrm{y}(\phi_i)} & 0 \\ 0 & 1 \end{bmatrix} \begin{bmatrix} \frac{(l - \mathrm{S}_{(\kappa_i l_{i_{\mathrm{d}}})})}{\kappa_i l_{i_{\mathrm{d}}}} & \frac{(1 - \mathrm{C}_{(\kappa_i l_{i_{\mathrm{d}}})})}{\kappa_i l_{i_{\mathrm{d}}}} & 0 & 1 \end{bmatrix}_n^{\mathrm{T}}. \tag{2.11}$$

Then, for the action we have $w_{\mathrm{b},q} = \sum\limits_{i=1}^{n_{\mathrm{s}}} \mathrm{g}\sigma a_{\mathrm{c}_i} l_i \rho_{i,q}$, where n_{s} is the number of modules in a multi-segment continuum manipulator. The summation of action for the external loads (f_{L}) acting at the position s_{L}) is $w_{\mathrm{L},q} = \sum\limits_{j=1}^{n_{\mathrm{L}}} f_{\mathrm{L}_j} \rho_{(s_{\mathrm{L}}),q}$, where n_{L} is

the number of concentrated external loads. For pneumatic pressure action we have $w_{\mathrm{p},q} = \sum_{i=1}^{n_\mathrm{s}} p_i V_{\mathrm{p_d}i,q}$ where $V_{\mathrm{p_d}}$ is the pressure chamber volume in the deformed state which is equal to the inner volume of the pneumatic chambers as $V_{\mathrm{p_d}i} = a_{\mathrm{p_d}i} l_{\mathrm{p_d}i}$. The pneumatic chamber deformation is constrained with the helical braids and the incompressibility of their shell. Next, we need to derive deformation action due to the elasticity of the module body and actuator chamber shells.

Braided Pneumatic Actuator Exact Mechanics

In the case of the well-known "OCT-Arm" series of continuum robots [14, 74] where the modules are created from actuators without a supporting shell, a map between the actuator pressure and elongation in combination with Eq. 2.9 can improve the modeling accuracy in prediction of the CC parameters [79, 74]. For pneumatic braided extensible actuators an analytical solutions is presented based on PVW work ($\sum w_{i,q} = 0$), incompressibility assumption and NH deformation energy relation ($U_{\mathrm{p_d}} = E/6 \left(\sum_{i=1}^{3} \lambda_{\mathrm{p}i}^2 - 3 \right)$) [85, 82, 74], where w is the action. The PVW for a chamber is $w_{\mathrm{pt},\lambda_{l_\mathrm{p}}} + w_{\mathrm{p},\lambda_{l_\mathrm{p}}} = 0$, where $w_{\mathrm{pt},\lambda_{l_\mathrm{p}}} = U_{\mathrm{pt},\lambda_{l_\mathrm{p}}} a_{\mathrm{pt}} l_\mathrm{p}$ is the pneumatic chamber body deformation action, $w_{\mathrm{p},\lambda_{l_\mathrm{p}}} = p V_{\mathrm{p_d},\lambda_{l_\mathrm{p}}}$ and $V_{\mathrm{p_d}} = l_{\mathrm{p_d}} a_{\mathrm{p_d}}$ is the total air pressure action, λ_{l_p} is considered as the only system state and $a_{\mathrm{pt}} = \pi(r_{\mathrm{p}2}^2 - r_{\mathrm{p}1}^2)$ is the pneumatic chamber shell thickness area. This can be solved for $p = f_\mathrm{S}^{-1}(q)$ by finding a relation between the principle stretches (λ_{p_i}) for the pneumatic chamber in a cylindrical coordinates. Braid geometrical constraint is used to find this relation. The most famous model to incorporate the braiding effect, used by Trivedi for the first time for continuum manipulators, assumes the outer radius of a constant volume cylindrical pressure chamber is constrained to the helical braids deformation as ${\lambda_{r_\mathrm{p}}}^2 \mathrm{S}_{(\gamma)}^2 + \lambda_{l_\mathrm{p}}^2 \mathrm{C}_{(\gamma)}^2 = 1$, where λ_{r_p} is the radial stretch in a cylindrical coordinates and γ is the braid initial lead angle [74, 76]. Trivedi's presentation of this formula in his paper, [74], has some typographical errors which are corrected here. For a

single pneumatic actuator chamber we have

$$p = \frac{E({r_{\mathrm{p2}}}^2 - {r_{\mathrm{p1}}}^2)(\lambda_{l_\mathrm{p}}^2 - 1)}{6{\lambda_{l_\mathrm{p}}}^4 {r_{\mathrm{p1}}}^2 (1 - {\lambda_{l_\mathrm{p}}}^2 {\mathrm{C}_{(\gamma)}}^2)^3} (\lambda_{l_\mathrm{p}}^6 (-2{\mathrm{S}_{(\gamma)}}^6 + 5{\mathrm{S}_{(\gamma)}}^4 - 4{\mathrm{S}_{(\gamma)}}^2 + 1) + \lambda_{l_\mathrm{p}}^4 (7{\mathrm{S}_{(\gamma)}}^6 - 16{\mathrm{S}_{(\gamma)}}^4 + 11{\mathrm{S}_{(\gamma)}}^2 - 2) + \lambda_{l_\mathrm{p}}^2 (7{\mathrm{S}_{(\gamma)}}^6 - 4{\mathrm{S}_{(\gamma)}}^4 - 3{\mathrm{S}_{(\gamma)}}^2 + 1) + 3{\mathrm{S}_{(\gamma)}}^4). \quad (2.12)$$

Braided Pneumatic Actuator Simplified Mechanics

For a dense threaded chamber, as in most actuators of this type, where $\gamma \approx \pi/2$ and the chamber deformation does not change γ significantly, the thread helix radius change becomes negligible ($\lambda_{r_\mathrm{p}} \approx 1, r_{\mathrm{th_d}} \approx r_{\mathrm{th}} \rightarrow r_{\mathrm{p2_d}} \approx r_{\mathrm{p2}}$) and the Eq. 2.12 simplifies to

$$p = E({r_{\mathrm{p2}}}^2 - {r_{\mathrm{p1}}}^2)(\lambda_{l_\mathrm{p}}^2 - 1)(\lambda_{l_\mathrm{p}}^2 + 3)/6\lambda_{l_\mathrm{p}}^4 {r_{\mathrm{p1}}}^2, \quad (2.13)$$

where the braiding is on the outer surface of the chamber and subscript($_{\mathrm{th}}$) is used for thread parameters. An even simpler model is possible to drive by assuming independent mechanics for the pneumatic chamber and the manipulator body. A dense thread constraint is assumed on the inner surface of the pneumatic chamber ($r_{\mathrm{p1_d}} \approx r_{\mathrm{p1}} \rightarrow a_{\mathrm{p_d}} \approx a_{\mathrm{p}}$). For the gas pressure action, we have $w_{\mathrm{p}} = p a_{\mathrm{p}} l_{\mathrm{p}} \left(\lambda_{l_\mathrm{p}} - 1\right)$. Here, we neglect that the outer radius of the chamber shrinks as the actuator extends. Instead, the NH model suggests that the deformation energy of the incompressible body shell in an unconstrained uniaxial elongation is $w_{\mathrm{pt}} = E a_{\mathrm{p}} l_{\mathrm{p}} \left(\lambda_{l_\mathrm{p}}^2 + 2/\lambda_{l_\mathrm{p}} - 3\right)/6$ [103]. By superposing the results based on PVW, the pressure can be found as $p = E a_{\mathrm{pt}} \left(\lambda_{l_\mathrm{p}} - 1/\lambda_{l_\mathrm{p}}^2\right) / (3a_{\mathrm{p}})$. A comparison between the results of these methods with results of EXP.1 is presented in Fig. 2.7. The figure shows the good accuracy of the inner dense thread model in predicting the values and overall behavior of the actuator for E =105 [KPa]. The helix exact elongating and dense thread models can replicate the same result with slightly different overall behavior for E =205 [Kpa] [74]. We will observe, in the next chapter, that this difference in the identified value for E is due to neglecting the exact cross-section deformation in the dense inner braid model.

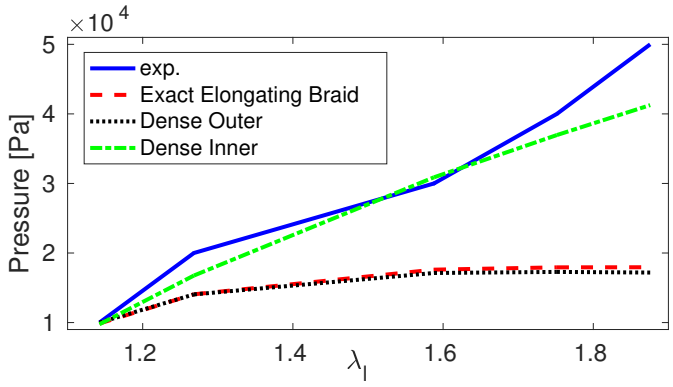

Figure 2.6: Comparison of different models for a braided pneumatic chamber with experimental results of EXP.1 for E_{p} =100 [KPa]. E_{p} is the chamber body elasticity modulus.

Geometry Deformation Model for Compound Structures

A supporting body shell is usually used to prevent the actuator chambers from bulking, i.e. STIFF-FLOP [26, 15]. A more accurate model can be derived by considering the compound structure consisting of the body shell (w_{c}) and braided actuators (w_{p} and w_{pt}). In this case, f_{S} need to be derived by considering the body deformation action (w_{c}) in Eq. 2.10. An accurate but complex solution is a general geometry deformation (GD) model presented in chapter 3 [82, 85]

$$w_{\mathrm{c}} = E/6 \int_{r_{\mathrm{c1}}}^{r_{\mathrm{c2}}} \Lambda_1 \mathrm{d}x,\ \Lambda_1 = (\lambda_l(2+\lambda_l^3) - 2\kappa x\sqrt{\lambda_l}(1-\lambda_l^3))/(1-2\kappa x\sqrt{\lambda_l}), \quad (2.14)$$

where the exact cross-section deformation for elongation-bending of the body and actuator chamber shell are modeled. Simulation results in comparison to experiments for a STIFF-FLOP manipulator section are presented in Fig. 2.8. The model has an average of 28% error mainly because of CC assumption errors; however, it increases the model accuracy by 3% compared to a simple EB beam method.

Simple Compound Model

In a simple model similar to the simple model for a braided pneumatic chamber with dense thread, $w_{\mathrm{pt},\lambda_l}$, the bending deformation action and the interaction of

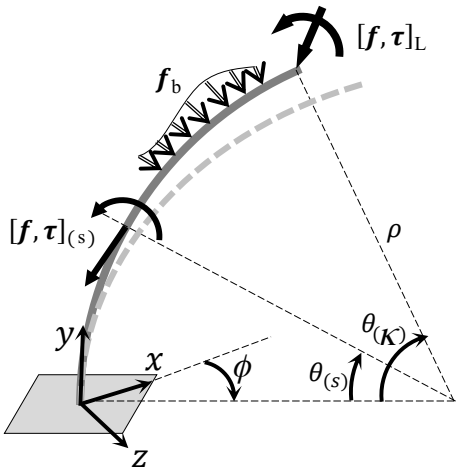

Figure 2.7: Two-step modified CC (MD) model diagram.

the braids with the module body are neglected. Then, from NH assumption and assuming a simple uniaxial elongation, we have $w_{\mathrm{c},\lambda_l} = Ea_{\mathrm{c}}l\left(\lambda_l^2 + 2/\lambda_l - 3\right)/6$ and $w_{\mathrm{p}\lambda_l} = \Sigma_{i=1}^{3}(p_i V_{\mathrm{p}i_{\mathrm{d}},\lambda_l})$, where $V_{\mathrm{p}} = l_{\mathrm{p}}a_{\mathrm{p}}$ and λ_l is considered as the only system state. This model is a combination of the simple NH model for the module body and inner dense thread model for the pneumatic chambers. A careful choice of the combination of models for the actuator and body shell is important to achieve the best accuracy as well as comprehensiveness. The simulation results for the forward model are compared to the experimental results of EXP.3-I. We observed, 28% error for the general GD method and fix cross-section actuator (fix r), 31% for the EB model with fix cross-section actuator, and 28% for the NH symmetric elongation (NH sym.) model with extensile braided actuator (elong. helix). This shows 3% increase in the accuracy of compound models as well as their comprehensive modeling ability (Fig. 2.8). The inner dense thread method is used to model the STIFF-FLOP manipulator using CC approach in the next sections, because of simplicity.

2.2.4 Two-Step Modified Constant Curvature Model

To compensate high modeling errors related to CC assumption, Mahvash et. al. used a two-step approximate model where the CC kinematic map is used to model an eccentric tube catheter with no external and negligible body loading. Then, a

modified mechanical map based on Beam Theory is used to model the deflections from the CC geometry due to external and body loading [106]. Here, we investigate a similar solution for continuum manipulators. Any change in the input pressures or actuator lengths results in a CC geometry. Then the resulted curved beam undergoes small deformations due to body and external loads, based on the EB beam model (Fig. 2.7). Castigliano's method for a linear-elastic structures is used [107] to find an analytical solution for the modifying deformation at the tip and the middle of the manipulator. For the load distribution along a CC geometry we have

$$
\begin{aligned}
f_{\hat{d}_1(\theta)} &= \Big(r_\kappa f_{\mathrm{b}_{\hat{\jmath}}} (\theta_\kappa - \theta) + f_{\mathrm{L}_{\hat{\jmath}}} \Big) \mathrm{C}_{(\theta)} + \big(r_\kappa f_{\mathrm{b}_{\hat{\imath}}} (\theta_\kappa - \theta) + f_{\mathrm{L}_{\hat{\imath}}} \big) \mathrm{S}_{(\theta)}, \qquad (2.15)\\
\tau_{\hat{d}_2(\theta)} &= -r_\kappa^2 f_{\mathrm{b}_{\hat{k}}} \big(\mathrm{C}_{(\theta_\kappa - \theta)} - 1 \big) + r_\kappa f_{\mathrm{L}_{\hat{k}}} \mathrm{S}_{(\theta)} \left(\theta_\kappa - \theta \right) \ - \tau_{\mathrm{L}_{\hat{\jmath}}} \mathrm{S}_{(\theta)} + \tau_{\mathrm{L}_{\hat{\imath}}} \mathrm{C}_{(\theta)},\\
\tau_{\hat{d}_1(\theta)} &= r_\kappa^2 f_{\mathrm{L}_{\hat{k}}} \big(\theta - \theta_\kappa + \mathrm{S}_{(\theta_\kappa - \theta)} \big) - r_\kappa f_{\mathrm{L}_{\hat{k}}} \big(1 - \mathrm{C}_{(\theta_\kappa - \theta)} \big) + \tau_{\mathrm{L}_{\hat{\jmath}}} \mathrm{C}_{(\theta)} + \tau_{\mathrm{L}_{\hat{\imath}}} \mathrm{S}_{(\theta)},\\
\tau_{\hat{d}_3(\theta)} &= r_\kappa^2 A_{\mathrm{MD}} f_{\mathrm{b}_y} \big(\mathrm{C}_{(\theta_\kappa)} - \mathrm{C}_{(\theta)} \big) + \tau_{\mathrm{L}_{\hat{k}}} + \rho f_{\mathrm{L}_{\hat{\imath}}} \big(\mathrm{S}_{(\theta)} - \mathrm{S}_{(\theta_\kappa)} \big)\\
&+ \rho^2 A_{\mathrm{MD}} (\Big(b\mathrm{g} - f_{\mathrm{b}_{\hat{\jmath}}} l_\mathrm{d} \Big) \left(\mathrm{S}_{(\theta_\kappa)} - \mathrm{S}_{(\theta)} + (\theta - \theta_\kappa) \, \mathrm{C}_{(\theta)} \right)) / l_\mathrm{d}\\
&+ r_\kappa^2 f_{\mathrm{b}_{\hat{\imath}}} \big(\mathrm{C}_{(\theta_\kappa)} - \mathrm{C}_{(\theta)} - (\theta - \theta_\kappa) \, \mathrm{S}_{(\theta)} \big) \, ,\\
w_\mathrm{c} &= \int_0^{\theta_\kappa} \Big(\tau_{\hat{d}_2}^2 / \left(2EJ_{\hat{d}_2} \right) + \tau_{\hat{d}_3}^2 / \left(2EJ_{\hat{d}_3} \right) + \tau_{\hat{d}_1}^2 / \left(2GJ_{\hat{d}_1} \right) + f_{\hat{d}_1}^2 / \left(2Ea_\mathrm{c} \right) \Big) \, \mathrm{d}\theta,
\end{aligned}
$$

where the shear strains are neglected, $r_\kappa = 1/\kappa$, $\theta_\kappa = l_\mathrm{d}/\kappa$, $(\hat{\imath}, \hat{\jmath}, \hat{k})$ is the directors for the inertial Cartesian frame $((x, y, z))$ and G is the shear module. A correction factor ($A_{\mathrm{MD}} = 0.01$) is used for the forces in $\hat{d}_1$ direction in calculating $\tau_{\hat{d}_3(\theta)}$ to adjust for the change in the moment arm in the static equilibrium compared to the initial CC configuration. This value should be identified for each loading condition from experiments. While this is a limiting factor, without A_{MD}, the formula results in a large error if the loading condition in the CC initial state is considerably different with the final equilibrium state. The final tip deflection from the CC geometry we have, $\delta_{\hat{\imath}} = w_{\mathrm{c},f_{\mathrm{L}_{\hat{\imath}}}}, \delta_{\hat{\jmath}} = w_{\mathrm{c},f_{\mathrm{L}_{\hat{\jmath}}}}, \delta_{\hat{k}} = w_{\mathrm{c},f_{\mathrm{L}_{\hat{k}}}}$ which can be derived analytically, not presented here due to the limitation of space. The actuator forces are not mentioned as they have been considered to find the initial CC geometry. The modified model improves the accuracy by %1 for all the CC models to preserves the accuracy of

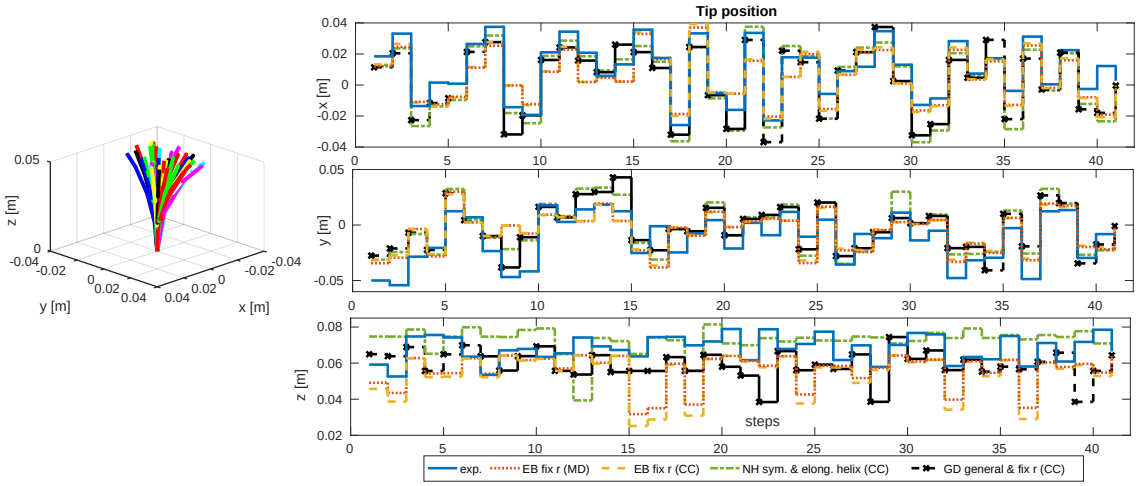

Figure 2.8: Simulation results for Constant Curvature (CC) and two-step modified Constant Curvature (MD) models compared to results from EXP.3-I.

CC model in the presence of small external and body forces (Fig. 2.8). However, this modification is not enough for a precise controller design. CC based models suffer from inaccuracy in presence of external and body forces and singularity at the straight configuration. However, they provide a simple solution to the continuous behavior of the manipulators; hence, being used for real-time or simple path planning and control applications [20]. Using PVW or the introduced two-step modified model enables this method to preserve its accuracy in the presence of small body and external loads and to account for the structural characteristics of the manipulator which helps with the design optimization problems [85, 82]. Lagrange method can be used for dynamic modeling of a continuum manipulator with CC assumption which the same singularities and accuracy problems.

2.2.5 Variable Curvature Kinematics and Mechanics

The VC model assumes the backbone consisting of a series of infinitesimal CC curves to improve the backbone deformation model as the most important factor in increasing the manipulator modeling accuracy [108, 74, 107, 91]. Besides, CC model does not account for the material twist due to any off-plan load which can be modeled in a VC framework.

Variable Curvature Kinematics

The VC kinematics use curvilinear frames, $[\hat{d}_2,\ \hat{d}_1,\ \hat{d}_3]$ for cross-section physical frame or $[\hat{n},\ \hat{t},\ \hat{b}]$ for Frenet – Serret frame (Fig. 2.9), to represent the continuum manipulator backbone as a series of infinitesimal CC curves [91, 11, 74]. VC Kinematics present the relation between the physical curvilinear coordinates ($[\hat{d}_2,\ \hat{d}_1,\ \hat{d}_3]$) and the curve spatial configuration (ρ) expressed in inertial Cartesian coordinates ($[\hat{i},\ \hat{j},\ \hat{k}]$). The physical frame $[\hat{d}_2,\ \hat{d}_1,\ \hat{d}_3]$, where $\hat{d}_1$ is tangent to the backbone and $\hat{d}_2$ is alongside the first air pressure chamber, is used in the forward VC kinematics. A 3×3 rotation matrix (R) relates the local linear strain in the physical curvilinear coordinates (v) to the spatial derivative of the manipulator geometry in the inertial Cartesian coordinates ($\rho_{,s}$) as

$$\rho_{,s} = Rv + \hat{d}_1 = R(v + [0,\ 1,\ 0]^{\mathrm{T}}). \tag{2.16}$$

The spatial derivative of R is found based on the local curvatures and torsion (u)

$$R_{,s} = R\ [u]_{\times}, \tag{2.17}$$

and the angular velocity of each element is $[\omega]_{\times} = R_{,t}R$, where $[\ ]_{\times}$ is an operator to create a skew symmetric matrix. The curvilinear and Cartesian coordinates are aligned at the manipulator base ($s = 0$) where $\rho_0 = 0$, $R_0 = I$ and I is a 3×3 unit matrix.

Cosserat Rod Method

The Cosserat rod model derives the equilibrium between the forces in an infinitesimal element of a continuum media using a free body diagram as in Fig. 2.9 and expressed

in the inertial frame [91]

$$\begin{aligned} n_{,s} + f_{\mathrm{b}} &= \sigma a_{\mathrm{c_d}} \rho_{,tt} \\ m_{,s} + \rho_{,s} \times n + \tau_{\mathrm{b}} &= J_{\mathrm{md}} \omega_{,t}, \end{aligned} \tag{2.18}$$

where f_{b} and τ_{b} are the uniform distributed force and torque on the element, σ is the material density and ω is the element angular velocity. The time-dependent acceleration terms ($\rho_{,tt}$ and $\omega_{,t}$) are zero in a static model. Hooke's law for the linear stress-strain relation is used to relate the spatial derivative of the element boundary force ($n_{,s}$) and moment ($m_{,s}$) to $[v, u]$ as

$$n = K_v v, \;\; m = K_u u, \tag{2.19}$$

where $K_v = \mathrm{diag}(a_{\mathrm{c}}[G, E, G])$ and $K_u = \mathrm{diag}([EJ_{\hat{d}_2}, GJ_{\hat{d}_1}, EJ_{\hat{d}_3}])$ are diagonal stiffness matrices in the physical curvilinear frame. Substituting Eq. (2.18) in (2.19) and rearranging to find $v_{,s}$ and $u_{,s}$ as a function of the loads, results in a static mechanical map [91] for which a simple derivation for the planar case is presented in [74].

To integrate the BVP formed by combining the static and kinematics map (Eq. (2.16-2.19)) over time and space, the initial boundary values for the system states (u , v , ρ , R) are needed. Initial values for ρ and R are known at the manipulator base ($s = 0$), while u and v are known at the tip ($s = l$). A numerical solver can be used to find initial boundary values in the equilibrium point at one of manipulator ends. Alternatively, a discrete finite element approach can be used to solve a large algebraic equation for all the elements' states at once. Duriez presented a real-time approach for this problem using the sparse format of the coefficient matrices [98]. Both methods are not suitable for control and design purposes due to high computational cost.

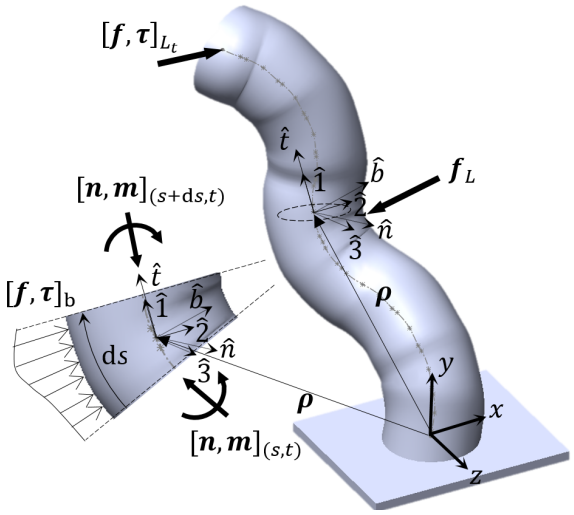

Figure 2.9: Variable curvature kinematics and the Cosserat model free body diagram for one element. $[\hat{d}_2, \hat{d}_1, \hat{d}_3]$ is the physical, $[\hat{n}, \hat{t}, \hat{b}]$ is the Frenet − Serret and $[x, y, z]$ is the inertial frame. Subscript L_{tip}, L and b are for the tip load, general external load and body load respectively.

Beam Theory Approach

Beam theory method is a simpler approach based on the resultant stresses due to the loads at each element which results in the same equations as the Cosserat rod method, but for v and u, unlike $v_{,s}$ and $u_{,s}$ in Eq. (2.18) and (2.19).

$$\begin{aligned} v &= {K_{v_d}}^{-1}.\left(R^{\mathrm{T}}.\left(f_{\mathrm{b}}+f_L\right)+f_p\right) \\ u &= {K_{u_d}}^{-1}.\left(R^{\mathrm{T}}.\left(\tau_{\mathrm{b}}+\tau_L\right)+\tau_p\right), \end{aligned} \tag{2.20}$$

where f_L is the external load exerting at $s = s_L,\ s_L > s$, $f_{\mathrm{b}} = \sigma a_{\mathrm{c}}(l-s)\mathrm{g}\hat{j}$ is the body weight load, $f_p = pa_{\mathrm{p_d}}.[0,1,0]^{\mathrm{T}}$ is the pneumatic pressure force, $\tau_{\mathrm{L}} = \left(\rho_{(s_L)} - \rho_{(s)}\right) \times f_{\mathrm{L}}$ is the moment of f_{L}, $\tau_{\mathrm{b}} = \sigma a_{\mathrm{c}} \int_s^l \left(\rho_{(s)} - \rho_{(\varepsilon)}\right) \mathrm{d}\varepsilon \times \mathrm{g}\hat{j}$ is the body weight moment, $\tau_p = pa_{\mathrm{p_d}}.[r_{J\hat{d}_2}, 0, r_{J\hat{d}_3}]_{\mathrm{d}}$ is the pneumatic pressure moment and $\lambda_{\hat{d}_1,s} = v_{\hat{d}_1} + 1$. $v_{\hat{d}_1}$ from the previous integration step is used in $\lambda_{\hat{d}_1,s}$ to prevent added nonlinearity to the equations. $\lambda_{\hat{d}_1,s}$ is used in Eq. (2.2) to update the change in planar dimensions of each element due to the highly elastic deformation. The downside of the beam theory approach is that we need to guess the equilibrium geometry to find the cross-sections' load, compared to the Cosserat rod model where only the initial boundary

values are needed. However, it is suitable for the forward spatial and time integration using an approximate series-solution. In the equilibrium state, the geometry found from the forward kinematic map (ρ) should mach the guessed geometry (ρ^*), used for the inverse kinematic in the mechanical map ($\rho \approx \rho^*$).

Single Shooting Optimization Based Solution

We can approximate the solution for the BVP with a series of finite terms, i.e. a polynomial of order n as a function of s, and investigating the equilibrium condition. This is considered as a special case of separation of variable method for Partial Differential Equation (PDE) systems that provides a weak form solution. The terms are consisting of separate space dependent shape functions and time dependent coefficients where the time dependent part is constant in static cases. The constants are being optimized so the guessed series solution represents the static equilibrium of the system. We fit a curve to seven points using Matlab 'interp1' function and then use Matlab 'fsolve' function for optimization of these points positions in the plane starting from a straight configuration as the initial guess. The algorithm usually needs only two trials to find the equilibrium configuration for a single-curve formation and three trials for a double-curve formation, i.e. in presence of high external force showing the possibility of real-time implementation of this method. A similar result can be achieved by having a polynomial of order at least three to model the 'S' shape configuration of a single module under high external loads with good accuracy (EXP.2). Similar to observations in the previous research [109], the overall accuracy of the Cosserat rod model is about 16% better than the CC models with a 12% mean error (Fig. 2.10) in comparison to our experimental results with extensive external loads (EXP.2). Different optimization Iterations are presented in Fig. 2.11. It is relatively hard to model the dynamics of a system using Cosserat and beam theory methods; however, they are the best in terms of accuracy to find the manipulator static equilibrium configuration with general loading conditions.

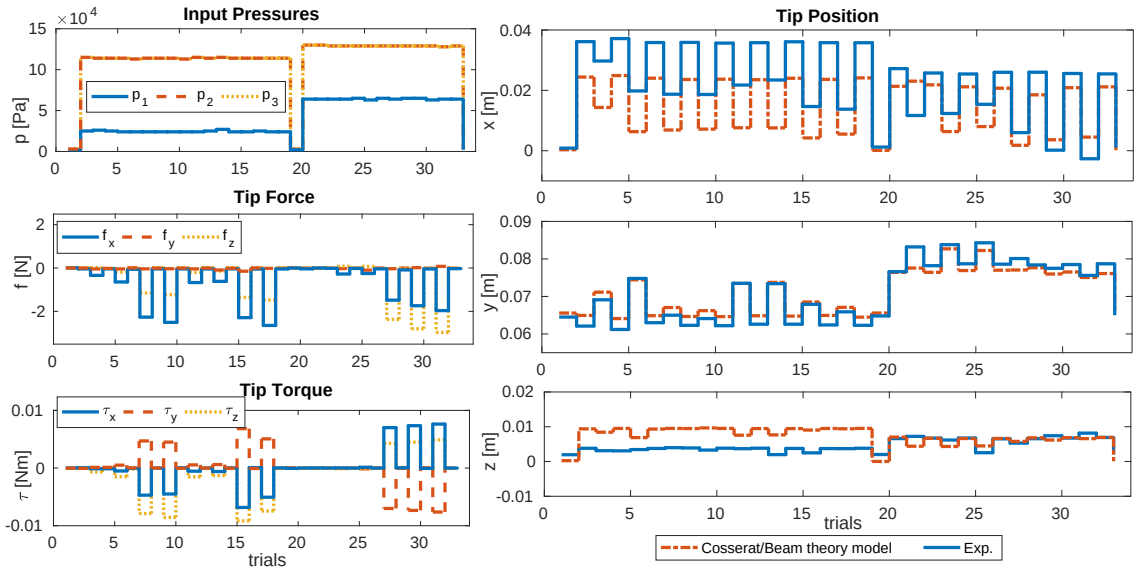

Figure 2.10: Cosserat/beam theory model results vs. experiments with extensive external loads (EXP.2).

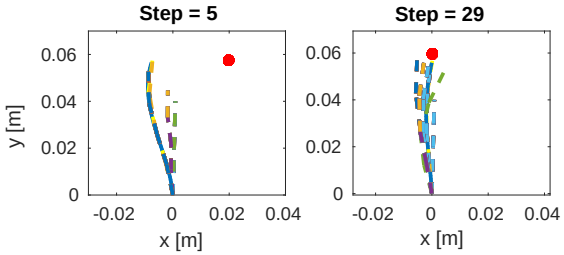

Figure 2.11: Optimization iterations for Cosserat/beam rod model.

2.2.6 Identification Based Series Solutions

Coefficients of a series solution can be identified based on the experimental results [92, 97]. Godage presented an identification based Taylor series solution for the kinematic map of a continuum manipulator (the relation between actuator chamber length and manipulator geometry) and later implemented the resulted identified solution in the Lagrange EOM for dynamic modeling of a continuum manipulator [92]. The spatial geometry is described using a time-dependent coefficient vector ($\Upsilon_{(t)}$) and a shape function matrix ($\Psi_{(s)}$) as $\rho_{(s,t)} = [x_{(s,t)}, y_{(s,t)}, z_{(s,t)}] = \Psi_{(s)}\Upsilon_{(t)}$, where $\in [0, 1]$ is a scalar variable defining the position of each point on the manipulator axis with 0 for the base and 1 for the tip. The final model can be as simple as a polynomial of order five [92]. Godage used three equations each with 56 shape functions of the form $A_1 l^{A_2} s^{A_3+1} R^{-A_3}$, where A_1, A_2 and A_3 are integers to be iden-

tified based on optimization, A_1 & $A_2 \in [0, 1]$ and $A_3 \in [0, 5]$ [92]. Choice of the shape function and time-dependent coefficient can be based on observation, guessed solution or completely arbitrary. Similar to other weak approximation solutions, they should satisfy the boundary and initial conditions and the convergence should be investigated for increasing the number of terms. Here, we introduce a simple series with eight time dependent coefficients (C_{ij}) to be identified using Least Square Value optimization as,

$$\Psi_{(s)} = C_{3\times 8}.\mathrm{diag}[s, s, s, s, s^2, s^2, s^2, s^3] \tag{2.21}$$

where $\Upsilon_{(t)} = [1, l_{\mathrm{p1_d}}, l_{\mathrm{p2_d}}, l_{\mathrm{p3_d}}, l_{\mathrm{p1_d}} l_{\mathrm{p2_d}}, l_{\mathrm{p1_d}} l_{\mathrm{p3_d}}, l_{\mathrm{p2_d}} l_{\mathrm{p3_d}}, l_{\mathrm{p1_d}} l_{\mathrm{p2_d}} l_{\mathrm{p3_d}}]^{\mathrm{T}}$ is for a system with kinematic inputs and $\Upsilon_{(t)} = [1, p_1, p_2, p_3, p_1p_2, p_1p_3, p_2p_3, p_1p_2p_3]^{\mathrm{T}}$ is for a system with pressure inputs. To satisfy boundary conditions we have $[\ C_{11} \quad C_{21} \quad C_{31}\ ] = [\ x_0 \quad y_0 \quad z_0\ ]_{\mathrm{tip}}$. The model trains and performs very fast, suitable for real-time and precise control purposes in a known condition. The simulation results show 11% mean error which is the most accurate results in predicting the static behavior of EXP.3-I after being trained with 30% of the experimental points (Fig. 2.12). However, the accuracy is limited to the condition for which the model is trained with, and the necessary structural information for design optimization is not incorporated in the model. Besides, the complexity of the series solution makes any further analytical analysis, such as dynamic modeling, controller design and stability analysis, a hard task. This method can be assumed as a basis for both optimization and control frameworks.

2.3 Comparison on Manipulator Models

In Table 2.1, a comparison between the different modeling methods is presented based on the derivation and implementation complexity, the level of structural characteristics in the model, sensitivity to model parameters, computation cost as a

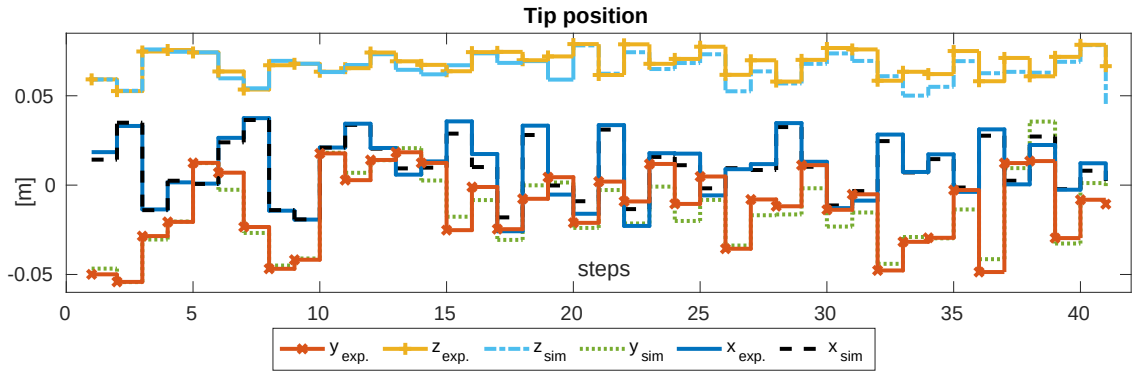

Figure 2.12: Identification based series solution model results compared to EXP.3-I.

measure of real-time performance, overall accuracy and suggested applications. It worth mentioning that the information in Table 2.1 is provided based on the feasibility, ease and popularity of the model usage for a specific purpose; however, all the methods can be used for different purposes after some modification.

	Lumped System	CC & EB	CC & PVW
Specification	Dynamic, Forward, Inverse	Static, Forward, Inverse	Static, Inverse
Complexity	Hard	Easy	Medium
Structural Details	Medium	Low	High
Parameter Sensitivity	Med.-High	Low	High
Computational Cost	High	Low	Medium
Accuracy (error)	Medium (13 [mm], 22%)	Low (19 [mm], 31%)	Low-Med. (17 [mm], 28%)
Application	Simulation, Control	Non-accurate Control	Design
	Modified CC	Cosserat & Beam Theory	Series Identification
Specification	Static, Forward	Static, Forward	Static, Forward, Inverse
Complexity	Medium	Hard	Medium
Structural Details	Low-Med.	Medium	Low
Parameter Sensitivity	Medium	Medium	Low
Computational Cost	Low	High	Low-Med.
Accuracy (error)	Low-Med. (16.5[mm], 27%)	High (7[mm], 12%)	High (6.5[mm], 11%)
Application	Non-accurate Control	Simulation	Control

Table 2.1: Comparisons of different modeling approaches for a continuum manipulator.

2.4 Conclusion

In this chapter, a review on derivation and implementation of five different approaches for modeling of continuum manipulators is presented. Lumped system dynamic model, Constant Curvature, two-step modified Constant Curvature, Variable Curvature Cosserat rod and Beam Theory approach, and series solution identification are derived and the modeling results are compared with experimental data, with identical conditions, using a STIFF-FLOP continuum manipulator module. Our study shows the competency of the identification based model in comparison to the other methods in accuracy (11% mean absolute error) and real-time performance.This method is suitable to provide a real-time approximate estimation when all the experimental conditions are similar to those of the identification training data set. From a different perspective, we conclude that dynamic behavior prediction and control method implementation are streamlined in lumped system model with 22% mean absolute error. This approach makes it easy to design and stability analysis of a nonlinear control scheme based on traditional rigid body dynamics and control theory. Different constant curvature models, including its modified version, based on the principle of virtual work show less accuracy (28-31% mean absolute error) but the better incorporation of structural characteristics makes them suitable for structural design optimization purposes. Besides, they are a good candidate for simple model-based control and observation problems, e.g. in state estimation using a nonlinear Kalman filter. Finally, the Cosserat rod and beam theory methods provide an exact model (12% mean absolute error) for general conditions which makes them the most reliable model for continuum manipulators working in unknown conditions. However, their implementation complexity and infinite modeling state space make it hard to use them for planning, control and observation tasks. Furthermore, through the sections of this chapter, simple mathematical derivations of the manipulator deformation energy are discussed; a comparison between different models for a braided extensile pneumatic actuator is presented and a novel two-step modified Constant

Curvature solution using Castiglianos method is suggested to simplify the design optimization, control and path planning problems of continuum manipulators.

However, exact general behavior estimation, simple stable controller design and real-time performance are needed in most real-world applications. Besides, the model used for control is better to be used for the manipulator design optimization too, to be able to guarantee an optimized output behavior from the final product. These issues prevent the discussed models from effective implementation in real-world engineering scenarios. In the next chapter, we try to address these issues by looking into exact semi-analytical modeling of a continuum manipulator deformation in general loading condition by looking into the underlying principles and individual elements in the compound structure of a continuum manipulator.

Chapter 3

Exact Real-Time Geometry Deformation Model for Continuum Manipulators

Abstract

This chapter focuses on the need for a general and comprehensive analytical methods for exact modeling of multi-segment continuum manipulators, suitable for design optimization and real-time control applications.

For the first time, we introduce the bending effect in the model of a braided extensile pneumatic actuator with both stiff and bendable thread. Then, as the first objective of this chapter, the effect of the manipulator cross-section deformation on the constant curvature and variable curvature models is investigated using simple analytical results from a novel geometry deformation method and is compared to experimental results. We achieve 38% mean reference error simulation accuracy using our constant curvature model for a braided continuum manipulator in presence of body load (EXP.3-I) and 10% using our variable curvature model in presence of extensive external loads (EXP.2). With proper model assumptions and taking to

account the cross-section deformation, an 7-13% increase in the simulation accuracy is achieved compared to a fixed cross-section model, based on mean absolute error value. This statement is valid independent of the manipulator slenderness due to the hyper elastic behavior of the continuum material. The presented models can be used for the exact modeling and design optimization of compound continuum manipulators by providing an analytical tool for the sensitivity analysis of the manipulator performance.

Then, as the second objective of this chapter, to address the challenges with real-time accurate modeling of this class of manipulators in the presence of significant external and body loads, we introduce a novel series solution for variable-curvature Cosserat rod static and Lagrangian dynamic methods. By combining a modified Lagrange polynomial series solution, based on experimental observations, with Ritz and Ritz-Galerkin methods, the infinite modeling state space of a continuum manipulator is minimized to geometrical position of a few number of physical points (in our case two). As a result, a unified easy to implement vector formalism is proposed for the nonlinear impedance and configuration control. We showed that by considering the mechanical effects of highly elastic axial deformation, the model accuracy is increased up to 6%. The proposed model predicts experimental results with 6-8% (4-6 [mm]) mean error for the Ritz-Galerkin method in static cases and 16-20% (12-14 [mm]) mean error for the Ritz method in dynamic cases, in planar (EXP.2) and general 3D (EXP.3-I) motions. To evaluate our objectives in this chapter, our error analysis is compared to other five different commonly used models in the literature, our approximate solution is shown to be more accurate with the smallest possible number of modeling states and suitable for real-time modeling, observation and control applications.

The modeling approaches presented in this chapter make it easy to integrate the model of a stiffness controllable interface with that of the manipulator with an exact, real-time and general solution for different loading conditions.

3.1 Introduction on Geometry Deformation Approach

The texture and flexibility of soft robots match well with biological properties of natural actuators. Different mechanisms to control soft robot stiffness for safe interaction and minimally invasive applications have gained increasing interest recently. To this end, stiffness-tuneable structures by granular jamming [62, 110, 60] and low-melting-point-alloys [50, 48], morphing structures [111], stiffness controllable interfaces by granular [37, 112], layer [61] and scale jamming [41, 38] are investigated recently. The new interest in the continuum manipulators with stiffness varying and inhomogeneous compound structures indicates the need for further investigation of their exact modeling and control problems incorporating their complex deformations.

Any General deformation of a continuum manipulator element is a combination of a pure rotation due to the backbone curvatures and torsion, and a 3D stretch in the rotated frame due to the element axial stretch and the cross-section distortion. The material stretch is responsible for storing or releasing energy due to deformation while the pure frame rotation doe does not have any contribution. To find the manipulator continuum material deformation energy, the manipulator cross-section and axial deformation should be considered. The cross-section of an unconstrained cylinder deforms uniformly in elongation. To distinguish the bending effect, the cross-section distortion (asymmetric deformation) is needed to be considered, independent of the manipulator slenderness.

In order to achieve comprehensive accuracy as well as computational efficiency, to constitute a base for modeling manipulators with compound and tuneable stiffness structure, and to fill the gap between approximate and finite solutions discussed in the previous chapter, a novel geometry deformation based approach is introduced in this chapter [85], The presented geometry deformation model is based on a famous

work by Rivlin on 'The Problem of Flexure' [113], where he presents a geometrical approach to derive the strain energy function for an incompressible highly elastic cube under pure bending with certain geometrical assumptions about the deformed and initial states. In this chapter, an approximate analytical model for compound continuum manipulators with pneumatic braided extensor actuators in the presence of external forces is presented. Utilizing experimental observation of the deformed system to model the deformation energy of the continuum media, the principle of virtual work is used to account for the behavior of compound structures. The constant curvature assumption is used for the kinematics of the manipulator backbone as an initial but not essential assumption. A new method is introduced to model the pure elongation of pneumatic braided extensile pneumatic actuators using geometry deformation approach.

In the first section of this chapter, this idea is extended by presenting an exact yet simpler model for the actuator chamber braid in elongation and bending with two types of braids, a highly deformable and a stiffer one. A shorter and simpler derivation method is discussed for deformation energy of the continuum media in the planar deformation case compared to the model presented in [85]. Then a more realistic solution without the planar deformation restriction is introduced. Finally, two comprehensive models for compound manipulators are discussed. First, by using the principle of virtual energy, Neo-Hookean evaluation of deformation energy and constant curvature assumption for the backbone deformation. Second, by employing Variable Curvature kinematics, Hooks linear stress-strain relation and the Cosserat rod method, as the general approaches and assumption used in literature, for general bending of an externally loaded continuum manipulator.

Our approach benefits from implementation of compound structure complexities in the proposed model, i.e. braided chamber and continuum media exact behavior modeling, and accurate estimation of the cross-section and backbone deformation, by combining geometry deformation and Cosserat rod methods in a simple to derive and efficient to simulate procedure. The characteristic parameters of the chambers

are not considered in most of the models based on lumped system [114] and Cosserat rod method despite some efforts for modeling of the braids in the pure elongation case [74]. An exact model for the cross-section deformation has three main benefits; it increases the modeling accuracy for general design and control applications (discussed in this chapter), provides the necessary tool for the trending research on the design of continuum manipulators with tuneable regional stiffness structure [23]; and enables exact planning for minimal invasive and safe robot-environment interaction applications where the working space is limited, i.e. continuum manipulators in surgery [12] and space exploration [115]. The need for comprehensive modeling of cross-section deformation of a continuum manipulator has been suggested in [94] too. Our comprehensive modeling tool for compound structures provides a better insight in design, optimization and control of this class of mechanisms in a simpler, more efficient and accurate way which is based on and in agreement with experimental observations. Besides, Comparing the accuracy and sensitivity of the models help to understand what level of modeling complexity is needed to incorporate effects of certain structural parameters and achieve a desired modeling accuracy in different applications. To this end, the effect of different modeling assumptions on the modeling and sensitivity analysis accuracy is investigated.

Focusing on the modeling and control of the manipulator backbone in the second section, 1) we introduce a model with finite number of states while preserving the modeling accuracy and generality based on which the design of a nonlinear impedance and configuration feedback controller is possible; 2) the solution is extended to the dynamic case based on a vector formalism for PVW, in general 3D motions of a multi-segment manipulator; 3) the modeling accuracy is increased by considering the mechanical effects of the manipulator axial highly elastic deformation as well as in the planar direction. We introduce a novel, accurate yet real-time approximate series-solution for the Cosserat beam method in the static case and a PVW based model in the dynamic case for the general 3D motion of a multi-segment continuum manipulator in the presence of significant external and body loads. Based

on the experimental observations, a modified Lagrange polynomial, as a differentiable polynomial of finite order, is chosen to drive a weak-form series-solution for the mechanics of a continuum manipulator using continuous Ritz and Ritz-Galerkin methods. To the best of our knowledge and compared to the most recent similar research in the field [75], this is the first time that the infinite modeling state space of such problem minimizes to the geometrical positions of two points at the tip and in the middle of the manipulator. As a result, different dynamic impedance and configuration control scenarios are formulated using traditional nonlinear control theories in a unified and easy to implement vector formalism. We neglect the close loop terms in the first part to highlight the performance and accuracy of our method. A PID term is incorporated in the inverse control model later. Modeling results are verified against experimental results in the static and dynamic cases. The proposed model is the most accurate mechanics of materials based model with the smallest possible number of modeling states compared to the other well-known approaches in the literature [84] and can be used for precise static and dynamic modeling, observation and control in real-time applications.

In sections 3.2, first, we discuss the exact modeling of a compound continuum manipulator using the geometry deformation approach. We start with the unit deformation energy in section 3.2.1 as the basis for our first modeling framework. The models for a braided extensor actuator in simple elongation, general elongation and bending cases are discussed in section 3.2.2. The exact modeling of the manipulator cross-section with planar and general assumptions are discussed in section 3.2.3. Our approach to model compound continuum structures based on the constant curvature assumption using the principle of virtual work, and the extension of the modeling tool to variable curvature kinematics using Cosserat rod method is explained in section 3.2.4. The simulation results and comparison between the models' accuracy and sensitivity to structural parameters are discussed in section 3.2.5, followed by the related discussion on the presented exact geometry modeling approaches in section 3.2.7. In section 3.3, first, the extended modeling framework is discussed

consisting of the inverse VC mechanics and a dynamic model based on PVW. The Ritz and Ritz-Galerkin series solutions are detailed in section 3.3.3 for static and dynamic models followed by a vector form derivation for the nonlinear control and observation problems in section 3.3.4. Experiments and discussions of this section are described in section 3.3.5. Finally, conclusions are presented in section 3.4

3.2 Exact Modeling of Compound Continuum Manipulators

Our approach in this section to modeling of a continuum manipulator consists of a manipulator specific dynamic map (f_{S}) solving the linear strains (v), and curvatures and torsion (u) based on the internal and external loads, and a general kinematic map (f_{G}) finding the manipulator geometry based on the $[v, u]$. The forward and inverse dynamic maps can be found based on various methods; however, some methods are better to evaluate the forward map, while others are more suitable for the inverse map. The continuum form of Lagrange EOM is better for the forward and inverse dynamic maps, the Cosserat rod model is appropriate for the forward static map, and it is more straightforward to derive the inverse static map for a continuum manipulator using the principle of virtual work [85]. Static and quasi-static models are investigated here as special cases of the dynamic model, where the inertial forces are neglected assuming static equilibrium and slow transitions in the system states. This is a reasonable assumption since the application of continuum manipulator in precise manipulation tasks, e.g. minimally invasive surgery as the main application of the outcomes from this research, involve less rapid dynamic movements and more quasi-static transition of the states in the task space [12]. Hooke's law of linear stress-strain relation is widely used in the dynamic model, while using Neo-Hookean assumptions and the principle of virtual energy results in a more accurate static model [103] as the body specific map (f_{S}). A constant curvature assumption for

simplicity and variable curvature assumption for precise modeling are used to find the manipulator kinematic map (f_{G}). The manipulator backbone deformation has been assumed to play the dominant role in the modeling of continuum manipulators and the cross-section deformation has usually been neglected in the literature. However, as the manipulator becomes softer and the cross-section diameter ratio to the module length increases, the cross-section deformation becomes more important. This cannot be neglected in case of emerging studies on embedding regional stiffness tuneable structures in continuum manipulators [48, 59, 43].

Here, we use the principle of virtual work to model the cross-section deformation caused by constant curvature bending of one manipulator module under general external loads. The use of Neo-Hookean and Hooke's linear stress-strain relations have been utilized in this case. This method makes it possible to model the continuum manipulators with compound structures. Despite the methods based on Newtonian dynamics such as Cosserat rod theory, our approach solves for the inverse static map (f_{G}^{-1}) directly. Subsequently, we combine our models for the cross-section geometry deformation with the variable curvature kinematics and Cosserat rod theory to find a more accurate forward static map. This model improves the modeling accuracy in the case of having large external forces. For this combined model, we only use the linear Hooke's law for stress-strain relation.

3.2.1 Unit Deformation Energy

We start with the PVW presented in Eq. 2.10. Elastic deformation action of the continuum media ($w_{\mathrm{c|pt}}$) can be derived with good accuracy based on the Neo-Hookean relation for large deformations [103] using the unit deformation energy (U) as

$$w_{\mathrm{c}} = \int_{V_{\mathrm{c}}} U_{\mathrm{c}} \mathrm{d}V, \; U_{\mathrm{c}} = E(\Lambda_1 - 3)/6. \tag{3.1}$$

The unit deformation energy in an orthogonal frame can be derived based on the Cauchy-Green stretch tensor first invariant

$$\Lambda_1 = \sum_{i=1}^{3} \lambda_i^2, \tag{3.2}$$

in the case that stretch values along the principle axis are known [103], or by having the general deformation map (displacement vector, $\eta_{\mathrm{d}} = \rho_{\mathrm{d}} - \rho$) in one coordinate system we have [113],

$$\begin{aligned}
\eta_x &= x_{\mathrm{d}} - x,\ \eta_y = y_{\mathrm{d}} - y,\ \eta_z = z_{\mathrm{d}} - z, && (3.3)\\
\varepsilon_{xx} &= \eta_{x,x} + \left(\eta_{x,x}^2 + \eta_{y,x}^2 + \eta_{z,x}^2\right)/2,\\
\varepsilon_{yy} &= \eta_{y,y} + \left(\eta_{x,y}^2 + \eta_{y,y}^2 + \eta_{z,y}^2\right)/2,\\
\varepsilon_{zz} &= \eta_{z,z} + \left(\eta_{x,z}^2 + \eta_{y,z}^2 + \eta_{z,z}^2\right)/2,\\
\Lambda_1 &= 3 + 2\left(\varepsilon_{xx} + \varepsilon_{yy} + \varepsilon_{zz}\right). && (3.4)
\end{aligned}$$

Alternatively, (w_{c}) can be found based on Hooke's linear stress-strain relation law similar to an Euler-Bernoulli cantilever beam [103]. This is valid for small deformations; however, it can be used in finite element method. Here, the simple Euler-Bernoulli beam stress-strain relations are used, for a CC deformation around the local binormal axis ($\hat{b}$), by replacing the cross-section moment of area in the local frame ($J_{\hat{d}_i \mathrm{d}}$) based on the deformed geometry as

$$w_{\mathrm{c}} = \frac{1}{2} E(J_{\hat{\phi'}_{\mathrm{d}}} \kappa^2 + a(\lambda_l - 1)^2)\, l_{\mathrm{d}}, \tag{3.5}$$

where $J_{\hat{\phi'}_{\mathrm{d}}}$ and l_{d} are found from the geometry deformation maps. We call this the Hooke's law based model for the body deformation action.

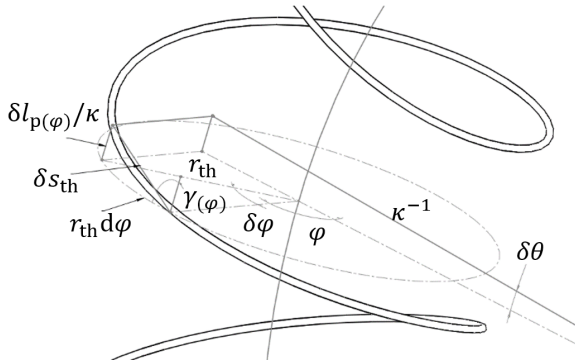

Figure 3.1: Parameters for a bent helical thread.

3.2.2 Braided extensile Actuator

Braided extensor actuators are threaded continuum chambers similar to McKibben actuators [116] except for the fact that they elongate when pressurized [76]. The thread constraints the curvilinear axial and radial deformation of the chamber shell but slips tangent to the shell tube cross-section as discussed in section 1.2.

Simple Elongation

The thread constraint for simple axial deformation is derived from the helix geometry, assuming that the thread length (s_{th}) and the helix total twist angle ($\varphi_{\mathrm{th}} = 2n_{\mathrm{th}}\pi$) are fixed [76] (Fig. 3.1), where n_{th} is the number of helix full turns.

For the unit length of the thread ($\mathrm{d}s_{\mathrm{th}}$), which remains constant, in deformed state we have $\delta l_{\mathrm{p_d}}^2 + (r_{\mathrm{th_d}}\delta\varphi)^2 = \delta s_{\mathrm{th}}^2$. Substituting $\delta l_{\mathrm{p_d}} = \lambda_{l_{\mathrm{p}}}\delta l_{\mathrm{p}}$, $r_{\mathrm{th_d}} = \lambda_{r_{\mathrm{p}}} r_{\mathrm{th}}$, $\delta l_{\mathrm{p}} = \delta s_{\mathrm{th}}\mathrm{C}_{(\gamma)}$ and $r_{\mathrm{th}}\delta\varphi = \delta s_{\mathrm{th}}\mathrm{S}_{(\gamma)}$, where $\lambda_{r_{\mathrm{p}}} = r_{\mathrm{th_d}}/r_{\mathrm{th}}$ and $\lambda_{l_{\mathrm{p}}} = l_{\mathrm{p_d}}/l_{\mathrm{p}}$, we get

$$\lambda_{r_{\mathrm{p}}}{}^2\mathrm{S}_{(\gamma)}^2 + \lambda_{l_{\mathrm{p}}}{}^2\mathrm{C}_{(\gamma)}^2 = 1, \tag{3.6}$$

A simplified assumption to derive pneumatic pressure action for a STIFF-FLOP module is neglecting the pneumatic chamber thin shell and assuming $r_{\mathrm{p1}} = r_{\mathrm{th_d}} = \lambda_{r_{\mathrm{p}}} r_{\mathrm{th}}$. Then we have

$$w_{\mathrm{p}} = p l_{\mathrm{p}} \pi r_{\mathrm{th}}^2 \lambda_{l_{\mathrm{p}}} \lambda_{r_{\mathrm{p}}}^2,\ \lambda_{r_{\mathrm{p}}}^2 = (1 - \lambda_{l_{\mathrm{p}}}{}^2\mathrm{C}_{(\gamma)}^2)/\mathrm{S}_{(\gamma)}^2. \tag{3.7}$$

This is not valid for manipulators with a thick chamber shell and without an encapsulating body shell, i.e. OCT-Arm [74]. Note that, a single actuator chamber cannot be modeled by having the pneumatic pressure action only.

The typically adopted model in the literature [74, 76] assumes that the chamber shell volume is fully constrained to the thread and all the body volume points follow helical radial and axial deformations. We call this method the constrained volume model. The shell elastic deformation action can be derived based on the incompresibility criteria ($\lambda_{\varphi_\mathrm{p}} = 1/(\lambda_{l_\mathrm{p}}\lambda_{r_\mathrm{p}})$), $r_{\mathrm{p}1} = r_{\mathrm{th}}$, Eq. 3.1, Eq. 3.2 and $[\lambda_{l_\mathrm{p}}, \lambda_{r_{\mathrm{p_d}}}, \lambda_{\varphi_\mathrm{p}}]$ as the known stretches along the cylindrical coordinate principle axes [74][76]. Then for the actions we have

$$\begin{aligned} w_{\mathrm{pt}} &= \frac{E l_p a_{\mathrm{pt}}}{6}\left(\frac{\lambda_{l_p}^2 \mathrm{C}_{(\gamma)}{}^2 - 1}{\mathrm{S}_{(\gamma)}{}^2} + \frac{\mathrm{S}_{(\gamma)}{}^2}{\lambda_{l_p}^2(\lambda_{l_p}^2 \mathrm{C}_{(\gamma)}{}^2 - 1)} - \lambda_{l_p}^2 + 3\right), \\ w_{\mathrm{p}} &= p\lambda_{l_p} l_c \pi r_{p_1}^2(\lambda_{l_p}^2 \mathrm{S}_{(\gamma)}^2 - \lambda_{l_p}^2 + 1)/\mathrm{S}_\lambda^2,\ a_{\mathrm{p}} = \pi(r_{p1}{}^2 - r_{p2}{}^2). \end{aligned} \tag{3.8}$$

For one chamber, using eq. 2.10 ($(w_{\mathrm{pt},\lambda_l} + w_{\mathrm{G},\lambda_l})\delta\lambda_{l_\mathrm{p}} = 0$) and assuming λ_{l_p} as the only system state, we get [74]

$$\begin{aligned} p = {} & \frac{E(r_{p1}{}^2 - r_{p2}{}^2)(\lambda_{l_p}^2 - 1)}{6\lambda_{l_p}^4 r_{p1}{}^2(\lambda_{l_p}^2 \mathrm{p}_{(\gamma)}{}^2 - 1)^3} \times \\ & (\lambda_{l_p}^6(-2\mathrm{S}_{(\gamma)}{}^6 + 5\mathrm{S}_{(\gamma)}{}^4 - 4\mathrm{S}_{(\gamma)}{}^2 + 1) + \\ & \lambda_{l_p}^4(7\mathrm{S}_{(\gamma)}{}^6 - 16\mathrm{S}_{(\gamma)}{}^4 + 11\mathrm{S}_{(\gamma)}{}^2 - 2) + \\ & \lambda_{l_p}^2(7\mathrm{S}_{(\gamma)}{}^6 - 4\mathrm{S}_{(\gamma)}{}^4 - 3\mathrm{S}_{(\gamma)}{}^2 + 1) + 3\mathrm{S}_{(\gamma)}{}^4). \end{aligned} \tag{3.9}$$

This assumption constrains the radial and axial deformation of the chamber to the helix. The chamber tangential deformation is free and can be found based on the incompressibility criteria. A small modeling error is observed in comparison with experimental results by Trivedi, because of non-perfect slip between the thread and the chamber surface [74]. An alternative derivation for a braided chamber with simple elongation is given in [85] using geometry deformation method which results in a more complex solution but with similar concept. It has been shown that the

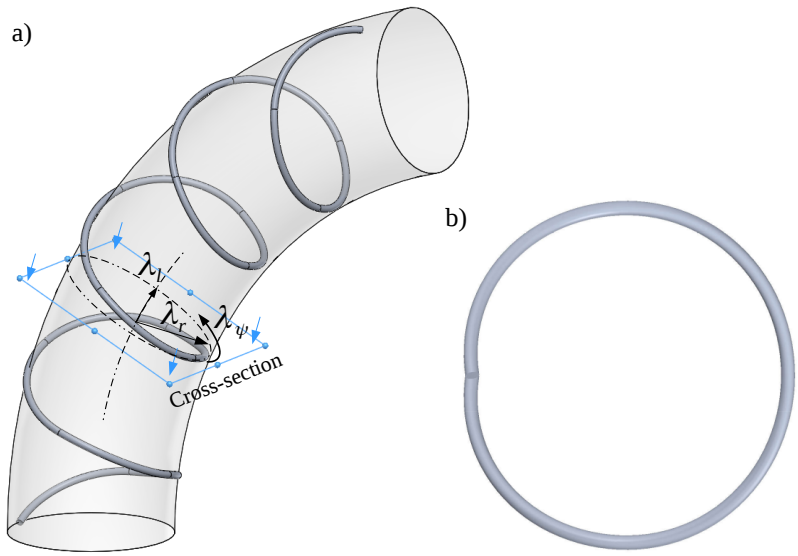

Figure 3.2: (a) A helix with only pure torsion of the braid and the definition of stretches in a cross-section cylindrical coordinates, (b) the enclosed tube heart-shape deformed cross-section due to torsion-only assumption for the braid, based on a Solidworks 3D model with 90 [deg] segments, r_2 =25 [mm], θ =135 [deg] and γ = 0.51 [rad]. The special shape is due to the combination of the helix lead angle and pure torsion of the helix cross-section.

effect of γ is negligible for a dense braid in the case of STIFF-FLOP modules [85] and a simpler result is possible assuming $\gamma \approx \pi/2$. Hence, from from Eq. 3.6 we have $\lambda_{r_\mathrm{p}}^2 = 1 - \lambda_{l_\mathrm{p}}^2(\pi/2-\gamma)^2$ and can further simplify the problem by assuming a fixed chamber radius ($\lambda_{r_\mathrm{p}} = 1$) due to $\gamma = \pi/2$. This suggests that the chamber radius does not change and it only twists. In the case of fixed radius for Eq. 3.8 and 3.9 we get

$$
\begin{aligned}
w_{\mathrm{pt}} &= E l_\mathrm{p} a_\mathrm{p} (2 - 1/\lambda_{l_p}^2 - \lambda_{l_p}^2)/6, \\
w_\mathrm{p} &= p \lambda_{l_\mathrm{p}} l_\mathrm{p} \pi r_{\mathrm{p}_1}^2, \qquad (3.10) \\
p &= \frac{E({r_{p2}}^2 - {r_{p1}}^2)(\lambda_{l_p}^2 - 1)(\lambda_{l_p}^2 + 3)}{6\lambda_{l_p}^4 {r_{p1}}^2}. \qquad (3.11)
\end{aligned}
$$

Elongation and Bending

To improve the model accuracy, the same constraint relation can be derived for a bending helix assuming no twist as shown in Fig. 3.1. With no-twist assumption, the tube cross-section does not undergo any torsion or twist around its main axis.

The geometrical model for a bent helix is

$$\begin{aligned} x_{\text{th}} &= 1/\kappa - (1/\kappa - r_{\text{th}}\text{C}_{(\varphi)})\text{C}_{(\theta_\varphi)}, \\ y_{\text{th}} &= (1/\kappa - r_{\text{th}}\text{C}_{\varphi})\text{S}_{(\theta_\varphi)}, \\ z_{\text{th}} &= r_{\text{th}}\text{S}_{(\varphi)}, \end{aligned} \tag{3.12}$$

where $\theta_\varphi = \kappa s_\varphi$. The helix deforms due to the thread cross-section pure torsion (ψ), neglecting material bending and strains. We consider any constant curvature elongation-bending deformation as a separate uniform elongation followed by a constant curvature pure bending. The uniform elongation changes γ uniformly, hence from Eq. 3.6 we get

$$\cot_{(\gamma_\text{p})} = \lambda_{l_\text{p}}\delta l_\text{p}/(r_{\text{th}_\text{d}}\delta\varphi), \tag{3.13}$$

where λ_{l_p} is the axial length stretch due to elongation, $r_{\text{th}_\text{d}} = \lambda_{r_\text{p}} r_{\text{th}}$ is the deformed radius because of pure elongation, $\gamma_\text{p} = \text{acos}_{(l_{\text{p}_\text{d}}/l_{\text{th}})}$ is the helix lead angle after pure elongation, $l_{\text{th}} = l_\text{p}/\text{C}_{(\gamma)}$ is the thread length which is fixed and $l_{\text{p}_\text{d}} = \lambda_{l_\text{p}} l_\text{p}$. A helix with only thread torsion, the definition of stretches in cross-section cylindrical coordinates and a view of the deformed enclosed tube cross-section are presented in Fig. 3.2.

In the case of pure bending, we assume $B_0 = \tau/(J_{\hat{1}_{\text{th}}} G_{\text{th}})$ as the local curvature along the thread central axis due to an external uniform bending moment (τ), where $J_{\hat{1}_{\text{th}}}$ is the helix cross secction polar second moment of area (Fig. 3.3). The change in the cross-section torsion angle is $\delta\psi_{(\varphi)} = B_0\text{C}_{(\varphi)}\text{S}_{(\gamma_{(\varphi)})}\delta s_{\text{th}}$, where $\delta s_{\text{th}} = r_{\text{th}(\varphi)}\delta\varphi/\text{S}_{(\gamma_{(\varphi)})}$ is the length of the thread element and $r_{\text{th}(\varphi)} = \lambda_{r_\text{p}(\varphi)} r_{\text{th}}$ is the local helix radius as a result of both uniform elongation and bending. Note the difference between r_{th_d} and $r_{\text{th}(\varphi)}$. Here, λ_{l_p} and λ_{r_p} are the stretches of the chamber axis caused by pure elongation. Then, for small rotations for which vector rules are valid, the variation of the bending angle ($\delta\theta_{(\varphi)}$) along the axis becomes

$$\delta\theta_{(\varphi)} = \kappa\delta l_{\text{p}\kappa(\varphi)} = \delta\psi\text{C}_{(\varphi)}\text{S}_{(\gamma_{(\varphi)})} = B_0\text{C}^2_{(\varphi)}\text{S}_{(\gamma_{(\varphi)})} r_{\text{th}(\varphi)}\delta\varphi, \tag{3.14}$$

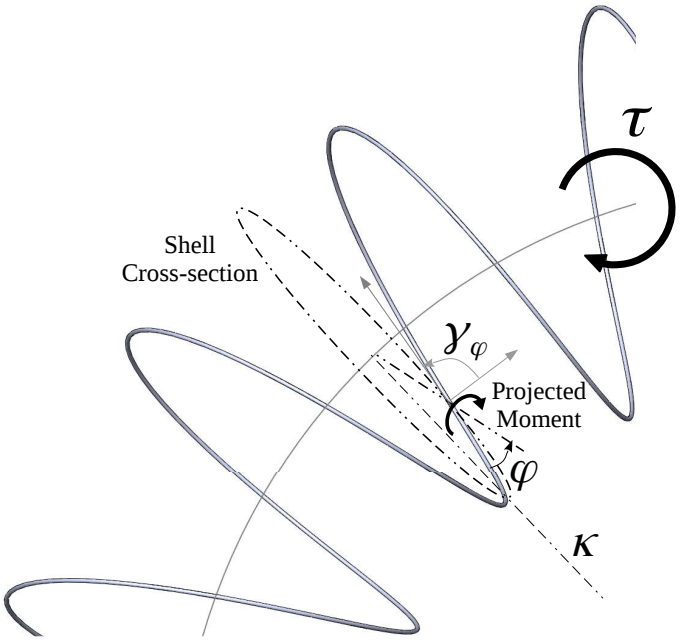

Figure 3.3: The uniform bending moment (τ), caused by a uniform bending, and it's projection on the helix cross-section. As a valid and commonly used assumption to model helical springs [76], the thread bending and strains due to the external uniform moment are neglected. The thread is circulated around a tube-shape continuum shell.

where $\delta l_{\mathrm{p}\kappa(\varphi)}$ is the local thread ascend due to bending. This relation is valid for infinitesimal changes in angles. Using the geometry of the local lead angle ($\gamma_{(\varphi)}$), superposition rule and Eq. 3.13 and 3.14 we have

$$\begin{aligned} \delta l_{\mathrm{p}(\varphi)} &= \delta l_{\mathrm{p}} + \delta l_{\mathrm{p}\kappa(\varphi)} = \cot_{(\gamma_{(\varphi)})}\, r_{\mathrm{th}(\varphi)} \delta\varphi, \\ &= (B_0 \mathrm{C}^2_{(\varphi)} \mathrm{S}_{(\gamma_{(\varphi)})}/\kappa + \cot_{(\gamma_{\mathrm{p}})}) r_{\mathrm{th}(\varphi)} \delta\varphi. \end{aligned} \tag{3.15}$$

Note that γ_{p} and $l_{\mathrm{p_d}}$ are the uniform values due to pure elongation of the helix, while $\gamma_{\mathrm{p}(\varphi)}$ and $l_{\mathrm{p}(\varphi)}$ are the local values at the thread element polar location φ. Eq. 3.15 results in a biquadratic quartic form equation for $\mathrm{S}^2_{(\gamma_{(\varphi)})}$ that can be solved as [117]

$$\mathrm{S}^2_{(\gamma_{(\varphi)})} = \frac{\kappa \left(\sqrt{4B_0^2 {\mathrm{C}_{(\varphi)}}^4 + 4\cot_{(\gamma_{\mathrm{p}})} B_0 \kappa {\mathrm{C}_{(\varphi)}}^2 + \kappa^2} - 2B_0 \cot_{(\gamma_{\mathrm{p}})} {\mathrm{C}_{(\varphi)}}^2 - \kappa \right)}{2B_0^2 {\mathrm{C}_{(\varphi)}}^4}, \tag{3.16}$$

where $\gamma_{\mathrm{p}} = \mathrm{acos}_{(l_{\mathrm{p_d}}/l_{\mathrm{th}})}$ is used to substitute for $\cot_{(\gamma_{\mathrm{p}})}$. This is considered as the

exact solution for $\gamma_{(\varphi)}$. This exact model gives complicated solutions for B_0 and $\gamma_{(\varphi)}$ in the following steps. Therefore, we assume $\gamma_{(\varphi)} \approx \pi/2$ (only in Eq. 3.14) which results in a simpler solution as $\delta\theta_{(\varphi)} = \kappa\delta l_{\mathrm{p}\kappa(\varphi)} = B_0 \mathrm{C}^2_{(\varphi)} r_{\mathrm{th}(\varphi)}\delta\varphi$. Integrating this w.r.t. φ we get

$$\theta_{(\varphi)} = r_{\mathrm{th}(\varphi)} B_0(\varphi + \mathrm{S}_{(2\varphi)}/2)/2. \tag{3.17}$$

Assuming the helix turns start and ends on the bending neutral plane, we have $l_{\mathrm{p}(\varphi_{\mathrm{th}})} = l_{\mathrm{p_d}} = \lambda_{l_{\mathrm{p}}} l_{\mathrm{p}}$. Then, B_0 is found from $l_{\mathrm{p}(\varphi_{\mathrm{th}})}$ and $\theta_{(\varphi_{\mathrm{th}})} = \lambda_{l_{\mathrm{p}}} l_{\mathrm{p}}\kappa$ as

$$B_0 = 2\lambda_{l_{\mathrm{p}}} l_{\mathrm{p}}\kappa / (\lambda_{r_{\mathrm{p}}(\varphi)} r_{\mathrm{th}}(2n_{\mathrm{th}}\pi + \mathrm{S}_{(4n_{\mathrm{th}}\pi)}/2)). \tag{3.18}$$

Using Eq. 3.15, 3.17, 3.18 and substituting for $\mathrm{cot}_{(\gamma_{\mathrm{p}})}$, the simplified solution for $\gamma_{(\varphi)}$ becomes

$$\mathrm{cot}_{(\gamma_{(\varphi)})} = B_0 \mathrm{C}^2_{(\varphi)}/\kappa + \mathrm{cot}_{(\gamma_{\mathrm{p}})}\,. \tag{3.19}$$

In initial state when the helix is straight, we have $\delta l_{\mathrm{p}(\varphi)} = \delta l_{\mathrm{p}}$. In the deformed bent state shown in Fig. 3.1, we have

$$\frac{\delta l_{\mathrm{p_d}}}{\delta l_{\mathrm{p}(\varphi)}} = \frac{\lambda_{l_{\mathrm{p}}}}{\lambda_{l_{\mathrm{p}}(\varphi)}} = \frac{1}{1 - \kappa r_{\mathrm{th}(\varphi)} \mathrm{C}_{(\varphi)}}. \tag{3.20}$$

Similar to eq. 3.6, in the local curvilinear frame, we have

$$\lambda^2_{r_{\mathrm{p}}(\varphi)} \mathrm{S}^2_{(\gamma(\varphi))} + \lambda^2_{l_{\mathrm{p}}(\varphi)} \mathrm{C}^2_{(\gamma(\varphi))} = 1. \tag{3.21}$$

By substituting $r_{\mathrm{th}(\varphi)} = \lambda_{r_{\mathrm{th}}(\varphi)} r_{\mathrm{p}}$ and assuming the thread constraint on the actuator chamber shell as $r_{\mathrm{th}} = r_{\mathrm{p}}$, Eqs. 3.19 and 3.20 in 3.21, we obtain a quadratic function

for $\lambda_{r_{\mathrm{p}}(\varphi)}$

$$
\begin{aligned}
0 &= A_{12}\lambda_{r(\varphi)}^2 + A_{11}\lambda_{r(\varphi)} + A_{10},\\
A_{12} &= \frac{\kappa^2 {l_{\mathrm{p}}}^2 {\lambda_{l_{\mathrm{p}}}}^4 \ {\mathrm{C}_{(\varphi)}}^2(\ \mathrm{C}_{(2\gamma_{(\varphi)})} - 1)(8n_{\mathrm{th}}\pi\ {\mathrm{C}_{(\varphi)}}^2 +\ \mathrm{S}_{(4\pi n_{\mathrm{th}})} + 4\pi n_{\mathrm{th}})^2}{4{n_{\mathrm{th}}}^2\pi^2(\ \mathrm{S}_{(4\pi n_{\mathrm{th}})} + 4\pi n_{\mathrm{th}})^2({\lambda_{l_{\mathrm{p}}}}^2\ \mathrm{C}_{(2\gamma_{(\varphi)})} + {\lambda_{l_{\mathrm{p}}}}^2 - 2)} + 1,\\
A_{11} &= -\frac{\kappa {l_{\mathrm{p}}}^2 {\lambda_{l_{\mathrm{p}}}}^4\ \mathrm{C}_{(\varphi)}(\ \mathrm{C}_{(2\gamma_{(\varphi)})} - 1)(8n_{\mathrm{th}}\pi\ {\mathrm{C}_{(\varphi)}}^2 +\ \mathrm{S}_{(4\pi n_{\mathrm{th}})} + 4\pi n_{\mathrm{th}})^2}{2{n_{\mathrm{th}}}^2 r_{\mathrm{p}}\pi^2(\ \mathrm{S}(4\pi n_{\mathrm{th}}) + 4\pi n_{\mathrm{th}})^2({\lambda_{l_{\mathrm{p}}}}^2\ \mathrm{C}_{(2\gamma_{(\varphi)})} + {\lambda_{l_{\mathrm{p}}}}^2 - 2)},\\
A_{10} &= \frac{{l_{\mathrm{p}}}^2 {\lambda_{l_{\mathrm{p}}}}^4(\ \mathrm{C}_{(2\gamma_{(\varphi)})} - 1)(8n_{\mathrm{th}}\pi\ {\mathrm{C}_{(\varphi)}}^2 +\ \mathrm{S}_{(4\pi n_{\mathrm{th}})} + 4\pi n_{\mathrm{th}})^2}{4{n_{\mathrm{th}}}^2 {r_{\mathrm{p}}}^2\pi^2(\ \mathrm{S}_{(4\pi n_{\mathrm{th}})} + 4\pi n_{\mathrm{th}})^2({\lambda_{l_{\mathrm{p}}}}^2\ \mathrm{C}_{(2\gamma_{(\varphi)})} + {\lambda_{l_{\mathrm{p}}}}^2 - 2)}\\
&\quad -\frac{{l_{\mathrm{p}}}^2 {\lambda_{l_{\mathrm{p}}}}^2(\ \mathrm{C}_{(2\gamma_{(\varphi)})} - 1)(8n_{\mathrm{th}}\pi\ {\mathrm{C}_{(\varphi)}}^2 +\ \mathrm{S}_{(4\pi n_{\mathrm{th}})} + 4\pi n_{\mathrm{th}})^2}{4{n_{\mathrm{th}}}^2 {r_{\mathrm{p}}}^2\pi^2(\ \mathrm{S}_{(4\pi n_{\mathrm{th}})} + 4\pi n_{\mathrm{th}})^2({\lambda_{l_{\mathrm{p}}}}^2\ \mathrm{C}_{(2\gamma_{(\varphi)})+{\lambda_{l_{\mathrm{p}}}}^2-2)}} - 1. \qquad (3.22)
\end{aligned}
$$

We call this the exact helix model for $\lambda_{r_{\mathrm{p}}(\varphi)}$. It is important to mention that this relation is valid for a dense braid ($\gamma \approx \pi/2$) due to our simplifying assumptions earlier. The final result is

$$
\begin{aligned}
\lambda_{r_c(\psi)} = {} & (32B_1\lambda_{l_c}^2 n_{\text{th}}^4 r_{\text{p}}\pi^4 - 32B_1 n_{\text{th}}^3 r_{\text{p}}\pi^3 \text{S}(4n_{\text{th}}\pi) - \kappa l_{\text{p}}^2\lambda_{l_c}^4 \text{S}(4n_{\text{th}}\pi)^2\text{C}(\psi) - \\
& 64B_1 n_{\text{th}}^4 r_{\text{p}}\pi^4 - 4B_1 n_{\text{th}}^2 r_{\text{p}}\pi^2 \text{S}(4n_{\text{th}}\pi)^2 - 64\kappa l_{\text{p}}^2\lambda_{l_c}^4 n_{\text{th}}^2\pi^2\text{C}(\psi)^3 - \\
& 64\kappa l_{\text{p}}^2\lambda_{l_c}^4 n_{\text{th}}^2\pi^2\text{C}(\psi)^5 + 2B_1\lambda_{l_c}^2 n_{\text{th}}^2 r_{\text{p}}\pi^2\text{S}(4n_{\text{th}}\pi)^2 + \\
& \kappa l_{\text{p}}^2\lambda_{l_c}^4 \text{C}(2\gamma_{\text{p}})\text{S}(4n_{\text{th}}\pi)^2\text{C}(\psi) + 32B_1\lambda_{l_c}^2 n_{\text{th}}^4 r_{\text{p}}\pi^4\text{C}(2\gamma_{\text{p}}) - \\
& 16\kappa l_{\text{p}}^2\lambda_{l_c}^4 n_{\text{th}}^2\pi^2\text{C}(\psi) + 16B_1\lambda_{l_c}^2 n_{\text{th}}^3 r_{\text{p}}\pi^3\text{S}(4n_{\text{th}}\pi) + \\
& 16B_1\lambda_{l_c}^2 n_{\text{th}}^3 r_{\text{p}}\pi^3\text{C}(2\gamma_{\text{p}})\text{S}(4n_{\text{th}}\pi) + 64\kappa l_{\text{p}}^2\lambda_{l_c}^4 n_{\text{th}}^2\pi^2\text{C}(2\gamma_{\text{p}})\text{C}(\psi)^3 + \\
& 64\kappa l_{\text{p}}^2\lambda_{l_c}^4 n_{\text{th}}^2\pi^2\text{C}(2\gamma_{\text{p}})\text{C}(\psi)^5 + 2B_1\lambda_{l_c}^2 n_{\text{th}}^2 r_{\text{p}}\pi^2\text{C}(2\gamma_{\text{p}})\text{S}(4n_{\text{th}}\pi)^2 - \\
& 8\kappa l_{\text{p}}^2\lambda_{l_c}^4 n_{\text{th}}\pi\text{S}(4n_{\text{th}}\pi)\text{C}(\psi) + 16\kappa l_{\text{p}}^2\lambda_{l_c}^4 n_{\text{th}}^2\pi^2\text{C}(2\gamma_{\text{p}})\text{C}(\psi) - \\
& 16\kappa l_{\text{p}}^2\lambda_{l_c}^4 n_{\text{th}}\pi\text{S}(4n_{\text{th}}\pi)\text{C}(\psi)^3 + 16\kappa l_{\text{p}}^2\lambda_{l_c}^4 n_{\text{th}}\pi\text{C}(2\gamma_{\text{p}})\text{S}(4n_{\text{th}}\pi)\text{C}(\psi)^3 + \\
& 8\kappa l_{\text{p}}^2\lambda_{l_c}^4 n_{\text{th}}\pi\text{C}(2\gamma_{\text{p}})\text{S}(4n_{\text{th}}\pi)\text{C}(\psi))/(r_{\text{p}}(64\lambda_{l_c}^2 n_{\text{th}}^4\pi^4 - 64n_{\text{th}}^3\pi^3\text{S}(4n_{\text{th}}\pi) - \\
& 128n_{\text{th}}^4\pi^4 - 8n_{\text{th}}^2\pi^2\text{S}(4n_{\text{th}}\pi)^2 + 32\lambda_{l_c}^2 n_{\text{th}}^3\pi^3\text{S}(4n_{\text{th}}\pi) + 4\lambda_{l_c}^2 n_{\text{th}}^2\pi^2\text{S}(4n_{\text{th}}\pi)^2 + \\
& 64\lambda_{l_c}^2 n_{\text{th}}^4\pi^4\text{C}(2\gamma_{\text{p}}) + 32\lambda_{l_c}^2 n_{\text{th}}^3\pi^3\text{C}(2\gamma_{\text{p}})\text{S}(4n_{\text{th}}\pi) + 4\lambda_{l_c}^2 n_{\text{th}}^2\pi^2\text{C}(2\gamma_{\text{p}})\text{S}(4n_{\text{th}}\pi)^2 - \\
& \kappa^2 l_{\text{p}}^2\lambda_{l_c}^4 \text{S}(4n_{\text{th}}\pi)^2\text{C}(\psi)^2 + \kappa^2 l_{\text{p}}^2\lambda_{l_c}^4 \text{C}(2\gamma_{\text{p}})\text{S}(4n_{\text{th}}\pi)^2\text{C}(\psi)^2 - \\
& 16\kappa^2 l_{\text{p}}^2\lambda_{l_c}^4 n_{\text{th}}^2\pi^2\text{C}(\psi)^2 - 64\kappa^2 l_{\text{p}}^2\lambda_{l_c}^4 n_{\text{th}}^2\pi^2\text{C}(\psi)^4 - 64\kappa^2 l_{\text{p}}^2\lambda_{l_c}^4 n_{\text{th}}^2\pi^2\text{C}(\psi)^6 - \\
& 8\kappa^2 l_{\text{p}}^2\lambda_{l_c}^4 n_{\text{th}}\pi\text{S}(4n_{\text{th}}\pi)\text{C}(\psi)^2 - 16\kappa^2 l_{\text{p}}^2\lambda_{l_c}^4 n_{\text{th}}\pi\text{S}(4n_{\text{th}}\pi)\text{C}(\psi)^4 + \\
& 16\kappa^2 l_{\text{p}}^2\lambda_{l_c}^4 n_{\text{th}}^2\pi^2\text{C}(2\gamma_{\text{p}})\text{C}(\psi)^2 + 64\kappa^2 l_{\text{p}}^2\lambda_{l_c}^4 n_{\text{th}}^2\pi^2\text{C}(2\gamma_{\text{p}})\text{C}(\psi)^4 + \\
& 64\kappa^2 l_{\text{p}}^2\lambda_{l_c}^4 n_{\text{th}}^2\pi^2\text{C}(2\gamma_{\text{p}})\text{C}(\psi)^6 + 8\kappa^2 l_{\text{p}}^2\lambda_{l_c}^4 n_{\text{th}}\pi\text{C}(2\gamma_{\text{p}})\text{S}(4n_{\text{th}}\pi)\text{C}(\psi)^2 + \\
& 16\kappa^2 l_{\text{p}}^2\lambda_{l_c}^4 n_{\text{th}}\pi\text{C}(2\gamma_{\text{p}})\text{S}(4n_{\text{th}}\pi)\text{C}(\psi)^4)),
\end{aligned}
\tag{3.23}
$$

where

$$
\begin{aligned}
B_1 \;=\; & (((64\lambda_{lc}^2 n_{\mathrm{th}}^4\pi^4 - 64n_{\mathrm{th}}^3\pi^3\mathrm{S}(4n_{\mathrm{th}}\pi) - 128n_{\mathrm{th}}^4\pi^4 - 8n_{\mathrm{th}}^2\pi^2\mathrm{S}(4n_{\mathrm{th}}\pi)^2 \\
& +32\lambda_{lc}^2 n_{\mathrm{th}}^3\pi^3\mathrm{S}(4n_{\mathrm{th}}\pi) + 4\lambda_{lc}^2 n_{\mathrm{th}}^2\pi^2\mathrm{S}(4n_{\mathrm{th}}\pi)^2 + 64\lambda_{lc}^2 n_{\mathrm{th}}^4\pi^4\mathrm{C}(2\gamma_{\mathrm{p}}) + \\
& 32\lambda_{lc}^2 n_{\mathrm{th}}^3\pi^3\mathrm{C}(2\gamma_{\mathrm{p}})\mathrm{S}(4n_{\mathrm{th}}\pi) + 4\lambda_{lc}^2 n_{\mathrm{th}}^2\pi^2\mathrm{C}(2\gamma_{\mathrm{p}})\mathrm{S}(4n_{\mathrm{th}}\pi)^2 - \kappa^2 l_{\mathrm{p}}^2\lambda_{lc}^4\mathrm{S}(4n_{\mathrm{th}}\pi)^2\mathrm{C}(\psi)^2 + \\
& \kappa^2 l_{\mathrm{p}}^2\lambda_{lc}^4\mathrm{C}(2\gamma_{\mathrm{p}})\mathrm{S}(4n_{\mathrm{th}}\pi)^2\mathrm{C}(\psi)^2 - 16\kappa^2 l_{\mathrm{p}}^2\lambda_{lc}^4 n_{\mathrm{th}}^2\pi^2\mathrm{C}(\psi)^2 - \\
& 64\kappa^2 l_{\mathrm{p}}^2\lambda_{lc}^4 n_{\mathrm{th}}^2\pi^2\mathrm{C}(\psi)^4 - 64\kappa^2 l_{\mathrm{p}}^2\lambda_{lc}^4 n_{\mathrm{th}}^2\pi^2\mathrm{C}(\psi)^6 - 8\kappa^2 l_{\mathrm{p}}^2\lambda_{lc}^4 n_{\mathrm{th}}\pi\mathrm{S}(4n_{\mathrm{th}}\pi)\mathrm{C}(\psi)^2 - \\
& 16\kappa^2 l_{\mathrm{p}}^2\lambda_{lc}^4 n_{\mathrm{th}}\pi\mathrm{S}(4n_{\mathrm{th}}\pi)\mathrm{C}(\psi)^4 + 16\kappa^2 l_{\mathrm{p}}^2\lambda_{lc}^4 n_{\mathrm{th}}^2\pi^2\mathrm{C}(2\gamma_{\mathrm{p}})\mathrm{C}(\psi)^2 + \\
& 64\kappa^2 l_{\mathrm{p}}^2\lambda_{lc}^4 n_{\mathrm{th}}^2\pi^2\mathrm{C}(2\gamma_{\mathrm{p}})\mathrm{C}(\psi)^4 + 64\kappa^2 l_{\mathrm{p}}^2\lambda_{lc}^4 n_{\mathrm{th}}^2\pi^2\mathrm{C}(2\gamma_{\mathrm{p}})\mathrm{C}(\psi)^6 + \\
& 8\kappa^2 l_{\mathrm{p}}^2\lambda_{lc}^4 n_{\mathrm{th}}\pi\mathrm{C}(2\gamma_{\mathrm{p}})\mathrm{S}(4n_{\mathrm{th}}\pi)\mathrm{C}(\psi)^2 + \\
& 16\kappa^2 l_{\mathrm{p}}^2\lambda_{lc}^4 n_{\mathrm{th}}\pi\mathrm{C}(2\gamma_{\mathrm{p}})\mathrm{S}(4n_{\mathrm{th}}\pi)\mathrm{C}(\psi)^4)(l_{\mathrm{p}}^2\lambda_{lc}^4\mathrm{S}(4n_{\mathrm{th}}\pi)^2 - \\
& l_{\mathrm{p}}^2\lambda_{lc}^2\mathrm{S}(4n_{\mathrm{th}}\pi)^2 - 128n_{\mathrm{th}}^4 r_{\mathrm{p}}^2\pi^4 + l_{\mathrm{p}}^2\lambda_{lc}^2\mathrm{C}(2\gamma_{\mathrm{p}})\mathrm{S}(4n_{\mathrm{th}}\pi)^2 - l_{\mathrm{p}}^2\lambda_{lc}^4\mathrm{C}(2\gamma_{\mathrm{p}})\mathrm{S}(4n_{\mathrm{th}}\pi)^2 - \\
& 64n_{\mathrm{th}}^3 r_{\mathrm{p}}^2\pi^3\mathrm{S}(4n_{\mathrm{th}}\pi) - 16l_{\mathrm{p}}^2\lambda_{lc}^2 n_{\mathrm{th}}^2\pi^2 + 16l_{\mathrm{p}}^2\lambda_{lc}^4 n_{\mathrm{th}}^2\pi^2 + \\
& 64\lambda_{lc}^2 n_{\mathrm{th}}^4 r_{\mathrm{p}}^2\pi^4 - 8n_{\mathrm{th}}^2 r_{\mathrm{p}}^2\pi^2\mathrm{S}(4n_{\mathrm{th}}\pi)^2 + \\
& 32\lambda_{lc}^2 n_{\mathrm{th}}^3 r_{\mathrm{p}}^2\pi^3\mathrm{S}(4n_{\mathrm{th}}\pi) - 8l_{\mathrm{p}}^2\lambda_{lc}^2 n_{\mathrm{th}}\pi\mathrm{S}(4n_{\mathrm{th}}\pi) + \\
& 8l_{\mathrm{p}}^2\lambda_{lc}^4 n_{\mathrm{th}}\pi\mathrm{S}(4n_{\mathrm{th}}\pi) + 4\lambda_{lc}^2 n_{\mathrm{th}}^2 r_{\mathrm{p}}^2\pi^2\mathrm{S}(4n_{\mathrm{th}}\pi)^2 + 16l_{\mathrm{p}}^2\lambda_{lc}^2 n_{\mathrm{th}}^2\pi^2\mathrm{C}(2\gamma_{\mathrm{p}}) - \\
& 16l_{\mathrm{p}}^2\lambda_{lc}^4 n_{\mathrm{th}}^2\pi^2\mathrm{C}(2\gamma_{\mathrm{p}}) + 64\lambda_{lc}^2 n_{\mathrm{th}}^4 r_{\mathrm{p}}^2\pi^4\mathrm{C}(2\gamma_{\mathrm{p}}) - 64l_{\mathrm{p}}^2\lambda_{lc}^2 n_{\mathrm{th}}^2\pi^2\mathrm{C}(\psi)^2 - \\
& 64l_{\mathrm{p}}^2\lambda_{lc}^2 n_{\mathrm{th}}^2\pi^2\mathrm{C}(\psi)^4 + 64l_{\mathrm{p}}^2\lambda_{lc}^4 n_{\mathrm{th}}^2\pi^2\mathrm{C}(\psi)^2 + 64l_{\mathrm{p}}^2\lambda_{lc}^4 n_{\mathrm{th}}^2\pi^2\mathrm{C}(\psi)^4 + \\
& 32\lambda_{lc}^2 n_{\mathrm{th}}^3 r_{\mathrm{p}}^2\pi^3\mathrm{C}(2\gamma_{\mathrm{p}})\mathrm{S}(4n_{\mathrm{th}}\pi) + 8l_{\mathrm{p}}^2\lambda_{lc}^2 n_{\mathrm{th}}\pi\mathrm{C}(2\gamma_{\mathrm{p}})\mathrm{S}(4n_{\mathrm{th}}\pi) - \\
& 8l_{\mathrm{p}}^2\lambda_{lc}^4 n_{\mathrm{th}}\pi\mathrm{C}(2\gamma_{\mathrm{p}})\mathrm{S}(4n_{\mathrm{th}}\pi) - 16l_{\mathrm{p}}^2\lambda_{lc}^2 n_{\mathrm{th}}\pi\mathrm{S}(4n_{\mathrm{th}}\pi)\mathrm{C}(\psi)^2 + \\
& 16l_{\mathrm{p}}^2\lambda_{lc}^4 n_{\mathrm{th}}\pi\mathrm{S}(4n_{\mathrm{th}}\pi)\mathrm{C}(\psi)^2 + 4\lambda_{lc}^2 n_{\mathrm{th}}^2 r_{\mathrm{p}}^2\pi^2\mathrm{C}(2\gamma_{\mathrm{p}})\mathrm{S}(4n_{\mathrm{th}}\pi)^2 + \\
& 64l_{\mathrm{p}}^2\lambda_{lc}^2 n_{\mathrm{th}}^2\pi^2\mathrm{C}(2\gamma_{\mathrm{p}})\mathrm{C}(\psi)^2 + 64l_{\mathrm{p}}^2\lambda_{lc}^2 n_{\mathrm{th}}^2\pi^2\mathrm{C}(2\gamma_{\mathrm{p}})\mathrm{C}(\psi)^4 - \\
& 64l_{\mathrm{p}}^2\lambda_{lc}^4 n_{\mathrm{th}}^2\pi^2\mathrm{C}(2\gamma_{\mathrm{p}})\mathrm{C}(\psi)^2 - 64l_{\mathrm{p}}^2\lambda_{lc}^4 n_{\mathrm{th}}^2\pi^2\mathrm{C}(2\gamma_{\mathrm{p}})\mathrm{C}(\psi)^4 + \\
& 16l_{\mathrm{p}}^2\lambda_{lc}^2 n_{\mathrm{th}}\pi\mathrm{C}(2\gamma_{\mathrm{p}})\mathrm{S}(4n_{\mathrm{th}}\pi)\mathrm{C}(\psi)^2 - \\
& 16l_{\mathrm{p}}^2\lambda_{lc}^4 n_{\mathrm{th}}\pi\mathrm{C}(2\gamma_{\mathrm{p}})\mathrm{S}(4n_{\mathrm{th}}\pi)\mathrm{C}(\psi)^2))/(4n_{\mathrm{th}}^4 r_{\mathrm{p}}^2\pi^4(\mathrm{S}(4n_{\mathrm{th}}\pi) + \\
& 4n_{\mathrm{th}}\pi)^4(\lambda_{lc}^2\mathrm{C}(2\gamma_{\mathrm{p}}) + \lambda_{lc}^2 - 2)^2) + (\kappa^2 l_{\mathrm{p}}^4\lambda_{lc}^8\mathrm{C}(\psi)^2(\mathrm{C}(2\gamma_{\mathrm{p}}) - 1)^2(\mathrm{S}(4n_{\mathrm{th}}\pi) + \\
& 4n_{\mathrm{th}}\pi + 8n_{\mathrm{th}}\pi\mathrm{C}(\psi)^2)^4)/(4n_{\mathrm{th}}^4 r_{\mathrm{p}}^2\pi^4(\mathrm{S}(4n_{\mathrm{th}}\pi) + 4n_{\mathrm{th}}\pi)^4(\lambda_{lc}^2\mathrm{C}(2\gamma_{\mathrm{p}}) + \lambda_{lc}^2 - 2)^2))^{1/2}.
\end{aligned}
\tag{3.24}
$$

The exact helix model is valid for stiff threads and springs without thread bending. This is not valid for soft braids, e.g. fishing or sewing threads being used in fabri-

cation of many pneumatic actuators. A simpler result is possible if we assume that the lead angle with the curvilinear axis is constant and equal to the lead angle after pure elongation ($\gamma_{(\varphi)} = \gamma_{\mathrm{p}}$). This model assumes that the thread tends to retain its lead angle and follows the shell deformation. From Eqs. 3.20 and 3.21 we have

$$0 = {\lambda_{r_{\mathrm{p}}(\varphi)}}^2 + {\cot_{(\gamma_{\mathrm{p}})}}^2 (\lambda_{l_{\mathrm{p}}}^2 \left(\kappa \lambda_{r_{\mathrm{p}}(\varphi)} r_{\mathrm{p}} \mathrm{C}_{(\varphi)} - 1\right)^2 - 1) - 1,$$

$$\lambda_{r_{\mathrm{p}}(\varphi)} = \frac{\sqrt{\lambda_{l_{\mathrm{p}}}^2 {\cot_{(\gamma_{\mathrm{p}})}}^2 (\kappa^2 r_{\mathrm{p}}^2 {\mathrm{C}_{(\varphi)}}^2 {\csc_{(\gamma_{\mathrm{p}})}}^2 - 1) + \csc_{(\gamma_{\mathrm{p}})}^2} + \kappa r_{\mathrm{p}} \mathrm{C}_{(\varphi)} {\cot_{(\gamma_{\mathrm{p}})}}^2 \lambda_{l_{\mathrm{p}}}^2}{{\cot_{(\gamma_{\mathrm{p}})}}^2 \kappa^2 \lambda_{l_{\mathrm{p}}}^2 r_{\mathrm{p}}^2 {\mathrm{C}_{(\varphi)}}^2 + 1}, \quad (3.25)$$

which we call the constant lead angle bending model.

As in the case of pure elongation, actions can be found base on incompressibility criteria ($\lambda_{\varphi_{\mathrm{p}}(\phi)} = 1/(\lambda_{r_{\mathrm{p}}(\varphi)} \lambda_{l_{\mathrm{p}}(\varphi)})$), $r_{\mathrm{th}} = r_{\mathrm{p2}}$, Eq.s 3.1 and 3.2 as

$$w_{\mathrm{p}} = l_{\mathrm{p_d}} \int_{r_{\mathrm{p1}}}^{r_{\mathrm{p2}}} \int_0^{2\pi} U_{\mathrm{p}} \mathrm{d}a_{\mathrm{p}}, \; w_{\mathrm{p}} = p l_{\mathrm{p_d}} \int_0^{r_{\mathrm{p1}}} \int_0^{2\pi} \mathrm{d}a_{\mathrm{p}}, \quad (3.26)$$

$$\mathrm{d}a_{\mathrm{p}} = r_{\mathrm{p}} \lambda_{r_{\mathrm{p}}(\varphi)} \mathrm{d}\phi \mathrm{d}r_{\mathrm{p}}, \; U_{\mathrm{p}} = E(\lambda_{\varphi_{\mathrm{p}}(\phi)}^2 + \lambda_{r_{\mathrm{p}}(\varphi)}^2 + \lambda_{l_{\mathrm{p}}(\varphi)}^2 - 3)/6, \quad (3.27)$$

where ϕ is the polar angle of the cross-section element and the integrals are dealt with numerically in the simulations. The actions depend on κ, hence a standalone relation for one chamber is not derived here. A similar result to Eq. 3.7 in the case that we neglect the chamber shell can be derived by substituting $\lambda_{r_{\mathrm{p}}}$ with $\lambda_{r_{\mathrm{p}}(\varphi)}$. Assuming a dense thread ($\gamma_{(\varphi)}, \gamma_{\mathrm{p}}, \gamma \approx \pi/2$) does not reduce the complexity of the final solutions in Eqs. 3.22 and 3.25 significantly; however, the fixed radius case($\gamma = \pi/2$), $\lambda_{r_{\mathrm{p}}(\varphi)} = \lambda_{r_{\mathrm{p}}} = 1$ results in a simpler solution for the actions as

$$w_{\mathrm{p}} = \frac{\pi E l_{\mathrm{p}} (\kappa^2 \lambda_{l_{\mathrm{p}}}^2 ({r_{\mathrm{p2}}}^2 - {r_{\mathrm{p1}}}^2)(-{\lambda_{l_{\mathrm{p}}}}^2 (\kappa^2 ({r_{\mathrm{p2}}}^2 - {r_{\mathrm{p1}}}^2) + 4) + 8) + 16)}{24 \kappa^2 {\lambda_{l_{\mathrm{p}}}}^2}, \quad (3.28)$$

$$w_{\mathrm{G}} = p\pi l_{\mathrm{p}} \lambda_{l_{\mathrm{p}}} {r_{\mathrm{p1}}}^2. \quad (3.29)$$

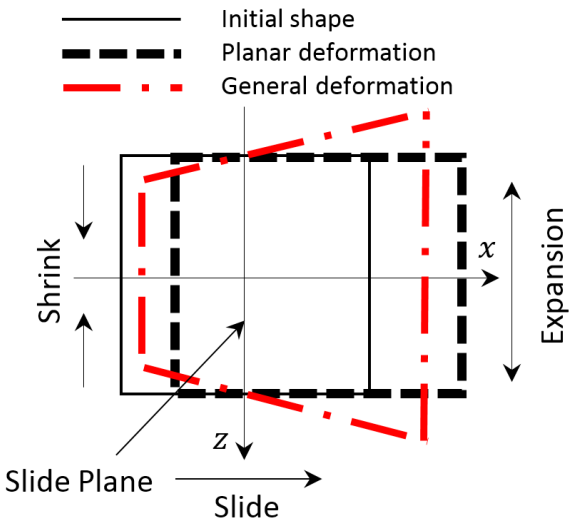

Figure 3.4: Planar and general assumptions for cross-section deformation in elongation-bending based on geometry deformation method. The bending is toward x-axis positive direction.

3.2.3 Cross-section Deformation

The unit deformation energy for simple pure elongation of a symmetric cylinder is presented in [103] based on incompressibility criteria and principal stretches. We use Eq. 3.1, 3.2 and

$$\Lambda_1 = \lambda_l^2 + 2/\lambda_l, \;\; \lambda_{r|\varphi} = 1/\sqrt{\lambda_l}, \tag{3.30}$$

to derive the unit deformation energy for the pure symmetric elongation case, where λ_i are the stretches along other principle directors (Similar to Fig. 3.2.a). This can be extended to a simple model for elongation-bending of a cylinder by substituting ϕ with φ in Eq. 3.20 as

$$\begin{aligned} \lambda_{y(x)} &= (1-\kappa x)\lambda_l, \lambda_{x(x)} = \lambda_{z(x)} = 1/\sqrt{\lambda_y}, \\ \Lambda_{1(x)} &= (1-\kappa x)^2\lambda_l^2 + \frac{2}{\lambda_l(1-\kappa x)}, \end{aligned} \tag{3.31}$$

where (x, y, z) is the element initial position in the inertial frame. This model accounts for the inhomogeneous elongation of the volume elements but does not consider their bending. We call this the simple bending model.

We use a similar approach similar to the solution by Rivlin for "The problem of Flex-

ure" [113] to find a simple but exact analytical solution for the general deformation map of a bent hollow cylinder. Following similar studies in literature [74], we assume the continuum bodies as an incompressible media and the cross-section plane remains planar under deformation as in the Euler-Bernoulli beam assumption. Therefore, the final orientation of the deformed cross-section planeis determined by the deformation of the backbone. The deformed state for each point ($\rho_{\mathrm{d}} = [x_{\mathrm{d}}, y_{\mathrm{d}}, z_{\mathrm{d}}]^{\mathrm{T}} = T_\kappa \rho'$) consists of the deformation of the backbone in the form of a transformation matrix (T_κ) and a vector function presenting the planar deformation of the cross-section ($\rho' = [x', y', z']^{\mathrm{T}}$) (Fig. 3.4). Assuming constant curvature, neglecting the placing holes for pneumatic chambers and dealing with the deformation of each module separately, we have

$$T_\kappa = \begin{bmatrix} R_{\mathrm{z}(\kappa l_{\mathrm{d}})} & \rho_{\mathrm{tip}} \\ 0 & 1 \end{bmatrix}. \tag{3.32}$$

The deformation map becomes,

$$\begin{aligned} x_{\mathrm{d}} &= \mathrm{C}_{\Delta\theta} x' + (1 - \mathrm{C}_{\Delta\theta})/\kappa, \\ y_{\mathrm{d}} &= -\mathrm{S}_{\Delta\theta} x' + \mathrm{S}_{\Delta\theta}/\kappa, \\ z_{\mathrm{d}} &= z', \end{aligned} \tag{3.33}$$

where $\Delta\theta = y'\kappa$. Incompressibility criteria holds if the determinant of the deformation map Jacobian w.r.t the initial states ($\rho = [x, y, z]$) becomes one [118],

$$|\rho_{\mathrm{d},\rho}| = 1. \tag{3.34}$$

The above relation is derived and then solved for ρ' following some assumptions on the shape function variable dependency and boundary conditions. Our general assumptions are having a fixed backbone on xz-plane ($\rho'(0) = 0$), symmetry w.r.t. yz-plane ($z'_{(z=0)} = 0$) and having the neutral plane along the main axis and perpendicular to the curvature radius ($x'_{(x=0)} = 0$ and $z'_{(x=0)} = z$); however, we drop some of these assumptions in different models. We discuss the solution based on two main

assumptions.

Planar Deformation

Here, the deformation only occurs in the xy-plane. Assuming no deformation in z direction ($z' = z$) similar to [113], we can separate the variables as $x'(x, z)$, $y'(y)$ and $z'(z)$. For Eq. 3.34 we get

$$\begin{vmatrix} x'_{,x}\mathrm{C}_{(\kappa y')} & (1-\kappa x')y'_{,y}\mathrm{S}_{(\kappa y')} & x'_{,z}\mathrm{C}_{(\kappa y')} \\ -x'_{,x}\mathrm{S}_{(\kappa y')} & (1-\kappa x')y'_{,y}\mathrm{C}_{(\kappa y')} & -x'_{,z}\mathrm{S}_{(\kappa y')} \\ 0 & 0 & z'_{,z} \end{vmatrix} = x'_{,x}y'_{,y}z'_{,z}(1-\kappa x') = 1. \tag{3.35}$$

By separation of variables we have

$$\begin{cases} x'_{,x}(1-\kappa x') = 1/(y'_{,y}z'_{,z}) = 1/(\lambda_2\lambda_3) \\ \quad y'_{,yy} = 0 \rightarrow y' = A_2 y + B_2 \\ \quad z'_{,zz} = 0 \rightarrow z' = A_3 z + B_3. \end{cases} \tag{3.36}$$

By integrating for x' we get

$$x' = \frac{1-\sqrt{1-2\kappa(A_1 x + B_1)}}{\kappa} + h_{1(z)}, A_1 = \frac{1}{A_2 A_3}, \tag{3.37}$$

where considering the fixed backbone root, yz-plane symmetry and neutral plane, we have $B_1 = B_2 = B_3 = h_{1(z)} = 0$. Then for Λ_1 and w_c form Eq. 3.1, 3.3 and 3.4 we have

$$\Lambda_1 = \frac{{A_3}^4\,{\lambda_l}^2 - 2\,\kappa\,x\,{A_3}^3\,\lambda_l + {A_3}^2\,{\lambda_l}^4 - 2\,\kappa\,x\,A_3\,{\lambda_l}^3 + 1}{A_3\,\lambda_l\,(A_3\,\lambda_l - 2\,\kappa\,x)}. \tag{3.38}$$

Λ_1 is not a function of y and the integration for w_c is dealt with numerically. From the neutral plane assumption ($z'_{(x=0)} = z$) and for the planar elongation-bending deformation case we get $A_3 = 1$; however, in the case of planar pure bending after a pure elongation, form Eq. 3.30 we have $z'_{(x=0)} = z/\sqrt{\lambda_l}$, hence $A_3 = 1/\sqrt{\lambda_l}$. A weak approximate analytical solution is presented in [85]. The elastic deformation action

for the body shell as a hollow cylinder is

$$w_{\mathrm{c}} = w_{\mathrm{c}(\mathrm{r}_{\mathrm{c}2})} - w_{\mathrm{c}(\mathrm{r}_{\mathrm{c}1})}. \tag{3.39}$$

General Deformation

A more realistic model can be derived based on a more general assumption for $z'_{(x,z)}$. Then, similar to Eq. 3.35-3.37 we have

$$\begin{aligned} 1 &= \begin{vmatrix} x'_{,x}\mathrm{C}_{(\kappa y')} & (1-\kappa x')y'_{,y}\mathrm{S}_{(\kappa y')} & x'_{,z}\mathrm{C}_{(\kappa y')} \\ -x'_{,x}\mathrm{S}_{(\kappa y')} & (1-\kappa x')y'_{,y}\mathrm{C}_{(\kappa y')} & -x'_{,z}\mathrm{S}_{(\kappa y')} \\ z'_{,x} & 0 & z'_{,z} \end{vmatrix} \\ &= y'_{,y}(x'_{,x}z'_{,z} - x'_{,z}z'_{,x})(1-\kappa x'). \end{aligned} \tag{3.40}$$

By separation of variables and from the result for x' in Eq. 3.36, the fixed backbone root, yz-plane symmetry and neutral plane assumptions we have

$$\begin{cases} x' = (1-\sqrt{1-2\kappa(h_{2(x)}+B_1)})/\kappa \\ y'_{,yy} = 0 \rightarrow y' = \lambda_l y \\ h_{2(x),x}z'_{,z} = 1/\lambda_l. \end{cases} \tag{3.41}$$

To satisfy the xy-plane symmetry neutral plane assumptions and reach a realistic cross-section deformation similar to Fig. 3.4, we propose $z' = A_3 z/\sqrt{1-\kappa x}$ based on the simple elongation-bending model in Eq. 3.31. Then, we have

$$h_{2(x)} = \frac{-2A_1(1-\kappa x)^{3/2}}{3\kappa}, B_1 = \frac{2A_1}{3\kappa}, \tag{3.42}$$

where $A_1 = 1/(\lambda_l A_3)$. For Γ_1 we get

$$\Lambda_1 = -\frac{12{B_5}^5 + 4{A_3}^3 B_4 \lambda_l {B_5}^3 - 4A_3 B_4 {\lambda_l}^3 {B_5}^4 + {A_3}^3 B_4 \kappa^2 \lambda_l z^2 B_5}{A_3 B_4 \lambda_l {B_5}^4}, \tag{3.43}$$

where $B_4 = 4(1-\kappa x)^{\frac{3}{2}} + 3A_3\lambda_l - 4$ and $B_5 = \kappa x - 1$. Similar to the planar pure bending case in the last section, we assume $A_1 = A_3 = 1/\sqrt{\lambda_l}$. A more general solution for the braided case is hard to achieve and has not been considered here.

3.2.4 Integration with Constant and Variable Curvature Models

In the next step, we use different combinations of the discussed methods to model the pneumatic chamber elastic deformation, gas pressure and a body shell elastic deformation actions for a STIFF-FLOP module. The inverse map that results from the principle of virtual energy is used to predict the required pressure for any constant curvature geometry. Instead of using Eq. 2.2, the deformed values are found based on equations from section 3.2.2 and 3.2.3. We substitute $r_{\mathrm{o_d}} = r_{\mathrm{o}}/\sqrt{\lambda_l}$ for r_{o} in Eq. 2.8 to approximate the deformation of the placing radius for the actuators too. The algorithm to implement the method is presented in Algorithm 1. There, to find the pressure inputs for any orientation, first the Jacobian of the inverse map between the pressure inputs and pressure action ($V_{\mathrm{p},q}^{-1}$) and the rest of actions in the system $w_{\mathrm{T},q}$ are calculated numerically using jacobian function. w_func function returns the actions (w) and pressure coefficients (V_{p}) where function action_fun is called in a for loop three times to return the actions for the pressure chamber shell w_{p}, hole in the body shell w_{h} and air volume V_{p} in the three set of chambers. action_fun if called once for the body shell actions (w_{c}) too. The body load action (w_{b}) and the external load action (w_{L}) are calculated in two for loops that iterate over the number of segments and eternal load locations respectively.

The constant curvature model does not account for the material twist due to any off-plan load. This solution can be extended to the variable curvature backbone model, where the backbone consists of a series of infinitesimal constant curvature curves [74] [91] [11]. The variable curvature assumptions improve the accuracy of the backbone deformation modeling, and the presented methods in this research can improve the

Data: *par*- structural parameters, $mthd_{\mathrm{c}}$, $mthd_{\mathrm{p}}$- modeling method used for body and chamber
Result: inverse static model for a continuum manipulator based on the principle of virtual work
initialization;
$[V_{\mathrm{p},q},\ w_{\mathrm{T},q}]$ = jacobian(w_func($par, mthd_{\mathrm{c}}$)); //numerical Jacobian
return $p\ =\ V_{\mathrm{p},q}^{-1}.w_{\mathrm{T},q}$; //inverse static map

---

Function $[V_{\mathrm{p}},\ w_{\mathrm{T}}]$ = w_func($par, mthd$) {
Data: *par*- structural parameters, *mthd*- modeling method, ρ_{L}- external load position vector
Result: actions and actuator volume
$\phi_{\mathrm{p}} = [0\ 2\pi/3\ -2\pi/3]$; //angular position for pneumatic chambers
for *i- number of pneumatic chambers* **do**
  $l_{\mathrm{p}} = l(1 - \kappa r_{\mathrm{o}}\mathrm{C}_{(-\phi+\phi_{\mathrm{p}})})$;
  $[V_{\mathrm{pt}}, w_{\mathrm{pt_{NH}}}, w_{\mathrm{pt_{EB}}}]$ =action_fun($l_{\mathrm{p}}, par, mthd_{\mathrm{p}}$); //$w_{\mathrm{pt}}$ for pneumatic chambers
  $V_{\mathrm{p(i)}} = V_{\mathrm{pt}}$; //air and chamber shell actions
  $w_{\mathrm{p}} += w_{\mathrm{pt_{E_{NH}}}}$;
  $[v_{\mathrm{pt}}, w_{\mathrm{cp_{NH}}}, w_{\mathrm{cp_{EB}}}]$ =action_fun($l_{\mathrm{p}}, par, mthd_{\mathrm{c}}$); //$w_{\mathrm{cp}}$ for the chamber holes in the body shell
  $w_{\mathrm{h}} += w_{\mathrm{cp_{NH}}}$; //for the chamber holes
end
$[V_{\mathrm{cp}}, w_{\mathrm{c_{NH}}}, w_{\mathrm{c_{EB}}}]$ =action_fun($l, par, mthd_{\mathrm{c}}$); // w_{c} for the body shell
$w_{\mathrm{c}} = w_{\mathrm{c_{NH}}} - w_{\mathrm{h}}$;
T : *unity matrix*; //initialize
for n_{s}- *number of segments in a manipulator* **do**
  $T = T.T_{\mathrm{COM}(n_{\mathrm{s}})}$; //COM transformation matrix calculation
  $\rho_{\mathrm{COM}} = T.[0001]^{\mathrm{T}}$; //COM position vector
  $w_{\mathrm{b}} = bg.\rho_{\mathrm{COM}}$; //weight action
end
for n_{L}- *number of external loads* **do**
  $w_{\mathrm{L}} = +f_{\mathrm{L}}\rho_{\mathrm{L}}$; //external load action
end
$w_{\mathrm{T}} = w_{\mathrm{c}} + w_{\mathrm{p}} + w_{\mathrm{L}} + w_{\mathrm{b}}$; //total action
return $[V_{\mathrm{p}}, w_{\mathrm{T}}]$ }

Algorithm 1: The pseudo code for a Matlab program to derive the inverse static relation for a continuum manipulator using the principle of virtual energy and constant curvature assumptions.

associated cross-section deformation models. Assuming EB relations in each element and $J_{\hat{d}_2} \approx J_{\hat{d}_3}$, the deformed values in each element along the backbone curve are found by substituting $\lambda_l = v_1 + 1$ and $\kappa = \sqrt{u_2^2 + u_3^2}/(v_1 + 1)$ in equations from section 3.2.2 and 3.2.3. We consider the backbone area and second moment of area

for the deformed body to account for the cross-section deformation. The algorithm to implement the method is presented in Algorithm 2. There, bvp function is a BVP problem based on beam theory method which is integrated over the continuum backbone using ode113 function and then solved, based on the optimization method, using fsolve function in Matlab software. bvp function returns the configuration spatial derivatives ($[\rho_{,s}, R_{,s}]$) at each location (s) along the continuum backbone. First, the location of the current backbone position in Cartesian coordinates ($[x_0, y_0]$) is interpolated, and the element axial stretch and bending curvature ($[\lambda_{l,s}, \kappa_{,s}]$) are found from the guessed geometry. The module and pressure chamber cross-section area, second moment of area and pressure chamber placings ($[a_{\mathrm{p_d}}, a_{p_\mathrm{d}}, J_{\mathrm{p}\hat{d_1}}]$, $[a_{\mathrm{c_d}}, J_{c\hat{d_1}}]$ and $r_{\mathrm{o_d}}$) are calculated using cross_sec based on the current element axial stretch and bending curvature. The external (τ) and body load (τ_b) moments are calculated and used to calculate $[v, u]$ and $[\rho_{,s}, R_{,s}]$.

The results are compared to the experimental measurements and the advantage of the geometry deformation approach in increasing the model prediction accuracy is presented in Table 3.1.

3.2.5 Simulation and Comparison of Different Models

We investigate the accuracy of the simulations from different models in predicting the experimental results and the sensitivity of each model to structural and kinematic parameters. The comparison between the models helps to understand how the modeling accuracy improves by increasing the mathematical derivation complexity and to find the proper model to observe certain behaviors, incorporate effects of important structural parameters and achieve a desired modeling accuracy. Modeling absolute error is defined as the positive value of the difference between the output vector (pressure (p) for the inverse model (section 3.2.5) and tip position vector (ρ_{tip}) for the forward model (section 3.2.5)) from the model simulation and the experiments. Error percentage is found by dividing the absolute error by the vector

Data: *par*- structural parameters, $mthd_{\mathrm{c}}$, $mthd_{\mathrm{p}}$- modeling method for the body and chamber
Result: inverse model for a continuum manipulator based on Cosserat rod model
initialization;
first guess for the position of interpolation points in equilibrium geometry (ρ_0) ;
q = fsolve(@(q_0)(ode113(@bvp(l,q_0,par)),q_0); //to solve the boundary value problem
return q; //equilibrium geometry

Function bvp(s,q_0,par) {
Data: *par*- structural parameters, *mthd*- modeling method, q_0- initial geometry, s- axial position
Result: ODE derivatives
$[x_0, y_0]$ = interp1(q_0, s); //interpolate the location of the current backbone position in Cartesian coordinates
$[\lambda_{l,s}, \kappa_{,s}]$=...; //the element differential kinematics based on the guessed geometry from section 2.2.5.
$[a_{\mathrm{p_d}}, a_{p_{\mathrm{d}}}, J_{\mathrm{p}\hat{d_1}}]$ =cross_sec($\lambda_{l,s}, \kappa_{,s}, par, mthd_{\mathrm{p}}$); //pneumatic chamber cross-section area, chamber cross-section area and second moment of area based on the element differential kinematics
$[a_{\mathrm{c_d}}, J_{\mathrm{c}\hat{d_1}}]$ =cross_sec($par, mthd_{\mathrm{c}}$); //boody shell cross-section area and second moment of area
$r_{\mathrm{o_d}}$=sqrt($a_{\mathrm{c_d}}$)r_{o}; //approximates the deformed chamber radial position
$\tau = \tau_{\mathrm{p}} + \tau_{\mathrm{L}}$; //total planar moment due to air pressure and the external tip moment
τ_{b}=$ba_{\mathrm{c}}g$(trapz(@(x)(interp1(q_0, x)-x_0),s, l)); //integration for the body load moment
$[v, u]$ = ...;
$[\rho_{,s}, R_{,s}]$ = ...; //substitute in Eq. 2.16, 2.17 and 2.20 to calculate the derivatives.
return $[\rho_{,s}, R_{,s}]$ }

Algorithm 2: The pseudo code for a Matlab program to solve the forward static relation for a continuum manipulator using Cosserat rod method.

value from the experiments as the reference value and used as a means to compare constant curvature and variable curvature modeling results despite their differences. To make comparison with similar research easier, a reference error percentage is defined where the absolute error is divided by a structural parameter as the reference value (E for the inverse model (section 3.2.5) and module length ($l + 2l_{\mathrm{fs}}$) for the forward model (section 3.2.5) [74]), where l_{fs} is the axial offset between the manipulator ends with the tracking sensors. We use error percentage to compare the different models in this research; however, the reference error percentage should

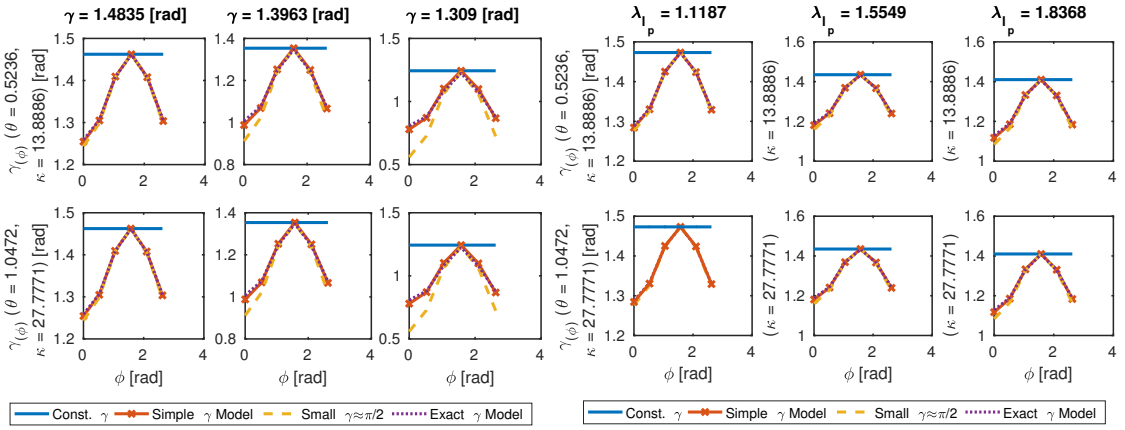

Figure 3.5: The change in the local lead angle ($\gamma_{(\varphi)}$) of a pneumatic chamber's helical thread in terms of different values of γ, κ and $\theta = \kappa l_{\mathrm{pd}}$ where (left six plots) $\lambda_{l_{\mathrm{p}}} = 1.2418$ and (right six graphs) $\gamma = 1.4835[rad]$. The model with dense thread (small $\gamma \approx \pi/2$) tends to predict more change in $\gamma_{(\varphi)}$.

be used for comparison with the results from other similar research.

Helix Lead Angle Models

Simulation results for $\gamma_{(\varphi)}$ in terms of different values of γ, κ and $\lambda_{l_{\mathrm{p}}}$ show considerable changes in the local lead angle, w.r.t. the initial lead angle (γ) and the uniform changes in the lead angle after pure elongation (γ_{p}), even for $\gamma \approx \pi/2$ (Fig. 3.5). The variations from the base lead angle (γ) increase significantly as the γ itself decreases and as $\lambda_{l_{\mathrm{p}}}$ increases. However, it decreases slightly when κ increases and there is no notable variation w.r.t. $\theta = \kappa l_{\mathrm{p}}$. γ produces the dominant effect and enhances the effect of other parameters as it decreases. Results from the exact model (Eq. 3.16) and the simplified model (3.19) are almost identical while the simplified model predicts slightly larger variations in the local lead angle. We continue with the simplified model. The small lead angle assumption ($\gamma_{(\varphi)} \approx \pi/2$) in all the derivations causes a larger error w.r.t the exact model and predicts more local change in $\gamma_{(\varphi)}$. With local changes in $\gamma_{(\varphi)}$, the errors of the three models remain small for $\gamma_{\mathrm{p}} > 80[\mathrm{deg}]$ and they have identical results for $\gamma = \pi/2$ as expected.

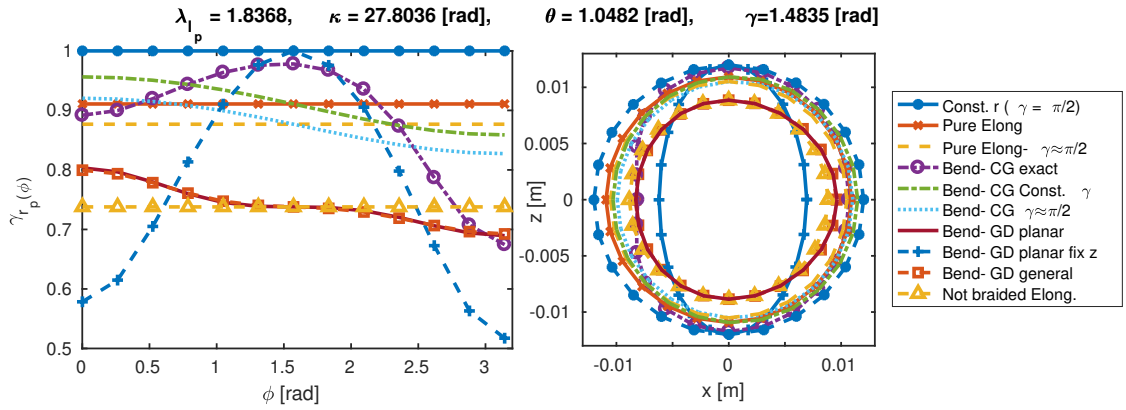

Figure 3.6: (left) The change in the outer radius stretch ($\lambda_{r_{\mathrm{p}}(\varphi)}$) and (right) shell cross-section deformation of a pneumatic chamber for $r_{\mathrm{p2}} = 12[\mathrm{mm}]$, $\lambda_{l_c} = 1.8368$, $\kappa = 27.8036[rad]$, $\theta = 1.0482[rad]$, $\gamma = 1.4835[rad]$. The bending is toward x-axis positive direction.

Braided Actuator Deformation Models

Simulation results for different derived models of $\lambda_{r_{\mathrm{p}}(\varphi)}$ and cross-section shapes of a STIFF-FLOP pneumatic chamber in terms of γ, κ, θ and $\lambda_{l_{\mathrm{p}}}$ are presented in Fig.s 3.6-3.8.b. The exact helix model as in Eq. 3.22 predicts the largest variation from the circular shape such that the cross-section radius will shrink more in both the inner (concave) and outer (convex) sides of the curve in the bending plane and w.r.t. the tangential plane. The deformation of the radius on the inner side is smaller than the deformation on the outer side, and this difference increases as either θ or κ increases, in addition the deformation magnifies when γ decreases and/or $\lambda_{l_{\mathrm{p}}}$ increases. However, it decreases when κ is increased for a constant θ and increases when κ is increased for a constant $\lambda_{l_{\mathrm{p}}}$. The most significant parameter on the cross-section asymmetric deformation is the bending angle (θ) and its effect is enhanced by the braid helix lead angle (γ) decreasing as well as the axial stretch ($\lambda_{l_{\mathrm{p}}}$) increasing. The observed effects intensify for bigger radii. The small lead angle case ($\gamma \approx \pi/2$) for the exact helix model predicts a larger uniform decrease in the shell radius which we found unsuitable for modeling purposes and is not presented in the graphs.

Despite the exact helix model, the constant lead angle assumption (Eq.3.25) predicts

an almost uniform shift in the cross-section toward the bending axis. The structural parameters have almost the same effects on the deformation predicted by this model as discussed for the exact helix model; however, their effects are not significant. The constant lead angle model in the general case corrects the pure elongation general case and the small lead angle case ($\gamma \approx \pi/2$) corrects the small angle case for the pure elongation. The small lead angle models predict a slightly smaller radius compared to the general cases; however, they are not significantly different from the fixed radius models ($\gamma = \pi/2$) and from each other in terms of the prediction of the shell radius deformation. Assuming $\gamma \approx \pi/2$ results in slightly larger predictions for radius and thread local lead angle. The results are in good agreement with the exact models for $\gamma_{\mathrm{p}} > 80$[deg]; however, the simplification does not reduce the complexity of derivations significantly.

The exact helix model assumes the braid helix deforms due to pure torsion of the thread cross-section, similar to a stiff spring, without any bending. This assumption for the constant lead angle model is not valid and this model's prediction is similar to the result from the pure elongation of a helix (3.6). We suggest using the exact helix model for the chambers with stiff braids, and using the constant lead angle model for more deformable braids, i.e. sewing threads, where the deformation of the chamber shell is more dominant. The deformation of the cross-section and the difference between the models become noticeable when $\gamma > 1.309$[rad] or $\lambda_{l_{\mathrm{p}}} > 1.8$. However, to understand the significance of this difference on the static model of a chamber, we investigate the action predicted by any of the models later. Note the different predicted profile for a module in nearly pure bending with a big radius ($\lambda_{l_{\mathrm{c}}} = 1.1187$ and $\theta = 1.0482$ [rad) in Fig. 3.6 compared to a module with smaller radius in Fig. 3.7.

Different predicted deformations based on different models for the outer and the inner radius of a braided pneumatic chamber with inner and outer diameter of respectively 12 and 18[mm] and $\gamma = 1.48354$[rad] are presented in Fig. 3.7. Results for a body shell without braids are presented for comparison purposes too. The

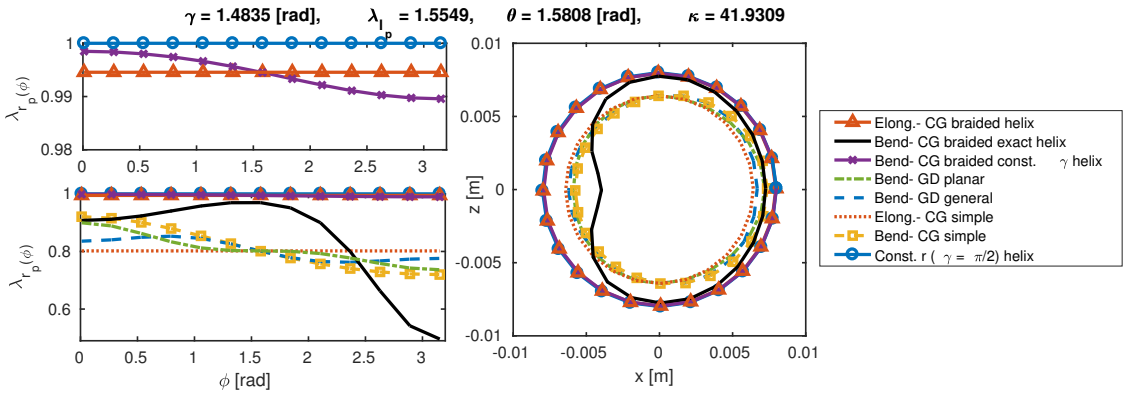

Figure 3.7: (left) The change in the inner radius stretch ($\lambda_{r_{\mathrm{p}}(\varphi)}$) and (right) cross-section deformation of a pneumatic chamber where $r_{\mathrm{p1}} = 8[\mathrm{mm}]$, $\lambda_{l_c} = 1.5549$, $\kappa = 41.6922[rad]$, $\theta = 1.0482[rad]$, $\gamma = 1.4835[rad]$. Note how the cross-section shape changes based on different model assumptions. The bending is toward x-axis positive direction.

deformation predicted by all the braided models other than the bending model with the exact helix γ assumption, are almost identical to the prediction of the constant radius model for this γ. A closer look shows a small decrease in the radius in case of pure elongation of a helix. The radius changes somewhat for the bending model with the constant γ assumption and slightly expands inward. The bending model with the exact γ assumption shows a helix that does not allow lateral deformation other than the uniform reduction due to the elongation of the axis. It causes a change in the twist angle at the back side of the bent where two consecutive rounds of the helix have different local lead angles and create a heart shape (Fig. 3.2 & 3.7). While a tube inside a helical spring behaves similarly to the exact γ assumption model, the thread tends to follow the deformation of the body shell for the softer braids and maintain γ; therefore, it behaves similarly to the constant γ assumption model. It is clear that the helix tends to maintain the radius and the braided chamber does not shrink in radius as does the simple cylinder without braids.

Cross section deformation of a pneumatic chamber for the STIFF-FLOP module is presented in Fig. 3.9 for different bending angles. It is clear that the change in the shape of the cross-section in the Fig. 3.9 is less obvious than in Fig. 3.7 with bigger inner and outer radius. The inner cross-section shape deformation is more obvious.

a)

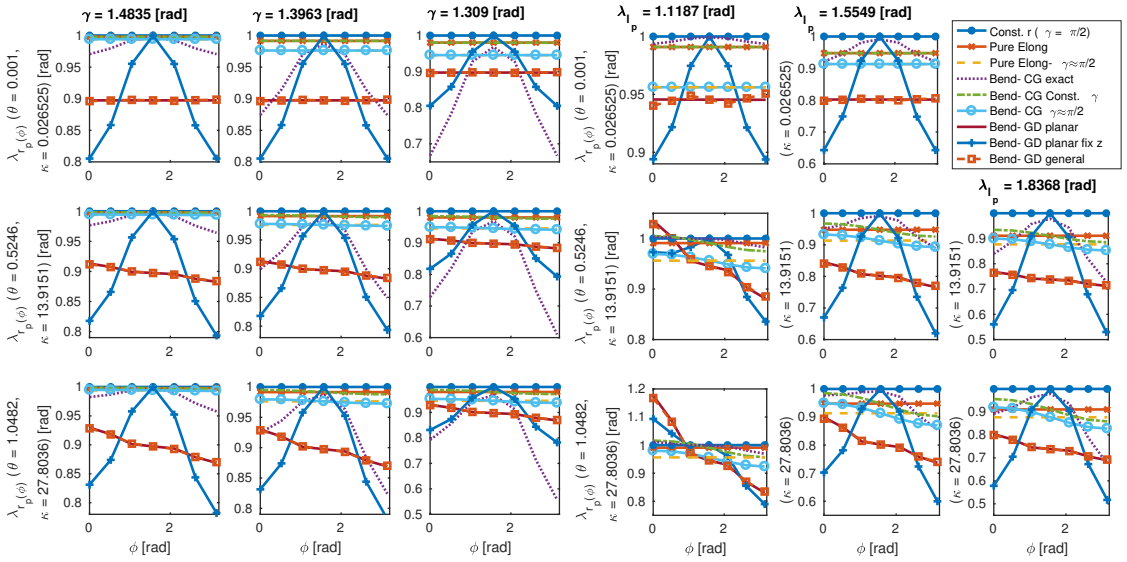

b)

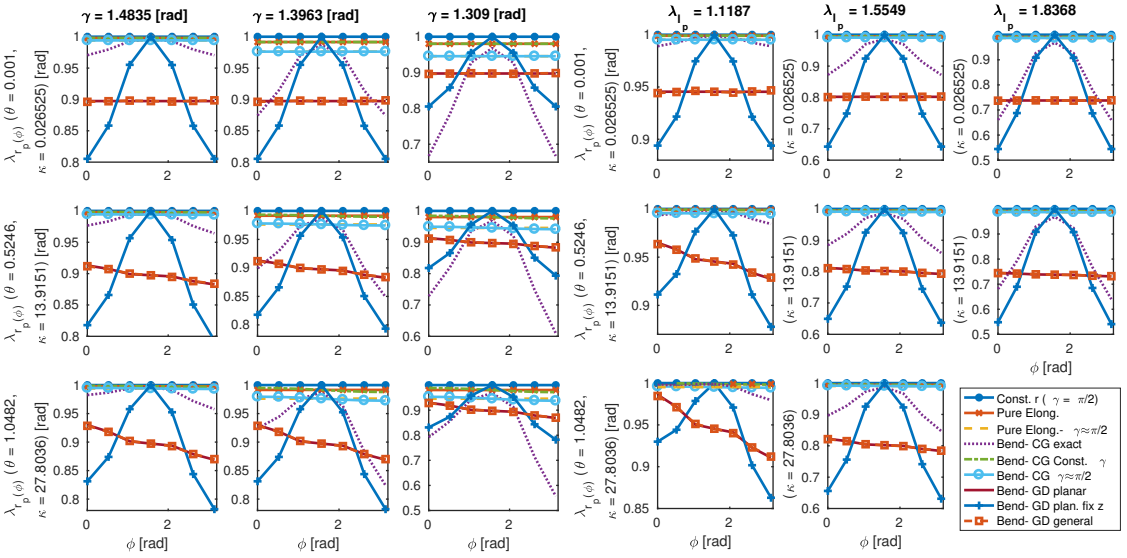

Figure 3.8: Results for (a) a module with large radius ($r_{\mathrm{p2}} = 12[\mathrm{mm}]$), for better presentation of the model assumption effects on the cross-section deformation, and (b) the STIFF-FLOP pneumatic chamber ($r_{\mathrm{p2}} = 3[\mathrm{mm}]$). (left nine graphs) The change in the outer radius stretch ($\lambda_{r_{\mathrm{p}}(\varphi)}$) and (right nine graphs) shell cross-section deformation of a pneumatic chamber in terms of different values of γ, $\lambda_{l_{\mathrm{p}}}$, κ and $\theta = \kappa l_{\mathrm{p}}$ where (left nine graphs) $\gamma = 1.4835[rad]$ and (right nine graphs) $\lambda_{l_{\mathrm{p}}} = 1.2418$. Different scales for the y-axis are used for better visibility. Note how the different assumptions change the cross-section shape by changing the $\lambda_{r_{\mathrm{p}}(\varphi)}$ profile; and the different predicted profile for a module in nearly pure bending with a large bending radius ($\lambda_{l_{\mathrm{p}}} = 1.1187$ and $\theta = 1.0482$ [rad]) in (b) compared to a module with bigger radius in (a).

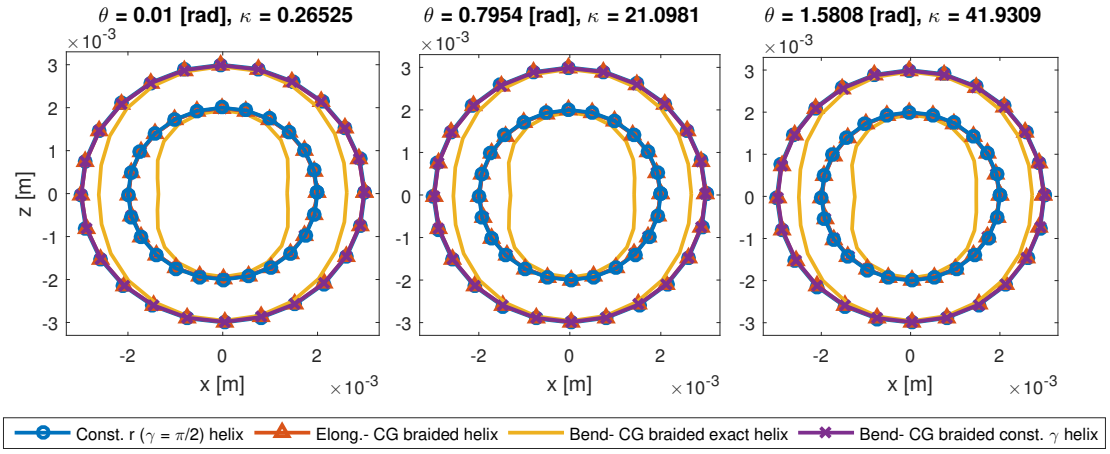

Figure 3.9: The cross-section deformation model for a STIFF-FLOP pneumatic chamber where $\lambda_{l_c} = 1.5549$ and $\gamma = 1.4835[rad]$. The bending is toward x-axis positive direction.

The chamber tends to remain circular in all cases except for the bending with exact γ model, where the tube shell tends to bend inward and become more like a bean.

The predicted deformation by different models for a STIFF-FLOP body shell is presented in Fig. 3.10, where deformation due to a pure symmetric elongation, as in Eq. (3.5), is presented too for comparison. The simple bending model based on Cauchy-Green stretches (CG simple bending model) and the planar bending model from the geometry deformation model (GD planar model) predicts more shift in the cross-section toward the bending side. The CG simple bending model predicts an almost uniform shift in the cross-section toward the bending axis. the planar bending model predicts an egg shape cross-section with the sharp side toward the bend center. The general geometry deformation model (GD general bending model) predicts a smaller shift toward the bending axis, and a small lateral shrink at the back of the bending side and a small lateral expansion at the inward. Based on the shift and the overall shape, we conclude that the GD general bending model predicts the most realistic deformation. A comparison between the GD general bending model and the actual cross-section deformation of the body shell is presented in Fig. 3.10 too.

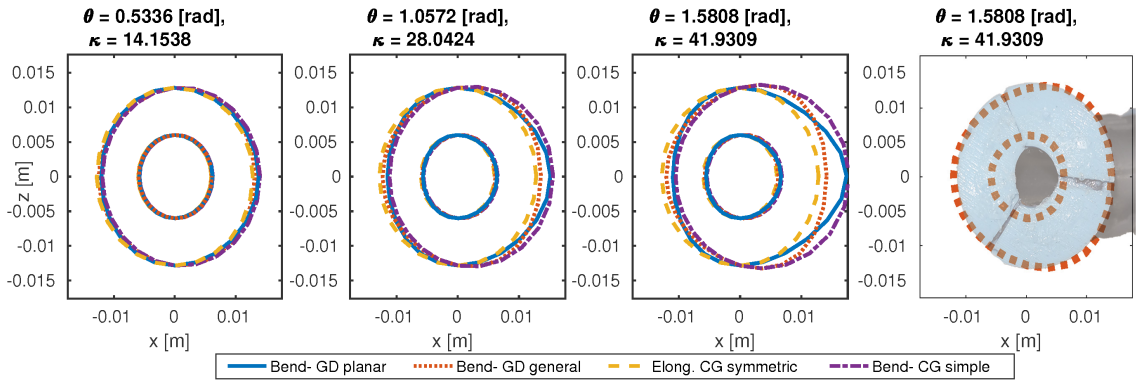

Figure 3.10: The cross-section model for deformation of STIFF-FLOP body shell where $\lambda_{l_c} = 1.5549$, $\gamma = 1.4835[rad]$ and the bending angle is increased between the plots from left to right (left & middle) and comparison with a STIFF-FLOP module cross-section deformation in bending (right). The area changes to an egg shape and shifts toward the inner of the bent. The GD planar model predicts less material shift compared to the general model. The GD general method provides a better prediction of the cross-section deformation. The bending is toward x-axis positive direction.

Braided Actuator Pressure and Action Models

The pressure required for one pneumatic chamber to reach a certain λ_l is found by exploiting the principle of virtual energy for one pneumatic chamber. The result from different braided chamber models is compared against experiments with a STIFF-FLOP chamber (EXP.1) in Fig. 3.11. The variation w.r.t the bent curvature is neglected for the bending models; however, as the standalone actuator chamber bends when it pressurized shown in Fig. 1.4, we simulate the results for different λ_{l_p} in $\theta = 1.482$[rad]. It is observed that the constant γ model and the exact helix model give the best prediction based on the actual measured values. The results are very sensitive to the verified parameters. For example in Fig. 3.11, by choosing a slightly different value for E and γ the bending with constant helix model can predict the pressure values precisely while this model is less sensitive to a change in E compared to the other models. Therefore, we choose the model that predicts the behavior trends in the experimental data and then we identify the unknown structural parameters to fit the model to the experimental readings. The trend in the experimental values and small sensitivity to the γ value shows that the constant γ model has the best prediction for this chamber. This result was predictable due

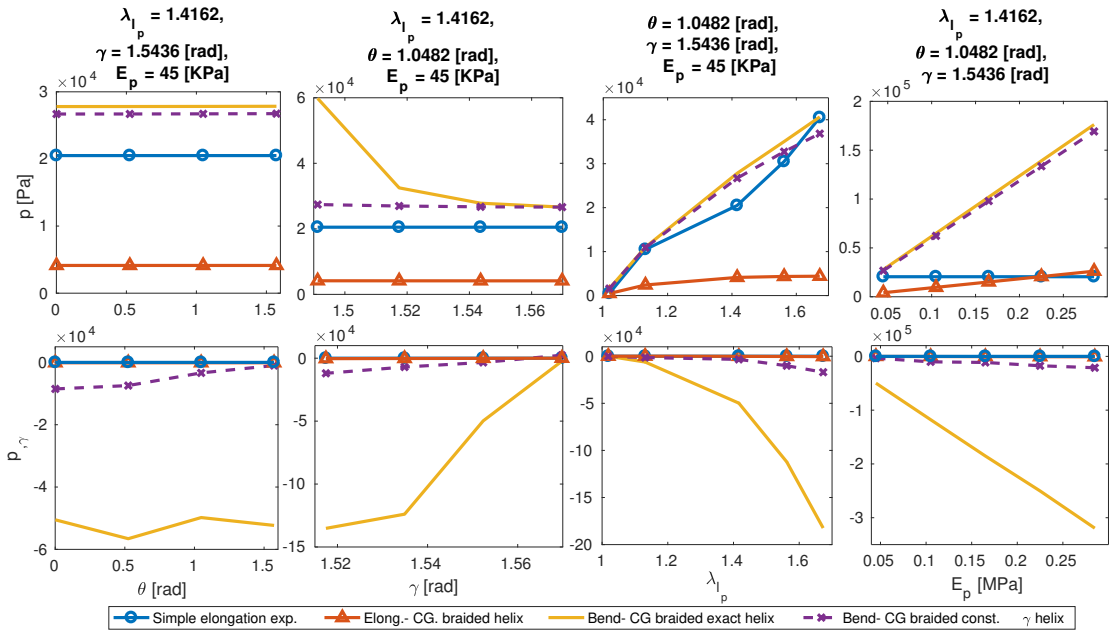

Figure 3.11: (top) Required gas pressure for a certain deformation of a STIFF-FLOP pneumatic chamber, experimental data from EXP.I vs. model simulations, (bottom) sensitivity of the predicted required pressure to the structural parameter γ by plotting $p_{,\gamma}$ for different values of θ, γ, λ_{l_p} and E. The CG exact helix model shows better prediction in terms of mean error and profile shape; however, predicts high nonlinear sensitivity.

to easily deformable threads having been used in making this chamber. There is no significant change in the model predictions for different values of θ and γ, other than the pressure value predicted by the GD general bending model which is shown to be very sensitive to the value of γ, where the pressure increases significantly as γ reduces. This very sensitive behavior needs more experiments for verification when using chambers with variable thread angles.

The elastic deformation from the Neo-Hookean (NH) and Euler-Bernoulli (EB) methods, and gas pressure actions w.r.t different values of θ, λ_{l_p} and γ predicted by different models are presented in Fig. 3.12.a for a STIFF-FLOP pneumatic chamber. The gas pressure action does not change for different values of θ and γ, except for the GD exact helix model that demonstrate a significant increase as γ increases. The most important parameter is λ_{l_p} where causes a significant increase in the actions. For the CG bending model with fixed radius (the case of dense braids, $\gamma \approx \pi/2$) a decrease in the Neo-Hookean elastic deformation action is observed which sug-

gests this assumption cannot be used with the Neo-Hookean method. The graphs show some models predict the actions up to 3 times more compared to other models which show the importance of a proper choice of modeling method. The predictions from GD exact γ and the planar deformation assumptions are quite similar. The Euler-Bernoulli method predicts significantly higher values than the Neo-Hookean method. For the models with fixed radius, dense thread or neglecting the pneumatic chamber shells, larger values for the actions are calculated. In general, any simplifying assumption causes an overestimation of the actions. While the action values are representations of the energies stored in the system, the actions variation w.r.t system states determine the final static map for the system.

Integration with Constant Curvature Model

We attempted to identify the unknown values such as γ, E and sensor frame initial register by fitting the model simulations to the actual experiment information from EXP.3-I for eight data points and subsequently verifying the result against 43 data points. All the remaining parameters were measured manually. It was observed that a combination of the geometry deformation method with general assumptions for the body shell and the bending model with the exact helix lead angle assumption provides the best modeling accuracy. This might have been predicted based on the previous observations about the body shell and pneumatic chamber. This method increases the accuracy of the model by up to 13% mean error compared to a simple CG symmetric elongating body shell with fixed radius chambers and 14% compared to Euler-Bernoulli bending model with fixed cross-section. A better accuracy is possible if a CG pure elongating braided helix model is used instead of the helix fixed radius model. Using the simplified models such as the CG simple bending or fixed radius assumption increases the modeling error by up to 57% compared to the best possible solution. The general deformation derivation (Eq. 3.41) provides a better solution for the problem of flexure compared to the planar deformation method (Eq. 3.36) based on Rivlin's method [113]. The Euler-Bernoulli model with fixed radius

a)

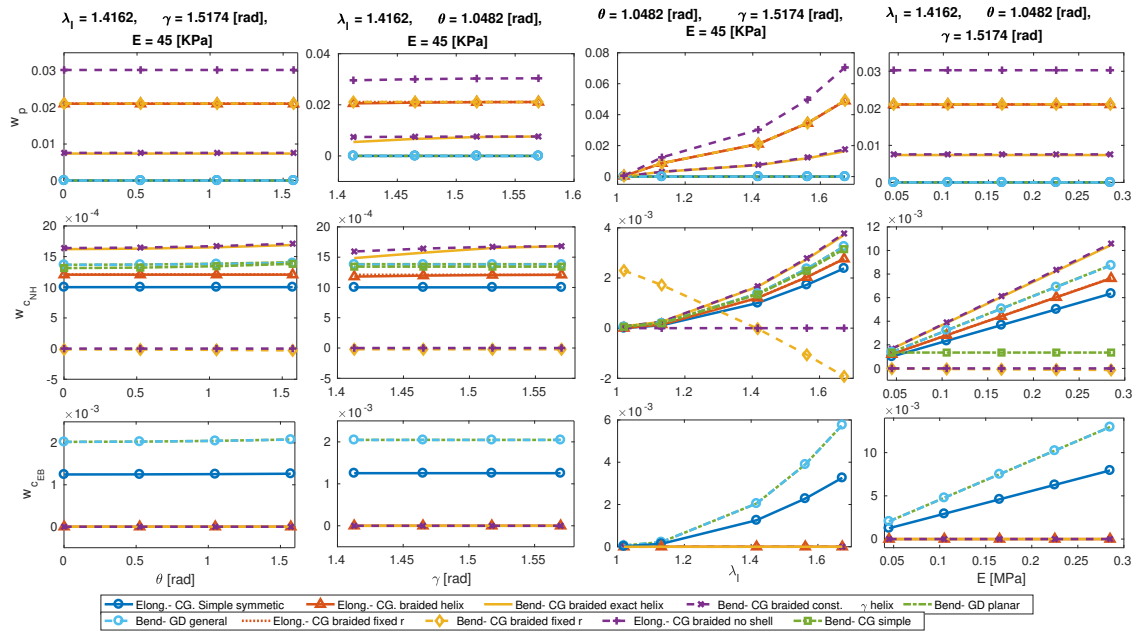

b)

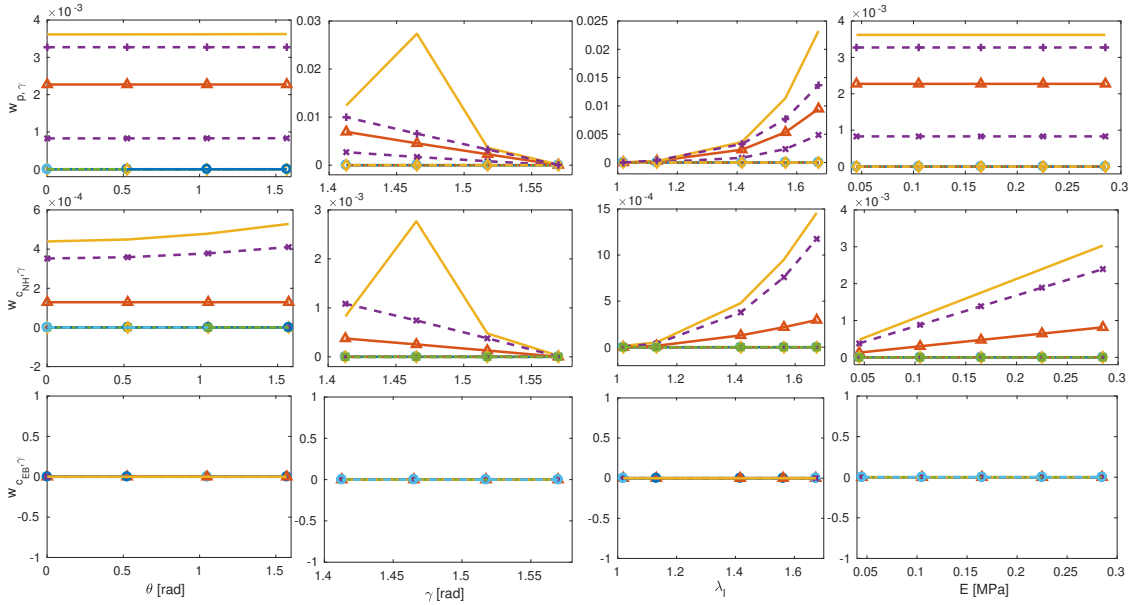

Figure 3.12: (a) The air pressure action (w_{p}), body deformation energy using Neo-Hookean ($w_{\mathrm{c_{NH}}}$) and Hooke's ($w_{\mathrm{c_{EB}}}$) methods vs. change in the helix and curvature parameters. (b) Sensitivity analysis of the action values w.r.t. γ by plotting $w_{,\gamma}$ for different values of θ, γ, $\lambda_{l_{\mathrm{p}}}$ and c. High complexity models, i.e. GD exact helix models, predicts high nonlinear sensitivity and the simplified models, i.e. CG braided fix radius, predicts higher and, in some cases, incorrect sensitivity values and profile.

assumption for the actuator chambers result in better accuracy compared to the Neo-Hookean models in this case; however, the correct choice of the combination of

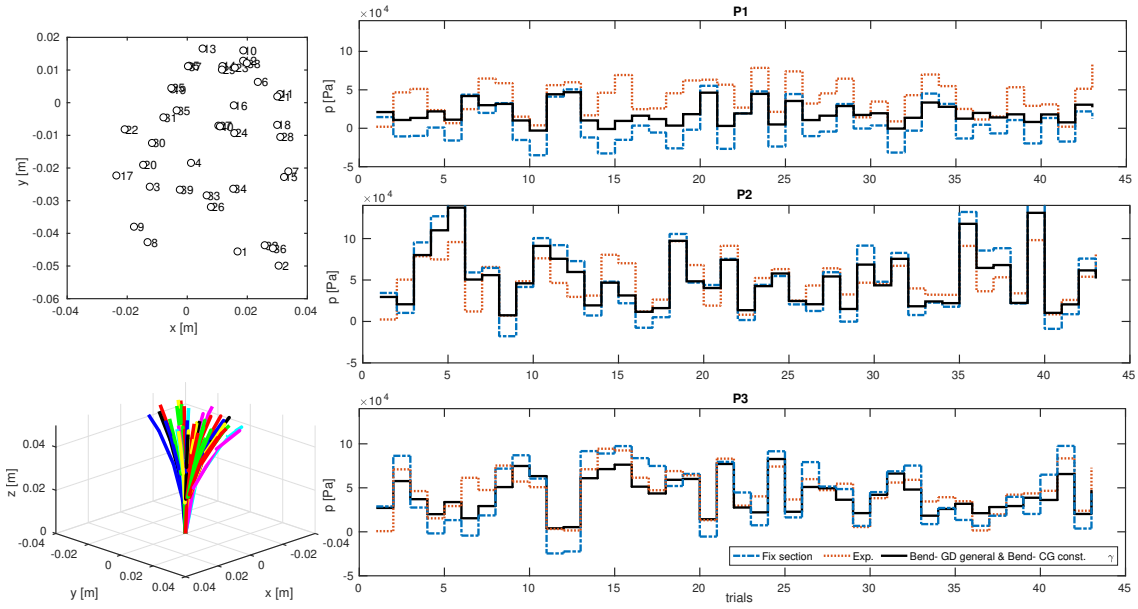

Figure 3.13: The simulation vs. experimental results of EXP.3-I from 43 data points for inverse static relation between the input pressures and the tip position ($p = f_{(\rho_{\text{tip}})}$) for a STIFF-FLOP pneumatic module, using principle of virtual work. A combination of the GD general method and the constant γ model shows 13% lower mean error percentage and 23% lower mean reference error percentage compared to the Euler-Bernoulli rod model without any cross-section deformation.

the methods is still important, i.e. in incorporating the structural parameters' effect. It is clear that more exact modeling of the deformation of the cross-section increases the modeling accuracy significantly, even if this prediction has been made based on a simple symmetric pure elongation model. However, a carefully chosen combination of the models based on the nature of the module is important to achieve the best result. The overall mean error of the model is high (61% mean error percentage and 38% mean reference error percentage) because of the inaccuracy in constant curvature assumption, especially for near straight configurations, as observed in similar previous research [74, 92]. A comparison between the best and the worst model prediction is presented in Fig. 3.13 showing the importance of considering the cross-section deformation.

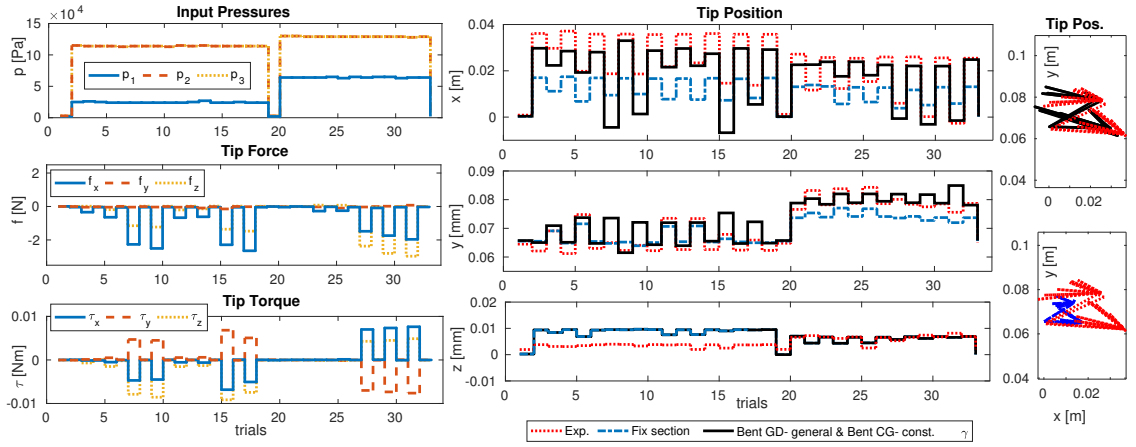

Figure 3.14: The simulation vs. experimental result from 33 data points for planar deformation of one STIFF-FLOP module under extensive external loads (EXP.2). A combination of GD general method and exact helix model shows 7% lower mean error percentage and 10% lower mean reference error percentage compared to the Euler-Bernoulli rod model with no cross-section deformation. The VC model shows 52% lower mean reference error percentage than the CC model (Fig. 3.13).

Integration with Variable Curvature Model

Eq. 2.20 needs to be solved for the deformed geometry in the equilibrium state. We start with a guess for the deformed geometry, i.e. straight configuration, and solve for the manipulator geometry where the result should be identical to the first guess. This leads to a system of nonlinear equations that can be solved with numerical methods such as Powell dogleg [119] used in Matlab 'fsolve' function. Starting from the straight undeformed state shows good convergence and the algorithm usually needs two trials to find the equilibrium configuration for a single-curve formation and three trials for a double-curve formation (Fig. 1.7).

We investigate the Cosserat rod model accuracy to simulate the planar deformation of one STIFF-FLOP module with extensive external loading of EXP.2, shown in Fig. 1.7. A Matlab program algorithm is presented in 2. The overall accuracy of the Cosserat rod model is about 52-100% better than the constant curvature model for any combination of the models. Approximately the same trend in the accuracy of the models is observed here compared to the constant curvature model. The combination of the bending GD general deformation or planar assumption and the exact or constant γ helix model results in a small 9-10% error. The error for the

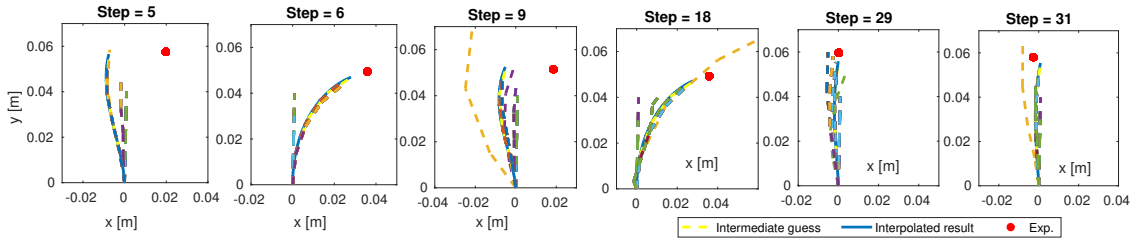

Figure 3.15: The iterations to solve the BVP problem for some of the simulation steps.

combination of the CG symmetric elongation model and the helix pure elongation results in 12% error which is slightly less than the accuracy of the models based on the general deformation method. A comparison between the combination of the GD general bending models and the constant helix angle (γ) model with the model without any change in the cross-section is presented in Fig. 3.14 showing 7% increase in the model accuracy by taking into account the cross-section deformation based on mean reference error. The iterations to solve the BVP problem for some of the simulation steps are presented in Fig. 3.15. The model reference error percentage is 10% for the case with extensive external load and less than 5% in the case that only the body weight is present which is similar to the reported results in [74, 25]. Model complexity provides a more accurate solution; but, increases the time that the numerical nonlinear solver needs to find a feasible solution. This is due to increased computation time and highly nonlinear behavior of the model complexity.

Body Shell Model	Pneumatic Chamber Model	Abs. Error CC [KPa] - VC [mm]	Error (%) CC - VC	Ref. Error (%) CC - VC
Elong. CG simple sym.	Fixed radius	60 - 7.6	74 - 10	60 - 12
Elong. CG simple sym.	Elong. braided	111 - 9	179 - 12	113 - 14
Bend. Eu-Be fix section	Fixed radius	61 - 13	75 - 17	61 - 20
Bend. CG simple model	Elong. braided	95 - 9	118 - 12	95 - 14
Bend. GD planar	Bend. const. γ	40 - 10	65 - 14	40 - 16
Bend. GD general	Elong. braided	53 - 14	93 - 19	53 - 22
Bend. GD general	Bend. exact helix	38 - 7	62 - 10	38 - 11
Bend. GD general	Bend. const. γ	38 - 6.6	61 - 9	38 - 10

Table 3.1: Performance comparison between different models for random pressurization of one STIFF-FLOP module under body weight loads vs. 43 experimental data points (EXP.3-I), and under an extensive external load vs. 33 experimental data points (EXP.2). Error percentage is used for comparison between the CC and VC models and reference percentage error is used for comparison with previous research.

3.2.6 Sensitivity Analysis

An analytical model is beneficial for design by providing an efficient means for sensitivity analysis and optimization of the system performance w.r.t. the structural parameters. Here, we investigate the sensitivity of the predicted deformation profiles, the input pressure and deformation energy actions to changes in γ and E, as the two important structural parameters in the design of stiffness controllable braided actuators, by deriving the gradient of these values w.r.t. γ and E. The resulting nonlinear relations are plotted for different values of γ, κ, λ_{l_p} and E, showing the sensitivity of the results in any geometrical action point and for any combination of the other structural parameters.

For $\gamma_{(\varphi)}$ as in Fig. 3.16, the exact γ and the dense thread ($\gamma = \pi/2$) models sensitivity to a change in γ decreases as γ decrease and $\lambda_{l\mathrm{p}}$ increases. Unlike $\gamma_{(\varphi)}$, the sensitivity of $\lambda_{r_\mathrm{p}(\varphi)}$ to the change of γ increases by the increase in $\lambda_{l\mathrm{p}}$ and κ and decrease in γ showing more sensitivity in pure elongation cases for a module with a less dense braid. The model with simplifying assumption of $\gamma \approx \pi/2$ overestimates the predicted values as observed in the previous sections.

The sensitivity of the deformation action, gas pressure action (Fig. 3.12.b) and required pressure for a braided actuator to reach a certain elongation (Fig. 3.11) to changes in γ increases for a more stiff actuator (increase in E) with a less dense thread (decrease in γ) and in a pure elongation case (decrease in θ and increase in λ_{l_p}). The sensitivity of p decreases for a high bending angle cases while slightly increases for the deformation actions. p and w are linear functions of E and their sensitivity to changes in the module stiffness is similar to the graphs for p and w where the values are divided by the value of E in our simulation (10 [KPa]).

The CG exact model which uses a simplifying assumption for γ, as in Eq. 3.17, results in a highly nonlinear gradient w.r.t.γ which is not similar to that of the exact γ model in Fig. 3.16. This is predictable as the simplifying assumption only

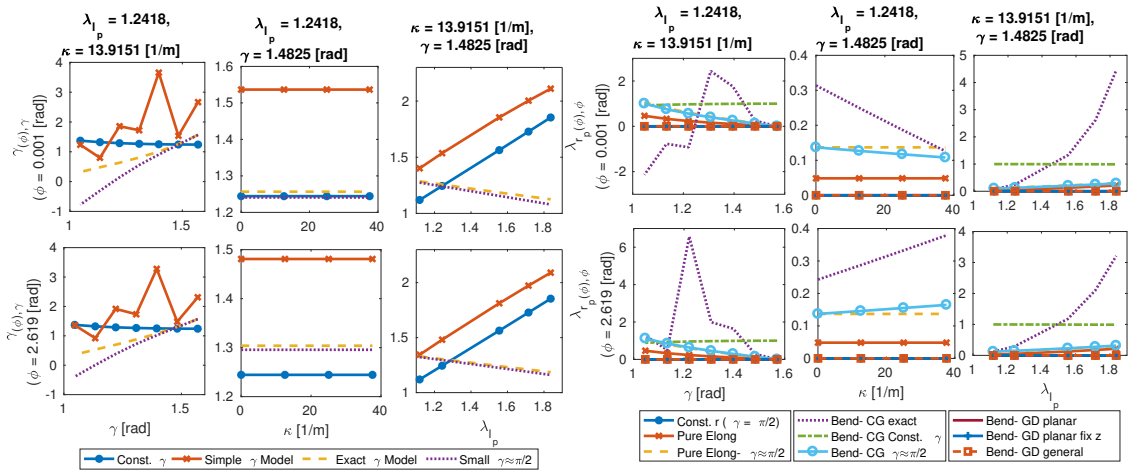

Figure 3.16: (left six graphs) Sensitivity of predicted values of $\gamma_{(\varphi)}$ ($\gamma_{(\varphi),\gamma}$) and (right six graphs) λ_{l_p} ($\lambda_{l_p,\gamma}$) from different models to change in γ for different values of γ, κ and λ_{l_p}. The CG exact model which uses simple γ model shows highly nonlinear sensitivity for different values of γ which is not similar to that of the exact γ model. The model with dense thread assumption ($\gamma \approx \pi/2$) shows higher sensitivity.

holds for small values of γ and predicts greater changes in the sensitivity, similar to the other models with similar simplifying assumption.

3.2.7 Discussion on Exact Modeling of Compound Continuum Manipulator

First, cross-section deformation of a STIFF-FLOP chamber in terms of structural and bending parameters using different methods is presented in Fig. 3.6 and 3.8.b. The exact helix model predicts a bean like cross-section with small lateral deformations, and the constant γ assumption predicts a uniform shift in the cross-section toward the bending axis. A larger uniform decrease in the cross-section is predicted for the small lead angle assumption ($\gamma \approx \pi/2$). The most effective parameter on the asymmetric deformation of the cross-section is the decrease in the bending angle (θ) and the braid helix lead angle (γ), where the increase in the axial stretch (λ_{l_p}) and initial radius enhance these effects. The structural parameters have fewer effects on the models with the constant γ and dense braid assumptions. The dense braid assumption predicts a slightly smaller deformed radius compared to the model for

simple elongation of a helix. These models are valid for $\gamma > 80$[deg], however, are not recommended as they do not reduce the derivation complexity significantly.

The braided chamber cross-section deformations predicted by any of the models are presented in Fig. 3.7. The elongation of a helix results in a small uniform reduction of the radius and the constant γ assumptions added a small shift toward the bending angle too. There is no lateral deformation in the exact helix model in pure bending resulting in a heart shape deformed cross-section (Fig. 3.2) due to a notable different twist angle at the start and end of each thread rounds. In general, the braided chamber radius deformation is smaller than the cases without braids. The experimental results for a STIFF-FLOP module are presented in Fig. 3.9 and Fig. 3.10

The exact helix model assumes pure torsion of the thread cross-section which is valid for a stiff thread similar to metallic springs. The bendable thread, i.e. sewing threads, being use for many micro soft manipulators tend to follow the deformation of the chamber body; hence, the constant γ assumption should work better with them.

Next, we investigated the action predicted by the models. A considerable shift in the cross-section toward the bending axis is observed for the CG simple bending model (uniform shift), the GD planar models (egg shape) and the GD general bending model(trapezoidal shape). The most realistic shift and overall deformation compared to the experiment results are predicted by GD general bending model (Fig. 3.10). As predicted, the constant γ model gives the best prediction of pressure vs. λ_{l_p} for one pneumatic chamber (Fig. 3.11). Despite that the results are very sensitive to the identified value for E, we choose the model that shows a better agreement with the behavior trends observed from the experiments. The results for the GD general bending model shows to be very sensitive to the value of γ as can be predicted for a spring.

The elastic deformation and gas pressure actions are shown to be very sensitive to

the backbone elongation (λ_{l_p}) compared to the bending angle (θ), showing the dominance of the pure elongation effect over the bending for static modeling (Fig. 3.12.b). Simplifying assumptions (fixed radius, dense thread, neglecting the chamber shells and Euler-Bernoulli linear stress-strain relation), a results in the overestimation of the actions values (up to three times).

A comparison of using different combination of the models for the pneumatic chambers and the body shell with the experimental results shows that a combination of GD general bending model for the body shell and the bending helix with constant γ provides the best modeling accuracy as we anticipated from the previous observations (table 3.1 and Fig. 3.13). It is clear that the modeling accuracy increases by using more realistic models for the deformation of the cross-section (13% less mean error percentage). The results from the simple symmetric elongation and the fixed radius chamber models can be more accurate if, instead of using the real measured values, we identify the structural parameters by fitting the simulation results to the experiment values.

Despite all the improvements from implementing the cross-section deformation models, the overall simulation accuracy is relatively low (up to 62% mean error and 38% mean reference error). We showed 52-100% fewer simulation errors by using the Cosserat rod model in the case of high external loading (EXP.2) where the combination of the GD general deformation or planar assumption and the exact or constant γ helix model results in a small 8% error, and the combination of the CG symmetric elongation model and the helix pure elongation shows 10% error. (Fig. 3.14). The model error is less than 5% in the case that only the body weight is present (EXP.3-I). The Hooke's law for linear stress-strain relation used in Eq.2.20 can be substituted with a more realistic model, e.g. Neo-Hookean, Mooney-Rivlin or Gent relations based on the CauchyGreen deformation tensor invariants for a highly deformable material, in a future work, to further improve the modeling accuracy [103]. However, it is hard to predict how much it may increase the model accuracy due to the mentioned models' highly nonlinear property.

We observed that considering the cross-section deformation increases the simulation accuracy up to 10% for the Cosserat rod model and 13% for the constant curvature model compared to the constant cross-section models. The combination of the geometry deformation method and bending helix model has the best result with up to 2% more accurate results compared to the other models for the cross-section deformation. The reference error percentage is used to compare the modeling accuracy with similar research where we showed 38% error for the inverse relation in the model with constant curvature assumption and body loads, 5% error for the forward relation in the model with variable curvature assumption and body loads, and 10% error for the case with extensive external loads. Our results comply with the 5% error observed by the modeling errors reported in [74, 92] for the cases without extensive external loads, while our models incorporate the information about the cross-section deformation too. Our results suggest the importance of the cross-section deformation in the modeling accuracy, which confirms its evident importance for minimal invasive manipulation with small workspaces and for the manipulators with regional controllable stiffness in their cross-section.

The sensitivity of local cross-section radius stretch ($\lambda_{r_{\mathrm{p}}(\varphi)}$), predicted pressure for a certain elongation (p), and deformation and pressure actions (w) to changes in the braid initial lead angle (γ) increase as the module elongates and for a less dense braiding, while the sensitivity of the local lead angle ($\gamma_{(\varphi)}$) w.r.t. γ decreases in the same conditions. $\gamma_{(\varphi)}$ is not sensitive to the actuator curvature, p becomes less sensitive and the sensitivity of w slightly increases as the actuator bends. The sensitivity of $\lambda_{r_{\mathrm{p}}(\varphi)}$ to γ for different bending angles is related to the polar position of the points with decreasing sensitivity for the points on the inside of the bending module and increasing sensitivity for the ones on the outside. The model is linearly sensitive to changes in the module stiffness (E) as all the relations are linear functions of this parameter. Models with more complexity or simplifying assumptions about the thread lead angle predict higher values and nonlinearity for the model sensitivity. This shows the importance of an accurate derivation for the models

with increased complexity and avoiding simplifying assumption about the thread lead angle to achieve robust results. The fact that the resulting predictions for the system behavior and model sensitivity to parameters can be different for different models show the importance of proper choice of model assumptions and complexity level.

We believe our simple analytical model for the cross-section deformation can play the same role as the constant curvature assumptions in providing a simple estimation of the backbone kinematics, for the manipulators with a variable stiffness cross-section. As a suggestion for a future research is to improve the model by considering the material hysteresis and damping effects as well as incorporating adaptive terms in the model to take into account for the changes in the material properties and repeatability of experimental results as presented to some extent in [94]. For the minimal invasive surgery applications with limited workspace, as the main aim of this research, the tactile information from the continuum manipulator can be integrated in the modeling and verification steps to investigate safe skin guiding of a robot movements against soft organs where having information about the robot cross-section deformation in contact with the tissue is beneficial.

3.3 Control Space Reduction and Real-Time Accurate Modeling

Slenderness and compliance of most continuum manipulators make the external and body forces important in the modeling of their behavior. In this section, we use VC kinematics to relate a series-solution geometry in 3D space ($\in R^3$) to the strains, curvatures and torsion (v, u) that are found from the Cosserat rod static model and to calculate the PVW terms for the dynamic model. Besides, we show how to incorporate a feedback term, such as PID, in the controller design to deal with real working disturbances and setup uncertainties in an inverse model. Eq. 2.2 is used

to approximate the mechanical effect of the manipulator highly elastic deformation in planar direction. To consider the effect of highly elastic deformation in the axial direction, in this section, we update the material elasticity (E) and shear (G) modulus as $E|G_{\mathrm{d}} = E|G/\lambda_{\hat{d_1}}$, where $\lambda_{\hat{d_1}}$ is the local axial stretch [103, 84]. Following our findings from the previous section, the pneumatic chamber cross-section is assumed to be constant due to dense braiding [85, 120]. Dependent variables are functions of space and time (s, t) unless specified.

3.3.1 Inverse Variable Curvature Mechanics: Beam Theory

For the inverse VC kinematics, where the manipulator geometry is known as ρ^*, we use Frenet − Serret curvilinear frames with tangent ($\hat{t}$), normal ($\hat{n}$) and binormal ($\hat{b}$) unit vectors. Here, $\hat{b}$ expresses the direction of the local bending vector. The rotation matrix to relate Frenet − Serret to Cartesian coordinates is $R^* = [\hat{n},\ \hat{t},\ \hat{b}]$, where $\hat{t} = \rho^*_{,s}/|\rho^*_{,s}|$, $\hat{n} = \hat{t}_{,s}/|\hat{t}_{,s}|$ and $\hat{b} = \hat{t} \times \hat{n}$. Unlike curvilinear frames in the forward VC kineamtics (R); for the Frenet − Serret frame in the inverse VC kinematics (R^*), the frame local twist around $\hat{t}$ is a combination of a physical geometrical twist due to torsional stresses and a purely mathematical twist due to the side bending of the modules based on the mathematical definition of $\hat{b}$. To cancel the mathematical twist and to find the physical curvilinear frame ($[\hat{d_2},\ \hat{d_1},\ \hat{d_3}]$) for the i^{th} pneumatic module, we use

$$R^*_{\mathrm{r}} = R^*.\Pi_{j=1}^{i} R^{\mathrm{T}}_{\phi_{\kappa j}}, \tag{3.44}$$

where Π is the post-multiplication operator, R_ϕ is a 3×3 rotation matrix around $\hat{j}$, $\phi_\kappa = \mathrm{atan}(\sqrt{3}(p_2 - p_3)/(p_2 + p_3 - 2p_1))$ is the angle of the bending plane due to internal pressure in the local cross-section plane [20] and p is the pressures vector in a pneumatic actuator [20] or tendon forces vector in a tendon driven design [4, 42]. Alternatively, for inverse model where no information about the actuator pressure

values are known, from curvilinear coordinates we have

$$R_{\mathrm{r}}^{*} = R_{\phi_s}^{\mathrm{T}},\ \phi_s = \int_0^s \hat{n}^{\mathrm{T}}.\hat{b}. \tag{3.45}$$

The later relation assumes no physical twist , e.g. due to out of plan loads. Hence, it may not be reachable and should be considered as an initial approximate guess for an inverse problem. Unlike [74], There is no need for a transformation between the segments.

The relationship of $[v, u]$ with the loads is found from the system mechanical map as in section 2.2.5. Here, R_{r}^{*} is used where any transformation from the curvilinear coordinates to the Cartesian, or vise versa, is needed. R_{r}^{*} is used in inverse map for path following tasks and nonlinear control, but not for the forward model. Here, R is used in Eq. 2.20 for the mechanical map and in Eq. 2.16-2.17 to solve the forward kinematic map. As mentioned earlier, the beam theory approach is suitable for the forward spatial and time integration using an approximate series-solution as ρ^{*}. In the equilibrium state, the geometry found from the forward kinematic map (ρ) should match the guessed geometry (ρ^{*}), used for the inverse kinematic in the mechanical map ($\rho \approx \rho^{*}$).

3.3.2 Variable Curvature Dynamics: Principle of Virtual Work

Among all possible changes in the states of a system, the system follows the one set that minimizes the system action (w). This is known as the Principle of Virtual Work or the Principle of Least Action. The spatial integration over the backbone from the summation of all the virtual works in one element of the continuum manipulator maintains an equilibrium

$$0 = \int_s (\sum_i \mathrm{d}w_{i,q}), \tag{3.46}$$

where $\mathrm{d}w_{i,q}$ is the differential virtual work of the i^{th} action in each element derived using the corresponding load (f) and virtual displacement ($x_{,q}$) vector as $\mathrm{d}w_q = f.x_{,q}^{\mathrm{T}}$.

The gas pressure virtual work ($\mathrm{d}w_{p,q} = C_{p,q}p\mathrm{d}s$, where $C_p = C_{p_v,q} + C_{p_u,q}$) is the summation of the axial virtual work with

$$C_{p_v,q} = a_p[1,1,1]^{\mathrm{T}} v_{\hat{d}_1,q}, \tag{3.47}$$

and the bending virtual work is

$$C_{p_u,q} = a_p(r_{J\hat{d}_{2\mathrm{d}}} u_{\hat{d}_2,q} + r_{J\hat{d}_{3\mathrm{d}}} u_{\hat{d}_3,q}). \tag{3.48}$$

The body shell virtual work ($\mathrm{d}w_{\mathrm{c},q} = \mathrm{d}w_{\mathrm{c}_v,q} + \mathrm{d}w_{\mathrm{c}_u,q}$), including the actuators' chamber body, is the summation of the axial virtual work

$$\mathrm{d}w_{\mathrm{c}_v,q} = E_{\mathrm{d}} a_{\mathrm{c}_{\mathrm{d}}} v_{\hat{d}_1} v_{\hat{d}_1,q} \mathrm{d}s, \tag{3.49}$$

using the Euler-Bernoulli linear stress-strain assumption or

$$\mathrm{d}w_{\mathrm{c}_v,q} = (E/6) a_{\mathrm{c}_{\mathrm{d}}} ((v_{\hat{d}_1} + 1)^2 + 2/(v_{\hat{d}_1} + 1) - 3)_{,q} \mathrm{d}s, \tag{3.50}$$

based on the Neo-Hookean method assuming a symmetric uni-axial deformation [85, 103], and the bending virtual work

$$\mathrm{d}w_{\mathrm{c}_u,q} = K_{u_{\mathrm{d}}} u u_{,q} \mathrm{d}s, \tag{3.51}$$

using the Euler-Bernoulli assumption.

The virtual work of the gravitational body load is

$$\mathrm{d}w_{\mathrm{b},q} = \sigma a_{\mathrm{c}} \mathrm{g} y_{,q} \mathrm{d}s. \tag{3.52}$$

The virtual work due to an external force ($\mathrm{d}w_{L,q} = C_{f_L,q} f_L \mathrm{d}s$) and torque ($\mathrm{d}w_{\tau_L,q} = C_{\tau_L,q}\tau_\mathrm{e}\mathrm{d}s$) expressed in the inertial frame and exerting at $s = s_L$ with $0 \leq s \leq s_L$ are

$$C_{f_L,q} = \rho_{,sq},\ C_{\tau_L,q} = u_{,q}. \tag{3.53}$$

A vector form for the body inertia virtual work can be found using the TMT method [87]. Here, the position vectors in the Cartesian space (ρ) are mapped to the state space (q) by $T = [\rho_{,q}\ \bar{\omega}]^\mathrm{T}$, where $\bar{\omega}$ is found by rearranging ω as $\omega = \bar{\omega} q_{,t}$. The mass matrix for disk elements with an infinitesimal thickness is $\mathrm{d}M = \mathrm{diag}([\ [1\ 1\ 1]a_\mathrm{c}\ J_\mathrm{d}\ ])\sigma\mathrm{d}s$. Following the TMT derivations in [87], the transformed mass matrix is

$$\mathrm{d}M_q = T^\mathrm{T}\mathrm{d}MT\mathrm{d}s, \tag{3.54}$$

and the coefficient matrix for the velocity dependent terms is

$$\mathrm{d}D_{m,q} = T^\mathrm{T}\mathrm{d}M(Tq_{,t})_{,q}\mathrm{d}s. \tag{3.55}$$

Then, we have $\mathrm{d}d_{m,q} = \mathrm{d}D_{m,q}q_{,t}$, and the total inertial virtual work is $\mathrm{d}w_m = (\mathrm{d}M_q q_{,tt} + \mathrm{d}d_{m,q})\mathrm{d}s$.

The linear and angular viscous damping of the material is $\mathrm{d}w_{\mu,q} = C_\mu q_{,t}\mathrm{d}s$, where

$$C_\mu = (\epsilon_{,q})^\mathrm{T}\mathrm{diag}([\mu_v\ \mu_u])\epsilon_{,q}, \tag{3.56}$$

where $\epsilon = [v\ u]^\mathrm{T}$, μ_v and μ_u are the material linear and rotational viscous damping coefficient.

The vector form of the dynamic EOM in each element is

$$\begin{aligned} &\overbrace{\mathrm{d}M_q q_{,tt}}^{\text{Acceleration}} + \overbrace{\mathrm{d}d_{m,q}+\mathrm{d}w_{\mu,q}}^{\text{Velocity Dependent}} + \overbrace{\mathrm{d}w_{\mathrm{c},q} - \mathrm{d}w_{\mathrm{b},q}}^{\text{Conservative Actions}} \\ &\qquad = \underbrace{\mathrm{d}w_{p,q} + \mathrm{d}w_{f_L,q} + \mathrm{d}w_{\tau_L,q}}_{\text{Non-conservative Actions}}, \end{aligned} \tag{3.57}$$

which is integrated along the backbone curve at each time step. We use a trapezoidal rule for the spatial and a 4^{th} order Runge-Kutta method for the time numerical integration.

3.3.3 Ritz and Ritz-Galerkin Methods

Direct single shooting, multiple shooting and concatenation methods are used to find weak-form solutions for a BVP, in which the separation of variables method is used to separate the time and space domains and makes the forward integration possible. Using the direct single shooting method, an approximate series-solution is assumed for the backbone kinematics (ρ^*) with a finite number of terms that satisfies the initial and boundary conditions

$$\rho^* = \sum_i c_{(t)i} \Psi_{(s)i}, \tag{3.58}$$

where $c_{(t)i}$ is a time dependent coefficient which is constant in the static case and $\Psi_{(s)i}$ is a spatial shape function.

Based on the Ritz method for BVPs, widely being used in the finite element analysis [121], Eq. 3.58 is substituted in the BVP equation, Eq. 2.20 for the static or Eq. 3.57 for dynamic model, and the coefficients ($c_{(t)i}$), that approximate the BVP with minimum error, are found. Numerical nonlinear solvers, i.e. Matlab 'fsolve' function, can be used to find the coefficients (c_i) that minimize the approximation error in the static case. The coefficients' time series ($c_{(t)i}$) are found from the time numerical integration of the EOM in the dynamic case.

A better approximation is possible with the Continuous Galerkin method of weighted residuals, known as the Ritz-Galerkin method, where the weighted residuals of the system are minimized instead of the system function itself. The shape functions ($\Psi_{(s)i}$) are considered as the weighting functions ($W_i = \Psi_{(s)i}$) for the Ritz-Galerkin

method [121]. The weighted version of Eq. (2.16) for the static case is

$$0 = \int_0^l W\rho^*_{,s}\mathrm{d}s - \int_0^l WR(v + [0,\ 1,\ 0]^{\mathrm{T}})\mathrm{d}s, \tag{3.59}$$

where W is the weighting matrix and each coordinate equation is weighted with the shape functions of the same coordinate in the series-solution. In the dynamic case, both sides of Eq. (3.57) is multiplied by $(W.T)$ to transfer the EOM from the generalized state space (q) to the Cartesian state space and weight the equation for each coordinate with the corresponding weighting functions.

Tunay used the Galerkin series-solution in a discrete finite element domain for numerical simulation of the static deformation and inflation of continuum manipulators in the presence of conservative forces. He achieved a two order of magnitude improvement in the computation efficiency compared to a common large deformation finite element model. However, the choice of a 7-D linear shape function and the discrete finite element approach make his method hard to be interpreted physically and unsuitable for inverse mechanics, path planning, control and stability analysis.

Based on experimental observations, we present a continuous and easy to interpret series solution where the coefficients of a series of Lagrange polynomial shape functions are assumed to be the system states $(q = c_{(t)})$ for optimization in the static case or for time integration in the dynamic case. A Lagrange polynomial (ρ^*) is fit to three points, at the manipulator base $(\rho_{(0,t)} = [x_0, y_0, z_0] = [0, 0, 0])$, middle $(\rho_{(l_c/2,t)} = [x_{1(t)}, y_{1(t)}, z_{1(t)}])$ and at the tip $(\rho_{(l_c,t)} = [x_{2(t)}, y_{2(t)}, z_{2(t)}])$ of the form

$$\begin{aligned} \rho^* &= \sum_{j=0}^{2} \left(\Psi_{j(s)}.[\ x_{j(t)}\ ,\ y_{j(t)}\ ,\ z_{j(t)}\ ]^{\mathrm{T}}\right), \\ \Psi_{j(s)} &= C_\Psi.\prod_m \left(\frac{s - s_m}{s_j - s_m}\right),\ 0 \le m \le N,\ m \ne j. \end{aligned} \tag{3.60}$$

where $C_\Psi = \mathrm{diag}([s/s_j, 1, 1])$ is a modification coefficient guaranteeing the manipulator axis to be perpendicular at the base $(\hat{t}_0 = \hat{j})$, the points' position vector

($q = c_{(t)} = [x_{1(t)}, y_{1(t)}, z_{1(t)}, x_{2(t)}, y_{2(t)}, z_{2(t)}]$) is the constant coefficients in the static model or the time dependent coefficients as the system generalized state vector for the dynamic model, $\Psi_{j(s)}$ is the shape function and $W = [\Psi_{1(s)}, \Psi_{2(s)}]^{\mathrm{T}}$ is the weighting matrix for the Ritz-Galerkin method.

3.3.4 Toward Nonlinear Control and Observation

A unified vector form for the modeling, nonlinear control and observer design, based on feedback linearization method is derived. Defining the input pressure and external load vector as the system states and adding algebraic constraints for the desired controls to the system EOM, for Eq. (3.57) after the spatial integration, we have

$$\begin{bmatrix} M_q & -[C_p & C_{f_L} & C_{\tau_L}] \\ A_1 & & A_2 & \end{bmatrix} \begin{bmatrix} q_{,tt} \\ q_p \\ q_{f_L} \\ q_{\tau_L} \end{bmatrix} = \begin{bmatrix} -d_{m,q} - w_{\mathrm{c},q} + w_{\mathrm{b},q} - w_{\mu,q} \\ B \end{bmatrix}, \quad (3.61)$$

where A_1 and A_2 are matrices resulting from algebraic relations for the constraint or desired controls, B is the desired and/or input value vector, q_p, q_{f_L} and q_{τ_L} are the input pressure, external force and torque vector, introduced as system states. The coefficient matrix is $[3n_q + 9] \times [3n_q + 9]$, A_1 is a $9 \times 3n_q$ and A_2 is a 9×9 matrix and B is a 9×1 vector where n_q is the number of states. A and B are adjusted according to the required modeling, control and/or observation tasks and can be switched easily to achieve complex control strategies. Eq. (3.61) is numerically integrated w.r.t time by having the initial values for $[q,\ q_p,\ q_{f_{\mathrm{L}}},\ q_\tau]$. The control or observation values for $[q_p,\ q_{f_{\mathrm{L}}},\ q_{\tau_{\mathrm{L}}}]$ is found by two times numerical differentiation of the integration results w.r.t time, since they are already integrated twice alongside the system EOM.

For simple forward simulation we have $A_1 = \mathbf{0}, A_2 = I$ and $B = [p\ f_L\ \tau_L]^{\mathrm{T}}$, where I is the identity matrix. In the case of tip position control in the presence of

external loads, we have $A_1(3n_q+1, n_q) = 1, A_1(3n_q+2, 2n_q) = 1, A_1(3n_q+3, 3n_q) = 1, A_2(3n_q + 4 : end, 4 : 9) = I$ and $B = [(\rho_{\text{tip}_\text{h},tt} + \text{pid})\ f_L\ \tau_L]^{\text{T}}$, where $\rho_{\text{tip}_\text{h},tt}$ is the desired tip position and pid is a PID or any other feedback control term. Configuration control can be achieved by changing A_1 to control the position vector of any other intermediate point on the backbone.

Force control at the tip using the pressure inputs and for a known tip torque (τ_L) and position profile ($\rho_{\text{tip},tt}$) is possible by setting $A_1(3n_q+1, n_q) = 1, A_1(3n_q+2, 2n_q) = 1, A_1(3n_q+3, 3n_q) = 1, A_2(3n_q+4 : end, 4 : 9) = I$ for the tip vector position control and $B = [\rho_{\text{tip},tt}\ (f_{L_\text{h}} + \text{pid})\ \tau_L]^{\text{T}}$, where f_{L_h} is the desired force vector. For the tip torque control (τ_{L_h}), we have the same A matrix with $B = [\rho_{\text{tip},tt}\ f_(\tau_{L_\text{h}} + \text{pid})]^{\text{T}}$.

Simultaneous force and position control is possible by fast enough switching between different control scenarios or having a combination of non-overlapping force and position directions to derive a proper control matrix set for.

Shape-based force estimation is possible by proper adjustment of the matrices. For example, for the tip force estimation based on the tip position vector we have $A_1(3n_q+4, n_q) = 1, A_1(3n_q+5, 2n_q) = 1, A_1(3n_q+6, 3n_q) = 1, A_2(3n_q+1 : 3n_q+3, 1 : 3) = I, A_2(3n_q + 7 : 3n_q + 9, 7 : 9) = I$ and $B = [p\ (\rho_{\text{tip},tt} + \text{pid})\ \tau_L]^{\text{T}}$, in which the known tip geometry is assumed as geometrical constraint and the PID term is for numerical analysis error compensation, and not as a term for physical feedback control.

3.3.5 Experimental Results and Discussion

The experimental setup, scenarios and structural parameters for the experiments in this section are as in section 1.2. Note that a new higher value for the module of elasticity ($E = 205$ [KPa]) is identified due to considering highly elastic deformation in the axial direction ($\hat{t}$).

33 static points and 100 [s] dynamic motion recorded data of a module in planar

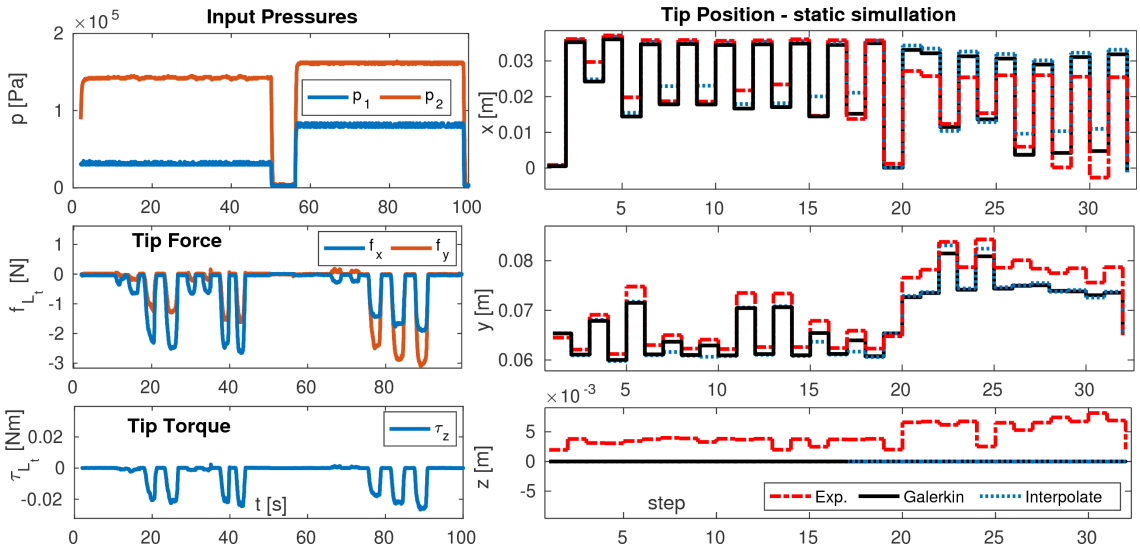

Figure 3.17: Results for planar deformation of a STIFF-FLOP module with extensive external load at the tip (EXP.2) in static case: (left) pressure inputs, external force and torque at the tip; (right) tip position time series in comparison to experimental results.

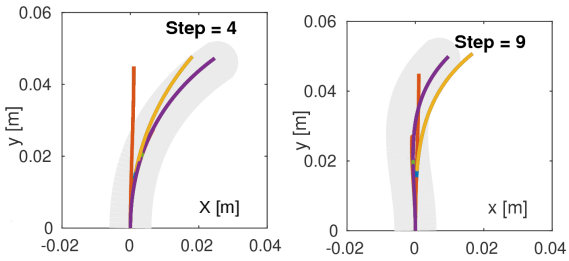

Figure 3.18: Single shooting method iterations for steps 4 and 9 to solve the BVP in the static case.

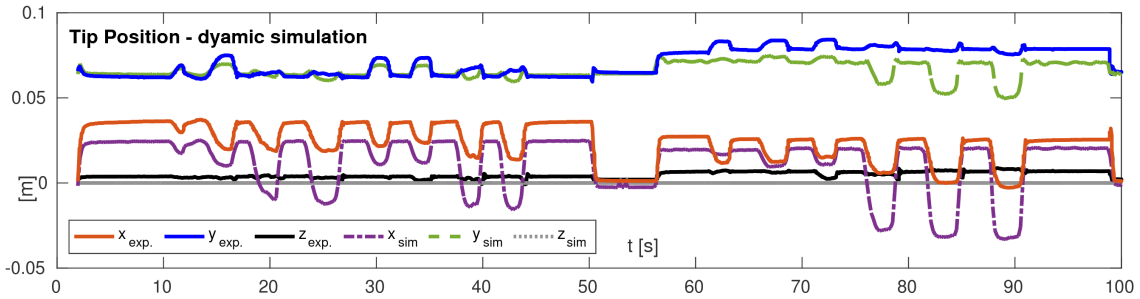

Figure 3.19: The tip position time series from simulation and experimental for planar deformation of a STIFF-FLOP module with extensive external load at the tip (EXP.2) in dynamic case with the same pressure inputs, external force and torque at the tip as in Fig. 3.17

motion with extensive external load (EXP.2) and 43 static points and 200 [s] dynamic motion recorded data of a multi-segment manipulator in general 3D motion with one active module (EXP.3-I) are used to verify the accuracy of our model.

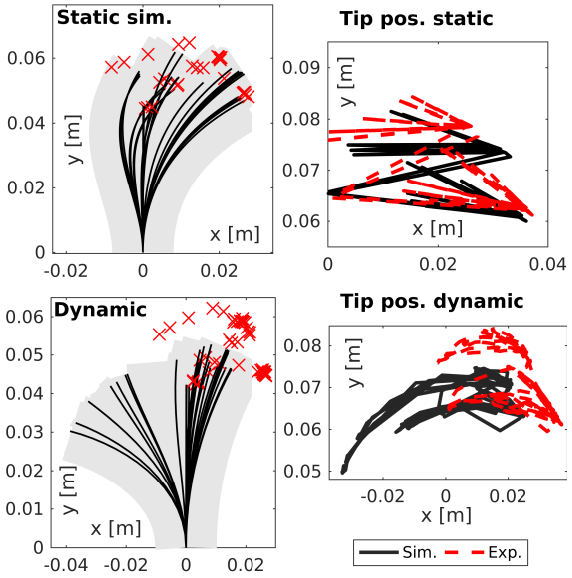

Figure 3.20: The tip position in task space for planar deformation of a STIFF-FLOP module with extensive external load at the tip (EXP.2) in (top) static and (bottom) dynamic case in comparison to experimental results.

Seven points from the static test are used to identify E and $\mu_{v|u}$. Error is defined as the distance between the tip position in the model and experiments divided by the initial length of the manipulator as a reference length [74]. High external load brings the manipulator to an "S" shape configuration in the planar motion case (Fig. 1.7). Iterations for the single shooting method to solve the BVP in the static case is presented in Fig. 3.18. Using a polynomial of order three, an average 6% (≈4 [mm]) mean error is observed for the static model in the 2D (Fig. 3.17) and 8% (≈6 [mm]) in the 3D (Fig. 3.21.b) motion using both the Ritz and Ritz-Galerkin method. For the Cosserat beam method, Our model shows to be at least twist faster and as accurate as a numerical interpolation solution with the same number of nodes [84]. Despite Tunay's conclusion, a Galerkin solution that works fine in the static case cannot easily be extended to a dynamic problem [99] and we found that the Ritz-Galerkin solution in the dynamic case is not stable and results in large errors, but the Ritz solution maintains a mean error of 20% (≈14 [mm]) in the 2D (Fig. 3.19) and 16% (≈12 [mm]) in the 3D (Fig. 3.21.c) case throughout the dynamic test. The mean accuracy of the Ritz and Ritz-Galerkin solutions are similar in the static case with no significant different in the simulation speed while the Ritz solution in

the dynamic case is more accurate than for the static case, 14% in the planar and 8% in the 3D motion. This difference is due to large inertial effect in the dynamic case which shows the need and importance of a more accurate damping model to be considered in our future work. The simulation results for the tip position in task space in comparison to experimental results are presented in Fig. 3.20 for EXP.2 and in Fig. 3.22 for EXP.3-I. The models are more accurate for lower input pressures. Inaccuracy in the fabrication of the STIFF-FLOP module causes that the experimental results show out of plane deformation in the z direction in the planar motion and twist in the general 3D motion, despite a symmetric actuation strategy and planar external force. This deformation is not captured in our model since any term to model the parameters' inaccuracy is not considered. Considering the effect of the manipulator axial highly elastic deformation on the segments shear and elasticity modulus results in a 6% increase in the model accuracy; however, a higher value for the elasticity modulus is identified compared to the resultss in previous section [85, 82, 84]. Our modeling results in the planar case shows to be the most accurate solution compared to CC (31% error), PVW using CC kinematics (28%), the Cosserat rod model (6-12%) and the approximate solutions similar to [92] (11%) in the static case and compared to the lumped system model (22% error) in the dynamic case [84]. The series-solution with two points (four states in a planar motion and six states in a general 3D motion) shows to be efficient and accurate enough to predict the "S" shape configuration of the manipulator under significant external loads. However, simulations for general 3D motion of a multi-segment manipulator with two active modules (Fig. 3.21.e) shows the different results from polynomial of order four and five (Fig. 3.23). These simulations are not verified with experimental results. This shows the importance of a proper choice for the polynomial order, especially where the manipulator needs to perform in the confined maze-like space of a minimally invasive surgery as the final goal of our research. Using Matlab software on a regular laptop computer, the direct single shooting algorithm usually takes about 2 [s] to find the equilibrium configuration for a single-curve formation

and 3 [s] for a double-curve formation ("S" shape) in the static case, and almost the same time as the actual experiment duration for the dynamic case. Compared to the presented established methods in the literature, our method has the highest static and a high dynamic modeling accuracy with exceptional real-time computational performance which shows the feasibility of real-time implementation of this approach in real-world applications. Our weak-from solution provides a powerful analytical means for sensitivity analysis of the model performance w.r.t. the system parameters for structural design optimization. We observed that a slight change in the module cross-section dimensions affect the accuracy by 2% similar to [82] while a change in the stiffness module, i.e. not considering the elasticity reduction due to axial highly elastic deformation, affect the accuracy by up to 6%. A detailed sensitivity analysis, as in [82], can be carried out in the future to predict how inaccuracy in the model parameters can affect the simulation results for a successful control system design. This model is derived from a framework with coaxial homogeneity in the manipulator cross-section and any other anomaly due to fabrication, aging and fatigue with a stochastic nature will be compensated with a feedback control term. These affects can be addressed using statistical approach and by incorporating stochastic terms in the future control model. A precise forward model contributes in increasing the stability, reducing the controller gains, better estimation of the system states and compensation of measurement noises. After using the absolute error for the verification and comparison of our model in the first step, the performance of our model (Eq. 3.61) should be investigated for force estimation and control with application in soft tissue palpation and stiffness imaging. A continuum manipulator with 5-15 [gram-force] and 6-43% estimation error, achievable with STIFF-FLOP modules [60], is shown to be successful in such tasks [122]. The controller repeatability and durability are important for such tasks which can be address in a future work.

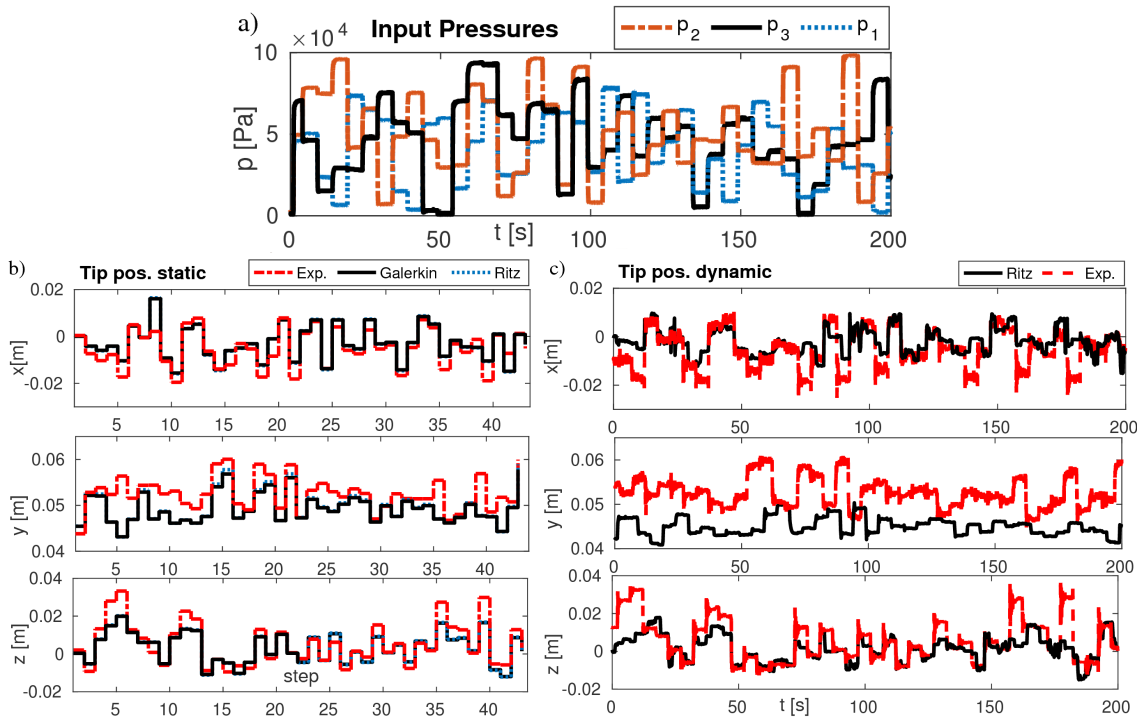

Figure 3.21: Results for general 3D deformation of a multi-segment manipulator in static and dynamic case: (a) pressure inputs and tip position time series in (b) static and (c) dynamic cases for the manipulator with one actuated module as in EXP.3-I.

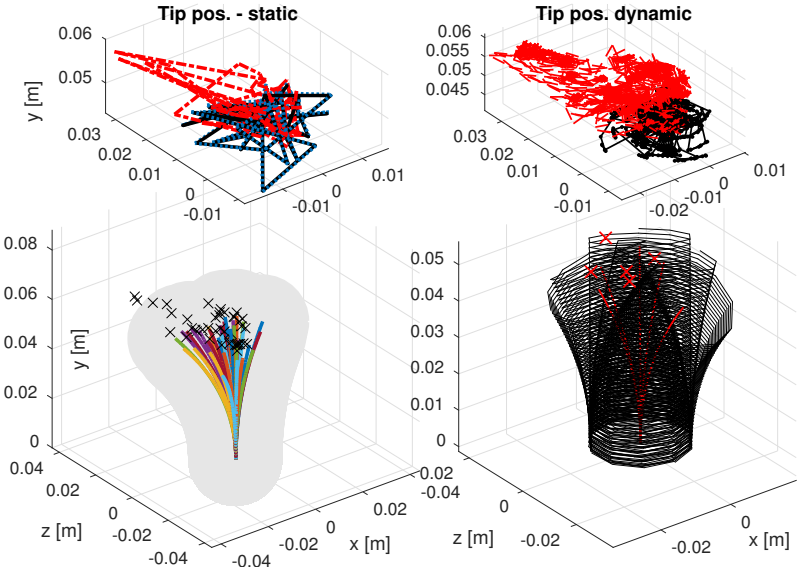

Figure 3.22: Tip position in the task space and simulation frames for general 3D motion of a multi-segment manipulator with one active module in (EXP.3-I) in (left) static and (right) dynamic cases.

3.4 Conclusion

In this chapter, supported by experimental validation using the real characteristics of a STIFF-FLOP module base, we present a new geometry deformation ap-

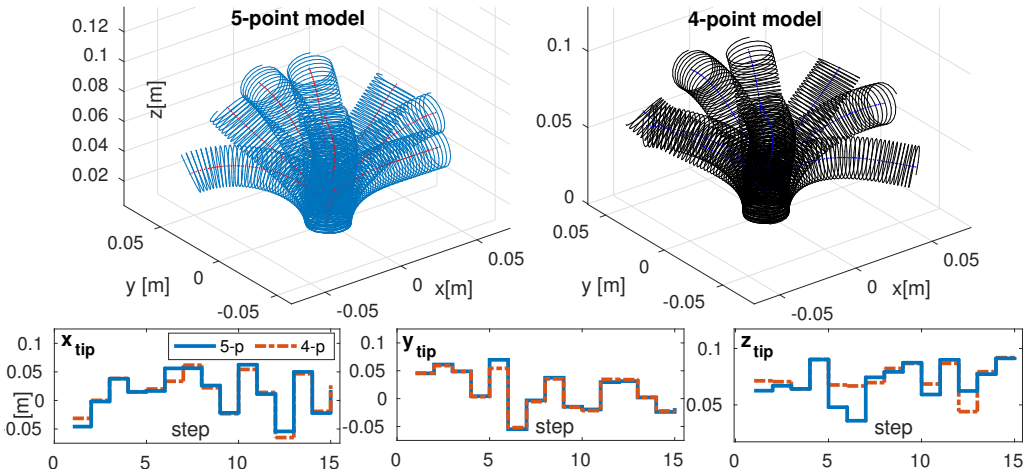

Figure 3.23: Tip position time series and simulation frames for a multi-segment manipulator with two active modules in general 3D motion (EXP.3-IIs) in static case with a modified Lagrange polynomial of order (top left) four (4-p) and (top right) five (5-p). (bottom) The tip position results of the two modeling assumptions.

proach for comprehensive analytical modeling of compound continuum manipulators with braided extensile actuators under high external loading. For the first time, elongation-bending deformation of a braided extensile pneumatic chamber is modeled for both the stiff (exact helix model) and bendable (constant γ assumption) threads and the effects of simplifying assumptions on the results are investigated. Subsequently, two novel yet simple analytical solutions are derived for the prediction of the cross-section deformation in constant curvature elongation-bending of a continuum media. The effects of different structural and curvature parameters on the predictions of the models are investigated. We show that the energy action values are more sensitive to the axial stretch of the backbone than the curvature of the bending curve, and the model benefits from an accurate backbone model more than the accuracy of prediction of the cross-section deformation. We also show that consideration of the cross-section deformation increases the modeling accuracy significantly for constant (up to 13%) and variable curvature (up to 7%) kinematics using the principle of virtual work and Cosserat rod theory. We show the combination of the general bending model based on the geometry deformation approach and the constant γ model for the helix gives the best set of simulation results which is in agreement with our predictions, suggesting the importance of considering the cross-section deformation in the modeling accuracy. The sensitivity of the models'

prediction to changes in γ and E, as the two important structural parameters in the design of stiffness controllable continuum modules with braided actuators, is investigated analytically, showing that our models can be used for comprehensive exact modeling and design optimization of manipulators with compound structures especially for the minimal invasive applications where the task space is limited and for the manipulators with regional tuneable stiffness cross-sections. Our results provide a comprehensive insight in choosing proper modeling assumptions and complexity to observe certain behaviors and achieve the desired accuracy.

Then, a modified Lagrange polynomial series-solution, based on experimental observation, was presented to produce a new technique for deriving the Cosserat rod static and Lagrangian dynamic model of a continuum manipulator. Our approach featured a small number of states (six in our analysis) which are the Cartesian positions of two points on the manipulator (at the tip and in the middle). We used a direct single shooting method to solve the Cosserat rod static model and forward numerical integration for the Lagrange dynamic model using the Ritz and Ritz-Galerkin approaches. A unified vector form for the manipulator Lagrange dynamics was derived using which the modeling, control and observation scenarios can be easily implemented by adjusting three control matrices and a vector for the desired and input values. Noting the importance of considering highly-elastic axial deformations of the manipulator, the Ritz method is found to be more accurate in dynamic cases while the Ritz-Galerkin method is slightly more accurate in static cases. The final model is compared with five other well-known models and shown to be the most accurate and efficient approach with the smallest possible number of states, suitable for real-time static and dynamic modeling and controller design. This method can be used to control an integrable stiffness tunable interface for continuum manipulator with application in medical robotics.

Our proposed approaches close the gap significantly between theoretical analysis and real-world application of continuum manipulators in general applications. However, the achieved improvements in the cross-section modeling accuracy and computation

performance are still very sensitive to the modeling assumptions and need to be verified with a higher fidelity model, e.g. finite element model, before being used for manipulator optimization design. It is better to avoid a detailed cross-section model for real-time and precise control tasks. That is why we continued with the simplest model, that considers the cross-section deformation, to calculate the real stress-strain values in our former model for the manipulator backbone. The presented shape-function based backbone model is shown to be accurate and robust enough for real-world applications; however, its stability and performance in 3D general deformation of long manipulators with many segments are not thoroughly inspected. The material visco-elastic behavior and the control saturation and delay are needed to be investigated before putting our inverse nonlinear control structure in use in the real engineering scenarios. Besides, from an analytical point of view, a proof for the convergence of the proposed series solution with polynomial terms is needed and should be investigated before making more general claims about this approach.

Most of these complexities are addressed in nature with an intelligent morphological design and smart structures with controllable stiffness. In the next chapter, we look into the jamming properties of a real fish skin scales to design and later exploit the morphological computation power of a bio-inspired integrable helical interface for stiffness control of continuum manipulators.

Chapter 4

Stiffening Continuum Manipulators: A Low Hysteresis Scale Jamming Interface

Abstract

Inspired by teleost fish scale , this chapter investigates the possibility of implementing stiffness control as a new source of robots dexterity and flexibility control. Guessing about the possibility of biological scale jamming in real fish, as the first objective of this chapter, we try to understand the possible underlying jamming mechanism of such a behavior in a real fish. We conduct experiments on a real fish skin, encapsulated in a thin latex layer, in the unjammed and vacuum jammed cases for compression, bending and bulking scenarios. This shows a biological scale jamming, with very small hysteresis, reduction in the damping and increase in the elasticity of the jammed skin, due to the unique scale morphology and jamming pattern. Inspiring by this unique morphology and helical arrangement of the fish scales, a novel idea of geometrical scale jamming is presented to control the stiffness of a continuum manipulator, as the second objective in this chapter, by controlling the Coulomb friction force, modeled by LuGre friction model, between curved rigid

scales that are arranged as an integrable helical interface. Jagged contact surfaces replicates the biological scale morphology and jamming pattern to achieve the same low hysteresis behavior. First, a low stiffness spring is used as the backbone for a set of round curved scales to maintain an initial helix formation while two thin fishing steel wires are used to control the friction force by exerting tension. The challenges with a long design and local stiffness regulation are addressed through removing the backbone, addition of bearing to minimize the tendon-pathway friction and use of shape memory alloys (SMA) for more uniform and locally controllable actuation. The interface is integrated on a pneumatic continuum actuator module and the effectiveness of the designs are shown for uniaxial elongation and bending deformation tests through mathematical modeling and experiments and the results are compared with similar research. To evaluate our objectives in this chapter, the manipulator tip bending stiffness controllability and range, as the two commonly used factors for evaluating a continuum device performance in medical applications, is compared with the requirements of minimally invasive surgeries and catheter medical devices. We showed the importance of tendon-pathway friction and the advantages of using SMA actuators on the uniform actuation and the local stiffness regulation. The specific design of contact surfaces enables full lubrication of these surfaces for reduced hysteresis and wear while it benefits from the tunable stiffness through jamming.

4.1 Introduction on Bio-inspired Scale Jamming

Fabrication of variable stiffness material [111] and variable stiffness soft manipulators, mostly inspired by octopus arms [28], as well as wearable robots have been widely investigated recently. They have numerous applications specially in soft surgeries where their deformable structure is beneficial to improve manoeuvrability, control and sensing [123], with less invasive interactions with organs [34, 110, 35].

4.1.1 Stiffening Through Jamming

Similar to Turgor Pressure, where the plasma membrane is pushed against the cell wall due to water pressure in a plant cell, [124, 125], the idea of jamming has been used to design variable stiffness endoscope for medical applications through increasing the friction in-between rigid segments [126, 57, 127, 128, 129, 130, 131, 132, 133, 134, 135], granular media [34, 136, 137, 138, 139, 40, 26, 140, 141], layers [33, 142, 61, 143, 144] and wires [58, 145], on which a through review is recently presented by L. Blanc, et. al. [21]. Granular jamming, being investigated more widely in the recent years due to their flexibility and easy implementation on different design, has been utilized in design of flexible manipulators [34, 110, 26] and also variable stiffness joints [34, 35]. As an instance, Cheng and co-workers [34] have obtained a wider stiffness range than Jiang and co-workers [110] through granular jamming for a soft manipulator.

Most segment locking designs are driven by tendons and the vacuum or internal pressure are used mainly for other types of jamming. J. Santiago and co-workers [146] presented a new scale layer jamming design with a wire driven actuation method without any pneumatic actuation. A tendon driven jamming is more suitable for micro-scale fabrication and have new applications such as in-space exploration where pressurization is not possible. However, the routing and tendon-structure friction are the problems with this type of actuation [130]. Granular jamming apparatus is

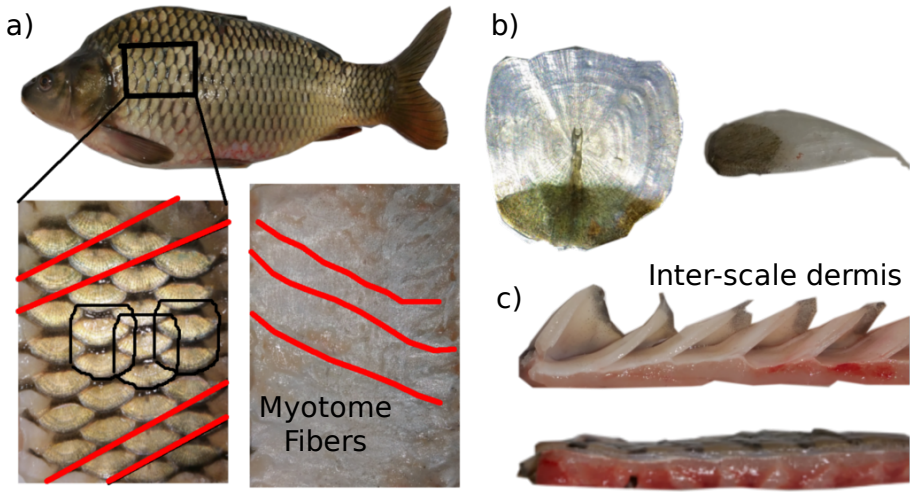

Figure 4.1: (a) Skin sample surgery location on a Cyprinus carpio fish, helical myotome attachment sites and overlapping scales in relaxed state, (b) top and side view of a real scale used in the experiments, structural fibers are visible as in [148], (c) side view of the experimental sample skin without scales, open space after removal of the scales and the intermediate skin preventing direct contacts of the scales.

bulky and not appropriate for wearable applications. Layer jamming, which recalls the bird feathers, has the problem of design, fabrication and modeling, despite being the only suitable choice for an integrable and wearable interface. Their bulky design and low deformability, due to their multilayer structure, necessary for the jammed layer to resist buckling, and the long flap length, required to achieve large deformations, are the problems with this type of jamming design [147, 61]. It is hard to implement local stiffness control with most of jamming designs. The hysteresis loss is also inevitable in this kind of stiffening. In this chapter, we investigate how a stiffness controllable interface can be designed by taking inspiration from natural scales of the teleost fish. An interface has the advantages of easy integration on different designs with minimum added complexities due to separate design and actuation path, enough space inside to accommodate the actuators and other necessary tools and possibility of directional stiffness control by inhomogeneous modulation of the stiffness along the manipulator circumference.

4.1.2 Biological Scale

As a biological instance for wearable stiffness controllable interfaces, animals' skins and scales in nature show stiffness regulation in response to irritation or penetrating forces. Many animal species such as fish, turtles, armadillos and snakes have hard scale or osteoderms as flexible armor and a means of friction regulation in contact with the environment [29]. It is necessary to distinguish the scales protection role, by understanding their structure, to be able to investigate their possible stiffening effects. Mechanical properties of scale as a biological composite material is optimized toward its specific tasks providing unique natural features such as unusual stiffness, toughness and strength [149, 150]. The scales contain a bony mineralized tissue reinforced with an underlying collagen fiber matrix and covered with a six times stiffer thin layer as hardening material for the outer surface and provide an effective fracture mechanism for protection against predators [151, 29, 152, 153] (Fig. 4.1). It complies with the engineered composite material observations where a reinforced structure presents higher toughness if covered with a hardened thin surface [149]. The scale structure consists of multiple distinct composite layers with their unique deformation mechanics [152]. The fracture begins with sudden cracks in the outer harder layer but the softer underlying layer, which is 1000 times less stiff than the scales in the case of collagens of a fish skin, prevents the cracked sides to bend inward resulting in a more stable fracture process with a %50 higher penetration resisting force [29]. A key observation made by Chintapalli, showed that hard finite composite scales of hexagonal shape embedded in a 1000 times softer subtract (similar to the biological case of scales and tissue system), provides 70% higher penetration resistance compared to a continuous plate of the same materials and thicknesses. This increase in the penetration resistance is because of the reduced span of the continuous media, that allows the scales to move relatively to adjust to the stress concentration, resulting in flexural stress decrease and fracture delay [154]. The scale properties such as angular and overlapping arrangement, aspect ratio, material properties, curved extruded geometry, tip overlapping and volume fraction of

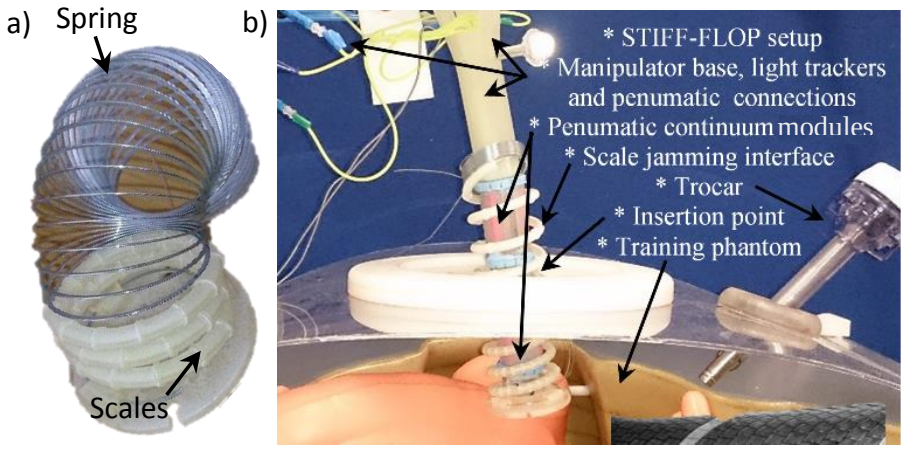

Figure 4.2: (a) Curved scales on a low stiffness spring backbone, inspired by helical arrangement of interlocking scales in real fish, as stiffness controllable integrable interface for a continuum manipulator, (b) sample application of a scale jamming interface on a STIFF-FLOP continuum manipulator.

the scaled area affect its deformation and are important protection characteristic parameters [155, 156].

Chemical compound of fish scales, especially the surface material, have been investigated to better understand the scales' different directional friction coefficient in snakes [157] and the turbulent-flow regime drag reduction effects due to riblet overlapping structure in fish, i.e. shark [158]. Fish scale properties differ cosiderably from one point to another on the animal body and are very sensitive to the hydration level. The dried scales have almost the same stiffness and flexibility which means the natural softer scales in the hydrated state, i.e. the tail scales, are affected more by the moisture loss [159]. While in the hydrate state, the elastic modulus and strength of the head scales are twice as those properties for the tail, these values are almost equal for the fully dehydrated state [160].

4.1.3 Toward an Integrable Scale Jamming Interface

Wall [33] and zuo [143] have investigated scale-like jamming recently. In [33], the rigid scales, implemented on a soft silicon base, are packed together in an inclined orientation which minimizes their resistance since part of the external pressure works

in favor of the tension. Besides, multiple overlapping layers are needed to achieve high enough stiffness due to the soft silicon base. In [143], rigid scales, with jagged contact surfaces for increased friction, are integrated as an external layer on a hard backbone which makes it the most similar design to our work. Similar to layer jamming [147, 61], both of these designs suffer from large hysteresis and low deformation range due to the bulky volume of the overlapping scales and short size of the straps.

In this research, a new simpler design is presented by taking inspiration from the role and special helical arrangement of scales in flexural stiffness of real fish and snake skin [148] (Fig. 4.2). First, we choose Cyprinus carpio scales, as a good example of the most common type of teleost scales in modern fish species [29, 153], to conduct experiments on the jamming characteristics of real fish scales (Fig. 4.1). Then, a novel stiffening design is introduced in which 3D printed curved scales with jagged contact surfaces are placed in a helical formation. The stiffness of the interface is controlled by scale jamming that resists the torsion shear force of the helical structure. The inclination of the jagged surfaces is chosen to be smaller than the contacting material coefficient of friction that mimics the functionality of biological scale special geometry. The ultimate goal is to design a wearable interface (exoskeleton), consisting of rigid interlocking (jamming) elements (scales), for easy integration on different continuum manipulators. Here, the interface is designed and tested based on a continuum manipulator consisting of some STIFF-FLOP modules as our basis. While the design performance is important, our main goal is to test and identify the potentials and limitations of such bio-inspired design, and to provide insights and suggestions for a successful final product in the future.

As a result, for the first time in a jamming design, a very low hysteresis is achieved even for the case of plastic deformations. Placing the scales in a helix formation guarantees their face-to-face contact even in large deformations despite their small size and an easy to integrate low volume design. For the first time in jamming research, the stiffness of the structure is controlled through modulation of the resisting shear torque acting on the helix cross-section, and not through the resisting shear

force that withstands the normal stress due to the manipulator bending. Three actuation designs are presented as follows.

1. Tendon driven jamming through radial force.
2. Tendon driven jamming through tangential force.
3. Shape memory alloy (SMA) actuated design.

A detailed explanation of the designs are presented in section 4.3. To our best knowledge, a design featuring these ideas was not previously investigated for stiffening purposes in robotics. To model the scaled helical spring, the theoretical background already existing for the helical springs under eccentric loading [12,13] is used base on variable curvature kinematics for a constant lead angle ($\gamma \approx$ cte.) helix, LuGre friction model for a smooth transition between static and dynamic friction models [161] and Principle of Virtual Work. A single STIFF-FLOP continuum actuator is used to verify the stiffening property and shape locking of the scales in bending. A sample scale interface and its integration on a STIFF-FLOP multi-segment manipulator are presented in Fig. 4.2.

In this chapter, first, a series of experiments on a real fish skin sample is carried out in section 4.2. Different bio-inspired designs for the scale jamming interface are explained in section 4.3. A new two-step mathematical model is proposed in section 4.4, where the stiffness tensor for the elements along the manipulator backbone are found using the Principle of Virtual Work (PVW) for the rounds of scales in each element, followed by the jamming model for the jagged contact surfaces. The experimental results are discussed in section 4.5 where our model is verified for the simple elongation and bending tests of the tendon driven design with a low stiffness spring backbone (case 1). The shape locking and increase in the bending stiffness of a STIFF-FLOP module, challenges with long continuum manipulator designs and integration on cylinders with different radius are investigated as well. Finally, the advantageous and shortcomings of the proposed designs are addressed in comparison

with similar recent research in section 4.6, followed by a conclusion on this chapter in section 4.7.

4.2 Biological Scale Morphology and Jamming

We choose Cyprinus carpio scales in our experiments which is a teleost scale commonly used in similar research [29] (Fig. 4.1). Theoretically, the stiffness of a biological tissue with scales should change from the low stiffness of the underlying soft tissue (almost negligible) in the unjammed state to the rigidity of the scales ($E \approx 850$ [MPa], $\sigma_{\text{yield}} \approx 30$ [MPa] [29]) in the fully jammed state. However, the maximum value of the stiffness is determined by the inter-scale coefficient of friction which is very low because of the intermediate skin that prevents the direct contact of the scales (Fig. 4.1.c).

A 62.55×50.14 [mm] ($width \times length$) sample of the skin with 4 by 7 arrangement of the scales is cut and sealed in a low stiffness latex glove (Fig. 4.4.a). The scales have an average size of 21 × 19.5 [mm] and the overall sample thickness (including the latex glove layers) is 1.06 [mm] with three ovelaping scales. The sample is placed in a force measurement setup with an ATI Nano-17 force sensor (Fig. 4.3.a,b). Three cycles of test with stroke of 10 [mm] are carried out in quasi-static condition. Experimental data are collected at 0.01 [s] intervals and smoothened using Matlab software 'smooth' function based on a moving average filter with the step of 15. The sample is tested for uniaxial compression (Fig. 4.3.b), simple pure bending (Fig. 4.3.c) and bulking (Fig. 4.3.d) each in two rounds, one with a large more realistic bending curvature (Fig. 4.4) and one with a smaller (Fig. 4.5) bending curvature. Scales are placed on the bent inward direction and the reported results are the change in the blocking force, stress at the sample root and equivalent modulus of elasticity in the jammed (vacuumed) and unjammed states. Scales do not jam if placed on the outer side of the bent as seen in the bulking test results (Fig. 4.4).

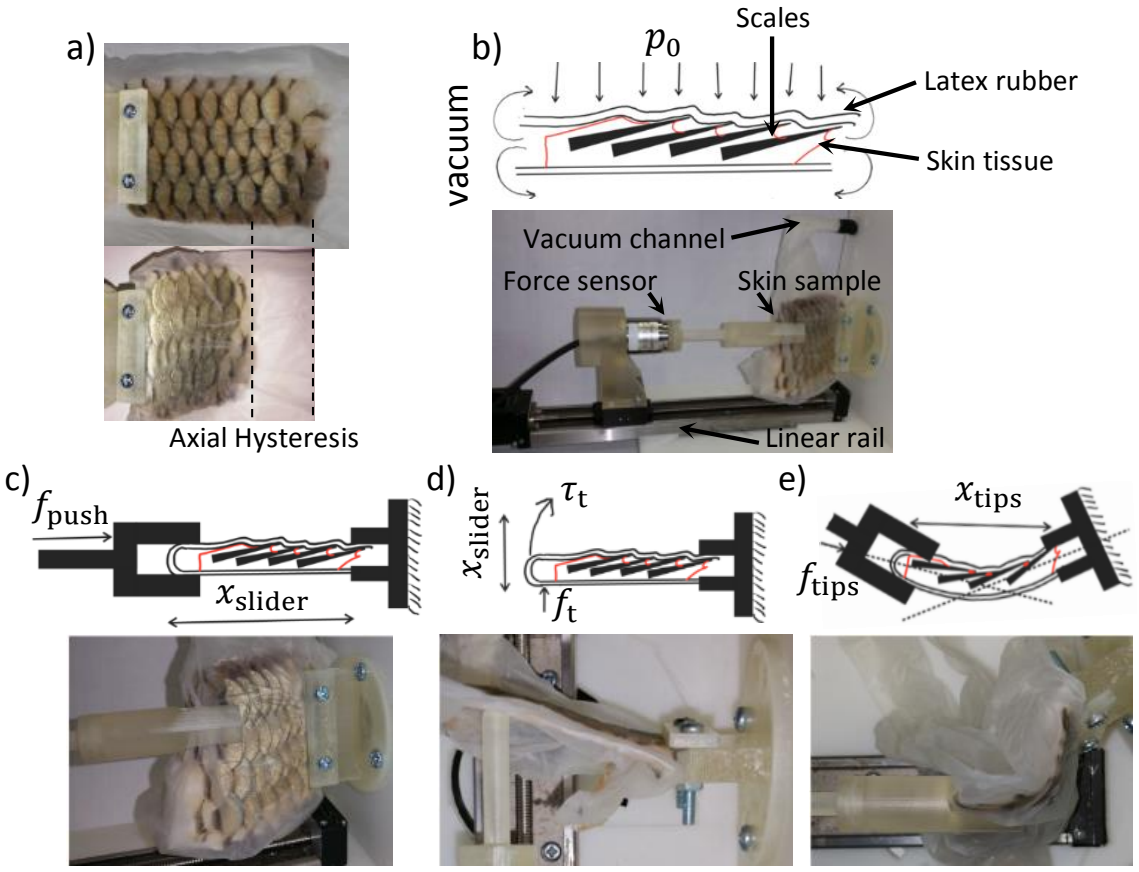

Figure 4.3: (a) The experimental sample of the fish skin enclosed in latex rubber layer before and after uniaxial compression tests, (b) schematic of inclined stacked arrangement of the scales and real test setup, (c) axial compression test schematic and test setup, (d) bending test schematic and test setup, (e) bulking test schematic and test setup.

The results of the first test cycle, which we call the warm-up cycle, are noticably different from the next cycles and hence, are neglected. The latex glove contribution in the jamming due to capillary forces is neglected too. The elasticity modulus is found based on a simple Euler-Bernoulli beam model.

The test results are presented in Fig. 4.4. The scales in the axial compression test are jammed with a noticeable 80% increase in the resisting force which reaches up to 2 [N] for a 10 [mm] stroke, only after a large low friction sliding deformation (strain$\approx$ 0.4) and by getting to the physical limitation of their underlying tissue. At this point, the inclined colagen fibers become nearly perpendicular to the compression direction and five scales are overlapped. The dermis and myotoms fiber helical arrangement helps preserving a small stiffness over a large uniaxial deformation,

providing large deformability with small stiffness change. This usually damages the tissue irreversibly as shown in Fig. 4.4.a. The jammed media stiffness is decreased in the first 4 [mm] displacement as a result of perfect alignment of the jammed scales with a very small friction coefficient. In this region, the scales slide in parallel rather than stacking in an inclined formation. The stiffness is increased quadraticly afterwards. The jamming starts and amplifies as soon as the scales ramp up and constitute an inclined stacking formation. The skin dermis natural limit and the hysteresis value, observed here, are anticipated to be proportional to the sample length due to the repetitive structure of the tissue and the scales' number. However, it will be harder to achieve perfect axial deformation in a long sample as the thin tissue tends to bulk (bend out of deformation plane).

The jamming is not noticeable in the simple bending test, where the bending neutral axis is aligned with the skin and, similar to the simple compression test, only the atmospheric pressure is pushing the scales together. The most realistic deformation is the bulking test since the natural scales are attached with an offset from the fish vertebrae as the neutral axis of body curvature is bending and undergoes longitudinal as well as bending deformations.

The longitudinal deformation amplifies the jamming by pushing the scales against the inclined stacking formation of the jamming state. The scale jamming limits the skin curvature as well as preventing penetration by stacking together. Similar to the compression test, an 80% increase in the stiffness is observed in this case but with a smaller ≈ 0.65 [N] resisting force and in a reversible manner with lower hysteresis due to the smaller deformation (5 [mm] stroke). Bulking test for a longer 10 [mm] stroke (100 $[1/m]$ curvature) and different vacuum pressure (Fig. 4.5) shows a smaller 18% increase in the resisting force due to jamming with 1.55 [N] maximum resisting force and 1.1 [MPa] maximum root stress value. This shows that for a larger curvature value, the stacking formation is more important than the vacuum pressure on the maximum resisting force value. The maximum stress in this case is about 3.6% of the scale structural yield stress (≈ 30 [MPa] [29]) showing

that the inter-scale friction coefficient determines the jamming yield stress. The small inter-scale friction reduces the hysteresis, but results in immediate sliding of the scales where only the dynamic friction coefficient is important. A linear stiffness is observed w.r.t. curvature and vacuum pressure. Comparing the results from the compression and bulking tests suggests that the stiffness increase in the bulking is mainly due to the inclined stacking formation of the scales.

It seems that the scales are designed for not jamming together, because a multi-layer armor with small inter-layer friction, 1000 times less than the scale stiffness, results in a 50% increase in the protection against penetration [29]. However, a linear low hysteresis jamming behavior with good reversibility is observed which results in 18-80% increase in the stiffness mainly due to the inclined stacking formation of the jammed scales. The linear reversible jamming, due to low friction coefficient and inclined staking formation, and the helical formation, that preserves the stiffness in a large deformation, can inspire a design for jamming media surface and arrangement to achieve the same linear reversible performance for a large deformation range. These are beneficial for the design of an integrable interface for continuum manipulators. However, this is not clear if the jamming actually happens for a real fish, and if so, what causes it. As a guess, the fish may use the myotome attachment fibers (similar to our tendon driven design) and the inter-layer dermis for active jamming and external hydrostatic pressure due to swimming depth or turbulent flow hydro-dynamic pressure as means of passive jamming.

4.3 Bio-Inspired Scale Arrangement and Design

In this chapter, we propose a scale jamming interface, for axial and bending stiffness control of a continuum backbone, by controlling the torsional stiffness of a helical interface cross-section through inter-locking (jamming) of a finite number of contacting rigid elements (scales). The interface is consisting of a high number of

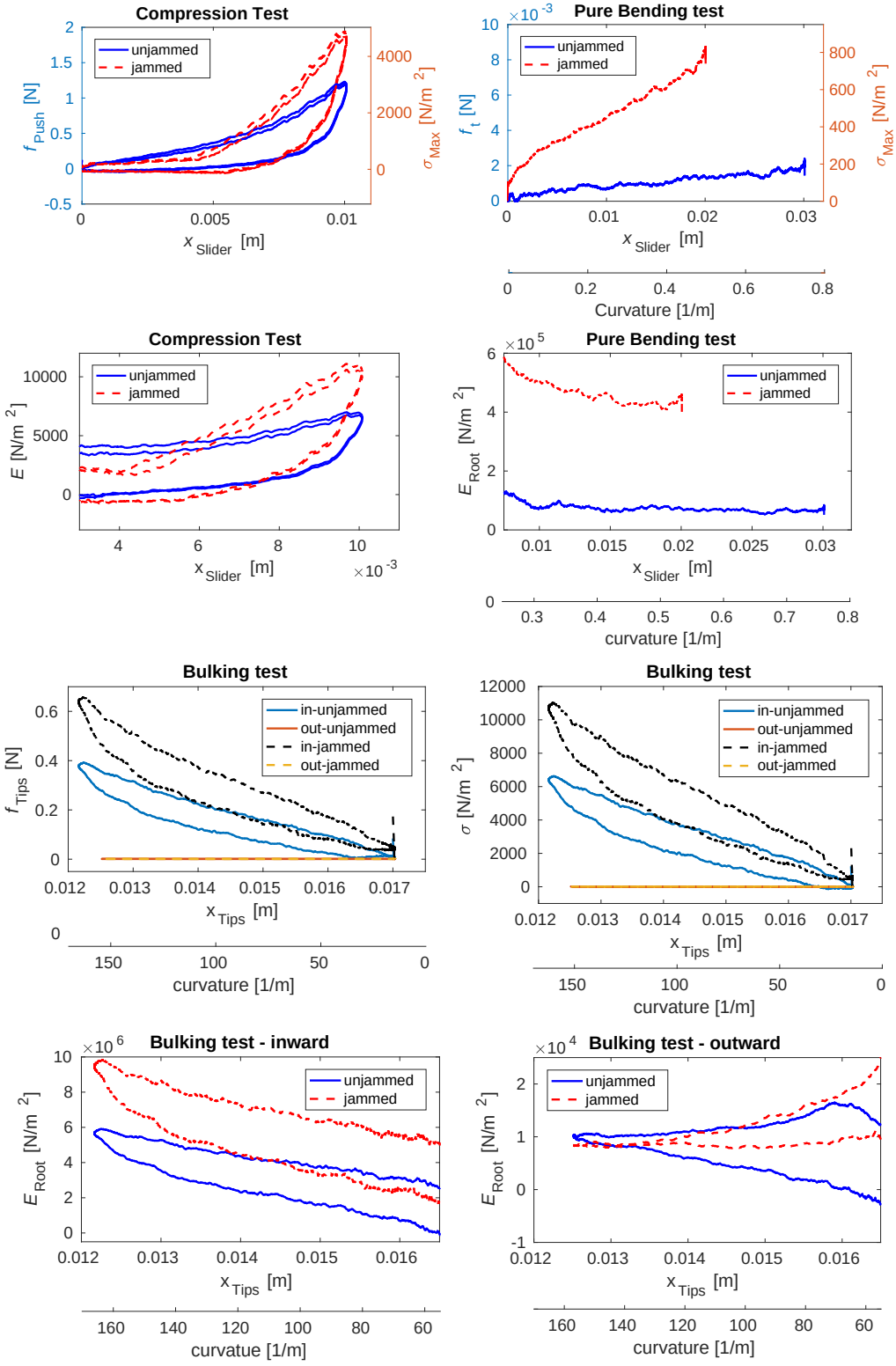

Figure 4.4: The experimental results of vacuum jamming for a real fish skin sample: deforming force (f), maximum stress (σ_{Max})and equivalent Euler-Bernoulli beam Young modulus (E) vs. linear deformation (x) and bending curvature for compression, simple bending and bulking tests. Tests are carried out twice with the scales on the inward side of the bend and once, on the outward side of the bend.

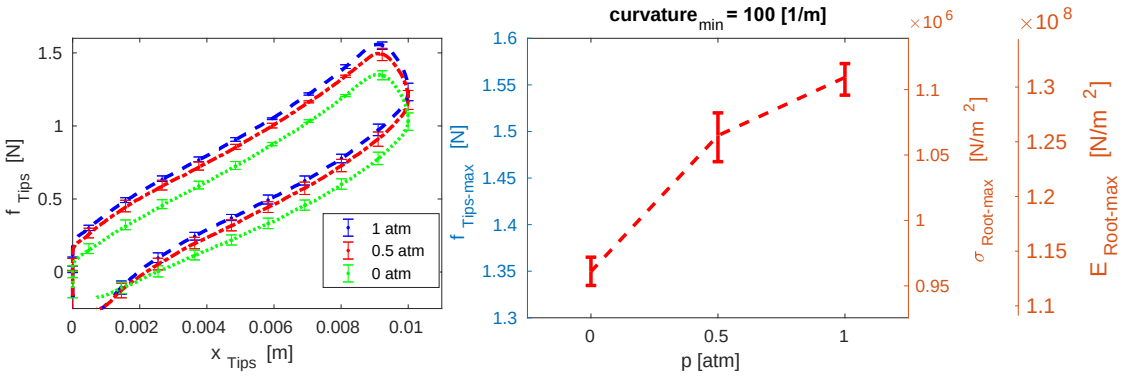

Figure 4.5: Results for bulking test (Fig. 4.3.e) with large deformation and different vacuum pressure, resisting force (f_{Tips}) vs. curve hypotenuse deformation (x_{Tips}); maximum force between the bulking tips (f_{Tips}), stress ($\sigma_{\text{Root}-\text{max}}$) and Euler-Bernoulli equivalent beam elasticity modulus ($E_{\text{Root}-\text{max}}$) vs. vacuum pressure.

articulated joints aligned with the helix cross-section (cross-section of the helical thread, Fig. 4.6). The helical interface provides large axial and bending deformations and regional and directional stiffness controllability by having multiple points of stiffness adjustment on each ring of the helix.

The inclined stacking geometry of jammed biological scales is exploited to introduce a geometrical jamming design. Tendons are used to jam the jagged surfaces of two scales with carefully selected slope angle that replicates the stacking of the biological scales in jamming. The contact surfaces push together and move apart by sliding up the slopes as a result of any relative rotation of the helical cross-section. This results in an increase in the jamming friction and wire tension. The tendon initial tension controls the stiffness by regulating the normal force acting on the surfaces and adjusting the pre-tension of the wire that undergoes a further tension due to the relative upward movement of the scales as in Fig. 4.6.c,f. In contrary to the conventional friction based jamming, our design benefits from reversiblity, higher stiffness range, low hysteresis and small surface wear. In a geometrical jamming, contact surfaces can be lubricated for better reversibility and smooth operation with the same stiffening properties.

It should be noted that biomimicry is not the objective of this study. Rather, we aim to test the hypothesis that contact friction/locking control using scales is a

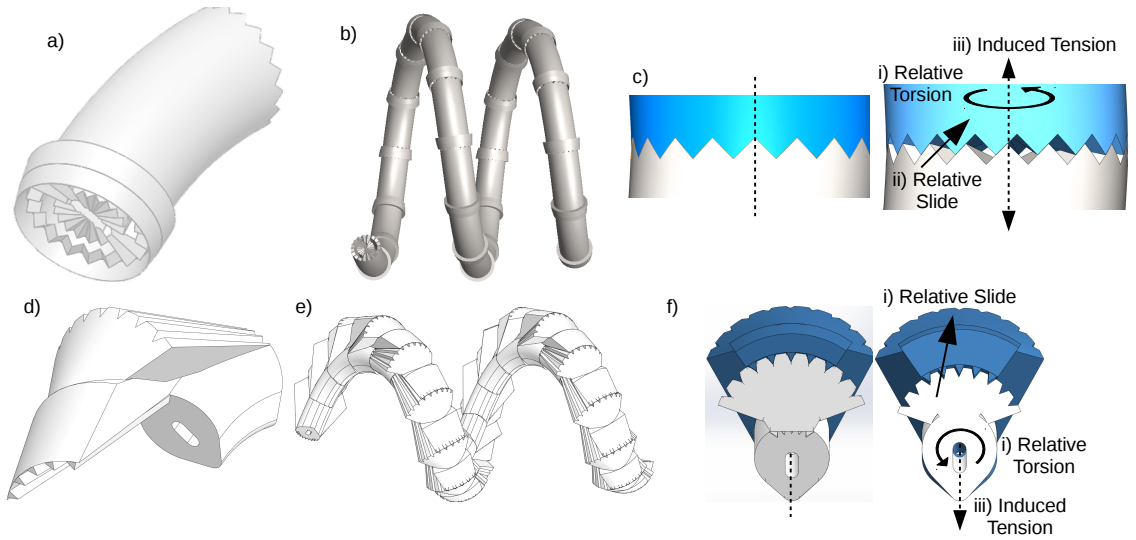

Figure 4.6: (a-c) Bio-inspired inter-locking scale designs with tangential and (d-f) radial jamming force, (a,d) scale design with two jagged contacting surfaces on both ends and a central hole for passing the actuation tendon and a low stiffness spring backbone if needed, (b,e) helical arrangement of the scales while the tendon is passed through their central hole pathway and (c,f) jagged contact surfaces inspired by inclined stacking formation of natural scales. Relative axial (for the scales with tangential jamming force) and radial (for the scale with radial jamming force) movement and increasing tension in the wire due to relative slip of jagged surfaces between two scales (white and blue) in c & d. The jagged surface in the design with tangential force has 16 teeth with 0.5 [mm] height and 35 [deg] slope on a flat surface. The jagged surface in the design with radial force has 9 teeth with 1 [mm] height and 72 [deg] slope on a 40 [deg] cone-shape surface in d-f. While a low stiffness spring backbone is not necessary for a design with tangential jamming force, it is necessary for a design with radial jamming force to withstand the tendon radial force.

viable method for stiffness control of exoskeletons for soft robots. However, such design may be useful to uncover or test hypotheses about the operation of biological structures [162, 68, 69]. Three scale designs are presented.

1. A scale like design where the reduced length of the wire due to the tension results in a radial force that pushes the scales together (Fig. 4.6.d).

2. A helical scale with smaller circular contact surface, with no need for a low stiffness spring backbone, where the tangential force resulting form tensioning the wire pushes the surfaces together (Fig. 4.6.a).

3. A similar helical scale but with an actuation mechanism based on SMA.

The helix cross-section and the jagged surface should withstand the torsional force for preserving the shape of a STIFF-FLOP module, a uniform moment of $p_{\max}\pi r_{\mathrm{p1}}^2 r_{\mathrm{o}} = 26.5$ [Nmm] and axial force of $3p_{\max}\pi r_{\mathrm{p1}}^2 = 8.8$ [N] due to actuation of the three pneumatic chamber with $p_{\max} = 1.5$ [bar] pressure. The helix cross-section minimum area is set to be $a_{\mathrm{j}} = \pi(r_{\mathrm{j2}}^2 - r_{\mathrm{j1}}) = 20$ [mm^2] (a tube with inner radius of $r_{\mathrm{j1}} = 1.1$ [mm] and outer radius of $r_{\mathrm{j2}} = 2.75$ [mm])) which provides a factor of safety of $2(0.0265 + r_{\mathrm{o}} \times 8.8)/(a_{\mathrm{j}}\sigma_{\mathrm{yield}}(r_{\mathrm{j1}} + r_{\mathrm{j2}})) = 23$ for the Acrylic plastic with yield stress of $\sigma_{\mathrm{yield}} = 33$ [MPa]. This area provides the necessary space for the jagged surface and the necessary high stiffness interface while jammed.

The jagged surface should provide a non-self-locking contact that is jammed by controlling the contact surfaces' normal forces and slides freely when is not jammed, withstand the locking force and provide necessary angular resolution for general configuration locking with having as small and as many as possible teeth. In theory, a helical interface, with thread cross-sectional pure torsion, follows any configuration of an enclosed continuum manipulator (continuum backbone) by changing the cross-sections' relative polar angle. The relative polar rotation is accumulated along a scale and results in a large sudden rotation of the joints in our interface design with finite number of joints. The interface is able to follow any configuration as long as the large enough number of small jags are implemented at the joint cross-section. The slope should be less than $\tan^{-1}(0.2) = 11$ [deg] (for static coefficient of friction of 0.2 between two acrylic plastic surfaces) in theory to prevent scales from self-locking, where the slope angle is greater than the static friction coefficient and the surfaces does not slide relatively if pushed against each other, but this value is greater in reality because of wear of the small jagged design and wax (3D printing process support material) residue.

The total jagged area should be more than $2(0.0265+r_{\mathrm{o}}\times 8.8)/(\sigma_{\mathrm{yield}}(r_{\mathrm{j1}}+r_{\mathrm{j2}})) = 0.86$ [mm^2] to prevent normal and shear wear of the teeth. This means that in theory $2\pi(r_{\mathrm{j1}} + r_{\mathrm{j2}})^2/(\sqrt{2} \times 86e^{-8}) = 34$ teeth are possible to implement with a height of 0.17 [mm]. The number of teeth multiplies by the teeth height should be more than

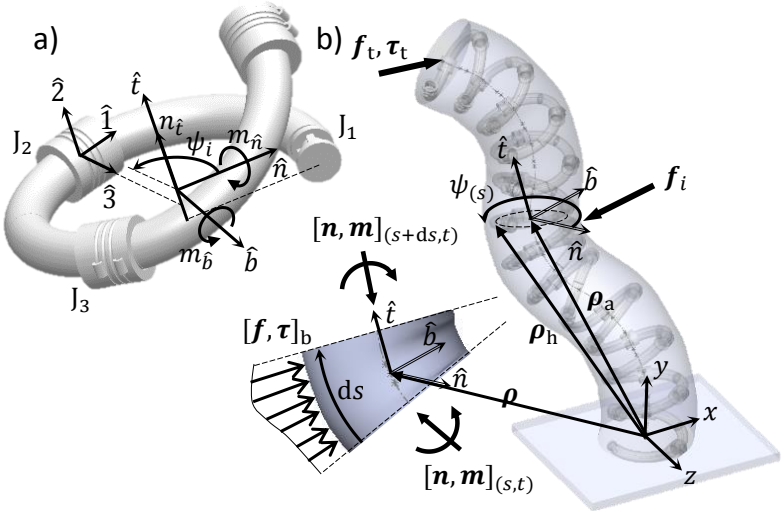

Figure 4.7: (a) Loads and kinematics of a ring segment with three scales, (b) VC kinematics and Cosserat rod method parameters for the continuum interface. The details of the jagged contacting surfaces, as in Fig. 4.6, are not implemented in this figure.

$34 * 0.17$ [mm] for any other number of teeth. The teeth are small and wear rapidly for such dimensions in our real 3D printed scales. The final values are chosen based on these values and experimental trials. Besides, the contact surface is modified as a cone to increase the contacting area and teeth strength.

4.4 Scale Jamming Interface Mechanics

Local stiffness regulation along a continuum manipulator backbone enables simultaneous task space impedance and configuration control as well as disturbance rejection. We propose a helical interface consisting of 3D-printed scales with four stiffness tunable rotational joints in each full turn with and without a low stiffness spring backbone. Each full turn adjusts the stiffness coefficient matrix of an element along the continuum manipulator backbone by the actuation of stiffness controllable joints. Castigliano's method is used to model the helix stiffness matrices (K_v and K_u) in Eq. 2.20 to be used for the manipulator VC kinematics (Fig. 4.7.b).

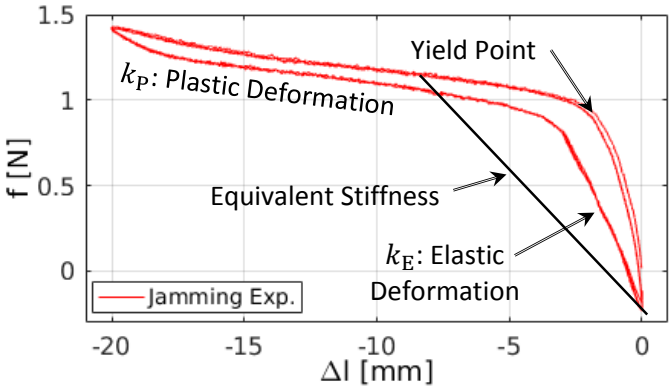

Figure 4.8: Deformation regions and definition of equivalent stiffness in a jamming media.

4.4.1 Helix Variable Curvature Kinematics

Exact and simplified kinematics of a constant curvature bending helix is presented in section 3.2.2. Assuming no axial twist, for the geometry of a helix (ρ_{h}) with variable curvature backbone we have

$$\rho_{\mathrm{h}} = R.R_{(2,\psi)}.[r_{\mathrm{h}}\ 0\ 0]^{\mathrm{T}},\ \psi = 2\pi n_{\mathrm{h}} s/l, \tag{4.1}$$

where $R_{i,x}$ is a standard rotation matrix of x around the i^{th} axis, n_{h} is the number of helix turns and l is the backbone initial length. Local helix lead angle (γ) can be found from the above equation as in the section 3.2.2, although its effect is neglected here.

4.4.2 Interface Stiffness Model

The load-deformation plot for jamming designs usually consists of an elastic deformation followed by a plastic one with two distinctive stiffness coefficients (slopes of the $n_{\hat{t}} - \Delta l$ curve in Fig. 4.8), k_{E} for the fully jammed state (elastic region) and k_{P} for the case when the jammed media begins to slide (plastic region). This means the stiffness is not controllable continuously. For the first time, we introduce an equivalent stiffness as in Fig. 4.8 for continuous stiffness modulation with such a design. We assume no torsion ($m_{\hat{t}} \approx 0$) and shear forces ($n_{\hat{n}} = n_{\hat{b}} \approx 0$) on the manipulator

cross section (infinite shear modulus assumption) and helix lead angle to be $\gamma \approx$ cte with relatively small changes due to the backbone deformation. Hence, based on the free body diagram (Fig. 4.7.a) we have $m_{\mathrm{h}} = R^{\mathrm{T}}_{(2,\psi)}.([r_{\mathrm{h}}\ 0\ 0] \times n + m)$, where subscript ($_{\mathrm{h}}$) is for the helix curvilinear frame, m and n are the moment and force respectively, r_{h} is the helix mean radius, ψ is the planar angle around $\hat{t}$ axis and $\mathrm{C}|\mathrm{S}_x = \cos|\sin(x)$. The scale body and the joint act as a series of elastic elements. Using the principle of virtual work, the differential virtual work for the i^{th} scale in each element ($\mathrm{d}w_{\mathrm{sc}_i}$) is

$$\begin{aligned} w_{\mathrm{sc}_i} &= \int_{\psi_(i-1)}^{\psi_i} \mathrm{d}w_{\mathrm{sc}_i},\ \psi_i = 2i\pi/n_{\mathrm{sc}}, \\ \mathrm{d}w_{\mathrm{sc}_i} &= (m^2_{\mathrm{h}_3}/(2EJ_3) + (m_{\mathrm{h}_1} + \tau_{\mathrm{y}_i})^2/(2EJ_1))\mathrm{d}\xi, \end{aligned} \tag{4.2}$$

where $\mathrm{d}\xi = r_{\mathrm{h}}\mathrm{d}\psi$, p_{sc} is the number of scales in a full turn, τ_{y_i} is the yield resistance torque of the i^{th} joint, E is the modulus of elasticity and J_i is the second moment of inertia around the i^{th} principle axis of the scale and spring backbone system. For the i^{th} joint we have

$$\begin{aligned} w_{\mathrm{j}_i} &= w_{\mathrm{E_i}} + w_{\mathrm{P_i}} + w_{\mu_{\mathrm{i}}}, \\ w_{\mathrm{E_i}} &= (m_{\mathrm{h}_1(\psi_i)} + \tau_{\mathrm{y}_i})^2/(2k_{\mathrm{E}}), \\ w_{\mathrm{P_i}} &= (m_{\mathrm{h}_1(\psi_i)} - \tau_{\mathrm{y}_i})^2/(2k_{\mathrm{P}}), \\ w_{\mu_{\mathrm{i}}} &= \tau_{\mathrm{y}_i}(m_{\mathrm{h}_1(\psi_i)} - \tau_{\mathrm{y}_i})/k_{\mathrm{P}}, \end{aligned} \tag{4.3}$$

where $w_{\mathrm{E_j}}$ is the virtual work for the elastic deformation, $w_{\mathrm{P_j}}$ is the virtual work for the plastic deformation and $w_{\mu_{\mathrm{j}}}$ is the virtual energy dissipated by the joint friction. The total energy of each element is $w = \sum_{i=1}^{n_{\mathrm{sc}}}(w_{\mathrm{sc}_i} + w_{\mathrm{j}_i})$. For $\epsilon = [v, u]$ and equivalent stiffness of the element ($K_{v|u}$), using Castigliano's method, we have $v = w_{,n},\ u = w_{,m}$ and

$$K_v = \mathrm{diag}^{-1}(v).n,\ K_u = \mathrm{diag}^{-1}(u).m, \tag{4.4}$$

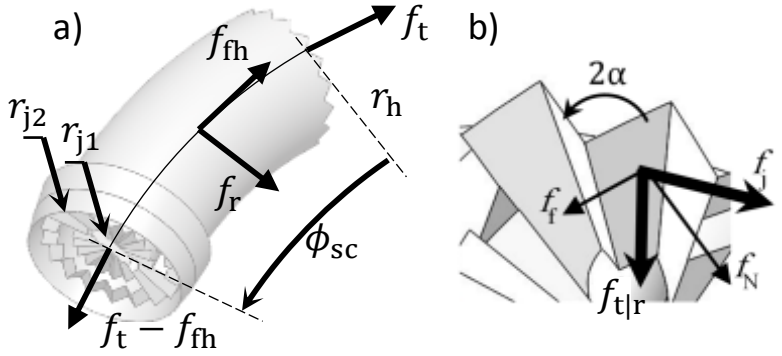

Figure 4.9: (a) Force distribution on a scale and (b) jagged surface. The surface is flat in our model.

where v, u and K are functions of τ_{y} and $f = [n, m]$, and for each scale we have the following piecewise rule.

- *Elastic region* ($m_{\mathrm{h}_1(\psi_i)} \leq \tau_{\mathrm{y}_i}$ and $\nu_{\mathrm{j}} = 0$): the terms resulting from $w_{\mathrm{P}_i, n|m}$ and $w_{\mu_{\mathrm{i}}}$ are neglected, and $\tau_{\mathrm{y}_i} = 0$ in all other terms.
- *Plastic region* ($m_{\mathrm{h}_1(\psi_i)} > \tau_{\mathrm{y}_i}$ or $|\nu_{\mathrm{j}}| > 0$): $[n, m] = 0$ in the terms resulting from $w_{\mathrm{E}_i, n|m}$ and $w_{\mathrm{sc}_i, n|m}$.

ν_{j} is relative velocity of the surfaces in plastic deformation. Eq. (4.4) is rearranged to find $\tau_{\mathrm{y}(f,\epsilon)}$ and $\tau_{\mathrm{y}(f,K)}$ for stiffness planning and control. The resulting equations for (τ_{y}) are not independent, since the scales are arranged in series and the axial and bending stiffnesses cannot be controlled simultaneously. Using the symmetry in a formation with four scales in each turn, the element axial stiffness is controlled by $\tau_{\mathrm{y}_i} = \tau_{\mathrm{y}(f,k_{v_{\hat{t}}})}$ and for the bending stiffness control we have $\tau_{\mathrm{y}_1} = \tau_{\mathrm{y}_3} = \tau_{\mathrm{y}(f,k_{u_{\hat{b}}})}$ and $\tau_{\mathrm{y}_2} = \tau_{\mathrm{y}_4} = \tau_{\mathrm{y}(f,k_{u_{\hat{n}}})}$. Then, the stiffness matrix is found from $K_{v|u} = K_{v|u(f,\tau_{\mathrm{y}})}$ and used in the beam theory mechanics. $k_{\mathrm{E|P}}$ is a function of the joint material and design.

4.4.3 Jagged Contact Surfaces Model

The joint is 3D printed as a part of the scale with the same stiffness modulus. Hence, terms with k_{E} in Eq. 4.3 are neglected in this case. However, the jagged

surface slope angle (α) and the engagement of the actuation tendon in the plastic deformation should be considered to calculate τ_{y_i}, k_P and to model the return cycle hysteresis. Any backlash between the teeth in the jagged surface, Coulomb friction and viscous damping cause further resistance and hysteresis.

The acting force on the contact surfaces is the tendon tension (f_t) for the scale design driven by the tangential force, or the tendon radial force ($f_r = 2f_t S_{(\phi_{sc}/2)}$) for the scale design driven by the tendon radial force (Fig. 4.9.b). The tendon tension reduces by f_{fh} for any scale due to friction with the routing path. We assume the wire tension to be constant along each scale to avoid solving a first order differential equation for f_{fh}. Cosequently, from the scale geometry (Fig. 4.9.a), we can achieve the equations below for the i^{th} scale

$$\begin{aligned} f_{fh_i} &= f_{r_i}\mu_t r_h \phi_{sc},\ f_{r_i} = (2f_{t_{i-1}} - f_{fh_i})S_{(\phi_{sc}/2)}, \\ \rightarrow f_{fh_i} &= 2f_{t_{i-1}}\mu_t r_h \phi_{sc} S_{(\phi_{sc}/2)}/(1 + \mu_t r_h \phi_{sc} S_{(\phi_{sc}/2)}), \end{aligned} \tag{4.5}$$

where μ_t is the routing friction coefficient per unit length. The tension force at the i^{th} scale (f_{t_i}) is

$$f_{t_i} = f_{t_{i-1}} - f_{fh_{i-1}} + f_{tk}, \tag{4.6}$$

where f_{tk} is the extra tendon tension due to the wire elasticity, explained in Eq. 4.10. Substituting Eq. 4.5 in 4.6, for f_{t_i}, we have an exponential function of the form

$$\begin{aligned} f_{t_i} &= f_{t_{i-1}} \left(\frac{1 - \mu_t r_h \phi_{sc} S_{(\phi_{sc}/2)}}{1 + \mu_t r_h \phi_{sc} S_{(\phi_{sc}/2)}} \right) + f_{tk}, \\ f_{t_i} &= f_t \left(\frac{1 - \mu_t r_h \phi_{sc} S_{(\phi_{sc}/2)}}{1 + \mu_t r_h \phi_{sc} S_{(\phi_{sc}/2)}} \right)^i + f_{tk}, \end{aligned} \tag{4.7}$$

This shows that the tendon effective tension reduces along the scales, resulting in a less stiffness at the tip. The LuGre friction model is used to calculate the jagged

surface Coulomb friction coefficient (C_{j}) and the friction force (f_{f}) as [161]

$$C_{\mathrm{j}} = \mathrm{sgn}\left(\nu_{\mathrm{j}}\right)\left(\mu_{\mathrm{D}} + \left(\mu_{\mathrm{S}} - \mu_{\mathrm{D}}\right) e^{-\left(\nu_{\mathrm{j}}/\nu_{j0}\right)^{2}} + \sigma_{\mathrm{j}}\left|\nu_{\mathrm{j}}\right|\right),\ f_{\mathrm{f}} = f_{\mathrm{N}} C_{\mathrm{j}}. \tag{4.8}$$

Based on the force equilibrium in the direction of the inclined surface (Fig. 4.9), the joint resisting torque (τ_{y_i}) at the yield point and after it becomes

$$f_{\mathrm{j}} = f_{\mathrm{t}_i}\left(\mathrm{C}_{(\alpha)} + C_{\mathrm{j}}\mathrm{S}_{(\alpha)}\right) / \left(\mathrm{S}_{(\alpha)} - C_{\mathrm{j}}\mathrm{C}_{(\alpha)}\right),\ \tau_{\mathrm{y}_i} = r_{\mathrm{j}} f_{\mathrm{j}}, \tag{4.9}$$

where sgn is the sign function, C_{j} is the Coulomb friction coefficient form LuGre model, $\nu_{\mathrm{j}} = r_{\mathrm{j}}\psi_{\mathrm{j},t}/(\mathrm{S}_{(\alpha)})$ is the relative slip velocity along the slop surfaces, ψ_{j} and $\psi_{\mathrm{j},t}$ are the joint rotation angle and angular velocity based on the module $[v, u]_{,t}$, r_{h} is the scale curve radius, $\nu_{\mathrm{j}0}$ and σ_{j} are the LuGre model Stribeck velocity and viscosity coefficient respectively. The joint yield torque threshold in the piecewise rule (4.4.2) is found from Eq. 4.9 for $\nu_{\mathrm{j}} = 0$.

The joint elasticity in plastic deformations (k_{P}) is resulted from relative upward movement of the contact surfaces along the inclined jags. $f_{\mathrm{tk}} = k_{\mathrm{t}}\Delta l_{\mathrm{t}}$ is the extra tendon tension due to the wire elasticity ($k_{\mathrm{t}} = E_{\mathrm{t}} l_{\mathrm{t}}/a_{\mathrm{t}}$) and the relative movement (Δl_{t}). l_{t} is the total tendon length and Δl_{t} is the cumulative relative upward movement of all the joints for the tendon driven design ($\Delta l_{\mathrm{t}} = r_{\mathrm{j}}\cot_{(\alpha)}\Sigma_i \Delta\psi_i$), where the tendon is connected to the last scale and any extra tension at any point propagates along the whole tendon. On the other hand, for the SMA actuated design, l_{t} is the active SMA wire length in each joint and Δl_{t} is ($\Delta l_{\mathrm{t}_i} = r_{\mathrm{j}}\cot_{(\alpha)}\Delta\psi_i$), where only the local extra tension of the active wire length is important. For k_{P} at each joint, from the surface jagged geometry, we have

$$k_{\mathrm{P}} = k_{\mathrm{t}} r_{\mathrm{j}}\cot_{(\alpha)}\left(\mathrm{C}_{(\alpha)} + C_{\mathrm{j}}\mathrm{S}_{(\alpha)}\right) / \left(\mathrm{S}_{(\alpha)} - C_{\mathrm{j}}\mathrm{C}_{(\alpha)}\right), \tag{4.10}$$

where $r_{\mathrm{j}} = r_{\mathrm{j}1} + \sqrt{J_{\mathrm{j}\hat{1}}/a_{\mathrm{j}}}$, $r_{\mathrm{j}1}$ is the joint routing path inner radius, a_{j} and $J_{\mathrm{j}\hat{1}}$ are the joint area and second moment of area respectively, subscript ($_{\mathrm{t}}$) is used for the

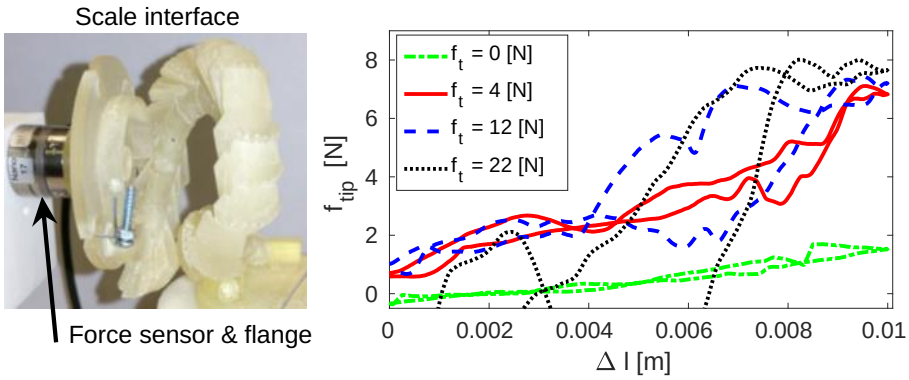

Figure 4.10: Scale jamming interface with radial actuation force in experiments and results in uniaxial tension test. The jagged surface has 9 teeth with 1 [mm] height and 72 [deg] slope on a 40 [deg] cone-shape surface.

actuation tendon or SMA wire parameters and subscript ($_j$) is used for the joint parameters. In our numerical calculations, the calculated value for $\Delta\psi_i$ from the previous time or spatial interval is used as a linearization approximation to avoid increasing the differential order of the equations.

Using Eq. 4.4 alongside the piecewise rules in 4.4.2, the system hysteresis in the full return cycle can be modeled. As a result of the Coulomb damping, a sudden decrease is observed in the resisting force when the movement direction is reversed. Combining Eq. 4.5-4.9, to find the stiffness of each element along the variable curvature backbone, with Eq. 4.4 and 2.20 for the continuum manipulator mechanics, the manipulator stiffness can be controlled based on the scale interface stiffness in different loading scenarios. A simpler derivation of such combinations without consideration of k_{t} and f_{h} for pure elongation and bending cases is presented in [41].

4.5 Experiments and Numerical Simulations for Different Designs

Three different scale designs are 3D-printed with UV curable acrylic plastic ($E_{\mathrm{sc}} =$ 3.3 [GPa], $G_{\mathrm{sc}} = 1.1$ [GPa], σ_{sc} =2e-3 [s/m], ν_{sc} =1e-3 [m/s], $\mu_{\mathrm{S}} = 0.03$, $\mu_{\mathrm{D}} = 0.015$) and tested in simple tension tests. A tendon driven sample with backbone is tested

in simple bending as well and in integration with one STIFF-FLOP module. The results for the later case is compared with the numerical simulations to verify our modeling method.

The first design, actuated with radial tendon force (Fig. 4.6.d), needs a backbone spring with low axial but high radial stiffness to oppose the tendon force as a base. To guarantee the jamming, the tendon route is designed so that the scale touches the next scale before contacting the backbone spring. We used a springy helix with rectangular cross section (1.2×0.2 [mm] dimension, $E_{\text{sp}} = 60$ [GPa], $r_{\text{sp}} = 19.2$ [mm] diameter, $\phi_{\text{sc}} = 30$ [deg]) as the backbone which satisfies our requirement, which are easy integration on STIFF-FLOP continuum modules, small but effective shape memory feature to achieve uniform results and providing a backbone to resist against radial component of the tendon tension force. In a simple tension test for one turn of the radial scales (Fig. 4.10), a smooth 3.9 times increase in the resisting force (1.8-7 [N]) and stiffness is observed for 4 [N] wire tension. For higher tension values and up to 22 [N], the deformation profile is not smooth, with large hysteresis and only 60% increase in the blocking force. However, the scale has a bulky design to prevent the breakage of the thin unsupported contact surface at the scale tip. As a result, the deformation happens only in the elastic region. The scales are actuated by the tendon direct radial force which makes this design less sensitive to the tendon routing friction. The contact surface curvature center is not on the spring wire and the surface needs to slide as well as rotate to adjust with any change in the helix lead angle. As a result, large hysteresis and fluctuations are observed despite the good reversibility.

For a smaller design with better geometrical consistency with the spring backbone, a curved cylindrical design is introduced ($r_{\text{j1}} = 0.8, r_{\text{j2}} = 2.35$ routing and outer radius, $\alpha = 25$ [deg], $\phi_{\text{sc}} = 30$ [deg]) (Fig. 4.6.a) with contact surfaces perpendicular to the spring backbone and the interface is actuated based on the tendon tangential force (Fig. 4.11). The tendon is connected to the last scale. The actuation tangential force is propagated through the tendon routing friction and through the interface

Figure 4.11: Scale jamming interface with tangential actuation force and a low stiffness spring backbone in experiments and numerical simulation; experimental setup. The jagged surface has 16 teeth with 0.5 [mm] height and 35 [deg] slope on a flat surface.

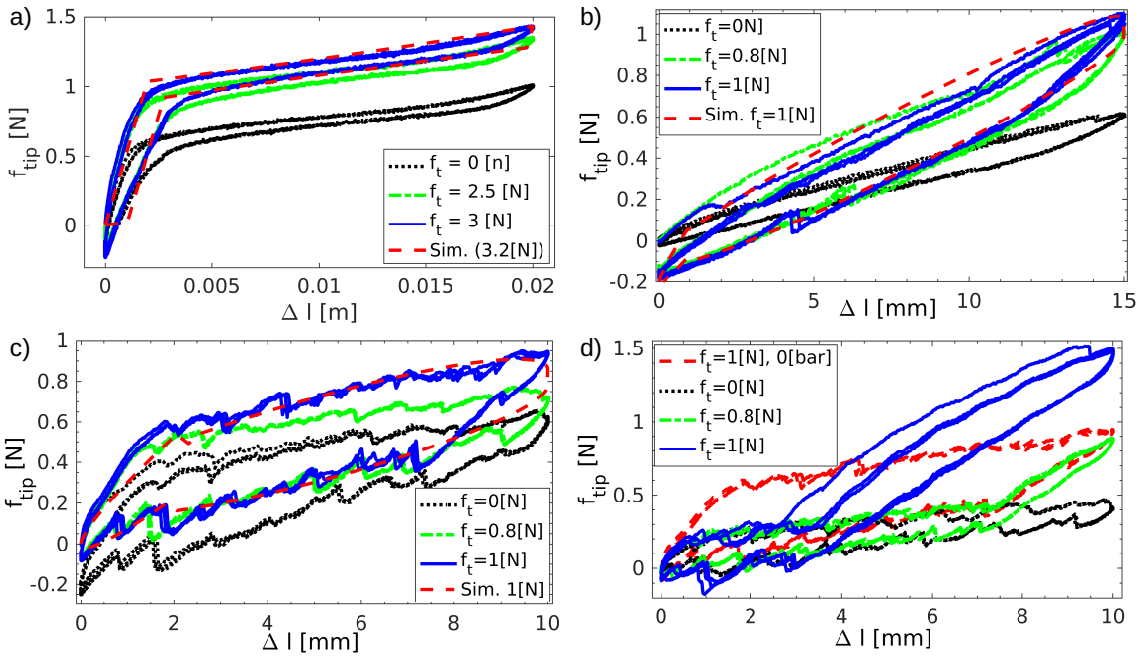

Figure 4.12: (a) Results for uniaxial tension test, (b) results for simple bending test when integrated on a STIFF-FLOP module, (c) in initially straight configuration, in bent configuration with inactive and (d) active (p = 2.5 [bar]) STIFF-FLOP module.

from the last scale. A sinusoidal cyclic linear movement is considered with stroke (Δ_l) 20 [mm] in tension test (3 turns, 17.1 [mm] initial length, γ = 87.3 [deg], Fig. 4.12.a), 15 [mm] in bending test from a straight initial condition (5 turns, 35 [mm] initial length, γ = 94 [deg], Fig. 4.12.b) and 10 [mm] in bending test from a curved initial condition (Fig. 4.12.c,d). The interface is integrated on a STIFF-FLOP module in the bending tests where the manipulator dynamic contributes in the force measurements. For tip horizontal movements, stiffness value of 40 [N/m]

in the straight and 26.7 [N/m] in the bent initial configuration and viscous damping of 30 [Ns/m] in the straight and 60 [Ns/m] in the bent initial configuration are identified based on a simple spring-damper model for the STIFF-FLOP module. 42% increase in the blocking force is observed for the tension (f_{tip} =1.0-1.42 [N], $f_{\text{t}} = 0 - 3$ [N], Fig. 4.12.a) and 80% for the bending from straight configuration (f_{tip} =0.6-1.1 [N], $f_{\text{t}} = 0 - 1$ [N], Fig. 4.12.b) tests. The interface can fix an inactive STIFF-FLOP module in a bent configuration with up to 50% increase in the blocking force (f_{tip} =0.6-0.9 [N], $f_{\text{t}} = 0 - 1$ [N], Fig. 4.12.c). Up to 365% increase in stiffness is observed for antagonistic actuation of the module with 2.5 [bar] and interface with $f_{\text{t}} = 1$ [N] (f_{tip} =0.41-1.5 [N], Fig. 4.12.d). Comparing the results for the tests in bent initial configuration, 0.3 [N] increase in the blocking force for the test with an inactive STIFF-FLOP module and up to 1.1 [N] increase for the case with an active module are observed. The blocking force with an active module is about twice as much as the simple summation of the manipulator and interface blocking forces. This shows an antagonistic behavior where the scales act as a secondary braiding for the manipulator adding extra rigidity to the system. A linear smooth and reversible behavior is observed, especially for the simple tension test, where the small hysteresis does not change the final blocking force. This results in the first cycle being slightly different from the later ones, especially in the bending tests; however, the load cycle is fully reversible from the second load cycle. The larger hysteresis in the bending tests are due to the STIFF-FLOP module viscous damping and larger deformations of the joints on the bending plane and at the interface route. Adding a low stiffness spring backbone helps smooth uniform operation of the interface; however, it reduces the blocking force, increases the tendon-routing friction and adds a nonzero minimum stiffness value to the system.

The tendon routing friction reduces the interface tip blocking force in a long design. A similar design with $\phi_{\text{sc}} = 90$ [deg] for increased joint effective rotation, cone-like surface for stronger teeth design, three roller bearings for friction reduction and without spring backbone is introduced to address this issue (Fig. 4.13). For simple

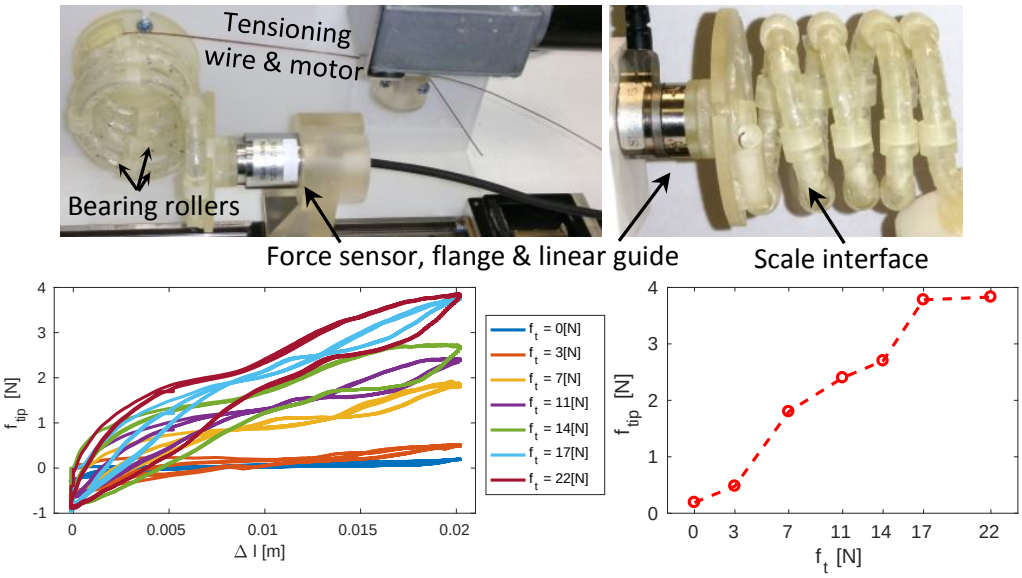

Figure 4.13: Scale jamming interface with tangential actuation force and roller bearings for friction reduction (top), resisting force-elongation ($f_{\text{tip}} - \Delta l$) and resisting force-tension ($f_{\text{tip}} - f_{\text{t}}$) plots from uniaxial tension test (bottom). The jagged surface has 10 teeth with 0.45 [mm] height and 45 [deg] slope on a 77 [deg] cone-shape surface.

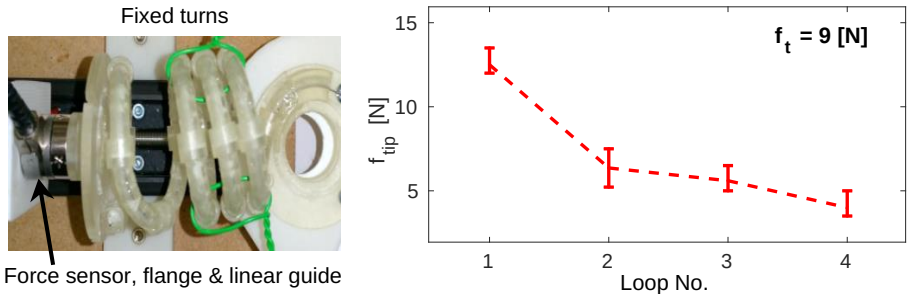

Figure 4.14: Experiments on exponential stiffness reduction in different helix turns due to tendon-routing surface friction.

tension tests of a sample with four turns and $l_0 = 40$ [mm], a linear, reversible and low hysteresis stiffness increase (f_{tip} =0.2-3.9 [N], 20 times increase) for different tendon tensions (f_{t} =0-17 [N]) is observed which has 278% larger blocking force (371% larger stiffness considering the different helix turns) compared to the previous design with full stiffness range approximately as small as zero. However, larger hysteresis, small load cycle fluctuations and less reversible results are observed compared with the version with a spring backbone. The new design does not present the same maximum blocking force in all the actuation cycles; however, the load cycles become more reversible after the first few warm-up cycles. This emphasizes the importance of a consistent geometrical relative movement which can be guaranteed using a low

Figure 4.15: (a) A SMA actuated scale design with a SMA wire passing through and fixed to the middle of the scales,(b) uniform (low stiffness) and non-uniform (high stiffness) deformation of a scale in uniaxial tension test, (c) SMA actuated helical interface integrated on a contiuum manipulator with two STIFF-FLOP modules. The jagged surface has 10 teeth with 0.45 [mm] height and 45 [deg] slope on a 77 [deg] cone-shape surface.

stiffness spring backbone. For tension forces higher than 17 [N], the hysteresis is increased without a noticeable change in the blocking force. Tests are carried out on the stiffness of different rings, showing an exponential decrease, as predicted in our model, with mean base value of 0.915±18% for each scale (Fig. 4.14). The reduction in the tendon tension is noticeable despite using the bearings. Additionally, it is hard to implement multiple tendons for local and directional stiffness control.

To address these issues, local actuation using a shape memory alloy (SMA) wire is tested for the same scale design (Fig. 4.15.a). The 3D printing material, UV curable acrylic plastic, is a thermally stable material with melting point of about 160 [°C], meaning that using SMA wires with near room temperature transition point does not melt or change the scale structure significantly. However, the material is soften if it is exposed to temperatures around 80 [°C] for a long time. Screws are used to fix the SMA wire in each scale and act as a local electric contact pin. 80 [mm] of a low hysteresis nitinol SMA wire (Standard Temperature NiTiCu wire from Kellogg's Research Labs, kelloggsresearchlabs.com), with r_{th} =0.75 [mm] and transition temperature of 45 °C is trained in a helical form with 2 [mm] diameter and 48 [mm] axial length. The wire resistance is found to be 33.56 Ω/m (2.68 Ω in total), almost independent of temperature as shown in Fig. 4.16. Simple tension tests are carried out for uniform actuation of the helix. The results contradict our

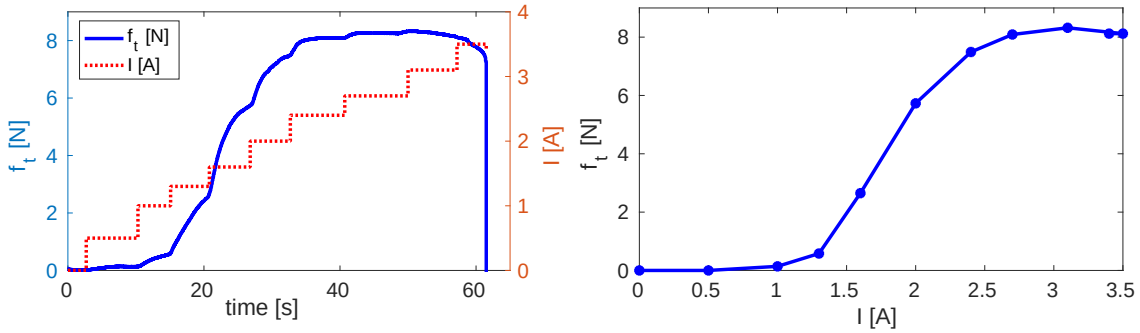

Figure 4.16: Trained helical SMA actuator performance.

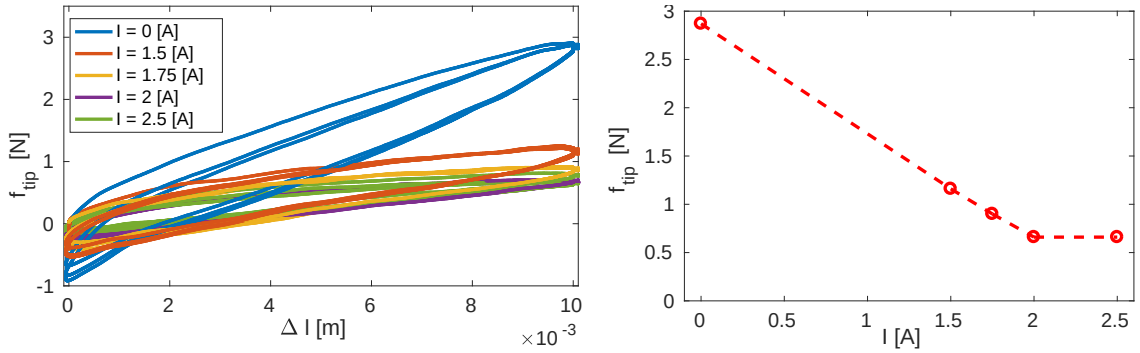

Figure 4.17: SMA actuated interface stiffness control in a uniaxial tension test.

predictions about achieving higher stiffness by actuating the SMA wire (Fig. 4.17). The thermal instability of the scale material and solidification of a wax composite used as the support material in the 3D-printing process result in the jamming of the contact surface when cooled and act as a lubricant when heated. Despite this unwexpected behavior, higher reversibility, smooth load cycle and 50% increase in the blocking force (0.5-3 [N]) are observed compared to the previous design, with similar load cycle hysteresis. The helix deformation is more uniform for the lower stiffness values (Fig. 4.15.b), suggesting that using a means of lubrication improves the interface deformation symmetry. The interface is able to lock the bent geometry of a continuum manipulator with two STIFF-FLOP modules (Fig. 4.15.c). It worth emphasis that

4.6 Discussion and Comparison with Other Jamming Solutions

Three actuation designs are presented as follows.

1. Tendon driven jamming through radial force, which needs a low stiffness spring backbone and represents the most similar design to a natural fish scale morphology. This design features high stiffness range and is less sensitive to tendon-structure friction; however, it is bulky and suffers from inconsistent geometry and low deformation range.

2. Tendon driven jamming through tangential force where a smaller more uniform design is possible that is capable of covering a large deformation range without any backbone. The tendon-structure friction plays a crucial role here.

3. Shape memory alloy (SMA) actuated interface for uniform and local stiffness control without any problem regarding the tendon-structure friction. Large thermal expansion of the 3D-printed scales and solidification of the wax composite residue from the fabrication process affect this design despite the achieved high stiffness range.

Results are compared with two well-cited articles on granular jamming by Jiang et. al. [110] and layer jamming by Kim et. al. [61]; results provided by Blanc in a review on different stiffening mechanisms for flexible medical devices [21]; and two recent research on granular [16] and tendon [59] stiffening of a STIFF-FLOP module. All the jamming designs present switching stiffness between two states; however, this is the first time in this research that an equivalent stiffness is introduced and a complete model for the return cycle is presented. The bending tests on the scale jamming design in Fig. 4.12.a and 4.13 shows higher axial stretch ($\Delta l/l_0 = 0.02/0.017 = 0.428, 0.02/0.04 = 0.5$) compared to the granular (0.01/0.04=0.25) and layer (0.02/0.4=0.05) jamming. Our design acts almost linearly in the whole

deformation region (100%), especially in the presence of a spring backbone, while the percentage of the linear region with respect to the whole deformation range in the later works are 18% for granular and 1% for layer jamming. Each experiment is carried out with three complete load cycles. Our design benefits from highly reversible load cycles with very small hysteresis. A large hysteresis and reversibility are observed in the granular jamming while the relevant data is not reported for the layer jamming design. The desired tip stiffness of continuum manipulators in simple bending test for Minimally Invasive Surgery (MIS) applications is about 0.27 [N/deg] (17.2 [N/rad]) [61]. This value is about 3.7 [N/rad] for scale, 12.4 [N/rad] for granular and 40-80 [N/rad] for layer jamming. The rotational stiffness of the designs at the root ($f_{\text{tip}} l_0^2 / \Delta l$) are 0.3 [N/rad] for scale, 0.5 [N/rad] for the granular and 32 [N/rad] for the layer jamming respectively. Despite similar and even higher load bearing capacity, the calculated tip and root stiffness show the advantage of both granular and layer jamming over scale jamming, because of the helical structure of the interface.

In comparison to similar stiffening solutions, the maximum flexural stiffness increase for our design when integrated on an active STIFF-FLOP module ($f_{\text{tip}} = 0.41 - 1.5$ [N], 3.5 times) is on the average of similar jamming designs (granular jamming 0.5-15, layer jamming 0.7-7, wire jamming 3 times) and less than the segment locking designs (6-50 times) in literature [21] This value falls in the lower range of stiffness range for similar design in literature when the inner module is not active. The stiffness range in elongation tests is not reported. A successful stiffness control design should achieve a wider range of stiffnesses than the commercially available medical endoscopes which is 15000-31000 [Nmm^2] [21]. The flexural stiffness of STIFF-FLOP through pressurization (510-5000 [Nmm^2]) increases to 5000-9165 [Nmm^2] after integration of the scale jamming interface, and to 510-18750 [Nmm^2] if both the actuator and interface are actuated. These values fall on the average of the bending stiffness range for different granular jamming designs and further improvements are needed to cover the whole stiffness spectrum.

However, the scale jamming interface is easily integrable on any continuum manipulator while the other designs need to be fabricated with the manipulator structure. As a result, the tip rotational stiffness of a STIFF-FLOP module increases from 2 [N/rad] to 3.6 [N/rad] ($f_{\text{tip}} = 0.6 - 1.1$ [N], 83% increase) in a straight configuration and from 2 [N/rad] to 7.5 [N/rad] ($f_{\text{tip}} = 0.41 - 1.5$ [N], 350% increase) in a bent configuration, making it more desirable to be used in MIS. These values are 10.34-14.5 [N/rad] ($f_{\text{tip}} = 2.2 - 3.1$ [N], 41% increase) in a straight and 13.16-15.5 [N/rad] ($f_{\text{tip}} = 2.8 - 3.3$ [N], 18% increase) in a bent configuration for the STIFF-FLOP module with granular jamming [16] and 6.2-12 [N/rad] ($f_{\text{tip}} = 1.32 - 2.56$ [N], 94% increase) in a straight and 11.4-14.2 [N/rad] ($f_{\text{tip}} = 2.43 - 3.2$ [N], 24% increase) in a bent configuration for the one with tendon stiffening design [59]. A similar reversible and low hysteresis behavior is observed with tendon stiffening [59]. The actual values are not comparable as a different version of STIFF-FLOP is tested in these research. The granular and tendon stiffening solutions for the STIFF-FLOP module are capable of covering the needed stiffness range for endoscopic applications [21] While all three designs cannot satisfy the MIS application necessity as in [61], the granular jamming design provides the highest blocking force, the scale jamming design achieves the highest axial stretch, variability and reversibility, and the tendon stiffening design provides a balance between these features. However, the tendon stiffening method distorts the structure, lacks the shape locking feature and relies on the opposing action from the manipulator actuators which severely limits its application to soft body manipulators. Table 5.1 presents a summary of the results in comparison to the relevant designs in literature.

Our design provides up to 20 times increase in the elongation and 3.6 times increase in the bending tests, featuring a low hysteresis highly reversible load cycle. The introduced geometrical jamming increases the stiffness control range and repeatability, and reduces the load cycle hysteresis and contact surface wear. However, the load bearing limitation of a helical interface is noticeable for long manipulators. Miniaturization of the scale design helps using multiple interfaces to act in parallel

and cover more of the manipulator surface. In addition, a helix in full contracted configuration presents a higher stiffness that can be considered where a higher blocking force is needed. The promising stiffening range as well as the possibility of local stiffness control, persuaded us to investigate the idea of designing a 3D-printable thermoactive helical interface in the next step of our research.

4.7 Conclusion

In this chapter, for the first time we briefly test the idea of pneumatic scale jamming on a real Cyprinus carpio fish skin. The results show an elastic deformation region with small hysteresis which, we believe, is because of the special curved and jagged morphology of the biological scales. It is not clear whether the scale jamming happens for a real fish, and if so, what causes it. As a guess, the fish may use the myotome attachment fibers (similar to our tendon driven design) and the interlayer dermis for active jamming and external hydrostatic pressure due to swimming depth, or turbulent flow hydro-dynamic pressure as means of passive jamming. Three scale jamming interfaces are designed, by taking inspiration from the spatial geometry and helical arrangement of biological fish scales, to control the stiffness of continuum manipulators with application in minimal invasive surgery. Three scale jamming interfaces are introduced and tested: a tendon driven design with radial actuation force, a tendon driven design with tangential actuation force and a design with shape memory alloy wire actuator. The stiffness is controlled by changing the torsional stiffness and damping of the helical interface cross-section in all mentioned designs. An equivalent stiffness value is introduced to model the full load cycle and hysteresis of our scale jamming design. We showed that the jagged contact surface reduces the hysteresis and increases the linear behavior range. Compared to the tendon stiffing, granular and layer jamming in the literature, we introduce a lighter and easily integrable design with shape locking capability, higher reversibility and stiffness variation ratio and smaller hysteresis, volume and complexity. Relatively

lower maximum blocking force of this design can be addressed by using multiple interfaces in parallel around a manipulator. We believe our design features promising opportunities for stiffness control of continuum manipulators for minimal invasive surgery.

Finally, it is worth mentioning that our findings about the scale jamming capability of a real fish skin need to be verified before making a general claim about its contribution to the real fish swimming efficiency. The dynamic behavior of the jammed scales is more important than their static characteristics for fish locomotion and needs to be investigated further in more dynamic tests. The observed low friction geometrical jamming is far from real-world application due to the scale bulky design and 3D printing limitations. The scales geometry need to be optimized for better load bearing, repeatability and uniform linear performance. A miniature metallic scale design with radial force actuation, low stiffness spring backbone and low friction wire rooting needs to be designed and fabricated to combine all the advantages of the presented helical scale jamming interface in a real-world engineering application. For such scenarios, the main drawbacks of the system, which are the lack of local stiffness control and the problem of wire rooting friction in long interface design, need to be addressed with more experiments and new scale and actuation designs.

Observing the potential of hydroxylated wax, used as the support material in our 3D printing process, as a stiffness variable material, we try to address the lack of local stiffness control problem of our interface with looking into a similar design with functionally graded thermoactive joints in the next chapter. We show how the stiffness planning and control complexities are simplified by exploiting the helical geometry and local stiffness controllability of the interface.

Chapter 5

A 3D-Printable Thermoactive Interface with Morphological Stiffness Control

5.1 Abstract

As the main objective of this chapter, a 3D-printable thermoactive scale jamming interface is presented as a new way to control a continuum manipulator dexterity by taking inspiration from the helical arrangement of a teleost fish scales. A highly articulated helical interface was 3D-printed with thermoactive functionally graded joints using a conventional 3D printing device that utilizes UV curable acrylic plastic and hydroxylated wax as the primary and supporting material. Nichrome wire was used to regulate the joint compliance by controlling the wax temperature in phase transition. Empirical relations between the induced current, temperature and system compliance for different joint designs are identified through comprehensive study of the wax melting profile and actuation scenarios. As the secondary objective of this chapter, a decentralized modeling and control approach is employed by relating the mathematical terms of the Cosserat beam method to their morpholog-

ical counterparts in which the manipulator local anisotropic stiffness is controlled based on the locally available strains, curvatures and load distribution information. As a result, a minimalistic central controller is designed in which the joints' thermo-mechanical states are observed based on measurements from a morphological observer, an external fully monitored replica of the observed system with the same input signal. Preliminary results for passive shape adaptation, geometrical disturbance rejection and task space anisotropic stiffness control are reported by integrating the interface on a continuum manipulator. To evaluate our objectives in this chapter, the tip bending stiffness range and controllability are compared with requirements of minimally invasive surgeries and catheter medical applications, and the feasibility of task space stiffness control and impedance disturbance rejection are shown as a proof for the presented decentralized morphological stiffness control and observation concepts.

5.2 Introduction on Thermoactive and Morphological Stiffening

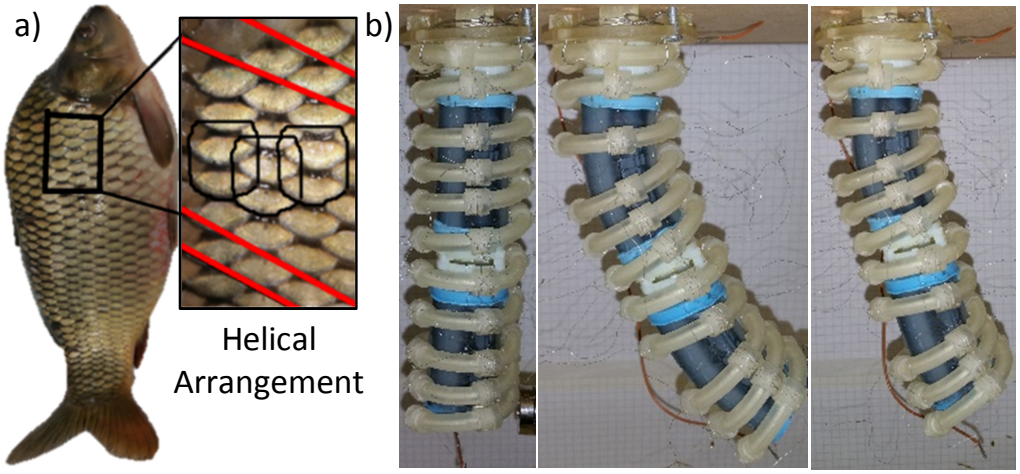

Figure 5.1: (a) Overlapping and helical arrangement of scales in a Cyprinus Carpio fish, (b) the thermoactive interface integrated on a two module STIFF-FLOP continuum manipulator for stiffness control and shape locking in the straight and bent configurations.

The jamming media behaves similarly to a ductile material that undergoes an elastic followed by a plastic deformation in which the yield stress, the elastic deformation threshold, is a function of the friction between the jamming media controlled by changing the normal force in between the contact surfaces. A high hysteresis in the return cycle is a result of this behavior and the jammed media should be used up to the yield threshold for an almost linear repeatable behavior. This behavior is similar to the stiffness change due to phase and glass transition in low melting point (LMP) alloys such as field's metal [43] and composite material with inherent thermal instability such as wax [50] and ABS [54] which is used in much recent research due to higher stiffness range (4.65-5.76 times increase in the stiffness [54]), easy electrical modulation through heating, self healing properties and possible 3D printable fabrication compared to the jamming media [21, 43]. However, the thermoactive design suffers from slow response time in the cooling process, poor controllability and repeatability due to complex phase transition, low efficiency due to heat dissipation, sensitivity to ambient temperature and safety issues due to high current and tem-

perature which are not adequately addressed in recent studies [21, 50, 54, 48] These should be addressed with proper structure and control design and implementation of a cooling mechanism based on the final application.Thermoactive materials are more suitable for applications in cold ambient temperature where rapid cooling improves the system response time and repeatability, e.g. underwater [162], space and high attitudes [115, 163], and for static tasks, e.g shape locking for continuum manipulators [143] and robotic surgeries with mostly quasi-static operations [21, 16, 61, 48].A recent review of stiffening solutions for continuum manipulators by Blank, et. al. shows the advantages of shape locking mechanisms to achieve higher stiffness values and low melting point material for higher stiffening ratio [21].

On the other hand, planning and control of stiffness reconfigurable mechanisms require cumbersome analytical and computation tools for which the idea of replacing the traditional central modeling and control circuits exploiting the embodied intelligence or morphological computation of the available physical hardware has been investigated recently [68]. By breaking a complex problem into simple sub-problems, a uniform decentralized control system is formed that benefits from parallel execution and lack of communication delay where the tasks are fulfilled based on simple repetitive actions with limited local sensory and computation capabilities [69].

It should be noted that biomimicry is not the objective of this study. Rather, we aim to test the hypothesis that contact friction/locking control using scales is a viable method for stiffness control of exoskeletons for soft robots. However, such design may be useful to uncover or test hypotheses about the operation of biological structures [162, 68, 69]. While usually the normal forces on the jammed surfaces are controlled for stiffening, in our recent work, we investigated the idea of using an active attachment mechanisms between the layers based on a novel electro-active velcro using shape memory alloy wire [86].

To achieve higher load bearing range, simpler actuation mechanism, smaller setup design and most importantly, local anisotropic control over the stiffness tensor, in

Figure 5.2: A 3D-printed interface before forming into a helix with 135 [deg] scales.

this paper, we investigate how the inter-scale elasticity and damping for the same helical interface can be controlled by phase transition temperature control of a LMP composite wax in a 3D-printable functionally graded thermoactive joint design. As a result, our design benefits from the advantages of an interlocking design and using low melting point material. First, a design overview is presented in section 5.3. First, a novel decentralized morphological controller is introduced in section 5.4 to simplify the problem of shape adaptation and stiffness regulation in response to external geometrical disturbances. The novel idea of morphological observer is introduced, where the system states are estimated based on the measurements from an external fully monitored joint with the same design and control signal. The repeatable characteristics of such joints is investigated based on the phase transition profile of the LMP hydroxylated wax and for deferent joint designs and actuation scenarios, and experimental relations are identified for forward control of such joints in section 5.5. In section 5.6, experiments are carried out to investigate the performance of the modeling approach and the identified forward control laws for the interface uniform and anisotropic stiffness control while the states are observed with the morphological observer. Finally, the proposed decentralized controller is tested for shape adaptation and task space stiffness regulation in presence of geometrical disturbances. The presented research in this chapter is closely related to the material discussed in the previous chapter resulting in cross-referencing in some sections.

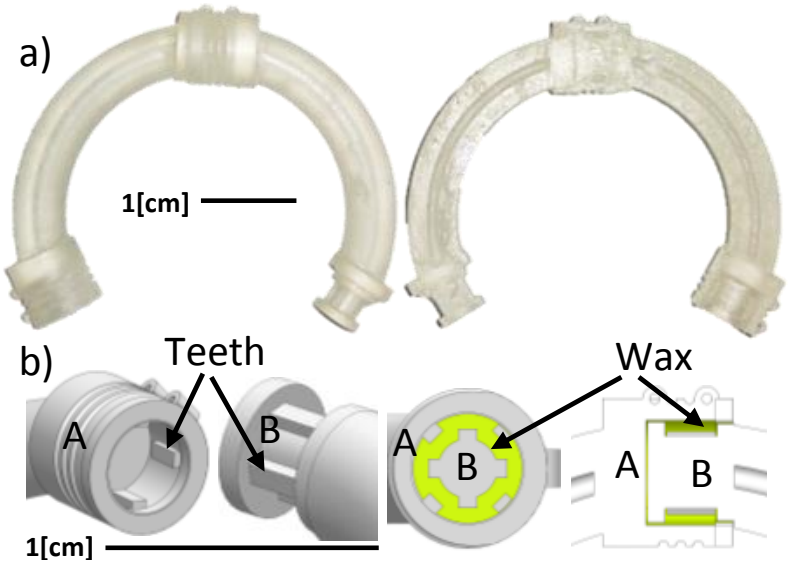

Figure 5.3: (a-left) Outer and (a-right) inner side of a $\alpha = 120$ [deg] interlocking scale with functionally graded thermoactive joints, (b) a thermoactive joint design.

5.3 A 3D-Printable Thermoactive Interface

UV curable acrylic plastic (elasticity modulus, $E = 3.2$ [GPa]) and hydroxylated wax are used widely in high definition 3D printing as the main and the supporting material, where the support material with melting point of 55-65 [°C] is removed in an oven or hot water after the process while the main material which is thermally stable remains intact to collect later. A helical interface with simple revolute joints is designed to be printed as a whole unit as in Fig. 5.2. A small empty space is left in the joint which is filled with the wax support material in the printing process and small clearances of 0.15 [mm] in diameter and length are provided to provide free rotation at the joints as well as preventing the wax from escaping from the joint inside. Four non-contacting teeth with 0.6 [mm] height are designed to increase the joint surfaces engagement with the wax. Based on the von Mises yield criterion, the tooth surface should be larger than 0.58 times the shear surface, so the material withstands the teeth bearing force before the shear sliding begins. A spiral path with 7.9 [mm] groove diameter and two small hinges hold three rounds of heating wire with length $l = 7.45$ [mm] in place (Fig. 5.3). The fully assembled interface is printed as a whole unit with a commercially available high definition 3D printer (PROJET HD

3000 Plus from 3D Systems, www.3dsystems.com) without any further modification to the printer. The interface is ready to be used straight away after addition of the heating Nichrome wires (nickel(80%)-chrome(20%) alloy wire, 0.1 [mm] diameter, resistance $R \approx 1[\Omega/\text{cm}]$, from rapidonline.com). The joint stiffness is regulated by controlling the wax temperature. The wax is fully jammed when cooled and becomes a lubricant when melted, providing high range of stiffness variability with small electric actuation due to using high performance heating wires. As a result of the small joint design, the small amount of wax forms a thin layer that facilitates heat conductivity and improves stiffness regulation repeatability and response time, while high-performance, low hysteresis and fat response heating wires are used for efficient temperature control compared to high current (3-5 [A]) Joule heating method in similar research [48]. A 120 [deg] scale curve is suitable for stiffness regulation along the actuation lines of continuum actuators with three pressure chambers, e.g. STIFF-FLOP [16] (Fig. 5.3.a), a 90 [deg] curve provides decoupled stiffness control in the Cartesian task space (5.1.b) and a 135 [deg] curve is suitable for a long interface design with smaller number of joints (Fig. 5.2). The same method as in section 4.4 is used, where $k_{\text{E|P}}$ is a function of the material temperature and density due to air bubbles in the wax or leakages from the joints. A proper temperature control can minimize the leakage of the wax from the joint gaps. The two-step modeling framework presented in section 4.4 is used for the analysis and simulations throughout this chapter.

5.4 Morphological Control and Observation

5.4.1 Shape Adaptation and Configuration Control

The interface is fully compliant during the manipulation of the internal continuum manipulator providing a passive shape adaptation feature (Fig. 5.1.b-left). The interface is fixed while the goal configuration is reached and a decentralized mor-

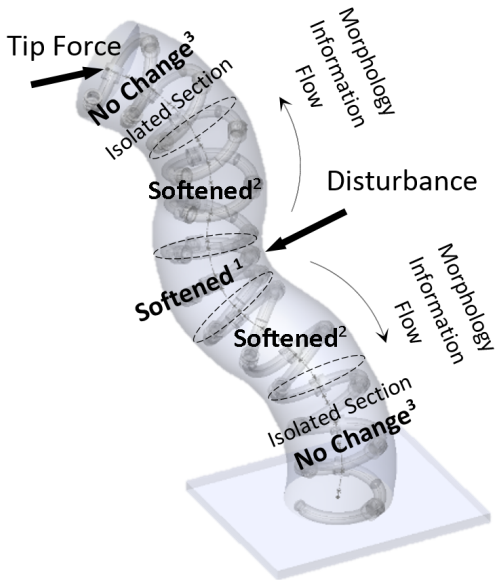

Figure 5.4: sample information flow in a disentralized stiffness regulation strategy for impedance disturbance isolation in the [1]contacting element, [2]adjacent elements and [3]rest of elements.

phological controller is used for impedance disturbance rejection (Fig. 5.1.b-right). A larger reachable configuration space is possible with minimal control inputs by selective directional stiffening of the interface elements which is not investigated here.

5.4.2 Decentralized Morphological Control

The complex problem of stiffness control for impedance disturbance rejection, at any point along the backbone, is addressed by introducing a model-based simple switching decentralized morphological controller. The advantageous of a decentralized controller is that both the control task target and disturbance rejection can be handled in parallel and independently in different places along the backbone. In theory, the local control scheme keeps updating the stiffness of the contacting and disturbing elements until both the task goal tracking and disturbance rejection are satisfied.

Model-Based Control:

A simple control law maintains a bias stress by changing local stiffness that can be used for shape adaptation, disturbance isolation and task space impedance control. Local strains (ϵ) are assumed to be known to the local controllers of each element while the stress (σ), distributed along the manipulator, is considered as a morphological signal that conveys the necessary information between the elements. In a real setup, strain and load sensors are needed to measure the local strain and load values in each element, which is trivial in biological creatures. We assume any impedance disturbance is canceled with a proper shape adaptation. This is the most common disturbance type caused by contacting with a moving soft tissue in most robotic surgeries; however, it does not include the case of constant external load. It means the final disturbed strains (ϵ_{e}) are known and the stiffness is adjusted to maintain a desired contact force (f_{d}) or isolate the caused unwanted deformation by trying to maintain the load distribution ($f_0 = K.\epsilon_0$) similar to before the disturbance, where ϵ_0 is the initial strain before the disturbance. The stiffness for the element at the contact point, either at the tip for task space impedance control or at any other point for impedance disturbance rejection, is adjusted to maintain a desired contact force (f_{d}) by using $\tau_{\mathrm{y}(f_{\mathrm{d}},\epsilon_{\mathrm{e}})}$ (Fig. 5.4.c[1]). The stiffness of the adjacent elements are adjusted to maintain the same load distribution of the undisturbed structure (f_0) with the disturbed configuration (ϵ_{d}) using $\tau_{\mathrm{y}(f_0,\epsilon_{\mathrm{e}})}$ (Fig. 5.4.c[2]). This strategy isolates the local impedance disturbances and no change in the rest of elements are necessary (Fig. 5.4.c[3]). The interface is solidified after the shape adaptation and as soon as the external disturbance force is canceled.

Simple Switching Control:

The contact and adjacent elements are softened to reach the desired force values based on passive shape adaptation and then solidified again.

5.4.3 Minimal Central Controller

Central Controller Design

Implementing large number of local sensors, computation and control units, necessary for the proposed decentralized control in section 5.4.2, is a challenge in fabricating a real robotic system. A simple central controller can be designed based on the proposed decentralized control paradigm, where a switching unit connects a single current controller unit to each of the joints one by one to regulate their temperature and stiffness with a frequency smaller than the stiffness regulation response delay. The manipulator geometry (ρ and R) is found by interpolating a polynomial through two tracked points at the manipulator middle and tip, using magnetic tracking sensors [81], based on which the elements' load distribution ($f = [n, m]$) and ϵ are calculated using Eq. (2.20). The drawback of using a minimal central controller is that the stiffness of the different elements cannot not be controlled in parallel and simultaneously. This can be addressed by considering a policy that prioritized the disturbance rejection and task space stiffness regulation needs.

Joint Morphological Observer

Feed forward relations based on experimental identifications are used to control the joint yield torque (τ_{y}) and temperature (T). However, these values cannot be measured directly to be used in a feedback controller due to the large number of joints, sensor size and space limitation. The novel concept of morphological observer is thus introduced, which is a fully monitored exact replica of the observed system with the same inputs. Similar to a conventional observer where a computer model is used to estimate inaccessible states, here we use a physical model for state estimation. Readings from the morphological observer provides an estimate of the main system behavior. A joint with the same dimensions and all the necessary sensors is designed (Fig. 5.5) through which the same current similar to the observed

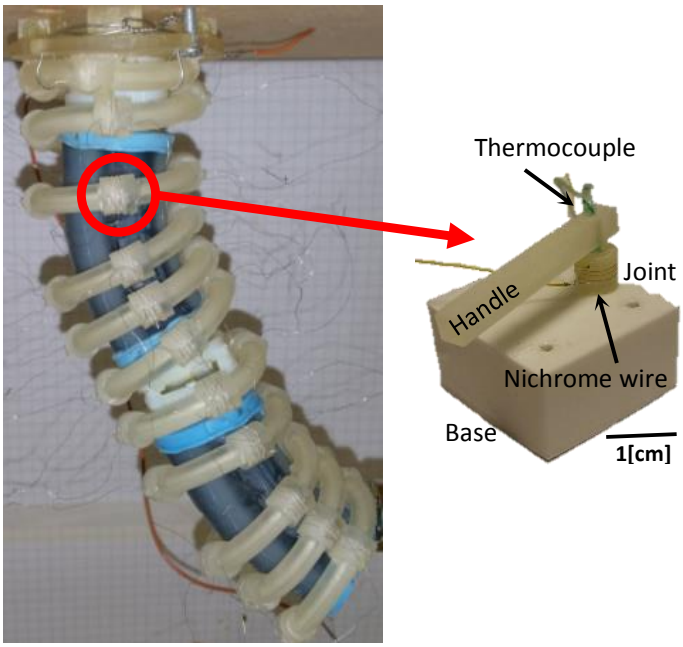

Figure 5.5: A sample joint with temperature sensor at the center which is used as a morphological observer.

system is passed. The system yield torque (τ_y) and temperature (T) are estimated and corrected as needed based on the morphological observer readings. A diagram of the central controller is presented in Fig. 5.6.

5.5 System Thermo-Mechanical properties

Nichrome wire is used as a robust low current heating element. The wire resistance is found to be $R \approx 1[\Omega/\text{cm}]$, almost independent of the wire temperature and with negligible hysteresis, with time constant, the time that a thermistor temperature is dropped by 63.2%, equal to 8.1 [s]. A Maxon Motors EPOS2 5/50 is used for current control of the heating wire based on a simple switching (Bang-Bang) controller to regulate the system mean temperature. The temperature is measured using a K-tupe thermocouple and a National Instruments NI-DAQmx 6210 for signal amplification and analogue to digital conversion. A HIWIN KKA40 precision linear actuator unit is used for accurate linear displacement and an ATI-Nano17 6-axis force sensor is used to measure the loads. All the tests are carried out in quasi-static conditions.

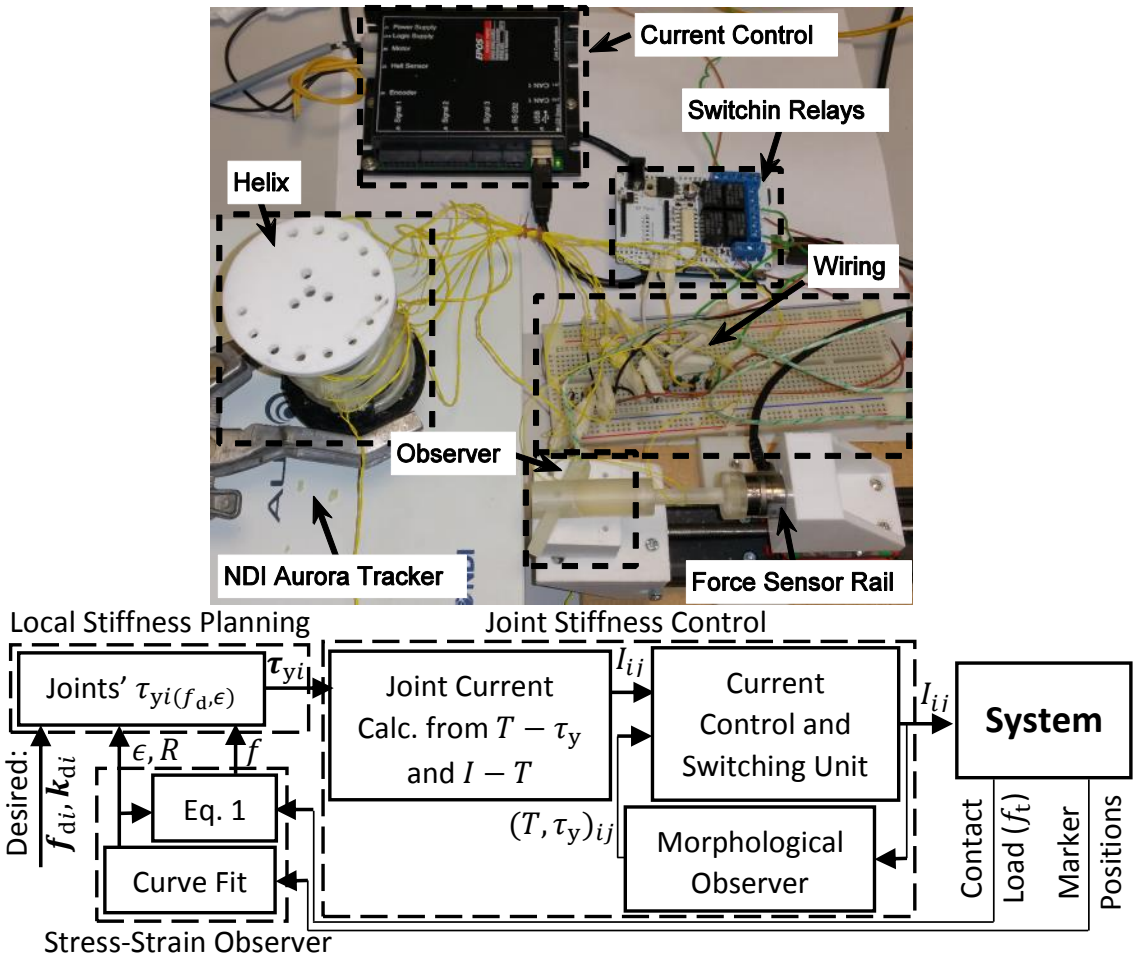

Figure 5.6: Experimental control setup (top), a minimal central controller for model-based decentralized impedance regulation. The joint current calculation unit is replaced with a switching term in the case of a simple switching controller (bottom).

5.5.1 Wax Melting Temperature and Pattern

The melting pattern, surface friction and shear stress of the hydroxylated wax support material was investigated. A cylinder with a 20 [mm] inner diameter and 20 [mm] height was filled with the support material wax while heated with a 3 [mm] diameter spiral Nichrome wire at the center passing a 200 [mA] current. The thermocouple tip was placed at the middle (10 [mm] height) and with 4 [mm] radial distance from the inner surface. The support material had a cream color in the solid state. The melting starts around the heating wire while the material color turns to brown. The wax state starts at ≈40 [°C] and stabilizes at ≈45 [°C]. The melting starts at ≈55 [°C] propagating from the vicinity of the heating spiral from top to bottom, due to natural heat convection in the melted wax, and stabilizes in ≈65

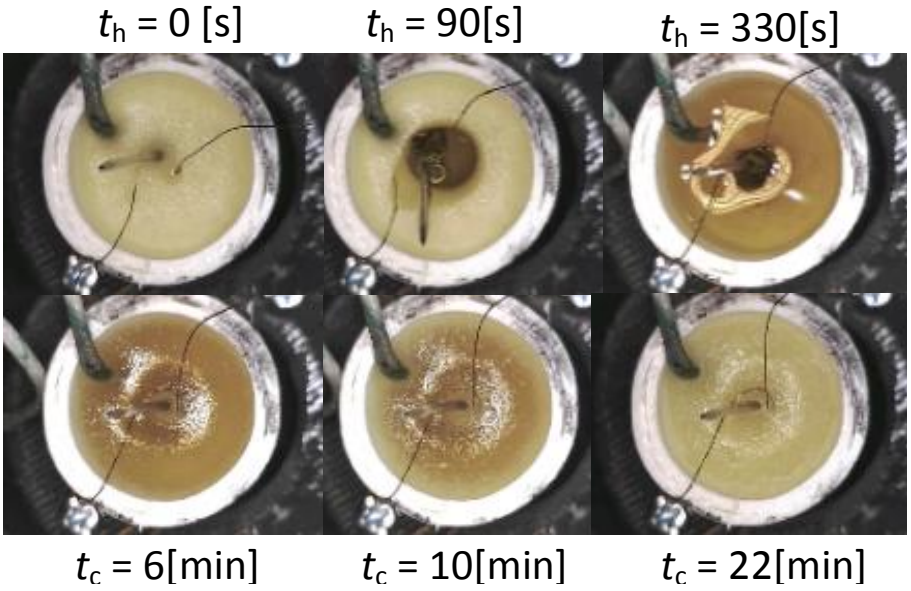

Figure 5.7: Wax melting pattern for a sample with 25 [mm] diameter and 12 [mm] depth.

[°C] until the whole material is fully melted in about ≈6 minutes. While cooled, the solidification starts at ≈55 [°C], when the air bubbles trap in the material, from the outer surfaces and completed in ≈22 minutes with free air cooling and in ≈11 minutes with water cooling, both at room temperature ($T_0 = 26$ [°C]). Small heat conductivity of the wax results in a slow nonuniform melting and solidification pattern with visible borders (Fig. 5.7). This provides a continuous range for material stiffness while a small enclosed volume design result in a more uniform and rapid stiffness change. While a large transition state is preferable for continuous stiffness control, compared to rapid melting of most LMP alloys [43, 48], a small enclosed volume should be designed to achieve uniform and fast response actuation.

5.5.2 Wax Shear Strength, Surface Friction and Stiffness

The same cylinder is covered with a cap and two shaft designs, a smooth cylinder to measure the resisting torque (τ) and shear stress (σ_{shear}) due to surface friction, and a toothed design to calculate τ and σ_{shear} due to the material yield stress (Fig. 5.8). The effective radius, where the breaking starts, is 5 [mm], similar to the shafts' base radius and $h_w = 12$ [mm] is the shaft active height The heating wire is placed on the

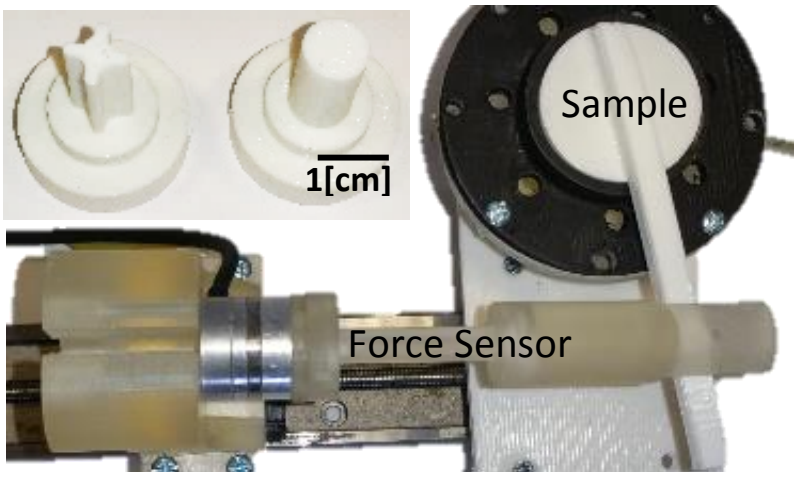

Figure 5.8: Cylindrical and toothed shaft designs and experiment setup.

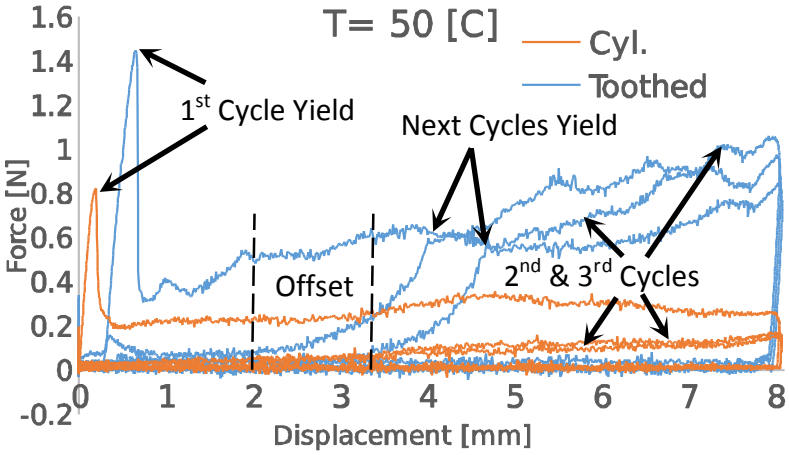

Figure 5.9: Sample results of repetitive actuation for both cylindrical and toothed shaft designs in Fig. 5.8 at T=50 [°C].

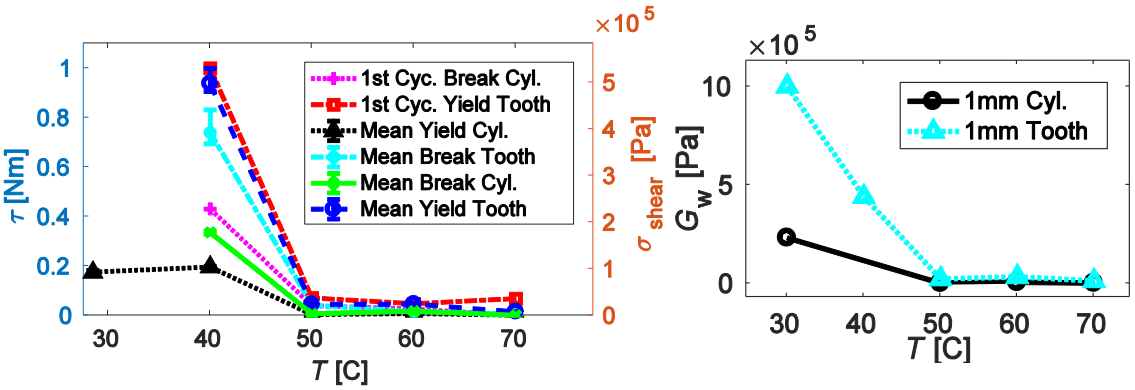

Figure 5.10: (left) Yield and breaking torque and shear stress vs. temperature, (right) shear modulus vs. temperature for small (1 [mm]≈1.16 [rad]) deformation for both cylindrical and toothed shaft designs in Fig. 5.8. The temperature is changed with 10 °C intervals due to large thermal latency of the system and small repeatability of the results, due to the wax complex melting behavior, for smaller interval values.

outer surface where the melting starts. While precise high resolution temperature regulation of the joint is possible, a step change of 10 [°C] was used in the experiments considering our real application with a smaller joint design. The temperature was not measured at the effective radius and is used only for comparison purpose. The yield and breaking values for the wax rigid state ($T < 40$ [°C]) is not reported due to force sensor saturation and damage to the joint structure. These values are reported for the final smaller joint design. Three full cycles of actuation was carried out in each experimental trials (Fig. 5.9). The material behaved like a brittle material in the first actuation cycle, where the resisting force sharply drops (Fig. 5.10(left) 1st Break/Yield), but more like a ductile material for the next cycles with distinctive yield point, where the plastic deformation begins (Fig. 5.10(left) Mean Yield), and breaking point, where the resisting force drops (Fig. 5.10(left) Mean Break). The breaking torque is higher for the first cycle especially for the cylindrical shaft ($\approx$%71) while in the toothed design this value is ($\approx$%9). The mean yield strength of the toothed design is 4.5 times higher than the smooth cylindrical one showing higher shear stress strength compared to the surface viscosity and friction of the wax. Variation of the material mean yield stress is noticeable, 8-500 [KPa] for the toothed design and 1-180 [KPa] for the cylindrical design, with a relatively sharp drop at the wax transition temperature specially for the cylindrical shaft.

To identify the wax shear modulus (G), we consider the resisting torque for 1 [mm] axial movement of the force sensor acting against the joint handle and assume; 1) the wax is fully rigid at the room temperature and the initial measured elasticity is only due to the joint structure (k_{js}), 2) the structure elasticity does not change with temperature. The later assumption is valid for UV curable acrylic plastic, used in our designs, but not for thermally unstable PVC material commonly used for low resolution 3D printing. G is found from the equation $1/k_{\text{j}} = 1/k_{\text{js}} + h_{\text{w}}/GJ_{\hat{\text{i}}_{\text{w}}}$, where k_{j} is the joint measured stiffness and $J_{\hat{\text{i}}_{\text{w}}} = 3e-7$ $[m^4]$ is the wax cross-section second moment of area. The results are presented in Fig. 5.10(right). The model can be improved by taking the stiffness change of the structure due to temperature

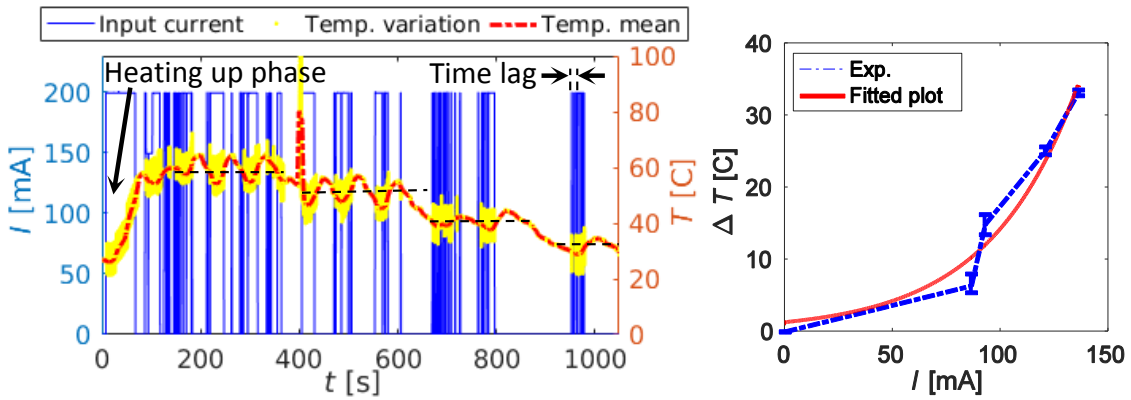

Figure 5.11: (left) Temperature and current plot for initial switching bang-bang feedback control, (right) mean current vs. mean temperature differences (ΔT) for a single 3D-printed functionally graded joint (Fig. 5.5) in room temperature ($T_0 = 26$ [°C]).

change.

The joint behavior presents some complexities. The joint elastic stiffness is linear in the first cycle but an increasing elastic stiffness is observed for the later cycles (Fig. 5.5). While the yield strength of the 2nd and 3rd cycles are almost equal, the transition is delayed with an offset, especially in lower temperatures, which results in a different equivalent stiffness. This is due to the wax melting pattern, self healing properties and variable density as a result of porous structure. The plastic deformation presents a non-smooth stick-and-slip behavior in the wax state that results in a large hysteresis in a full actuation cycle. As a result, the joint characteristics does not show good repeatability at the wax transition temperature especially for continuous cycles.

To achieve better repeatability and response time, we continue with a small toothed design and the characteristics of the first actuation cycle is used for the controller design due to better stiffness range, linear behavior and a smoother stiffness-temperature profile. Besides, a small enclosed wax volume is considered to reduce the variability of the wax properties at the transition temperature (Fig. 5.5).

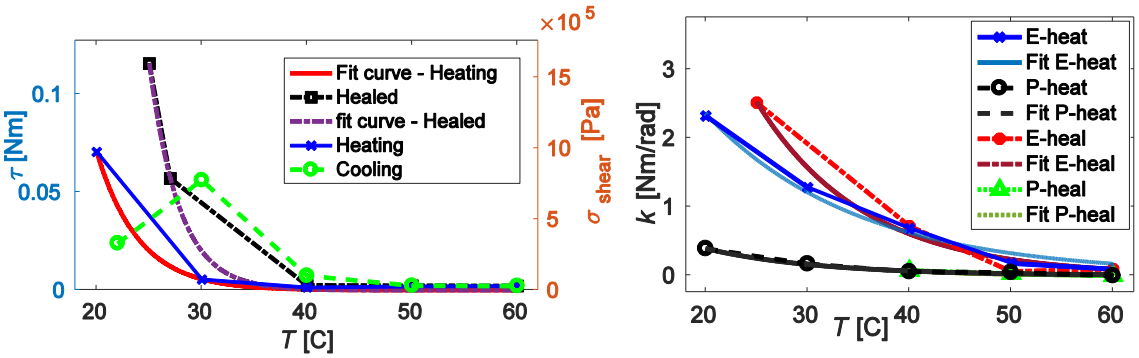

Figure 5.12: (left) Torque and shear stress vs. temperature for heating, cooling and healing control strategies, (right) joint stiffness (k) in elastic (E) and plastic (P) deformations for a single 3D-printed functionally graded joint (Fig. 5.5) in room temperature ($T_0 = 26$ [°C]).

5.5.3 A Single Joint Electro-Thermo-Mechanical Relation

Experimental relations for mean values of current-temperature ($I-T$), temperature-yield torque ($T - \tau_{\mathrm{y}}$) and temperature-elastic and plastic stiffness ($T - k_{\mathrm{E|P}}$) were identified to be used for forward control. A joint, as explained in section 5.3 (Fig. 5.3.b), was fabricated with a handle and a temperature sensor at the joint center (5.5). The temperature of the wax was slightly different from the measured temperature at the joint center and the relations in this section represent properties of the whole system. A similar test setup as in Fig. 5.8 and a switching control was used. The mean heat capacity coefficient of the system was found to be 0.45 [J/°C] from the nearly linear initial heating stage of the temperature control experiments (Fig. 5.11(left)). It takes 70 [s] to melt (50 [°C]) and 120-240 [s] to solidify the wax, 6-12 times faster than the bulky setup in section 5.5.2, with ≈14.5 [s] lag between the current actuation and the temperature increase, almost independent of the temperature, due to the material low thermal conductivity. The system response time is acceptable for most MIS quasi-static operations involving shape locking or configuration adaptation. For $(I - T)$ from Fig. 5.11(right) we have

$$T = C_{\mathrm{H}} 1.235\ \mathrm{e}^{24.4I} + T_0, \tag{5.1}$$

where C_{H} is a correction factor, mainly due to the change in the heat dissipation coefficient, to be set before each run and based on a measurement with the morphological observer. Resetting C_{H} helps with compensating the variation in the temperature range for a constant output range from one trial to another. The variation in the temperature was significant during the test due to the system large thermal response time and inertia. A 5-6 times higher resistance torque for the first actuation cycle, a small drop ($\approx 20-25\%$) in the resisting torque for the next test cycles, offset in initial position and lower resisting torque if the target temperature is lower than the joint initial temperature was observed as in the previous section. The breaking point of the first cycle was considered for the control design (Fig. 5.12(left)). Three temperature regulation strategies were tested; 1) heating, where the desired temperature is higher than the current temperature, 2) cooling, where the desired temperature is lower, 3) healing, where the wax is fully melted at 50 [°C] then cooled (healed) to the desired temperature. τ_{y} varies based on the initial T for the heating and cooling strategies; however, continuous control is possible here. For the material in wax state, the cracks remaining from previous tests in the cooling strategy resulted in a drop in τ_{y} which is unsuitable for real applications. The healing process provides higher τ_{y} and smoother $T-\tau_{\mathrm{y}}$ relation; however, it needs to be executed either very quickly or when the interface is not loaded. For τ_{y} based on the heating strategy, for continuous actuation, and the healing strategy, for static application or when the temperature is reduced, we have

$$\tau_{\mathrm{y}_{\mathrm{heat}}} = 10.69\mathrm{e}^{-0.251T},\ \tau_{\mathrm{y}_{\mathrm{heal}}} = 764.1\mathrm{e}^{-0.3518T}. \tag{5.2}$$

The joint small design resulted in an almost constant and repeatable stiffness during the test cycles and a smooth variation w.r.t. T. The torsional stiffness of the joint ($k_{\mathrm{E|P}}$) as a compound design is (Fig. 5.12(right))

$$\begin{aligned} k_{\mathrm{E}_{\mathrm{heat}}} &= 9.017\mathrm{e}^{-0.06715T}, k_{\mathrm{P}_{\mathrm{heat}}} = 2.328\mathrm{e}^{-0.08929T}, \\ k_{\mathrm{E}_{\mathrm{heal}}} &= 27.37\mathrm{e}^{-0.09533T}, k_{\mathrm{P}_{\mathrm{heal}}} = 12.83\mathrm{e}^{-0.1295T}. \end{aligned} \tag{5.3}$$

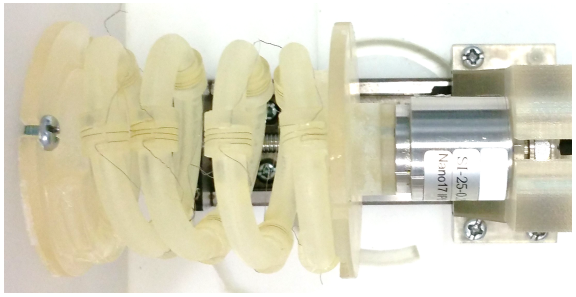

Figure 5.13: Model-based axial stiffness control for a helix with 3.5 turns and 120 [deg] scales.

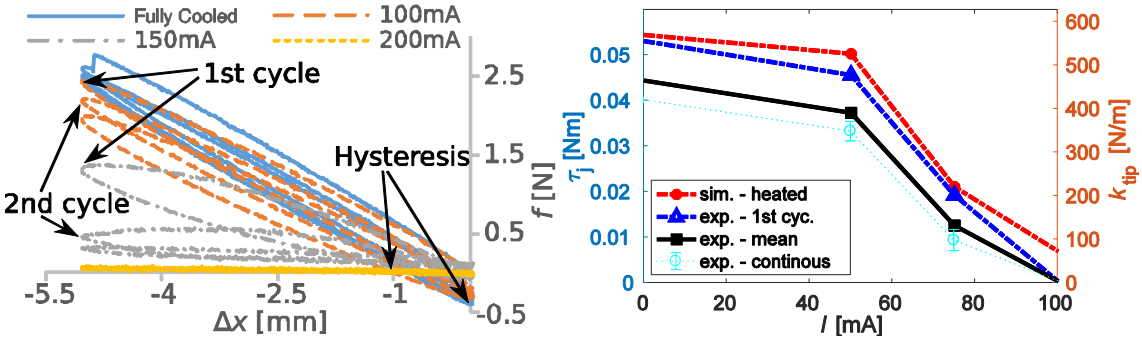

Figure 5.14: Model-based axial stiffness control results, (left) load cycles and (right) achieved stiffness for a helix with 3.5 turns and 120 [deg] scales (Fig. 5.13).

The identified relations were used for feed forward control while a switching bang-bang controller is used to compensate any other feedback error. This approach minimizes the temperature variation, seen in Fig. 5.11(right), in the final controller. The final relations do not consider the wax leakage, due to expansion while heated, from the joint gaps. The joint leakage is repaired, by pouring melted wax on them after a few trials, to maintain the identified properties.

5.6 Thermoactive Interface Experiments and Integration

5.6.1 Model-Based Observation and Control

The model-based observation and control method was used for uniform axial and bending stiffness control of a helical interface sample with 3.5 active turns and 120

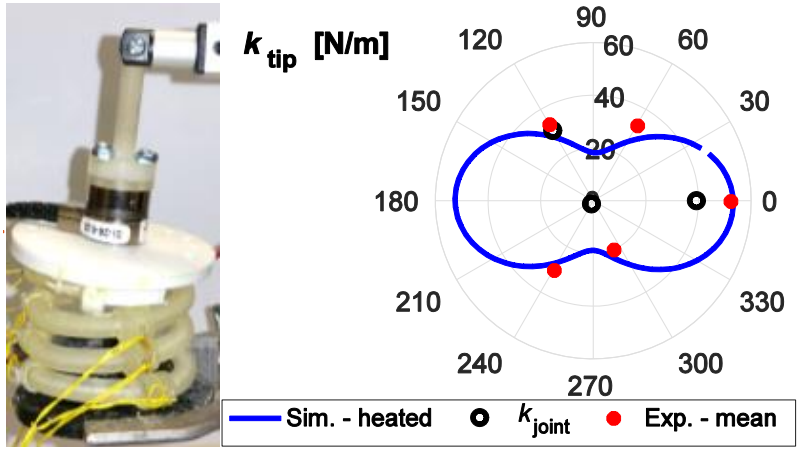

Figure 5.15: Model-based control: anisotropic stiffness control: bending experiment setup and task space stiffness results in polar coordinates.

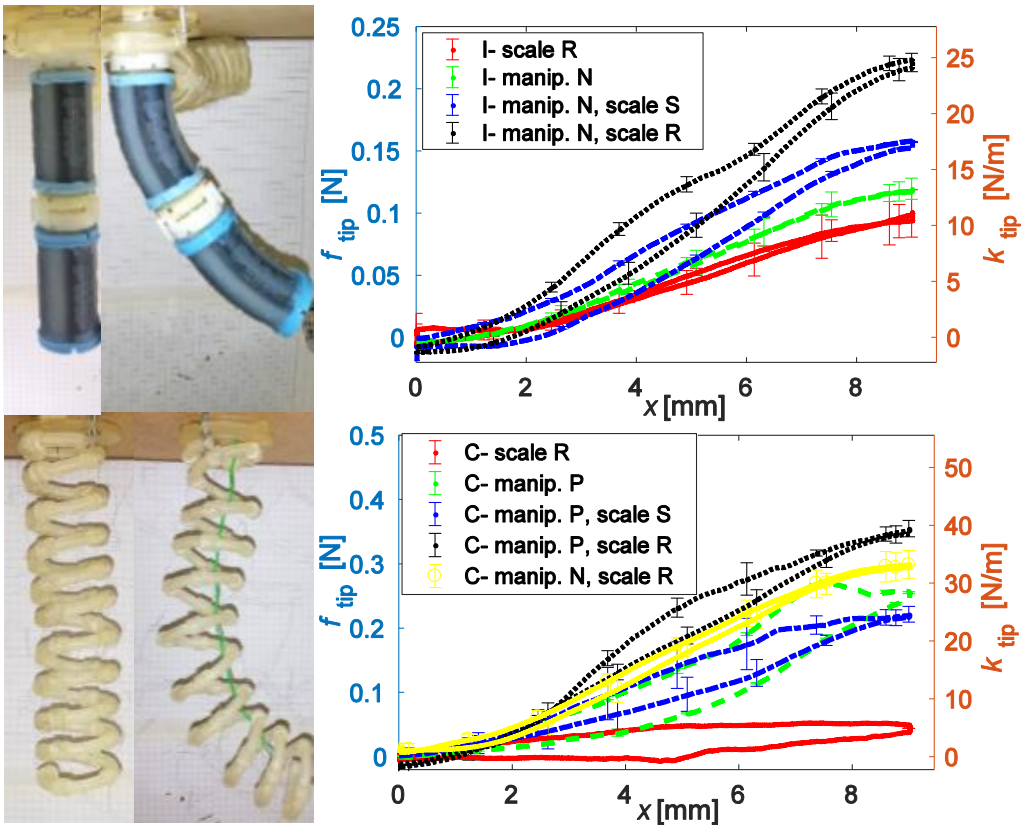

Figure 5.16: Results for a two-module STIFF-FLOP continuum manipulator (manip.) and a nine-turn helical interface with 90 [deg] scales (scale) for a 9 [mm] tip lateral deflection in (top) I: straight and (bottom) C: bent configuration. N: inactive manipulator, P: pressurized (active) manipulator, R: rigid (jammed) interface, S: soft (compliant) interface.

[deg] scales ($J_3 = 6.3e-11, J_1 = 2J_3$) from an initially straight position. A setup as in Fig. 5.6 was used where the current control unit was connected to the common input of an Arduino relay shield controlled by an Arduino Uno SMD Rev3 board.

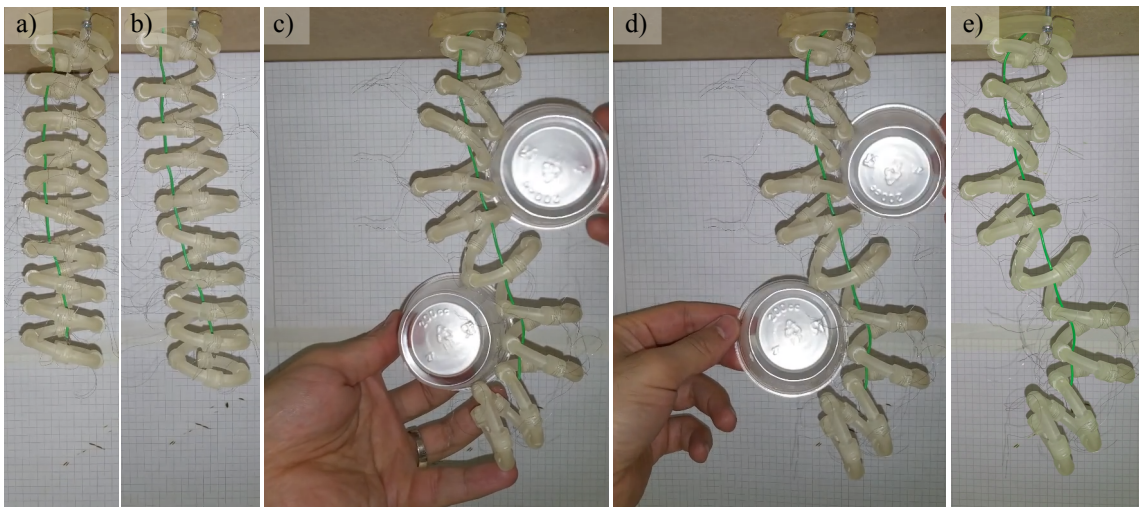

Figure 5.17: (a) Interface passive shape adaptation: initial stiff configuration, (b) compliant configuration by heating up the joints and slight deformation of the interface under body weight, (c) passive shape adaptation of the interface after being pushed by two cylindrical shapes from both sides, (d) cooling off the joints and shape fixing, (e) final fixed shape after removal of the contacting objects.

Each relay was connected to a morphological observer and a row of joints. A HIWIN precision actuator and an ACTUONIX L12 linear actuator (www.robotshop.com) with 10mm stroke were used for axial and bending tests respectively (Fig. 5.16). All the joints were activated with the same current in the axial test. Three measurements, each with three deformation cycles were carried on for each direction. An inhomogeneous stiffness matrix was formed in the bending case with inactive rigid joints at the 0 [deg], 40 °C temperature regulated joints ($I = 80$ [mA]) at 120 [deg] and fully melted ones ($I = 200$ [mA]) at 240 [deg] location. The modeling and control error were 7.5% (27.5 [N/m]) for axial stiffness ($C_1 = 1$, $T_0 = 22$°C, Fig. 5.13 & 5.14) and 14% (4.3 [N/m]) for inhomogeneous bending stiffness control ($C_1 = 2.1$, $T_0 = 22$°C, Fig. 5.15) at the tip. The axial stiffness range was much higher (0-556 [N/m] in axial, 0-62 [N/m] for 90 [deg] scales and 0-32 [N/m] for 120 [deg] scales in bending) due to low bending stiffness of the scales; however, the hysteresis and difference between the first cycle and continuous behavior of the system was lower for the bending stiffness test where the joins undergo a smaller elastic rotation. Directional bending stiffness is coupled with a 120 [deg] scale resulting in a reduced maximum stiffness compared to 90 [deg] scales; however, stiffness con-

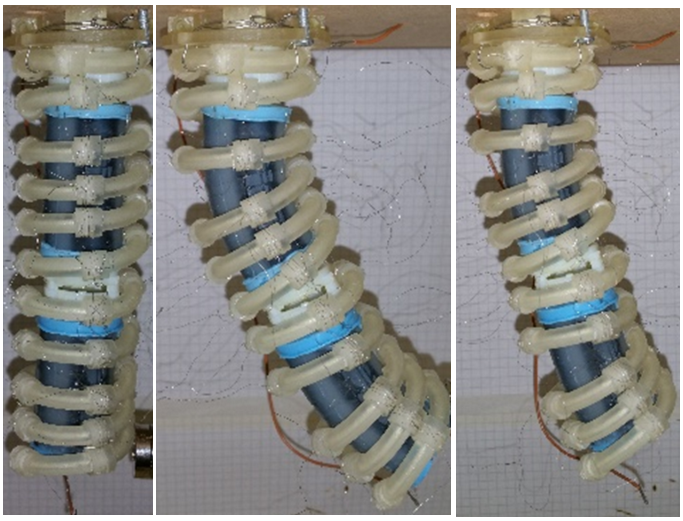

Figure 5.18: The thermoactive interface integrated on a two module STIFF-FLOP continuum manipulator for (left & middle) stiffness control and (left & right) shape locking in the straight and bent configurations. Note that the interface is not able to fully preserve the shape of the manipulator and the manipulator shape is fixed in a configuration with smaller curvature (the difference between the middle figure with active STIFF-FLOP module and the right figure with inactive manipulator).

trol is easier for continuum manipulators with 120 [deg] placement of the actuator chambers. Despite easier stiffness control for continuum manipulators with three actuators, the coupled directional stiffness of 120 [deg] scales results in a smaller maximum stiffness compared to a 90 [deg] one. Our new design has higher axial and bending stiffness compared to our previous tendon scale jamming design with 22 [N/m] axial and 33 [N/m] bending stiffness in similar tests [41].

5.6.2 Integration on a Continuum Manipulator

A helical interface with nine active turns and 90 [deg] scales was integrated on a continuum manipulator with two STIFF-FLOP (STIFFness controllable Flexible and Learn-able manipulator for surgical OPerations) pneumatic actuator modules [16, 15] for stiffness regulation and shape locking in straight and bent configuration (Fig. 5.18 & 5.16). Results for load bearing and stiffness of the interface and the module in a 9 [mm] tip horizontal deflection and for single and interactive actuation ($I = 135$ [mA]) are presented in Fig. 5.16. The module with softened scales needs

Design	**Tip bending stiffness***	**Stiffness change ratio**
STIFF-FLOP	0.51 [KNmm^2]	0
STIFF-FLOP & tendon driven scale jamming interface (Fig. 4.11)	3.6 [N/rad], 5 [KNmm^2]	3.5
STIFF-FLOP & thermoactive scale jamming interface (Fig. 5.18)	3.3 [N/ad], 67 [KNmm^2]	0.4
STIFF-FLOP & granular jamming [16]	14.5 [N/rad]	0.4
STIFF-FLOP & tendon stiffening [59]	12 [N/rad]	2
Granular jamming in literature [21]	0.1-2000 [KNmm^2]	0.5-15
Layer jamming in literature	40-80 [N/rad] [61]	0.7-7 [21]
Inter-locking in literature [21]	0.15-9000 [KNmm^2]	6-50
MIS requirements [61]	17.2 [N/rad] (0.3 [N/deg])	–
Commercially available catheter [21]	15-31 [KNmm^2]	2

* Measured in initial straight configuration.

Table 5.1: Comparisons of manipulator tip bending stiffness, as a commonly used measure in literature, for different stiffening methods used for a STIFF-FLOP continuum manipulator, MIS requirements [61] and commercially available catheters [21].

1.2 [bar] pressure to reach the same configuration that requires only 0.8 [bar] when there is no scale interface. Large system stiffness of STIFF-FLOP modules, to meet the precision and load bearing criteria of most robotic surgeries, make it hard to lock their exact shape (Fig. 5.18.middle & right). Two measurements, each with three deformation cycles were carried out, for each case where good repeatability was observed due to elastic deformation of the joints as a result of the manipulator long length. The tip stiffness in straight configuration (I) was 12 [N/m] for the rigid (R) scale interface, 13.5 [N/m] for the inactive (N) manipulator, 17.5 [N/m] for the manipulator with soft (S) interface (30% increase due to the added friction) and 25 [N/m] for manipulator with rigid scales (43% increase). This value in bent configuration (C) was 5 [N/m] for the rigid interface (interface shape locking), 29 [N/m] for the pressurized (P) manipulator, 25 [N/m] for the manipulator with soft interface

(14% decrease due to the added weight), 40 [N/m] for manipulator with rigid scales (60% increase) and 33 [N/m] for shape locking of the inactive manipulator (Fig. 5.16). The scale stiffness is lower in the bent case due to the body weight effect and concentration of the deformation at the root joints. The friction between the manipulator and scale interface in the soft state adds some hysteresis to the system in the straight case, but the hysteresis reduces in the bent case because of the helical interface act as a secondary external braid. The total stiffness in the straight case is a linear combination of the scale and manipulator stiffness; however, this value is higher for than the simple summation of stiffness for the bent case, because the manipulator causes a uniform distribution of deformation along the interface joints. This shows the interactive functionality of the interface and manipulator in the bent case which results in lowering the hysteresis and higher stiffness values than expected.

The tip bending stiffness when integrated on two STIFF-FLOP modules (straight: 2.3-3.3 [N/rad], 47-67 [KNmm^2], 43% increase, bent: 3.6-5.7 [N/rad], 73-118 [KNmm^2], 60% increase) is higher than the commercially available endoscopes (15-31 [KNmm^2]) [21], less than the desired value for MIS (17.2 [N/rad]) [61], and similar to low stiffness range granular and layer jamming designs [21]. This design has the best shape locking ability and the highest tip stiffness increase (straight: 43%, bent: 60%) compared to a STIFF-FLOP module with granular jamming (straight: 43%, bent: 18%) [16] and tendon antagonistic stiffening (straight: 94%, bent: 24.3% increase) [59], both with limited shape locking. Local and directional stiffness controllability, higher uniform load-bearing for long designs and similar simple integration are the advantages of the current design compared to our previous tendon scale jamming approach [41]. Besides better scalability, due to omitting tendon routing friction, and local and directional stiffness controllability, the presented design benefits from high load-bearing to weight ratio, axial stretch and simple integration similar to our previous tendon-driven interface [41], but presents lower stiffness increase (straight: 83%, bent: 330%), due to the contribution of the tendon stiffness, and suffers from

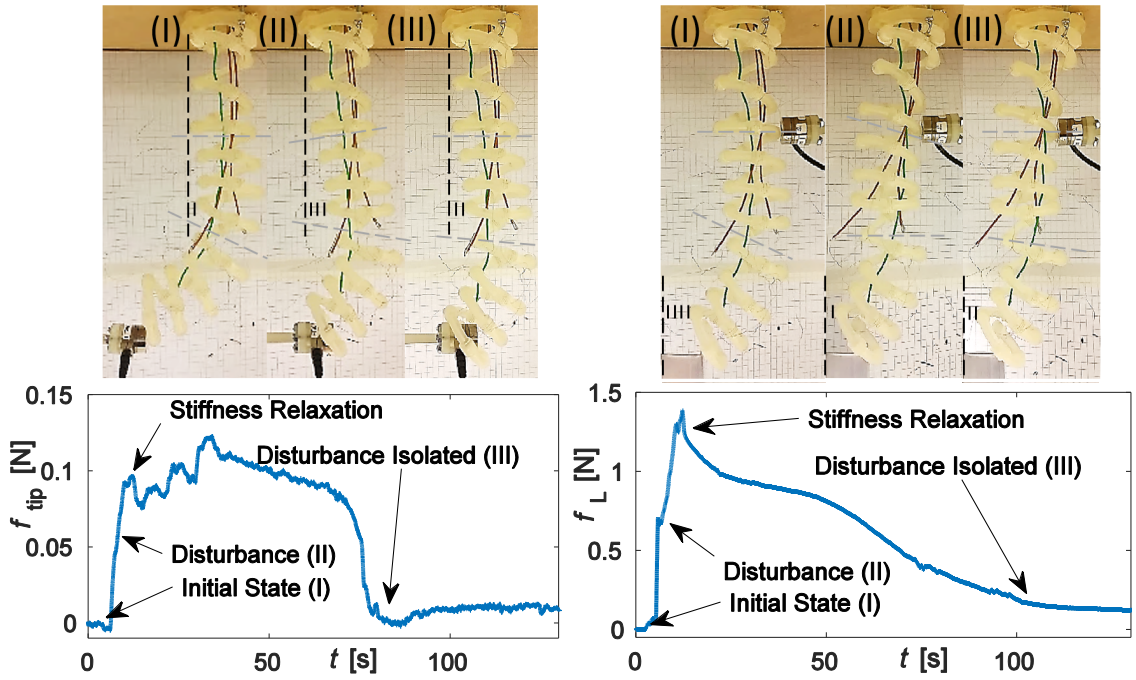

Figure 5.19: Preliminary results for (left) tip and (right) backbone disturbance rejection through passive shape adaptation with three independent stiffness controllable elements: (I) initial state, (II) disturbance, (III) effect isolation. The background grids, marked with a dash reference line and small black lines as distance units, are used to calculate the configuration disturbance recovery.

higher hysteresis, nonlinear behavior and lower repeatability. These issues can be addressed by an improved design based on a detailed heat transfer analysis, passing the interface through a helical tube filled with coolant fluid, proper isolation of the heating wires, using multiple parallel helical strands and changing the scale dimensions for better shape locking and stiffness range. Table 5.1 presents a summary of the results in comparison to the relevant designs in literature.

5.6.3 Simple Switching Control

The proposed simple switching controller was successfully used for passive shape adaptation (Fig. 5.17), tip force regulation and isolation (Fig. 5.19.left) and backbone impedance disturbance isolation (Fig. 5.19.right) of the helical interface. In Fig. 5.19.left, a force sensor is pushed against the interface tip. Fig. 5.19.right, the tip is leaning against a fixed obstacle while a force sensor is pushed against an arbitrary point along interface backbone. The stiffness of three elements along

the interface were controlled separately. The simple control method only decreases the stiffness of the adjacent elements to a configuration disturbance to cancel the external load and isolate its effects through passive shape adaptation. The background grids at the isolating element border in Fig. 5.19.left and at the tip in Fig. 5.19.right, marked with a dash reference line and small black lines as distance units, are used to calculate the configuration disturbance recovery percentage. The ratio of the final force value after the disturbance rejection to its pick value is used to calculate the force disturbance recovery percentage.

50% of the configuration at the element borders and 92% of the external force in the tip disturbance case (Fig. 5.19.left) and 33% of the configuration and 91% of the external force in the backbone disturbance case (Fig. 5.19.right) are canceled in less than 90 [s]. However, the recovery is limited due to the passive shape adaptation, meaning that the interface body weight is the only force that brings the interface to a relaxed configuration, with configuration and force disturbance isolated. An active control method is needed to take the backbone configuration, at the borders of the isolating elements, to its undisturbed shape for a full recovery.

5.7 Conclusion

A thermoactive scale jamming interface is 3D-printed with a commercially available device as both a new way to control a continuum manipulator dexterity and a method to fabricate general mechanisms with thermoactive functionally graded designs. The interface compliance is regulated by controlling the joints' wax temperature for which empirical relations are identified. The common problems of poor repeatability and response time with low melting point material are addressed with a small wax enclosure design and using empirical relations in the controller design. Novel morphological observation and decentralized control approaches are employed based on which a minimal central controller is implemented. Prelimi-

nary results for passive shape adaptation, geometrical disturbance rejection and task space anisotropic stiffness regulation are presented by integration of the interface on a continuum manipulator. Our results show potential of our platform and method for stiffness planning of continuum manipulators, especially for quasi-static operations in cold environments such as underwater and space. Similar functionally graded thermoactive jamming designs can be fabricated, e.g. a layer jamming design with interlayer thermoactive material for stiffness regulation. Besides, a similar joint idea can be used in designing different stiffness controllable structures.

Despite our promising results, the proposed design in this chapter is the proof of concept stage and needs more modification and analysis with an application-oriented perspective to be used in real-world engineering applications. As mentioned earlier, the issues with high temperature, slow response and stochastic phase change of the wax can be addressed by an improved design based on a detailed heat transfer analysis, passing the interface through a helical tube filled with coolant fluid, proper isolation of the heating wires, using multiple parallel helical strands and changing the scale dimensions for better shape locking and stiffness range. Before making any further claim about the integrability of our design on different continuum manipulators, the design criteria of such interface should be established. This helps addressing issues with miniaturization and scalability of the interface for micro robotic systems and clinical implementation of this technology in the future. The proposed concept for a morphological observer is introduced and implemented to address the lack of in-built sensing in our setup. A dedicated investigation is needed to define a morphological observer, discuss the novelties and similarities of this concept with previous research on morphological computation. The stability and robustness of the proposed morphological observer and decentralized controller designs need to be investigated when the interface is integrated on a continuum manipulator. This is more important when keeping in mind that the presented experimental results in this chapter and chapter 3 are based on a single module continuum manipulator. The limitations of using a minimal central controller with

a few stiffness controller units should be investigated further. A drawback of using such design is that the stiffness of different elements cannot be controlled in parallel and simultaneously. Besides, the effects of any differences, between the morphological observer environment and those of its counterparts on the helical interface, need to be studied in details. Finally, while in theory, the method should be applicable to a manipulator with any number of segments, this claim should be verified with further numerical and experimental studies based on an integration of the interface on a manipulator with more actuator segments. In the next chapter, a conclusion is presented where the methods and designs improvements, identified opportunities and challenges, possible applications and open questions followed by the research presented in this thesis are summarized.

Chapter 6

Conclusion

6.1 Summary of Thesis Achievements

This thesis investigates how the problem of stiffness regulation of continuum manipulators can be simplified by inspiration from morphology of biological fish scales and experimental observations of manipulator geometry deformations.

To this end, a comparative study of five main methods in the literature for kinematic, static and dynamic modeling of continuum manipulators is presented in a unified mathematical framework. The five widely used methods of Lumped system dynamic model, Constant curvature, two-step modified constant curvature, variable curvature Cosserat rod and beam theory approach, and series solution identification are reviewed here with derivation details in order to clarify their methodological differences. A comparison between computer simulations and experimental results using a STIFF-FLOP continuum manipulator is presented to study the advantages of each modeling method.

After a careful review and comparative study of current geometry and stiffness control and modeling of continuum manipulators, two new modeling approaches are introduced to improve the accuracy and reduce the state space dimension of dy-

namic models for braided continuum manipulators. We incorporate the mechanical effect of the axial and circumferential highly elastic deformations of the manipulator and assume an analytical framework to describe the geometry deformations of the manipulator based on our experimental observations. For the first time, we introduce the bending effect in the model of a braided extensile pneumatic actuator with both stiff and bendable threads. Then, the effect of the manipulator cross-section deformation on the constant curvature and variable curvature models is investigated using simple analytical results from a novel geometry deformation method and is compared to experimental results. We achieve 38% mean reference error simulation accuracy using our constant curvature model for a braided continuum manipulator in the presence of body load and 10% using our variable curvature model in the presence of extensive external loads. With proper model assumptions and taking into account the cross-sectional deformations, a 713% increase in the simulation mean error accuracy is achieved compared to a fixed cross-section model. The presented models can be used for the exact modeling and design optimization of compound continuum manipulators by providing an analytical tool for the sensitivity analysis of the manipulator performance. Our main aim is the application in minimal invasive manipulation with limited workspaces and manipulators with regional tunable stiffness in their cross section.

Extending our work to model the manipulator backbone general deformation, we introduce a novel real-time series solution for the variable-curvature Cosserat rod static model and Lagrangian dynamic model of continuum manipulators in the presence of significant external and body loads, by combining a modified Lagrange polynomial series-solution based on experimental observations with Ritz and Ritz-Galerkin methods. As a result, the infinite control state space is minimized to geometrical positions of a few number of points (in our case two) and the dynamic force, position and configuration nonlinear control scenarios are derived in a unified easy to implement vector formalism. The model is verified against experiments in a planar and general 3D scenarios, showing that the proposed Ritz-Galerkin method mean

error is 6-8% (4-6 [mm]) and 16-20% (12-14 [mm]) for the Ritz solution in the dynamic case. Our static solution is as accurate as the simple interpolation solution for the Cosserat rod static model. Comparing to five different models in the literature, our approximate solution is shown to be more accurate with the smallest possible number of states and suitable for real-time modeling, observation and control. We showed that by considering the mechanical effects of axial highly elastic deformation, the model accuracy is increased by up to 6%.

After successful implementation of our geometry deformation approaches to model compound braided continuum manipulators, two novel integrable helical interfaces inspired by the shape and special arrangement of fish scales is designed in which the stiffness is adjustable through tendon driven actuation, as a way for active modulation of the normal force on the jamming scales, and use of thermoactive stiffness tunable composite in-between the scale layers, as a means for regulation of the inter-layer coefficient of friction.

Estimating about the possibility of biological scale jamming in real fish, we try to understand the possible underlying actuation mechanism of such a behavior in a real fish. We conduct experiments on a real fish skin in the jammed and unjammed cases for simple compression, bending and bulking scenarios. The skin is encapsulated in a thin latex layer and the scales are jammed through creating a vacuum inside the latex layers. This shows the possibility of biological scale jamming in a real fish skin through modulation of the normal force between the scales especially when they are on the inner side of the bend. We observed a functional characteristic for the biological scales in jamming. Very small hysteresis for the jammed skin is identified as the normal force and the overlapping area of the scales increase. It is possible that the biological jamming can occur passively due to the water external pressure and body configuration as the fish body bends. The unique functional characteristics of the scales may contribute in increasing the swimming locomotion energy efficiency by tuning the structure stiffness.

We present the idea of scale jamming inspired by fish and snake scales to control the stiffness of continuum manipulators by modulating the Coulomb friction force between rigid scales. A low stiffness spring is used as the backbone for a set of round curved scales to maintain an initial helix formation while two thin fishing steel wires are used to control the friction force by tensioning. The effectiveness of the design is shown for simple elongation and bending through mathematical modeling, experiments and in comparison to similar research. The model is tested to control the bending stiffness of a STIFF-FLOP continuum manipulator module designed for surgery. High stiffness range, very low hysteresis and easy integration to different manipulator designs are the advantages of our jamming interface compared to the previous research.

Then, we investigate the possibility of implementing stiffness control as a new source of robots dexterity and flexibility control. Using a combination of UV curable acrylic plastic and hydroxylated wax being used as high definition 3D printer support material, we were able to design a highly articulated helical interface capable of modulating their resistance to deformation through the injection of joint temperature, meaning that low temperatures lead to high stiffness and low compliance, while high temperatures lead to low stiffness and high compliance. This temperature is induced via nichrome wire heating elements. Our results establish a clear relationship between temperature change and system compliance through a comprehensive study on the wax melting profile and the join different design. Future concepts involve the mathematical analysis and fabrication of a helical arrangement with precise control over the tip directional and local stiffness matrix. A minimalistic control approach is used for the stiffness regulation and temperature control of all the joints through Joule heating by implementing a novel morphological observer using a logical switching board and a current control unit. Other applications may involve the use of origami structures to change their shapes through the modification of their stiffness joints.

Our model enables us to better understand the elastic and damping behavior of a

jamming design and introduce equivalent coefficients for a simpler controller design. Using this model, we identify the effective parameters and optimize our scale jamming design for minimum hysteresis and increased repeatability as the two main problems with the stiffness tunable jamming designs in the literature.

Finally, By creating a relationship between the finite element analysis and the real morphology of a continuum manipulator, a new decentralized morphological approach is presented to regulate the regional stiffness of a continuum manipulator for configuration disturbance rejection and task space stiffness modulation. To investigate the performance of our decentralized controller, a setup is built consisting of our stiffness tunable interface integrated on a braided pneumatic continuum manipulator. We verify our design and control approach in maintaining the task space stiffness in the presence of the configuration disturbances for the application of soft tissue palpation. We believe, our analytical approach toward morphological design, identification and control of bio-inspired robotic platforms to achieve enhanced engineering performance and deeper understanding of the natural behavior of their biological counterpart, can be a standard practice in the future research in the field of morphological computation.

The presented geometry deformation based models for the manipulator cross-section and backbone, which are developed and compared based on our earlier comparative study on the different commonly used models for continuum manipulators, provides a basis for exact real-time modeling of compound structure continuum manipulators. These models are used later as a part of a two-step model for stiffness control and planning of the manipulator, covered with the presented designs for an integrable scale jamming interface. These interfaces are designed by taking inspiration from geometrical jamming of real fish scales after careful experiments on jamming properties of different fish skin samples. Different bio-inspired scale geometries (with tangential and radial jamming force) and actuation mechanism (tendon, SMA and thermoactive joints) are tested and compared with other stiffening solutions for medical applications. Finally, decentralized morphological control and observation

are investigated to simplify the complex problem of stiffness planning and controller design of such compound structure. In summary, this thesis presents the following novel principles:

- The advantages of the lumped model for dynamic control, Constant Curvature models for estimation and observation, Cosserat rod models for accurate general modeling and identification based methods for real-time control is discussed.

- Gathering most of the advantages of the different discussed models, i.e. accuracy, generality, real-time implementation and suitability for control design, is possible using shape function based semi-analytical solutions.

- To this end, the manipulator cross-section and backbone are modeled based on empirical observations of the manipulator geometry deformation that reduces the infinite modeling state space of such problems to the coordinates of a few number of points along the backbone. 6% absolute error, which is the smallest achieved error in our comparison, and 7-13% increase in the accuracy by considering the cross-section exact deformation are the results of such approach. Using real stress and strain are the key considerations to achieve such accuracy.

- A detailed analysis shows considering complex structural deformation using an analytical model helps with accurate sensitivity analysis which is necessary for design optimization only if reasonable assumptions and combination of models are taken into account.

- The possibility of biological scale jamming in a real fish skin, due to the biological scale special morphology and special inclined stacking formation in jamming, is observed in experiments which shows the possible role of a jamming mechanism in stiffness modulation of the fish body.

- As a result, for the first time, we proposed that a reversible and smooth load cycle with small hysteresis for jamming media is possible using geometrical jamming instead of traditional friction-based jamming.

- The geometrical jamming idea is tested based on three bio-inspired scale jamming interface designs, suitable for stiffness control of different types of continuum manipulators. The presented tendon driven design is the first and only jamming enable design that presents a very small hysteresis in the full return cycle. The thermoactive design provides the most comprehensive control over local and directional stiffness available for continuum manipulators.

- Modeling and control of the presented integrable interface on a continuum manipulator, consisting of STIFF-FLOP modules in our case, is possible with a two-step model where the manipulator element stiffness in the Cosserat rod model framework is pre-calculated based on a piecewise model for the equivalent stiffness of the integrated section of the scale jamming interface.

- We showed that the estimating model in a traditional observer can be substituted with the morphological computational power of a fully monitored physical replica of the actual system. This is called a morphological observer.

- The importance of a decentralized control framework is presented to simplify the stiffness planning task and controller setup design. This is supported by experimental results for impedance rejection at the tip and along the backbone of our helical scale jamming interface.

6.2 Applications

The main applications of the presented methods and designs in this thesis are as follows.

- Our comparative study helps choosing the right modeling approach in different research on continuum manipulators based on their applications and requirements.

- Our analytical models help with design optimization of more capable manipulators for medical and inspection applications based on sensitivity analysis of important structural parameters

- Real-time accurate modeling, control and disturbance rejection of continuum manipulators' configuration and impedance is possible with our model state space reduction and decentralized morphological control approach.

- Our easily integrable helical interface can be used for stiffness control of a wide range of different continuum manipulators in different applications.

- The main application of this work is in the field of Medical Diagnosis, Minimal Invasive Surgery and rehabilitation where stiffness controllable continuum manipulators are emerging for their combined safe interaction and precise task space control.

- Our modeling and stiffness control approach is useful for the application of continuum manipulators for inspection, maintenance and repair in underwater, space and disastrous environments.

- Our bio-inspired design and experiments can help unraveling the underlying principle of the similar behavior, scale jamming in this case, in nature.

- Our 3D-printed functionally graded design with a conventional 3D-printing machine can be used in fabrication of other deployable and origami mechanisms with stiffness controllable joints.

- The proposed control space reduction, decentralized control and morphological observation approach can be used in similar research on soft robots.

6.3 Future Work

The discussed methods and designs in this thesis can be improved and tested in more realistic environments in the future research by considering the following suggestions.

- As the main goal of the developed methods in this thesis, the integrated scale jamming interface on a continuum manipulator can be tested for more realistic medical tasks such as soft tissue palpation and manipulation.
- The proposed state reduction for continuum manipulator modeling can be extended to be used for stiffness imaging and observation in realistic medical applications.
- The contribution of the unique functional characteristics of the scales in increasing the swimming locomotion energy efficiency can be investigated further. For example, the scales may contribute in tuning the structure stiffness for effective trust generation during the tail motion cycle, or storing kinetic energy of the body at the end of each cycle, when they are fully jammed, to be used for easier initiation of the next cycle.
- The use of low friction geometrical jamming can be investigated further by looking into similar concepts in granular and layer jamming designs and its similarities with rheological fluids.
- The design of the scale jamming interfaces can be improved for better repeatability and uniform linear performance.
- A miniature metallic scale design with radial force actuation, low stiffness spring backbone and roller bearings for the wire contact points can be fabricated to combine all the advantages of the presented helical scale jamming interface in this research.
- The same geometrical feature, that enabled a helical interface to possess local and directional stiffness controllablity with easy modulation of helix cross

section torsional stiffness, can inspire the design of a tendril actuator interface based on SMA wires.

- A dedicated investigation is needed to define a morphological observer, discuss the novelties and similarities of this concept with previous research on morphological computation.

- The stability and robustness of the proposed morphological observer and decentralized controller designs need to be investigated.

- Similar functionally graded thermoactive jamming designs can be fabricated, such as a layer jamming design with interlayer thermoactive material for stiffness regulation. Besides, a similar joint idea can be used in designing different stiffness controllable structures.

Bibliography

[1] A. Albu-Schffer and A. Bicchi, "Actuators for Soft Robotics," in *Springer Handbook of Robotics*, pp. 499–530, Cham: Springer International Publishing, 2016.

[2] H. Tomori, S. Nagai, T. Majima, and T. Nakamura, "Variable impedance control with an artificial muscle manipulator using instantaneous force and MR brake," in *2013 IEEE/RSJ International Conference on Intelligent Robots and Systems*, pp. 5396–5403, Nov. 2013.

[3] Y. Zhu, J. Yang, H. Jin, X. Zang, and J. Zhao, "Design and evaluation of a parallel-series elastic actuator for lower limb exoskeletons," in *2014 IEEE International Conference on Robotics and Automation (ICRA)*, pp. 1335–1340, May 2014.

[4] F. Maghooa, A. Stilli, Y. Noh, K. Althoefer, and H. A. Wurdemann, "Tendon and pressure actuation for a bio-inspired manipulator based on an antagonistic principle," in *2015 IEEE International Conference on Robotics and Automation (ICRA)*, (Seattle, WA, USA), pp. 2556–2561, IEEE, May 2015.

[5] M. Chalon, W. Friedl, J. Reinecke, T. Wimboeck, and A. Albu-Schaeffer, "Impedance control of a non-linearly coupled tendon driven thumb," in *2011 IEEE/RSJ International Conference on Intelligent Robots and Systems*, pp. 4215–4221, Sept. 2011.

[6] U. K. Mller and J. L. Van Leeuwen, "Undulatory fish swimming: From muscles to flow," *Fish and Fisheries*, vol. 7, no. 2, pp. 84–103, 2006.

[7] K. Yuse, D. Guyomar, D. Audigier, A. Eddiai, M. Meddad, and Y. Boughaleb, "Adaptive control of stiffness by electroactive polyurethane," *Sensors and Actuators A: Physical*, vol. 189, pp. 80–85, Jan. 2013.

[8] Q. Luo and L. Tong, "Adaptive pressure-controlled cellular structures for shape morphing I: design and analysis," *Smart Materials and Structures*, vol. 22, no. 5, p. 055014, 2013.

[9] M. Laffranchi, N. G. Tsagarakis, and D. G. Caldwell, "Compact arm: a compliant manipulator with intrinsic variable physical damping," in *Robotics: Science and Systems*, vol. 8, p. 225, 2013.

[10] M. S. Erden and A. Billard, "Hand Impedance Measurements During Interactive Manual Welding With a Robot," *IEEE Transactions on Robotics*, vol. 31, pp. 168–179, Feb. 2015.

[11] J. Burgner-Kahrs, D. C. Rucker, and H. Choset, "Continuum Robots for Medical Applications: A Survey," *IEEE Transactions on Robotics*, vol. 31, pp. 1261–1280, Dec. 2015.

[12] M. Cianchetti and A. Menciassi, "Soft Robots in Surgery," in *Soft Robotics: Trends, Applications and Challenges*, vol. 9 of *Biosystems & Biorobotics*, pp. 75–85, Springer International Publishing, 1 ed., 2017. DOI: 10.1007/978-3-319-46460-2.

[13] K. Suzumori, S. Iikura, and H. Tanaka, "Flexible microactuator for miniature robots," in *[1991] Proceedings. IEEE Micro Electro Mechanical Systems*, pp. 204–209, Jan. 1991.

[14] W. McMahan, V. Chitrakaran, M. Csencsits, D. Dawson, I. D. Walker, B. Jones, M. Pritts, D. Dienno, M. Grissom, and C. D. Rahn, "Field trials and testing of the OcotArm continuum manipulator," in *Proceedings of*

the 2006 IEEE international conference on robotics and automation (ICRA), pp. 2336–2341, 2006.

[15] J. Fras, J. Czarnowski, M. Macia, J. Gwka, M. Cianchetti, and A. Menciassi, "New STIFF-FLOP module construction idea for improved actuation and sensing," in *2015 IEEE International Conference on Robotics and Automation (ICRA)*, pp. 2901–2906, May 2015.

[16] M. Cianchetti, T. Ranzani, G. Gerboni, I. De Falco, C. Laschi, and A. Menciassi, "STIFF-FLOP surgical manipulator: Mechanical design and experimental characterization of the single module," in *IEEE International Conference on Intelligent Robots and Systems (IROS)*, (Tokyo, Japan), pp. 3576–3581, IEEE, 2013.

[17] T. Ranzani, M. Cianchetti, G. Gerboni, I. D. Falco, G. Petroni, and A. Menciassi, "A modular soft manipulator with variable stiffness," no. September, pp. 11–14, 2013.

[18] K. Suzumori, T. Maeda, H. Watanabe, and T. Hisada, "Fiberless flexible microactuator designed by finite-element method," *IEEE/ASME Transactions on Mechatronics*, vol. 2, no. 4, pp. 281–286, 1997.

[19] A. D. Marchese and D. Rus, "Design, kinematics, and control of a soft spatial fluidic elastomer manipulator," *The International Journal of Robotics Research*, vol. 35, pp. 840–869, June 2016.

[20] R. J. Webster and B. A. Jones, "Design and Kinematic Modeling of Constant Curvature Continuum Robots: A Review," *The International Journal of Robotics Research*, vol. 29, no. 13, pp. 1661–1683, 2010.

[21] L. Blanc, A. Delchambre, and P. Lambert, "Flexible Medical Devices: Review of Controllable Stiffness Solutions," *Actuators*, vol. 6, p. 23, July 2017.

[22] S. Sareh, A. Jiang, A. Faragasso, Y. Noh, T. Nanayakkara, P. Dasgupta, L. D. Seneviratne, H. A. Wurdemann, and K. Althoefer, "Bio-inspired tactile sensor

sleeve for surgical soft manipulators," in *2014 IEEE International Conference on Robotics and Automation (ICRA)*, pp. 1454–1459, May 2014.

[23] M. Manti, V. Cacucciolo, and M. Cianchetti, "Stiffening in Soft Robotics: A Review of the State of the Art," *IEEE Robotics & Automation Magazine*, vol. 23, pp. 93–106, Sept. 2016. 00000.

[24] W. McMahan, B. A. Jones, I. D. Walker, W. McMahan B. A. Jones, I. D. Walker, W. McMahan, B. A. Jones, and I. D. Walker, "Design and implementation of a multi-section continuum robot: Air-octor," in *2005 IEEE/RSJ International Conference on Intelligent Robots and Systems, IROS*, pp. 3345–3352, 2005.

[25] I. S. Godage, E. Guglielmino, D. T. Branson, G. A. Medrano-Cerda, and D. G. Caldwell, "Novel modal approach for kinematics of multisection continuum arms," in *IEEE International Conference on Intelligent Robots and Systems (IROS)*, (San Francisco, California, USA), pp. 1093–1098, IEEE, 2011. 00034.

[26] M. Cianchetti, T. Ranzani, G. Gerboni, T. Nanayakkara, K. Althoefer, P. Dasgupta, and A. Menciassi, "Soft Robotics Technologies to Address Shortcomings in Today's Minimally Invasive Surgery: The STIFF-FLOP Approach," *Soft Robotics*, vol. 1, no. 2, pp. 122–131, 2014.

[27] J. S. Mehling, M. A. Diftler, M. Chu, and M. Valvo, "A minimally invasive tendril robot for in-space inspection," in *Proceedings of the First IEEE/RAS-EMBS International Conference on Biomedical Robotics and Biomechatronics, 2006, BioRob 2006*, vol. 2006, (Pisa, Italy), pp. 690–695, IEEE, 2006. 00035.

[28] C. Laschi, M. Cianchetti, B. Mazzolai, L. Margheri, M. Follador, and P. Dario, "Soft Robot Arm Inspired by the Octopus," *Advanced Robotics*, vol. 26, no. 7, pp. 709–727, 2012.

[29] D. Zhu, C. F. Ortega, R. Motamedi, L. Szewciw, F. Vernerey, and F. Barthelat, "Structure and mechanical performance of a "modern" fish scale," *Advanced Engineering Materials*, vol. 14, no. 4, 2012.

[30] F. J. Vernerey and F. Barthelat, "On the mechanics of fishscale structures," *International Journal of Solids and Structures*, vol. 47, no. 17, pp. 2268–2275, 2010.

[31] X. Dong, D. Axinte, D. Palmer, S. Cobos, M. Raffles, A. Rabani, and J. Kell, "Development of a slender continuum robotic system for on-wing inspection/repair of gas turbine engines," *Robotics and Computer-Integrated Manufacturing*, vol. 44, pp. 218–229, Apr. 2017.

[32] D. Nahar, P. M. Yanik, and I. D. Walker, "Robot tendrils: Long, thin continuum robots for inspection in space operations," in *2017 IEEE Aerospace Conference*, pp. 1–8, Mar. 2017.

[33] V. Wall, R. Deimel, and O. Brock, "Selective Stiffening of Soft Actuators Based on Jamming," *2015 IEEE International Conference on Robotics and Automation (ICRA)*, pp. 252–257, May 2015. 00006.

[34] N. G. Cheng, M. B. Lobovsky, S. J. Keating, A. M. Setapen, K. I. Gero, A. E. Hosoi, and K. D. Iagnemma, "Design and analysis of a robust, low-cost, highly articulated manipulator enabled by jamming of granular media," *Proceedings - IEEE International Conference on Robotics and Automation*, pp. 4328–4333, May 2012.

[35] A. Jiang, A. Ataollahi, K. Althoefer, P. Dasgupta, and T. Nanayakkara, "A variable stiffness joint by granular jamming," *Proceedings of the ASME Design Engineering Technical Conference*, vol. 4, no. PARTS A AND B, pp. 267–275, 2012.

[36] S. Hauser, P. Eckert, A. Tuleu, and A. Ijspeert, "Friction and damping of a compliant foot based on granular jamming for legged robots," in *2016 6th*

IEEE International Conference on Biomedical Robotics and Biomechatronics (BioRob), pp. 1160–1165, IEEE, June 2016. 00000.

[37] A. A. Stanley and A. M. Okamura, "Deformable Model-Based Methods for Shape Control of a Haptic Jamming Surface," *Visualization and Computer Graphics, IEEE Transactions on*, vol. PP, no. 99, pp. 1–1, 2016. 00000.

[38] J. L. C. Santiago, I. S. Godage, P. Gonthina, and I. D. Walker, "Soft Robots and Kangaroo Tails: Modulating Compliance in Continuum Structures Through Mechanical Layer Jamming," *Soft Robotics*, pp. soro.2015.0021–soro.2015.0021, June 2016.

[39] A. Jiang, T. Aste, P. Dasgupta, K. Althoefer, and T. Nanayakkara, "Granular jamming transitions for a robotic mechanism," *AIP Conference Proceedings*, vol. 1542, pp. 385–388, 2013. 00000.

[40] N. Cheng, J. Amend, T. Farrell, D. Latour, C. Martinez, J. Johansson, A. McNicoll, M. Wartenberg, S. Naseef, W. Hanson, and W. Culley, "Prosthetic Jamming Terminal Device: A Case Study of Untethered Soft Robotics," *Soft Robotics*, pp. soro.2016.0017–soro.2016.0017, Sept. 2016.

[41] S. M. H. Sadati, Y. Noh, S. E. Naghibi, A. Kaspar, and T. Nanayakkara, "Stiffness Control of Soft Robotic Manipulator for Minimally Invasive Surgery (MIS) Using Scale Jamming," in *Intelligent Robotics and Applications*, Lecture Notes in Computer Science, pp. 141–151, Springer, Cham, Aug. 2015.

[42] A. Ataollahi, R. Karim, A. S. Fallah, K. Rhode, R. Razavi, L. D. Seneviratne, T. Schaeffter, and K. Althoefer, "Three-Degree-of-Freedom MR-Compatible Multisegment Cardiac Catheter Steering Mechanism," *IEEE Transactions on Biomedical Engineering*, vol. 63, pp. 2425–2435, Nov. 2016.

[43] I. M. Van Meerbeek, B. C. Mac Murray, J. W. Kim, S. S. Robinson, P. X. Zou, M. N. Silberstein, and R. F. Shepherd, "Morphing Metal and Elastomer

Bicontinuous Foams for Reversible Stiffness, Shape Memory, and Self-Healing Soft Machines," *Advanced Materials*, vol. 28, pp. 2801–2806, Apr. 2016.

[44] J. Shintake, B. Schubert, S. Rosset, H. Shea, and D. Floreano, "Variable Stiffness Actuator for Soft Robotics Using Dielectric Elastomer and Low-Melting-Point Alloy Soft state," *IEEE/RSJ International Conference on Intelligent Robots and Systems (IROS)*, pp. 1097–1102, 2015.

[45] A. Tonazzini, S. Mintchev, B. Schubert, B. Mazzolai, J. Shintake, and D. Floreano, "Variable Stiffness Fiber with Self-Healing Capability," *Advanced Materials*, pp. n/a–n/a, Sept. 2016.

[46] S. H. E. E. Jeong, *Liquids Matter in Compliant Microsystems*. 2016. 00000.

[47] S. Janbaz, R. Hedayati, and A. A. Zadpoor, "Programming the shape-shifting of flat soft matter: from self-rolling/self-twisting materials to self-folding origami," vol. 3, pp. 536–547, Oct. 2016.

[48] F. Alambeigi, R. Seifabadi, and M. Armand, "A continuum manipulator with phase changing alloy," in *IEEE International Conference on Robotics and Automation*, vol. 2016-June, (Stockholm, Sweden), pp. 758–764, IEEE, May 2016.

[49] W. Wang, H. Rodrigue, and S.-H. Ahn, "Deployable Soft Composite Structures," *Scientific Reports*, vol. 6, no. November 2015, pp. 20869–20869, 2016.

[50] N. G. Cheng, A. Gopinath, L. Wang, K. Iagnemma, and A. E. Hosoi, "Thermally Tunable, Self-Healing Composites for Soft Robotic Applications," *Macromolecular Materials and Engineering*, vol. 299, pp. 1279–1284, Nov. 2014.

[51] Y. Yang and Y. Chen, "Novel design and 3d printing of variable stiffness robotic fingers based on shape memory polymer," in *2016 6th IEEE International Conference on Biomedical Robotics and Biomechatronics (BioRob)*, pp. 195–200, June 2016.

[52] Y. Yang, Y. Chen, Y. Li, and M. Z. Chen, "3d printing of variable stiffness hyper - redundant robotic arm," (Stockholm, Sweden), pp. 3871–3877, 2016.

[53] J. I. Lipton and H. Lipson, "3d Printing Variable Stiffness Foams Using Viscous Thread Instability," *Scientific Reports*, vol. 6, pp. 29996–29996, Aug. 2016.

[54] Y. Yang, Y. H. Chen, Y. Wei, and Y. Li, "Novel Design and 3d Printing of Variable Stiffness Robotic Grippers," *Journal of Mechanisms and Robotics*, vol. 8, no. c, 2016.

[55] M. C. Yuen, R. A. Bilodeau, and R. K. Kramer, "Active Variable Stiffness Fibers for Multifunctional Robotic Fabrics," vol. 1, no. 2, pp. 708–715, 2016. 00002.

[56] Y. Yao, T. Zhou, J. Wang, Z. Li, H. Lu, Y. Liu, and J. Leng, "Two way shape memory composites based on electroactive polymer and thermoplastic membrane," *Composites Part A: Applied Science and Manufacturing*, vol. 90, pp. 502–509, 2016. 00000.

[57] Y. Chen, J. H. Chang, A. S. Greenlee, K. C. Cheung, A. H. Slocum, and R. Gupta, "Multi-turn, tension-stiffening catheter navigation system," in *Proceedings - IEEE International Conference on Robotics and Automation*, pp. 5570–5575, 2010.

[58] M. S. Moses, M. D. M. Kutzer, H. Ma, and M. Armand, "A continuum manipulator made of interlocking fibers," 2013.

[59] A. Shiva, A. Stilli, Y. Noh, A. Faragasso, I. D. Falco, G. Gerboni, M. Cianchetti, A. Menciassi, K. Althoefer, and H. A. Wurdemann, "Tendon-Based Stiffening for a Pneumatically Actuated Soft Manipulator," *IEEE Robotics and Automation Letters*, vol. 1, no. 2, pp. 632–637, 2016.

[60] T. Ranzani, G. Gerboni, M. Cianchetti, and A. Menciassi, "A bioinspired soft manipulator for minimally invasive surgery," *Bioinspiration & Biomimetics*, vol. 10, p. 035008, May 2015.

[61] Y.-J. J. Kim, S. Cheng, S. Kim, and K. Iagnemma, "A novel layer jamming mechanism with tunable stiffness capability for minimally invasive surgery," *IEEE Transactions on Robotics*, vol. 29, pp. 1031–1042, Aug. 2013.

[62] E. Steltz, a. Mozeika, J. Rembisz, N. Corson, and H. M. Jaeger, "Jamming as an Enabling Technology for Soft Robotics," *Spie*, vol. 7642, pp. 764225–764225, 2010. 00035.

[63] A. Jiang, K. Althoefer, P. Dasgupta, and T. Nanayakkara, "Granular jamming for minimally invasive surgeries," *Journal of Endourology*, vol. 26, pp. A403–A404, 2012.

[64] S. Mintchev and D. Floreano, "Adaptive Morphology: A Design Principle for Multimodal and Multifunctional Robots," *IEEE Robotics & Automation Magazine*, vol. 23, pp. 42–54, Sept. 2016.

[65] Y.-J. Park, J.-G. Lee, S. Jeon, H. Ahn, J. Koh, J. Ryu, M. Cho, and K.-J. Cho, "Dual-stiffness structures with reconfiguring mechanism: Design and investigation," *Journal of Intelligent Material Systems and Structures*, vol. 27, pp. 995–1010, May 2016.

[66] R. Pfeifer, M. Lungarella, and F. Iida, "Self-Organization, Embodiment, and Biologically Inspired Robotics," *Science*, vol. 318, pp. 1088–1093, Nov. 2007.

[67] K. Oliver, A. Seddon, and R. S. Trask, "Morphing in nature and beyond: a review of natural and synthetic shape-changing materials and mechanisms," *Journal of Materials Science*, vol. 51, pp. 10663–10689, Dec. 2016.

[68] R. Pfeifer and J. Bongard, *How the Body Shapes the Way We Think: A New View of Intelligence*. MIT Press, Oct. 2006. Google-Books-ID: EHPMv9MfgWwC.

[69] T. Umedachi, V. Vikas, and B. A. Trimmer, "Softworms : the design and control of non-pneumatic, 3d-printed, deformable robots," *Bioinspiration & Biomimetics*, vol. 11, no. 2, p. 025001, 2016.

[70] K. Yasui, K. Sakai, T. Kano, D. Owaki, and A. Ishiguro, "Decentralized control scheme for myriapod robot inspired by adaptive and resilient centipede locomotion," *PLOS ONE*, vol. 12, p. e0171421, Feb. 2017.

[71] T. Umedachi, K. Takeda, T. Nakagaki, R. Kobayashi, and A. Ishiguro, "Fully decentralized control of a soft-bodied robot inspired by true slime mold," *Biological Cybernetics*, vol. 102, pp. 261–269, Mar. 2010.

[72] T. Sato, T. Kano, and A. Ishiguro, "On the applicability of the decentralized control mechanism extracted from the true slime mold: a robotic case study with a serpentine robot," *Bioinspiration & Biomimetics*, vol. 6, no. 2, p. 026006, 2011.

[73] A. D. Marchese, R. K. Katzschmann, and D. Rus, "A Recipe for Soft Fluidic Elastomer Robots," *Soft Robotics*, vol. 2, pp. 7–25, Mar. 2015.

[74] D. Trivedi, A. Lotfi, and C. D. Rahn, "Geometrically Exact Models for Soft Robotic Manipulators," *IEEE Transactions on Robotics*, vol. 24, pp. 773–780, Aug. 2008.

[75] I. S. Godage, G. A. Medrano-Cerda, D. T. Branson, E. Guglielmino, and D. G. Caldwell, "Dynamics for variable length multisection continuum arms," *The International Journal of Robotics Research*, vol. 35, no. 6, pp. 695–722, 2016.

[76] W. Liu and C. R. Rahn, "Fiber-Reinforced Membrane Models of McKibben Actuators," *Journal of Applied Mechanics*, vol. 70, no. November 2003, pp. 853–853, 2003.

[77] T. E. Pillsbury, Q. Guan, and N. M. Wereley, "Comparison of contractile and extensile pneumatic artificial muscles," in *2016 IEEE International Conference*

on Advanced Intelligent Mechatronics (AIM), (Munich, Germany), pp. 94–99, IEEE, July 2016.

[78] M. Pritts and C. Rahn, "Design of an artificial muscle continuum robot," in *IEEE International Conference on Robotics and Automation (ICRA)*, (Barcelona, Spain), pp. 4742–4746 Vol.5, IEEE, 2004.

[79] D. Trivedi, A. Lotfi, and C. D. Rahn, "Geometrically exact dynamic models for soft robotic manipulators," *IEEE International Conference on Intelligent Robots and Systems*, vol. 24, no. 4, pp. 1497–1502, 2007. 00036.

[80] S. M. H. Sadati, I. D. Walker, L. Sullivan, K. Althoefer, and T. Nanayakkara, "3d-Printable Thermoactive Helical Interface with Decentralized Morphological Stiffness Control for Continuum Manipulators," *IEEE Robotics and Automation Letters*, 2018.

[81] S. M. H. Sadati, S. E. Naghibi, I. D. Walker, K. Althoefer, and T. Nanayakkara, "Control Space Reduction and Real-Time Accurate Modeling of Continuum Manipulators Using Ritz and Ritz #8211;Galerkin Methods," *IEEE Robotics and Automation Letters*, vol. 3, pp. 328–335, Jan. 2018.

[82] S. Sadati, S. E. Naghibi, A. Shiva, Y. Noh, A. Gupta, I. D. Walker, K. Althoefer, and T. Nanayakkara, "A Geometry Deformation Model for Braided Continuum Manipulators," *Frontiers in Robotics and AI*, vol. 4, June 2017.

[83] J. Konstantinova, H. Wurdemann, and A. Shafti, *Soft and Stiffness-controllable Robotics Solutions for Minimally Invasive Surgery:*. River Publishers, Apr. 2018.

[84] S. Sadati, S. E. Naghibi, A. Shiva, I. D. Walker, K. Althoefer, and T. Nanayakkara, "Mechanics of Continuum Manipulators, A Comparative Study of Five Methods with Experiments," (Surrey, UK), Springer, 2017.

[85] S. Sadati, A. Shiva, A. Ataka, S. E. Naghibi, I. D. Walker, K. Althoefer, and T. Nanayakkara, "A Geometry Deformation Model for Compound Continuum

Manipulators with External Loading," in *2016 IEEE International Conference on Robotics and Automation (ICRA)*, (Stockholm, Sweden), pp. 4957–4962, IEEE, 2016.

[86] H. Afrisal, S. Sadati, and T. Nanayakkara, "A Bio-Inspired Electro-Active Velcro Mechanism Using Shape Memory Alloy for Wearable and Stiffness Controllable Layers," in *Information and Automation for Sustainability (ICIAfS), 9th Int. Conf. on*, pp. 1–6, IEEE, 2016.

[87] S. Sadati, S. Naghibi, and M. Naraghi, "An Automatic Algorithm to Derive Linear Vector Form of Lagrangian Equation of Motion with Collision and Constraint," *Procedia Computer Science*, vol. 76, pp. 217–222, 2015.

[88] M. Zheng, S. M. H. Sadati, P. Ghalamchi, and T. Nanayakkara, "Passive dynamics of high frequency bat wing flapping with an anisotropic membrane," in *7th International Conference on Information and Automation for Sustainability*, pp. 1–6, Dec. 2014.

[89] S. Hirose and M. Mori, "Biologically inspired snake-like robots," in *Robotics and Biomimetics, ROBIO 2004. IEEE International Conference on*, (Shenyang, China), pp. 1–7, IEEE, 2004.

[90] D. Rus and M. T. Tolley, "Design, fabrication and control of soft robots," *Nature*, vol. 521, no. 7553, pp. 467–475, 2015.

[91] M. Neumann and J. Burgner-Kahrs, "Considerations for Follow-the-Leader Motion of Extensible Tendon-driven Continuum Robots," 2016.

[92] I. S. Godage, D. T. Branson, E. Guglielmino, G. A. Medrano-Cerda, and D. G. Caldwell, "Shape function-based kinematics and dynamics for variable length continuum robotic arms," in *2011 IEEE International Conference on Robotics and Automation (ICRA)*, (Shanghai, China), pp. 452–457, IEEE, May 2011.

[93] I. S. Godage, R. Wirz, I. D. Walker, and R. J. Webster, "Accurate and Efficient Dynamics for Variable-Length Continuum Arms: A Center of Gravity Approach," *Soft Robotics*, vol. 2, pp. 96–106, Sept. 2015.

[94] Y. Shapiro, A. Wolf, and K. Gabor, "Bi-bellows: Pneumatic bending actuator," *Sensors and Actuators A: Physical*, vol. 167, pp. 484–494, June 2011.

[95] J. Fra, J. Czarnowski, M. Macia, and J. Glwka, "Static modeling of multisection soft continuum manipulator for stiff-flop project," in *Recent Advances in Automation, Robotics and Measuring Techniques*, vol. 267, pp. 365–375, Springer, 2014.

[96] E. Tatlicioglu, I. D. Walker, and D. M. Dawson, "Dynamic modelling for planar extensible continuum robot manipulators," in *IEEE International Conference on Robotics and Automation (ICRA)*, (Rome, Italy), pp. 1357–1362, IEEE, 2007.

[97] G. Chen, M. T. Pham, and T. Redarce, "Sensor-based guidance control of a continuum robot for a semi-autonomous colonoscopy," *Robotics and Autonomous Systems*, vol. 57, no. 6-7, pp. 712–722, 2009.

[98] C. Duriez and T. Bieze, "Soft Robot Modeling, Simulation and Control in Real-Time," in *Soft Robotics: Trends, Applications and Challenges*, vol. 12 of *Biosystems & Biorobotics*, pp. 103–109, Springer, 1 ed., 2017.

[99] I. Tunay, "Spatial continuum models of rods undergoing large deformation and inflation," *IEEE Transactions on Robotics*, vol. 29, no. 2, pp. 297–307, 2013. 00000.

[100] M. Khadem, C. Rossa, R. S. Sloboda, N. Usmani, and M. Tavakoli, "Ultrasound-Guided Model Predictive Control of Needle Steering in Biological Tissue," *Journal of Medical Robotics Research*, vol. 01, p. 1640007, Mar. 2016.

[101] V. Falkenhahn, T. Mahl, A. Hildebrandt, R. Neumann, and O. Sawodny, "Dynamic Modeling of Bellows-Actuated Continuum Robots Using the EulerLa-

grange Formalism," *IEEE Transactions on Robotics*, vol. 31, pp. 1483–1496, Dec. 2015.

[102] C. Duriez and C. Duriez, "Finite Element Method Control of Elastic Soft Robots based on Real-Time Finite Element Method," 2013. 00023.

[103] A. N. Gent, *Engineering with rubber: how to design rubber components*. Munich, Germany: Hanser Publishers, 2012.

[104] J. Jung, R. S. Penning, and M. R. Zinn, "A modeling approach for robotic catheters: effects of nonlinear internal device friction," *Advanced Robotics*, vol. 28, pp. 557–572, Apr. 2014.

[105] O. C. Zienkiewicz, R. L. Taylor, O. C. Zienkiewicz, and R. L. Taylor, *The finite element method*, vol. 3. McGraw-hill London, 1977.

[106] M. Mahvash and P. E. Dupont, "Stiffness control of surgical continuum manipulators," *IEEE Transactions on Robotics*, vol. 27, no. 2, pp. 334–345, 2011.

[107] R. C. Juvinall and K. M. Marshek, *Fundamentals of machine component design*, vol. 83. John Wiley & Sons New York, 2006.

[108] T. Mahl, A. E. Mayer, A. Hildebrandt, and O. Sawodny, "A variable curvature modeling approach for kinematic control of continuum manipulators," in *2013 American Control Conference*, pp. 4945–4950, June 2013.

[109] I. D. Walker, "Continuous Backbone "Continuum" Robot Manipulators," *International Scholarly Research Notices (ISRN Robotics)*, vol. 2013, p. e726506, July 2013.

[110] A. Jiang, G. Xynogalas, P. Dasgupta, K. Althoefer, and T. Nanayakkara, "Design of a variable stiffness flexible manipulator with composite granular jamming and membrane coupling," in *2012 IEEE/RSJ International Conference on Intelligent Robots and Systems*, (Vilamoura-Algarve, Portugal), pp. 2922–2927, IEEE, Oct. 2012.

[111] I. K. Kuder, A. F. Arrieta, W. E. Raither, and P. Ermanni, "Variable stiffness material and structural concepts for morphing applications," *Progress in Aerospace Sciences*, vol. 63, pp. 33–55, 2013. 00000.

[112] S. Follmer, D. Leithinger, A. Olwal, N. Cheng, and H. Ishii, "Jamming user interfaces: programmable particle stiffness and sensing for malleable and shape-changing devices," in *Proceedings of the 25th annual ACM symposium on User interface software and technology*, (Cambridge, Massachusetts, USA), pp. 519–528, ACM, 2012.

[113] R. S. Rivlin, "Large Elastic Deformations of Isotropic Materials. V. The Problem of Flexure," *Proceedings of the Royal Society A: Mathematical, Physical and Engineering Sciences*, vol. 195, no. 1043, pp. 463–473, 1949.

[114] N. Giri and I. D. Walker, "Three module lumped element model of a continuum arm section," in *IEEE International Conference on Intelligent Robots and Systems (IROS)*, (San Francisco, California, USA), pp. 4060–4065, IEEE, 2011.

[115] C. Cohen, B. Hiott, A. D. Kapadia, and I. D. Walker, "Robot tongues in space: continuum surfaces for robotic grasping and manipulation," vol. 9836, p. 98362B, International Society for Optics and Photonics, May 2016.

[116] B. Tondu and P. Lopez, "Modeling and control of McKibben artificial muscle robot actuators," *IEEE control systems*, vol. 20, no. 2, pp. 15–38, 2000. 00000.

[117] E. L. Rees, "Graphical Discussion of the Roots of a Quartic Equation," *Source: The American Mathematical Monthly*, vol. 29, pp. 51–55, Feb. 1922.

[118] R. S. Rivlin, "Large Elastic Deformations of Isotropic Materials. IV. Further Developments of the General Theory," *Philosophical Transactions of the Royal Society A: Mathematical, Physical and Engineering Sciences*, vol. 241, no. 835, pp. 379–397, 1948. 00000.

[119] M. Powell, "A Fortran subroutine for solving systems of non-linear algebraic equations," in *Numerical Methods for Nonlinear Algebraic Equations*, vol. 7, p. 199, London, United Kingdom: Gordon and Breach, 1970.

[120] P. Polygerinos, Z. Wang, J. T. B. Overvelde, K. C. Galloway, R. J. Wood, K. Bertoldi, and C. J. Walsh, "Modeling of Soft Fiber-Reinforced Bending Actuators," *IEEE Transactions on Robotics*, vol. 31, pp. 778–789, June 2015.

[121] J. S. Hesthaven, S. Gottlieb, and D. Gottlieb, *Spectral methods for time-dependent problems*, vol. 21. Cambridge University Press, 2007.

[122] A. Bajo and N. Simaan, "Hybrid motion/force control of multi-backbone continuum robots," *The International Journal of Robotics Research*, p. 0278364915584806, July 2015.

[123] N. Sornkarn, M. Howard, and T. Nanayakkara, "Internal impedance control helps information gain in embodied perception," *Proceedings - IEEE International Conference on Robotics and Automation*, pp. 6685–6690, 2014. 00000.

[124] T. R. Faisal, E. M. Khalil Abad, N. Hristozov, and D. Pasini, "The Impact of Tissue Morphology, Cross-Section and Turgor Pressure on the Mechanical Properties of the Leaf Petiole in Plants," *Journal of Bionic Engineering*, vol. 7, pp. S11–S23, Sept. 2010.

[125] L. Tadrist and B. Darbois-Texier, "Are leaves optimally designed for self-support? An investigation on giant monocots," *Journal of Theoretical Biology*, vol. 396, pp. 125–131, May 2016.

[126] T. M. Huh, Y.-J. Park, and K.-J. Cho, "Design and analysis of a stiffness adjustable structure using an endoskeleton," *International Journal of Precision Engineering and Manufacturing*, vol. 13, pp. 1255–1258, July 2012.

[127] A. Degani, H. Choset, A. Wolf, and M. Zenati, "Highly articulated robotic probe for minimally invasive surgery," in *Proceedings 2006 IEEE International*

Conference on Robotics and Automation, 2006. ICRA 2006., pp. 4167–4172, IEEE, 2006.

[128] R. H. Sturges and S. Laowattana, "A Flexible, Tendon-Controlled Device for Endoscopy," *The International Journal of Robotics Research*, vol. 12, pp. 121–131, Apr. 1993.

[129] T. Ota, A. Degani, D. Schwartzman, B. Zubiate, J. McGarvey, H. Choset, and M. A. Zenati, "A Highly Articulated Robotic Surgical System for Minimally Invasive Surgery," *The Annals of Thoracic Surgery*, vol. 87, no. 4, pp. 1253–1256, 2009.

[130] J. Jung, R. S. Penning, N. J. Ferrier, and M. R. Zinn, "A modeling approach for continuum robotic manipulators: Effects of nonlinear internal device friction," in *Intelligent Robots and Systems (IROS), 2011 IEEE/RSJ International Conference on*, pp. 5139–5146, IEEE, 2011.

[131] G. S. Raju, D. K. Rex, R. A. Kozarek, I. Ahmed, D. Brining, and P. J. Pasricha, "A novel shape-locking guide for prevention of sigmoid looping during colonoscopy," *Gastrointestinal Endoscopy*, vol. 59, pp. 416–419, Mar. 2004.

[132] D. K. Rex, M. Khashab, G. S. Raju, J. Pasricha, and R. Kozarek, "Insertability and safety of a shape-locking device for colonoscopy," *The American Journal of Gastroenterology*, vol. 100, pp. 817–820, Apr. 2005.

[133] L. L. Swanstrom, R. Kozarek, P. J. Pasricha, S. Gross, D. Birkett, P.-O. Park, V. Saadat, R. Ewers, and P. Swain, "Development of a new access device for transgastric surgery," *Journal of Gastrointestinal Surgery: Official Journal of the Society for Surgery of the Alimentary Tract*, vol. 9, pp. 1129–1136; discussion 1136–1137, Nov. 2005.

[134] A. Degani, H. Choset, A. Wolf, T. Ota, and M. Zenati, "Percutaneous Intrapericardial Interventions Using a Highly Articulated Robotic Probe," in

The First IEEE/RAS-EMBS International Conference on Biomedical Robotics and Biomechatronics, 2006. BioRob 2006., pp. 7–12, IEEE, 2006.

[135] Y. J. Kim, S. Cheng, S. Kim, and K. Iagnemma, "A Stiffness-Adjustable Hyperredundant Manipulator Using a Variable Neutral-Line Mechanism for Minimally Invasive Surgery," *IEEE Transactions on Robotics*, vol. 30, pp. 382–395, Apr. 2014.

[136] E. Brown, N. Rodenberg, J. Amend, A. Mozeika, E. Steltz, M. R. Zakin, H. Lipson, and H. M. Jaeger, "Universal robotic gripper based on the jamming of granular material," *Proceedings of the National Academy of Sciences*, vol. 107, pp. 18809–18814, Nov. 2010.

[137] J. R. Amend, E. Brown, N. Rodenberg, H. M. Jaeger, and H. Lipson, "A Positive Pressure Universal Gripper Based on the Jamming of Granular Material," *IEEE Transactions on Robotics*, vol. 28, pp. 341–350, Apr. 2012.

[138] H. M. Jaeger, "Celebrating Soft Matters 10th Anniversary: Toward jamming by design," *Soft Matter*, vol. 11, pp. 12–27, Dec. 2014.

[139] A. J. Loeve, O. S. v. d. Ven, J. G. Vogel, P. Breedveld, and J. Dankelman, "Vacuum packed particles as flexible endoscope guides with controllable rigidity," *Granular Matter*, vol. 12, pp. 543–554, Dec. 2010.

[140] R. M. Letts and D. A. Hobson, "The vacuum splint: an aid in emergency splinting of fractures," *Canadian Medical Association Journal*, vol. 109, pp. 599–600, Oct. 1973.

[141] Y. Wei, Y. Chen, T. Ren, Q. Chen, C. Yan, Y. Yang, and Y. Li, "A Novel, Variable Stiffness Robotic Gripper Based on Integrated Soft Actuating and Particle Jamming," *Soft Robotics*, vol. 3, pp. 134–143, July 2016.

[142] Y. J. Kim, S. Cheng, S. Kim, and K. Iagnemma, "Design of a tubular snake-like manipulator with stiffening capability by layer jamming," in *2012 IEEE/RSJ*

International Conference on Intelligent Robots and Systems, pp. 4251–4256, Oct. 2012.

[143] S. Zuo, K. Iijima, T. Tokumiya, and K. Masamune, "Variable stiffness outer sheath with Dragon skin structure and negative pneumatic shape-locking mechanism," *International Journal of Computer Assisted Radiology and Surgery*, vol. 9, pp. 857–865, Sept. 2014.

[144] A. Yagi, K. Matsumiya, K. Masamune, H. Liao, and T. Dohi, "Rigid-Flexible Outer Sheath Model Using Slider Linkage Locking Mechanism and Air Pressure for Endoscopic Surgery," in *Medical Image Computing and Computer-Assisted Intervention MICCAI 2006*, Lecture Notes in Computer Science, pp. 503–510, Springer, Berlin, Heidelberg, Oct. 2006.

[145] A. J. Loeve, D. H. Plettenburg, P. Breedveld, and J. Dankelman, "Endoscope Shaft-Rigidity Control Mechanism: FORGUIDE," *IEEE Transactions on Biomedical Engineering*, vol. 59, pp. 542–551, Feb. 2012.

[146] J. L. C. Santiago, I. D. Walker, and I. S. Godage, "Continuum robots for space applications based on layer-jamming scales with stiffening capability," in *2015 IEEE Aerospace Conference*, pp. 1–13, IEEE, Mar. 2015.

[147] J. Ou, L. Yao, D. Tauber, J. Steimle, R. Niiyama, and H. Ishii, "jamSheets: Thin Interfaces with Tunable Stiffness Enabled by Layer Jamming," in *Proceedings of the 8th International Conference on Tangible, Embedded and Embodied Interaction*, TEI '14, (New York, NY, USA), pp. 65–72, ACM, 2013.

[148] J. Long, M. Hale, M. Mchenry, and M. Westneat, "Functions of fish skin: flexural stiffness and steady swimming of longnose gar, Lepisosteus osseus," *Journal of Experimental Biology*, vol. 199, pp. 2139–2151, Oct. 1996.

[149] R. K. Chintapalli, S. Breton, A. K. Dastjerdi, and F. Barthelat, "Strain rate hardening: A hidden but critical mechanism for biological composites?," *Acta Biomaterialia*, vol. 10, no. 12, pp. 5064–5073, 2014. 00006.

[150] P. Y. Chen, J. McKittrick, and M. A. Meyers, "Biological materials: Functional adaptations and bioinspired designs," *Progress in Materials Science*, vol. 57, no. 8, pp. 1492–1704, 2012.

[151] W. Yang, B. Gludovatz, E. A. Zimmermann, H. A. Bale, R. O. Ritchie, and M. A. Meyers, "Structure and fracture resistance of alligator gar (Atractosteus spatula) armored fish scales," *Acta Biomaterialia*, vol. 9, no. 4, pp. 5876–5889, 2013.

[152] B. J. F. Bruet, J. Song, M. C. Boyce, and C. Ortiz, "Materials design principles of ancient fish armour.," *Nature materials*, vol. 7, no. 9, pp. 748–56, 2008. 00000.

[153] A. Khayer Dastjerdi and F. Barthelat, "Teleost fish scales amongst the toughest collagenous materials," *Journal of the Mechanical Behavior of Biomedical Materials*, vol. 52, pp. 95–107, 2015. 00000.

[154] R. K. Chintapalli, M. Mirkhalaf, A. K. Dastjerdi, and F. Barthelat, "Fabrication, testing and modeling of a new flexible armor inspired from natural fish scales and osteoderms.," *Bioinspiration & biomimetics*, vol. 9, no. 3, pp. 036005–036005, 2014.

[155] A. Browning, C. Ortiz, and M. C. Boyce, "Mechanics of composite elasmoid fish scale assemblies and their bioinspired analogues," *Journal of the Mechanical Behavior of Biomedical Materials*, vol. 19, pp. 75–86, 2013.

[156] Y. Chuaa, E. Lawb, F. Teoa, M. Kanga, S. Panga, and S. Queka, "BIO-INSPIRED FISHSCALE-CELLULAR COMPOSITE SYSTEM FOR PROTECTION AGAINST PENETRATION LOADS: A PROOF OF CONCEPT STUDY," 2014.

[157] X. Xiang, F. Long, A. Narkar, R. E. Kinnunen, R. Shahbazian-Yassar, B. P. Lee, and P. A. Heiden, "Is there value in chemical modification of fish scale

surfaces?," *Journal of Applied Polymer Science*, vol. 133, no. 3, pp. n/a–n/a, 2016. 00000.

[158] B. Dean and B. Bhushan, "Shark-skin surfaces for fluid-drag reduction in turbulent flow: a review," *Philosophical Transactions of the Royal Society of London A: Mathematical, Physical and Engineering Sciences*, vol. 368, pp. 4775–4806, Oct. 2010.

[159] B. C. Jayne, "Mechanical behaviour of snake skin," *Journal of Zoology*, vol. 214, no. 1, pp. 125–140, 1988.

[160] A. Marino Cugno Garrano, G. La Rosa, D. Zhang, L. N. Niu, F. R. Tay, H. Majd, and D. Arola, "On the mechanical behavior of scales from Cyprinus carpio," *Journal of the Mechanical Behavior of Biomedical Materials*, vol. 7, pp. 17–29, 2012.

[161] X. Song, H. Liu, K. Althoefer, T. Nanayakkara, and L. D. Seneviratne, "Efficient break-away friction ratio and slip prediction based on haptic surface exploration," *IEEE Transactions on Robotics*, vol. 30, no. 1, pp. 203–219, 2014. 00000.

[162] J. Jalbert, S. Kashin, and J. Ayers, *Design considerations and experiments of a biologically based undulatory lamprey AUV*. Jan. 1995.

[163] M. B. Wooten and I. D. Walker, "A Novel Vine-Like Robot for In-Orbit Inspection," 2015.